Enhancement of temperature diagnostics with application to dynamically compressed materials



Thomas Ota

Wolfson College

University of Oxford

A thesis submitted for the degree of

Doctor of Philosophy

Michaelmas 2019

UK Ministry of Defence ©Crown Owned Copyright 2019/AWE

Acknowledgements

This work was funded by AWE Plc. and the EPSRC and I am thankful for their support.

I must first acknowledge my supervisor, Dr. Daniel Eakins whose has been readily available to discuss results and share his insights. I also thank my co-supervisor Dr. David Chapman whose experimental expertise and dedication to maintaining high standards have ensured the quality of the results presented here.

A not inconsiderable portion of the work presented here derives from a collaboration with scientists at Los Alamos National Laboratory and undoubtedly the most significant figure in that collaboration was Dr. David Holtkamp; his untimely passing is a great loss. I also thank Dr. Neil Holmes and Dr. Minta Akin for their helpful discussions and providing the 'slurry recipe' which dramatically improved results.

For their instrumental roles in the conduct of the experiments I thank Dave Pitman and Rob Denning for operating the gas gun facility. I particularly thank them for their good spirits when my plans forced them to work in full coveralls in the compact confines of a tent. Two colleagues, Dr. James Richley and Dr. Mark Collinson were also extremely helpful in the fielding of a number of experiments.

Lastly, I thank my wife. This work has taken a long time and it is impossible to complete such an endeavour without support, which you have always provided.

Abstract

The behaviour of materials at high pressure is relevant for a number of fields, including defence, aerospace and Earth and planetary science where understanding of material behaviour under high strain-rate conditions such as impacts is required. State variables such as pressure and density are readily accessible in shock experiments but determination of temperature remains challenging.

Temperature affects material behaviour substantially, thus the determination of temperature in materials at high pressure (giga-Pascal range) enables progress in the fields noted above. This thesis outlines improvements to the technique of pyrometry which is a widely used diagnostic for determining temperature in shock experiments. Despite the popularity of pyrometry, concerns remain regarding the significance of different uncertainties and equivalence of independently-developed systems.

The primary goal of this research has been to improve the technique of pyrometry; this has been accomplished in a number of areas. First, an extensive review of potential components and their impact on pyrometer operation has been completed which more clearly defines the sources of uncertainty in pyrometry systems. Second, collaborative experiments have allayed concerns about the validity of comparisons of measurements from differing pyrometry systems. Finally, an integrated reflectivity diagnostic has been developed and demonstrated which enables simultaneous measurement of radiance and reflectivity, removing reliance on assumptions to determine temperature.

In addition to diagnostic development, equation of state (EoS) measurements on tin and lead have been made. Measurements of shock speed, particle velocity and radiance (converted to temperature) have been made during plate impact experiments. Results obtained from tin have validated existing EoS models however small but significant differences were identified. The measurements of lead temperature have been inconsistent, the results could indicate a phase transition.

In summary, the work presented here provides a clear framework for understanding uncertainties in pyrometry and has demonstrated multiple practical improvements to the technique.

Contents

1 Introduction **1**
- 1.1 High pressure behaviour of materials . . . 1
- 1.2 Introduction to shockwaves . . . 5
- 1.3 The need for temperature data . . . 8
- 1.4 The rationale for pyrometry . . . 11
- 1.5 Potential areas for development . . . 14

2 Introduction to pyrometry **17**
- 2.1 Pyrometry Background . . . 17
- 2.2 Evolution of high-speed pyrometry . . . 20
- 2.3 Pyrometer design discussion . . . 24
  - 2.3.1 Radiometry system . . . 24
  - 2.3.2 Design of radiometry system . . . 30
  - 2.3.3 Pyrometry probe head . . . 32
- 2.4 Laboratory testing . . . 34
  - 2.4.1 Time resolution . . . 34
  - 2.4.2 Spatial resolution . . . 36
  - 2.4.3 Minimum measurable temperature . . . 38
- 2.5 Summary . . . 39

3 Sources of uncertainty in pyrometry **41**
- 3.1 Introduction . . . 41
- 3.2 Sources of uncertainty in surface temperature . . . 41
  - 3.2.1 Sources of measurement noise . . . 42
  - 3.2.2 Emissivity uncertainty . . . 45
  - 3.2.3 Non-thermal signals . . . 46
- 3.3 Sources of uncertainty due to interface effects . . . 47
  - 3.3.1 Heat transport at an interface . . . 48
  - 3.3.2 Uncertainty in diffusivity ratio . . . 50
  - 3.3.3 Estimate of high pressure diffusivity . . . 54
- 3.4 Shock state uncertainties . . . 54
- 3.5 Predicted measurement effect . . . 57
- 3.6 Summary and conclusions . . . 58

4 Investigation of the effect of filter parameters on pyrometry accuracy 61
4.1 Introduction . . . 61
4.2 Background . . . 62
4.3 Development of a Monte-Carlo model . . . 63
4.3.1 Calculation of radiance . . . 63
4.3.2 Noise model . . . 66
4.4 Model validation experiments . . . 67
4.5 Monte-Carlo Model Results . . . 71
4.5.1 λ_c variation . . . 71
4.5.2 $\Delta\lambda$ variation . . . 73
4.5.3 Multiple passbands . . . 74
4.5.4 Simultaneous variation of λ_c and $\Delta\lambda$ . . . 74
4.6 Conclusions . . . 77

5 100 mm bore plate impact experiments 81
5.1 Introduction . . . 81
5.2 Plate impact overview . . . 81
5.3 Experiment design . . . 84
5.3.1 High speed sabot . . . 85
5.3.2 Impactor material selection . . . 86
5.3.3 Window material selection . . . 87
5.3.4 Sample material selection . . . 88
5.3.5 Pyrometer system . . . 89
5.3.6 PDV diagnostic . . . 91
5.3.7 Triggering . . . 93
5.3.8 Target geometry . . . 93
5.3.9 Target assembly process . . . 97
5.4 Results . . . 97
5.4.1 Experiment 1 . . . 98
5.4.2 Analysis of experiment 1 . . . 98
5.4.3 Experiment 2 . . . 101
5.4.4 Analysis of experiment 2 . . . 102
5.5 Conclusions . . . 103

6 Comparative experiments on a 100 mm bore gas gun 107
6.1 Experiment Overview . . . 107
6.2 Pyrometer systems . . . 108
6.2.1 Pyrometer 1 . . . 109
6.2.2 Pyrometer 2 . . . 109
6.2.3 Pyrometer 3 . . . 112

6.3 Experimental Design . . . 114
6.3.1 Sample material selection . . . 114
6.3.2 Target configuration . . . 115
6.3.3 Velocity Diagnostics . . . 116
6.3.4 Calibration . . . 117
6.4 Results . . . 119
6.5 Sample emissivity . . . 120
6.6 Temperature analysis . . . 122
6.7 Conclusions . . . 126

7 Radiance measurements of lead (Pb) during plate impact 131
7.1 Introduction . . . 131
7.2 Experiment overview . . . 131
7.2.1 Experiment design . . . 132
7.2.2 Target geometry . . . 135
7.2.3 Target assembly . . . 136
7.2.4 PDV diagnostic . . . 136
7.2.5 Radiometry system . . . 137
7.3 Results . . . 138
7.3.1 Experiment 1, Sn sample, 1556 m·s^{-1} impact . . . 138
7.3.2 Experiment 2, Pb target, 1433 m·s^{-1} impact . . . 140
7.3.3 Experiment 3, Pb target, 1233 m·s^{-1} impact . . . 141
7.3.4 Analysis of experiment 1 . . . 141
7.3.5 Analysis of experiment 2 . . . 142
7.3.6 Analysis of experiment 3 . . . 145
7.3.7 P-T phase diagram . . . 147
7.4 Summary . . . 147

8 Measurement of reflectivity at high strain rate 149
8.1 Overview . . . 149
8.2 Importance of emissivity measurements . . . 149
8.3 Review of high speed reflectivity literature . . . 151
8.4 Laboratory measurements of reflectivity . . . 154
8.5 Potential reflectivity diagnostic solutions . . . 157
8.5.1 Initial reflectivity diagnostic concepts . . . 157
8.5.2 Laboratory testing of reflectivity diagnostics . . . 159
8.5.3 Dynamic testing of a reflectivity diagnostic . . . 162
8.5.4 Initial dynamic reflectivity results . . . 163
8.5.5 Dual wavelength testing . . . 168
8.5.6 Results and analysis . . . 172
8.5.7 Conclusions . . . 176

9 Summary and conclusions **179**
9.1 Advances in radiometer design . . . 180
9.2 A high performance pyrometer . . . 181
9.3 Improved confidence in shock pyrometry . . . 182
9.4 Integrated reflectivity measurement . . . 182
9.5 Additional shock temperature data . . . 184
9.5.1 Tin data . . . 184
9.5.2 Lead data . . . 185
9.6 Additional information on LiF luminescence . . . 186
9.7 Future work . . . 188

Appendices

A Calibration and analysis **193**
A.1 Calibration procedure . . . 193
A.2 Analysis . . . 196
A.3 Voltage to temperature analysis script . . . 196
A.4 Filtering of radiance data . . . 197
A.4.1 Filtering example . . . 198
A.5 ZEMAX probe modelling . . . 199
A.6 STFT Analysis . . . 200

B Supplementary experimental results **205**
B.1 Initial 100 mm bore plate impact experiments . . . 205
B.2 Glue thickness measurements for collaborative experiments . . . 208
B.3 Reflectivity experiments . . . 209

C Derivations **211**
C.1 Rankine Hugoniot relations . . . 211
C.2 1D state . . . 215
C.2.1 x-t Diagrams . . . 215
C.2.2 Lateral release waves . . . 216
C.3 A method for the calculation of temperature . . . 216
C.3.1 Shock temperature . . . 216
C.3.2 Calculating the isentrope . . . 217
C.3.3 Calculation of temperature on an isentrope . . . 219
C.3.4 Calculation of release state temperature . . . 220
C.4 Percentage error transformation . . . 221
C.5 Calculation of tilt . . . 222

D Supplementary data **223**
D.1 100 mm gun performance 223
D.2 Reflectivity of tin (Sn) 224
D.3 Reflectivity of lead (Pb) 224

References **227**

1 Introduction

1.1 High pressure behaviour of materials

The study of the behaviour of materials at high pressure (the gigapascal range and above) through shock compression is an exciting and active area of research. Recent results have provided insights for a number of fields, for example studies showing the formation of Lonsdaleite (a carbon allotrope theoretically harder than diamond) at pressures above 170 GPa [1] provide insights into terrestrial meteor impact events. Indicative results confirming the 30 year-old prediction of superionic water at pressures of 190 GPa [2] will improve understanding of the planetary interiors of Neptune and Uranus and studies of aluminium crystal deformation during shock compression [3] are improving understanding of how rapid deformation may affect strength. More broadly, material properties can differ markedly at high pressures. These changes in material properties mean that to model problems in these fields, accurate descriptions of material properties at the relevant physical conditions are necessary.

When describing the behaviour of materials under high pressure loading the equation-of-state (EoS) of a material is often the most significant component of the description of system evolution. An EoS is an expression relating the thermodynamic variables of a material, such as pressure, density and temperature,

at equilibrium (see Figure 1.1). While models parameterising material strength [4–6] and, in the presence of contact surfaces, friction [7, 8] can account for significant components of observed behaviour, the component attributed to the EoS is often larger. Specifically, at stresses significantly above the material strength or the frictional forces present their associated contributions will be minor.

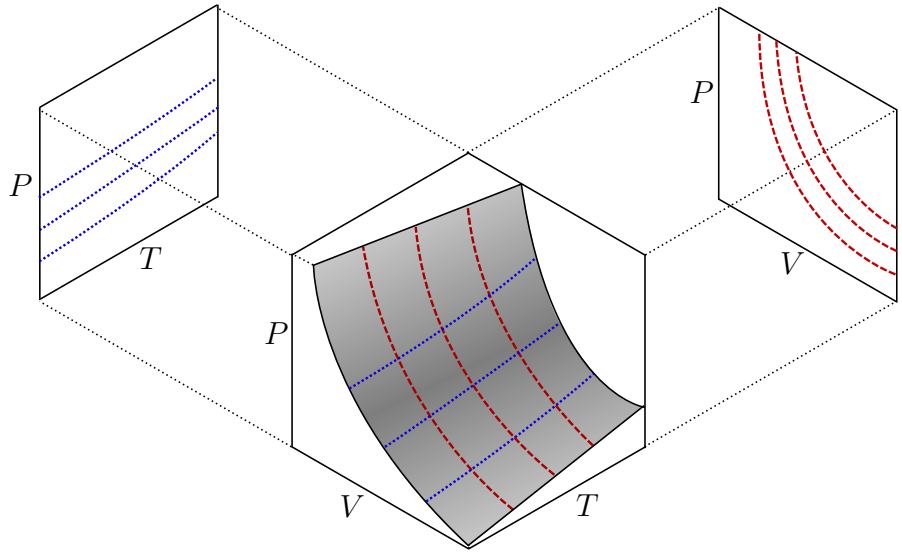


Figure 1.1: Visualisation of the equation of state (EoS) of a material. Lines of constant temperature, T, and volume, V, are projected to form iso-therms (red lines) and isochors (blue lines) in the pressure, P, plane.

A simple example of an EoS is the the 'ideal gas law' which describes the relationship between pressure, P, volume, V and temperature, T, for an ideal gas [9]. The ideal gas law relates three thermodynamic variables by the simple expression,

$$PV = nRT, \tag{1.1}$$

where, in addition to the definitions above, n is the number of moles and R is the gas constant. Most other EoSs are more sophisticated than Equation 1.1 reflecting the higher complexity of non-ideal gas materials, for example many EoSs are able to describe behaviour across phase changes which is beyond an ideal gas description. Nevertheless, the 'ideal gas law' illustrates the utility of EoS in describing material behaviour. Because of the importance of EoS, their development remains an active area of research investigated by both experimental [10, 11] and theoretical techniques [12, 13].

The prevailing experimental techniques for the investigation of high pressure material behaviour are plate impact [14], laser driven shock [15] and diamond anvil cells [16], see Figures 1.2 and 1.3. These three techniques have different advantages and disadvantages which are somewhat complementary.

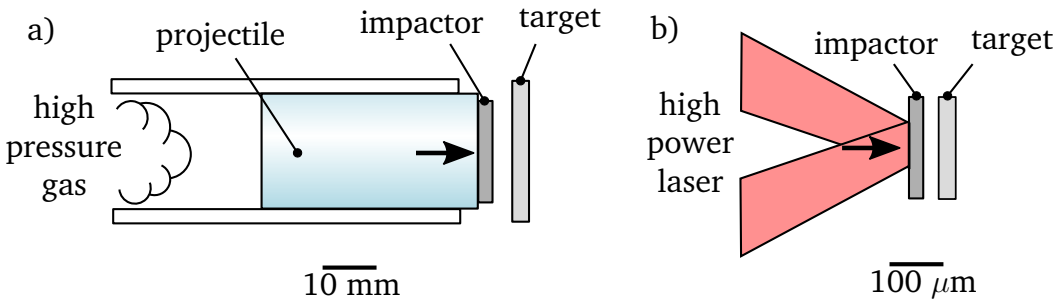


Figure 1.2: Schematic diagrams illustrating a) gas-driven and b) laser-driven impact experiments used to transiently attain high pressure.

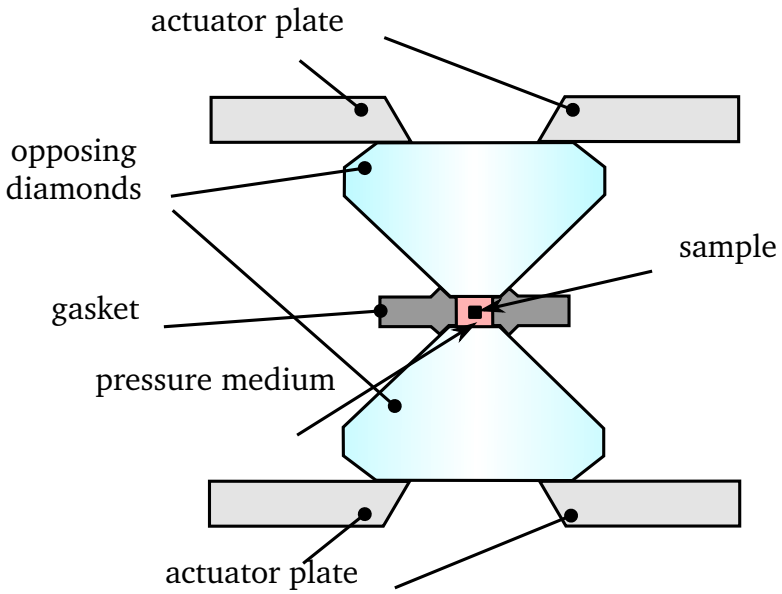


Figure 1.3: Schematic diagram illustrating a common configuration of a diamond anvil cell (DAC) compressing a sample.

Plate impact experiments involve a flat plate which impacts a planar target, the impact induces a high pressure 'shock' state in both the impactor and the target. The shock state is created rapidly, typically reaching full pressure in less than a nanosecond, and lasts for microseconds. The maximum pressure achievable

in plate impact experiments is determined by the attainable impact velocity, velocities of 16 km·s^{-1} have been reported in the literature [17] with attainable pressures of up to 2 TPa. Using energy sources such as nuclear explosions, pressures up to 750 TPa have been quoted [18] (but the associated reference only discusses 70 TPa [19]).

Laser-driven shock experiments are primarily in two configurations, either a scaled down version of a plate impact, where a high power laser is used to accelerate an impactor into a target [20], or a convergent geometry where lasers illuminate a hohlraum target which compresses a sample isotropically [21]. Using the accelerated impactor technique pressures of 40 TPa have been reported [22], although the duration of the experiment was 40 ps. Pressure of 75 TPa have been reported using the hohlraum technique [23].

Diamond anvil cells (DACs) use a different approach; high pressures are created by compressing a sample (with a diameter of $\sim$10 μm) between two diamond 'anvils' [24]. Pressure is typically increased slowly, allowing quasi-static compression, which generates different states in comparison to high strain rate methods (which are closer to an adiabatic process). While DAC techniques are now able to statically generate EoS data at the 100s of GPa pressures [25] there remain some key differences between dynamic and static loading:

- The strain rates in dynamic experiments are many orders of magnitude higher than DAC experiments. The higher strain rate can alter material behaviour significantly [26] and means phenomena with high equilibration times may be inaccessible to dynamic loading [27]. Conversely, the almost instantaneous change of state allows phenomena such as rapid phase change kinetics to be investigated which is not possible with DACs [28].

- Plate impact, particularly on gas gun facilities, supports larger sample sizes allowing macroscopic phenomena such as grain size to be investigated [29]. A significant drawback to DAC is the very small working volume they offer [30].

So although there is considerable overlap between the states achievable with DACs and those achievable with shockwaves, the quasi-static and dynamic techniques are complementary providing cross-validation in many areas. A relatively recent development has been the combination of both DACs and shocks (laser-driven) in a single experiment [31]. Despite these advances plate impact experiments remain an active area for providing data to develop and refine EoSs at high pressure. Shock experiments will be the focus of the following discussions.

1.2 Introduction to shockwaves

Impact experiments create a transient high pressure state, known as a shockwave, in a sample of the material. Like other waves, a shockwave (or 'shock') is a disturbance that transfers energy through a medium. However, shockwaves are non-linear, producing an abrupt change in the properties of the medium. While there is still some uncertainty about the precise mechanisms inside a shockwave, the material state in-front and behind a shockwave can be well-defined. A shock can be visualised by considering a cylindrical section of an infinite domain containing a shock; material ahead of the shock is in one state, material the shock has passed through is in another state, see Figure 1.4.

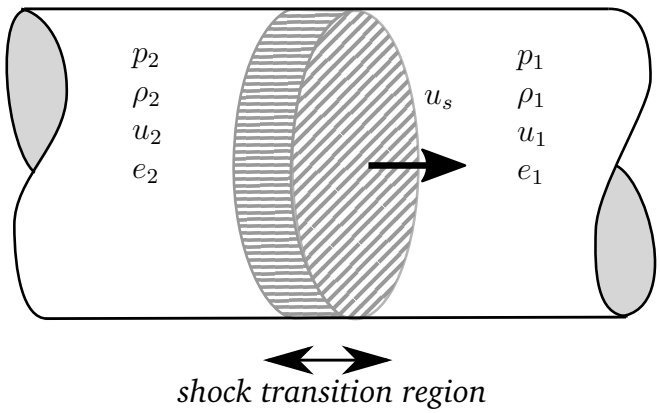


Figure 1.4: Schematic of a shock wave travelling at velocity, u_s, through a medium. As the shock travels through the medium, the properties of the medium (specifically pressure, p, density, ρ, particle velocity, u, and specific internal energy, e) change abruptly to new values.

Due to the almost discontinuous change in properties it is not possible to describe shockwaves using the wave equation, however, some conservation laws are still valid; these conservation laws are known as the Rankine-Hugoniot relations [32, 33]. Before presenting the equations it is helpful to define the concept of 'specific' variables; these are variables that are normalised to unit mass, *e.g.* specific energy is energy per unit mass. The use of specific variables simplifies some of the equations (intrinsic variables, such as pressure, do not have a 'specific' form). From conservation of mass it can be determined that,

$$\rho_1 u_1 = \rho_2 u_2, \tag{1.2}$$

where ρ and u are the density and particle velocity and the subscript denotes whether the variable is ahead, denoted 1, or behind the shock, denoted 2.

From conservation of momentum, it can be determined that,

$$\rho_1 u_1^2 + p_1 = \rho_2 u_2^2 + p_2, \tag{1.3}$$

where, in addition to the previously defined variables, p is pressure and the subscripts are as above.

Finally from conservation of energy, it can be determined that,

$$\rho_1 u_1 \left(e_1 + \frac{1}{2} u_1^2 + \frac{p_1}{\rho_1} \right) = \rho_2 u_2 \left(e_2 + \frac{1}{2} u_2^2 + \frac{p_2}{\rho_2} \right), \tag{1.4}$$

where, in addition to the previously defined variables, e is specific internal energy and the subscripts are as above.

A key benefit of the Rankine-Hugoniot relations is that they allow easily obtained measurements, such as shock velocity and particle velocity, to be related to the state variables pressure and density. Specifically, pressure behind the shock front, p_2, is given by,

$$p_2 = \rho_1 u_s u_p, \tag{1.5}$$

where ρ_1 is the initial density, u_s is the shock velocity and u_p is the particle velocity. Density behind the shock front, ρ_2, is given by,

$$\rho_2 = \rho_1 \left(\frac{u_s}{u_s - u_p} \right). \tag{1.6}$$

However, this expression is more commonly used in a different form, rather than density the specific volume (inverse of density) form is used,

$$v_2 = v_1 \left(\frac{u_s - u_p}{u_s} \right), \tag{1.7}$$

where v_1 is the initial specific volume and v_2 is the specific volume behind the shock. The locus of states that can be reached by shocking a material from an initial state is know as the Hugoniot.

The Hugoniots of an extensive number of materials have been measured. Figure 1.5 illustrates some experimental measurements of shock velocity and particle velocity and their subsequent conversion to pressure-volume data.

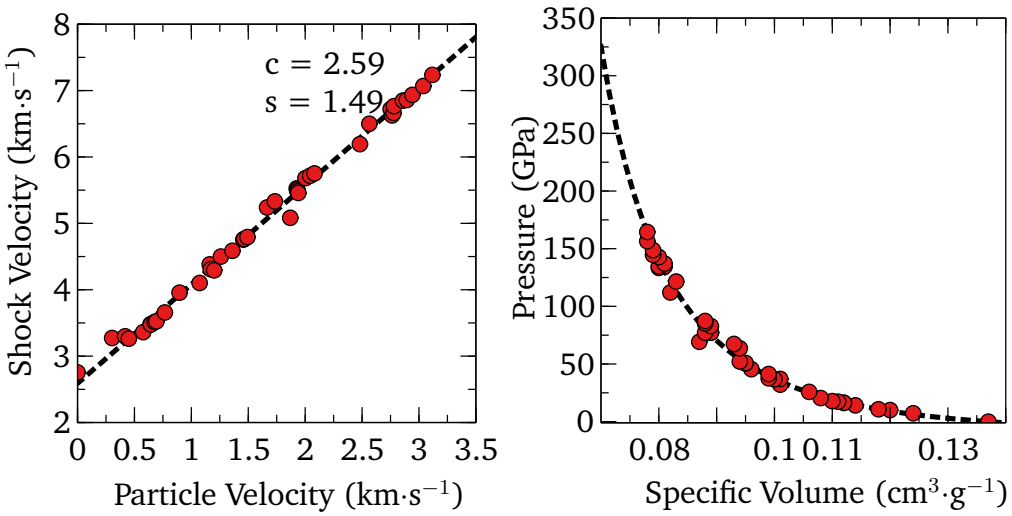


Figure 1.5: Reproduction of results from shock experiments conducted on tin by Marsh *et al*. The original shock velocity and particle velocity measurements are converted into pressure-volume points. The dashed lines represent curves generated by assuming shock velocity, u_s can be linearly related to particle velocity, u_p by the relation $c + su_p$.

It should be noted that as there are four variables, ρ, u, p, e, and three equations it is not possible to solve the expressions above without further information. Often it is an equation-of-state (EoS) that is used to 'close' the problem. Many EoS that extend to high pressures have been created and refined based on the pressure-volume data generated by applying the Rankine-Hugoniot relations to shock experiments. However, it should be noted that, while this approach does generate pressure-volume (P–V) data, it is not thermodynamically complete because neither temperature nor entropy are measured.

1.3 The need for temperature data

Developing EoS models primarily based on pressure and density data determined from the Rankine-Hugoniot relations has limitations. For example, in cases where multiple EoS models have been developed it is often difficult to distinguish between different models as they are based on the same datasets and thus their results appear similar in the P–V plane. In such cases temperature data can be extremely valuable to distinguish between different EoS models.

Work by Bernard and Maillet [34] illustrated how minor differences in the pressure-volume (P–V) plane can translate to much larger differences in the pressure-temperature (P–T) plane. Using two EoS [35, 36] and their own *ab-initio* model, the locus of states that can be attained by a single shock (also known as the 'Hugoniot') was calculated. Comparing P–V and P–T representations of the Hugoniot, see Figure 1.6, it can be seen it is easier to distinguish between the models in the P–T plane.

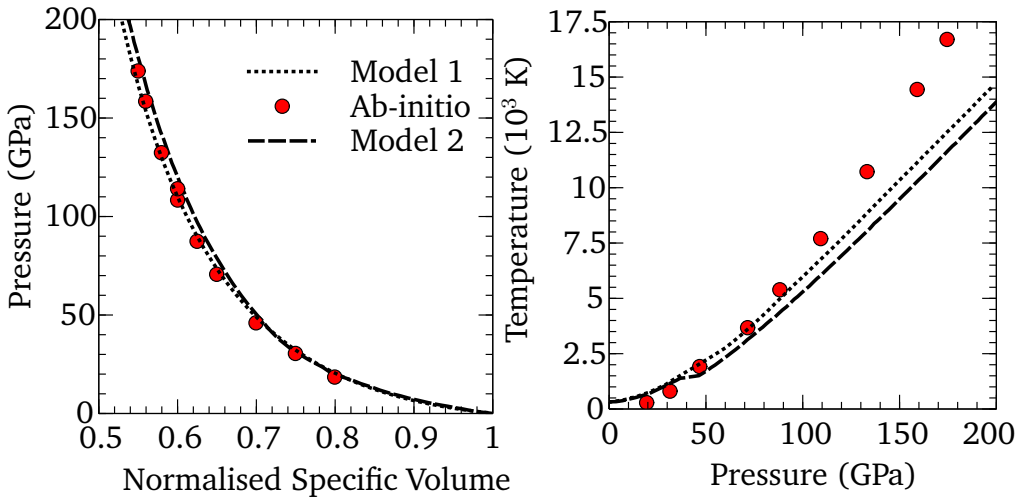


Figure 1.6: Reproduction of results from Bernard and Malliet [34] comparing the Hugoniot generated from two equations of state (model 1 and model 2) and an *ab-initio* model. In temperature-pressure space the models diverge distinctly, in comparison to pressure-volume space.

Another area where temperature data can be of particular value is the identification phase boundaries. Changes of phase are often one of the more difficult

areas of an EoS to model accurately. Furthermore, many phase changes are not associated with a significant volume change [37] meaning such phase changes are not visible in P–V data, with the bct to bcc phase change in tin being an example [38]. However, the latent heat that accompanies phase changes means that temperature varies relatively little in the region of a phase change making the boundary more readily identifiable.

The effects of phase changes in P–T space are clearly seen in work by Mabire and Héreil [39] on tin. In this work, both the phase boundaries and the Hugoniot, as determined by models. are shown in P–T space (see Figure 1.7 for a reproduction) and 'kinks' in the temperature along the Hugoniot are clearly visible. Temperature measurements on shock experiments allow these phase changes to be mapped with high accuracy.

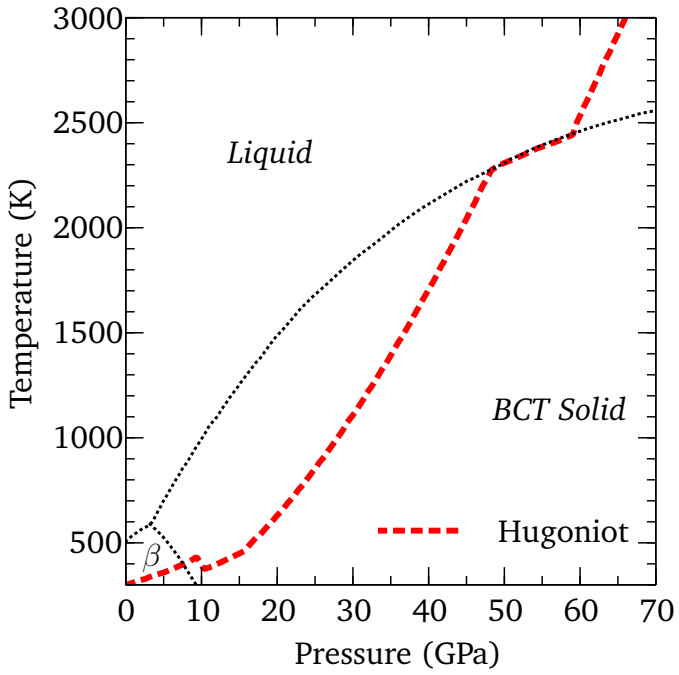


Figure 1.7: Reproduction of a plot from Mabire and Héreil [39] showing the tin pressure-temperature phase diagram. The tin Hugoniot is also plotted.

Many modern EoS are complex and optimised using minimisation routines, for example one multiphase tin EoS has 27 variables [40], this makes it difficult to visualise the impact of additional data. A more direct illustration of how temperature data can be used to determine EoS parameters is to consider a simple

Grüneisen equation of state. A Grüneisen EoS uses the simple assumption the EoS surface in the region of the Hugoniot can be linearly extrapolated to allow off-Hugoniot states to be determined, see Figure 1.1.

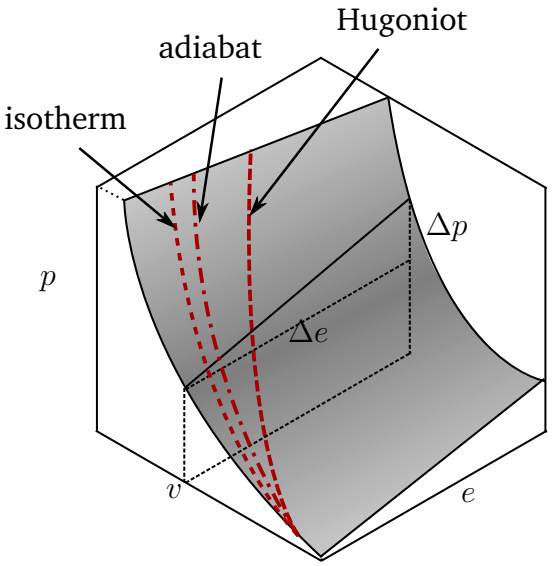


Figure 1.8: Illustration of a physical interpretation of the Grüneisen gamma parameter in pressure, p, volume, v, energy, e, space. The Hugoniot is shown on the EoS surface as a dashed red line, the Grüneisen parameter describes the gradient of the EoS in the pressure-energy plane.

The Grüneisen EoS uses γ, the Grüneisen gamma, defined as

$$\gamma = v \left(\frac{dp}{de} \right)_v , \tag{1.8}$$

where v is volume, p is pressure and e is internal energy. If it is assumed γ is independent of pressure and energy in the Grüneisen expression, it can be integrated to determine an expression relating pressure and energy:

$$p(v) - p_0 = \frac{\gamma}{v} \left(e(v) - e_0 \right) , \tag{1.9}$$

where $p\,(v)$ and $e\,(v)$ are functions giving pressure and energy, respectively, usually the Hugoniot. p_0 and e_0 are the pressure and internal energy of the reference state (usually standard temperature and pressure).

If a Grüneisen EoS is assumed, Equation 1.9, can be used to calculate other paths on the the EoS surface such as a line of constant entropy, the isentrope, see Appendix C.3. Both energy and temperature along the isentrope are well-defined

so any difference between the energies of the isentrope and the Hugoniot are due to shock heating. If the specific heat capacity at constant volume, c_v, is known then the difference in internal energy can be calculated with the expression,

$$\Delta e = c_v \Delta T \tag{1.10}$$

allowing γ to be determined, see Figure 1.9.

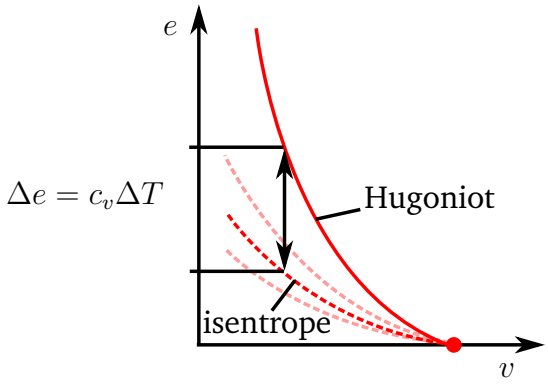


Figure 1.9: Plot illustrating how a measurement of temperature can be used to determine the Grüneisen gamma parameter, γ. Assuming a Grüneisen EoS and knowledge of specific heat at constant volume, the energy difference between the Hugoniot and adiabat can be calculated with temperature data, which allows γ to be calculated.

While this is an illustration of how temperature measurements can be used to parameterise a simple EoS, temperature measurements are similarly valuable for the development of more complex EoS.

1.4 The rationale for pyrometry

The preceding discussion has established the value of temperature data for the development of equations-of-state and the unique phase space accessible with shock experiments. The next consideration is how temperature should be determined. A number of methods have been used to attempt to determine temperatures in shock experiments, including thermocouples [41–44], neutron resonance spectroscopy [45, 46] and thermistors [47, 48], however optical pyrometry has been one of the most successful approaches.

There are a few key characteristics that make pyrometry suitable for application to shock experiments. First, pyrometry is a non-contact technique; this is important in shock experiments because any components in contact with shocked material are inevitably also perturbed, often leading to ambiguous results. Furthermore the shock response of a sensor often differs from the other components so the presence of a sensor in the sample often perturbs the experiment, adding further ambiguity. Second, as an optical technique, the temporal response of a pyrometer is usually determined by the temporal response of an associated optical detector. Optical detectors typically have fast response times ($\sim$1 ns) allowing the rapid transitions in shock experiments to be resolved. Finally, pyrometry is able to function at the very high temperatures (1,000s of Kelvin) which can be generated in shock experiments.

Before further comment it is relevant to discuss the practical considerations of a pyrometry measurement in a plate impact experiment. A further restriction to the discussion is that only opaque materials will be considered, as opacity adds unique complications to the application of pyrometry to plate impact experiments.

Pyrometry infers the temperature of a material from the radiation it emits; specifically the emission of a body is described by Planck's Law,

$$L_\lambda(\lambda, T) = \epsilon(\lambda, T)\,\frac{2hc_0^2}{\lambda^5}\frac{1}{e^{\frac{hc}{\lambda k_B T}} - 1}, \tag{1.11}$$

where L_λ is the spectral radiance, usually in W·sr^{-1}·m^{-3}, h is Planck's constant, c_0 is the speed of light in a vacuum, λ is wavelength, k_B is Boltzmann's constant, T is temperature of the source and ϵ is the emissivity of the emitting body (which may be a function of various parameters, commonly wavelength and temperature). Using Planck's Law measurements of spectral radiance can be converted into a temperature.

For an opaque material radiation is emitted from the surface of the sample. Thus pyrometry can only measure the surface temperature of an opaque material. This limitation results in two issues. First, a surface implies an interface, which will interact with the shock wave perturbing the state generated. Second, due to

the short timescales of shock physics experiments, thermal equilibrium cannot be assumed and the system must be considered in more detail.

While the preceding discussion of shock physics has discussed the high pressure states generated by shocks there has been no discussion of the interaction of shock waves with interfaces. In general the interaction of shocks with interfaces can be described using a 'impedance matching' approach [49], but here we shall consider a few simple cases.

First, the case when a shock reaches a 'free surface' interface, *i.e.* the edge of the material with nothing in contact with it, is considered. In this case when the high pressure wave reaches the interface, and hence sample surface, the pressure reduces to zero; clearly this is problematic if temperature measurements of high pressure states are required. To sustain pressure at the sample surface it is necessary to consider a second case where a shock wave reaches an interface between two materials. The shock will cause the two materials to change to different states with the resultant pressure dependent on the relative 'shock impedance' of the two materials. Considering the case where the second material is lower impedance, the high pressure state will partially release to an intermediate pressure. This is often the case in pyrometry experiments where an opaque, high impedance metal is interfaced with a transparent 'window' which allows light from the metal sample to be collected but also maintains a significant pressure state at the interface.

Thus a picture of a generic plate impact experiment, with a pyrometry diagnostic, is developed. The interface under measurement has an opaque sample, onto which a window is attached (usually with an adhesive). The emission of the sample is monitored with the pyrometer instrument. Emission from the sample is detected when the shock reaches the sample-window interface with the state of the sample determined by the strength of the shock wave and the relative impedance of the sample and window, see Figure 1.10.

While there are numerous reports of pyrometry applied to plate impact experiments in the literature, using the approach outlined above, there are

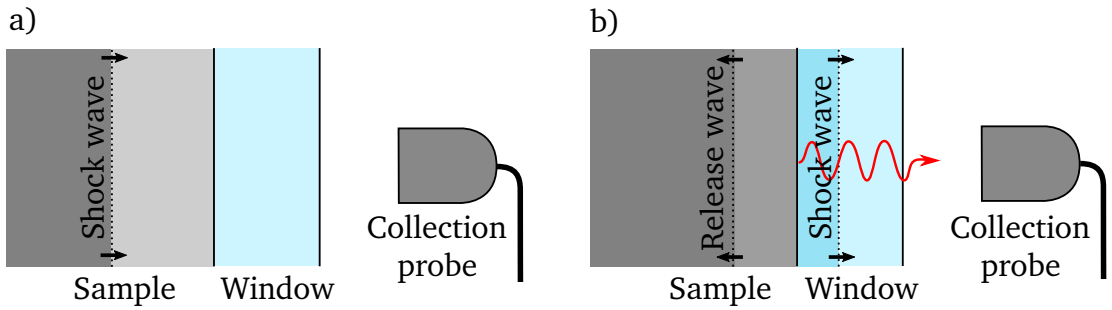


Figure 1.10: Schematic diagram of a generic pyrometry plate impact experiment. a) the shock wave generated by the impacting plate creates a high pressure region inside the material, but this is not visible. b) the shock has reached the sample free surface and is passing through the window. Emission from the sample surface is reaching the collection probe.

still concerns regarding its accuracy. The most significant causes for concern in pyrometry results are systematic errors which undermine trust in measurements and measurement of light from non-thermal sources.

The known sources of systematic error in pyrometry can cause errors in the derived temperature of over 10%. The two most significant causes of systematic error are emissivity uncertainty and heat transport issues; these are discussed in more detail in Chapter 3.

Non-thermal sources are also a common issue as the violent nature of shock experiments mean there are many potential non-thermal sources. These sources include shock response of the window [50], air flash [51] and edge effects [52]. The effects of non-thermal sources can range from completely undermining pyrometry measurements (leading to total dataloss) to adding a small source of uncertainty.

1.5 Potential areas for development

A detailed review of the literature related to the application of pyrometry to shock experiment follows in Chapter 2, but briefly, there are a number of areas where the capability of the pyrometry instrumentation can be improved. The time resolution of pyrometers at temperatures below 1500°K is typically low due to the light level requirements. This may result in the systematic errors due to the

averaging out of transient features. Additionally, the collection optics of many systems are sub-optimal. Two common approaches are bare fibre collection and optical (lens or mirror) coupling. Bare fibre maximises the level of collected light but collects from a large area. Many of the collection optics in the literature have numerical apertures of approximately 0.2.

Another issue is that there does not appear to be a systematic approach to the design of pyrometer systems and, anecdotally, much instrument development is based on trial-and-error. An extension of this lack of systematic approach is that a consolidated, quantitative understanding of the sources of uncertainty in a high-speed pyrometry measurement could not be identified; Chapters 3 and 4 discuss this issue in more detail.

One source of uncertainty that is known is sample emissivity. It is often one of the most significant sources of uncertainty and, as such, a technique to reduce emissivity uncertainty is desirable. The most promising route to achieving reduced emissivity uncertainty is to develop a dynamic reflectivity measurement diagnostic; Chapter 8 reviews and discusses this topic.

The primary motivation for the research presented here is to investigate the above concerns, resulting in a better understanding and more confidence in the pyrometry technique in high strain rate applications.

This will be accomplished as follows:

- Increased time resolution. The attainable time resolution of pyrometry measurements has been maximised as far as possible, reducing the risk of unknown systematic errors due to time averaging.

- Variable spatial resolution. Nominally identical pyrometry measurements are made with different spatial resolutions to demonstrate consistency and bound the size or density of hot spots.

- Improved understanding of uncertainties. Sources of uncertainty of pyrometry measurements in shock applications have been estimated and minimised as far as possible.

- Development of emissivity measurement techniques. A diagnostic to determine the emissivity of a material has been developed using a dynamic reflectivity diagnostic integrated with a pyrometry diagnostic.

2
Introduction to pyrometry

2.1 Pyrometry Background

It is instructive to review the historical development of pyrometry to provide context for the advances reported here. In modern usage the term 'pyrometer' refers to a device that determines the temperature of a sample using the electromagnetic radiation a sample emits, however, the term was first recorded in 1791 by Pearson and Banks [53]. The term was used in reference to a technique developed for the measurement of the temperature of pottery kilns reported in 1782 by Wedgwood [54]. Wedgwood's technique used the volumetric thermal change of a ceramic standard, which was placed in the kiln for measurement. The standard was then inserted into a tapered reference gap and the point at which the standard contacted both sides of the gap indicated the temperature on a proprietary temperature scale (the Wedgwood Scale, °W [55]).

The use of spectral radiance measurements to determine temperature was first proposed by Becquerel in 1862 [56] however it took until 1892 for Le Chatelier to implement an instrument that used light measurements to determine temperature [57]; a schematic of the device is shown in Figure 2.1. Like many optical devices before the advent of photodetectors, Le Chatelier's instrument relied on an operator matching the brightness of a standard source to that of the object.

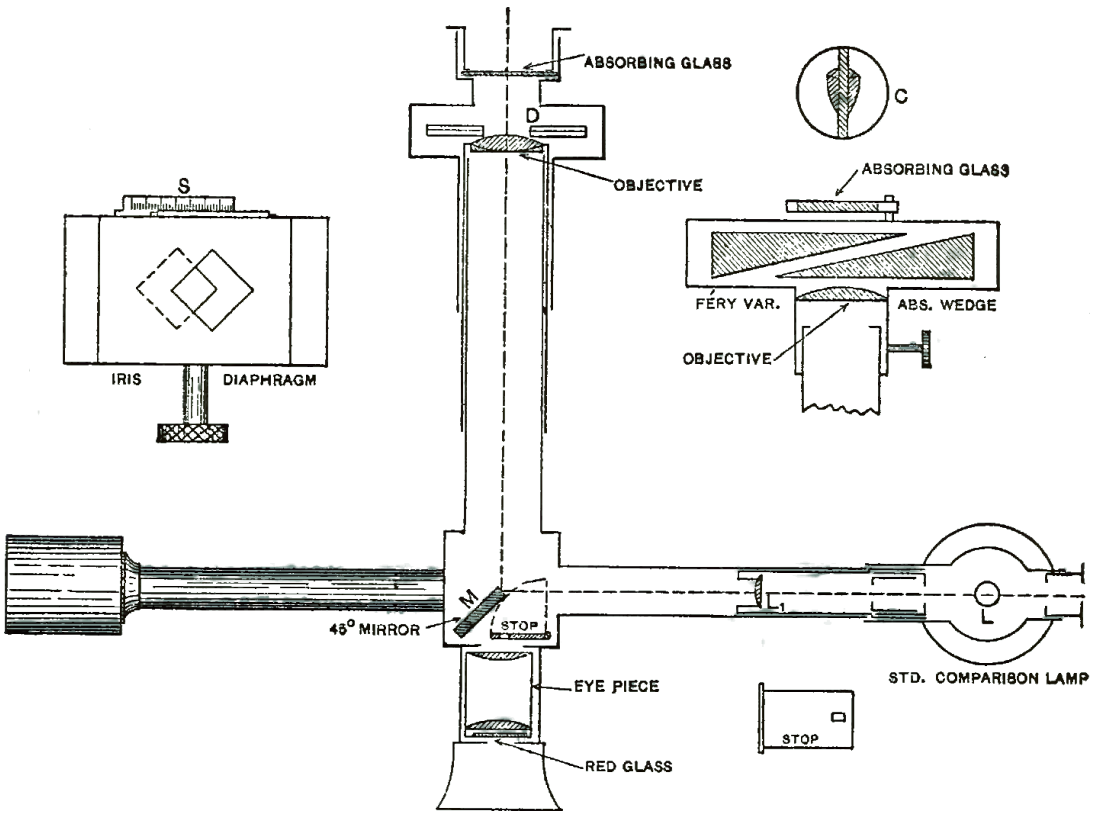


Figure 2.1: Schematic diagram of the optical pyrometer designed by Le Chatelier as reported by Waidner and Burgess [58] [Re-printed courtesy of the National Institute of Standards and Technology, US Department of commerce. Not copyrightable in the United States].

The development of the theory of blackbody radiation (*i.e.* the radiation emitted by an ideal absorber/emitter) by Planck created a quantitative understanding of the spectral distribution of thermal radiation [59]. Specifically Planck's Law describes the emission of a blackbody as,

$$L_\lambda(\lambda, T) = \frac{2hc_0^2}{\lambda^5} \frac{1}{e^{\frac{hc}{\lambda k_B T}} - 1}, \tag{2.1}$$

where L_λ is the spectral radiance, usually in W·sr^{-1}·m^{-3}, h is Planck's constant, c_0 is the speed of light in a vacuum, λ is wavelength, k_B is Boltzmann's constant and T is temperature of the source.

The advent of the photomultiplier tube allowed the human eye to be replaced with photoelectric detectors which improved accuracy [60] (primarily by enabling long duration temporal averaging). The uptake of detectors also established the

link between detector capabilities and pyrometer capabilities; detector performance is now a key factor in determining the capabilities of a pyrometer.

Pyrometry is now an established technique for the non-contact measurement of temperature. For static applications pyrometers are available as commercial off-the-shelf items. A CO55L handheld pyrometer, manufactured by LAND, illustrates the typical performance of such devices: temperature measurement range 1300–2300°K, <0.5% accuracy, 28 mm sampling diameter and 30 ms response time [61]. The response time and sampling diameter are not suitable for most shock experiments so systems tailored to high speed applications are required.

High-speed pyrometers, suitable for high strain applications, have been reported by some researchers, in particular multi-channel spectral-band instruments have been developed for plate impact applications and these are reviewed in the following section. In a multi-channel spectral-band pyrometer, light from a shocked target is collected and filtered into several detectors used to record the intensity at a set of wavelength bands. A fit to the wavelength dependent intensity using a Planck curve enables determination of the temperature, see Figure 2.2.

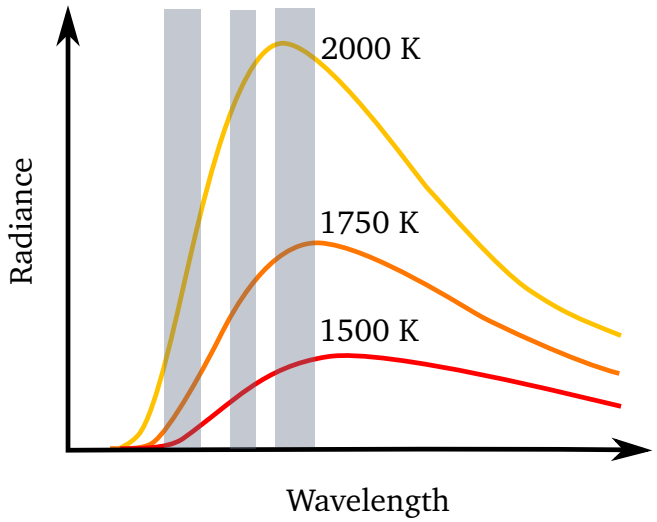


Figure 2.2: Illustration of the principle of operation of a spectral band pyrometer. The radiation emitted by the sample is integrated over one, or more, wavelength bands. The temperature can be determined from the absolute radiance, if emissivity is known, or by comparison of the radiances, if the relative emissivity is known.

2.2 Evolution of high-speed pyrometry

In principle, pyrometry is a straight-forward diagnostic; the radiance of a sample over a known spectral region is measured, this can then be related to the temperature. However, there are a large number of design and component choices to be made when constructing a pyrometer with the optimum choices depending on a number of considerations. Factors that need to be considered include the range of temperatures, expected radiance, time resolution required, spatial resolution required and the uncertainty in the temperature to be measured. A number of different high speed pyrometer systems, suitable for use in shock experiments, have been reported in the literature; it is instructive to review them.

It should be noted that the review that follows considers spectral band pyrometers; another prominent pyrometry technique is streaked optical pyrometry (SOP) which uses streak cameras to measure temporally-varying spectral emission. There are relative strengths and weaknesses between the two approaches but the key considerations are that spectral band pyrometers can more easily reach lower temperatures (SOP operates in the eV regime [62, 63]) and are practically simpler to integrate with experiments.

The first reported experiments using optical detectors to determine the temperature of shocked material were by Taylor 1963 [64]. He reported a simple arrangement where a photomultiplier tube (PMT) was placed in close proximity (for optical coupling) to a sample (unconstrained by an optical window) impacted by an explosively driven plate. The wavelength sensitivity of the PMT was constrained by the responsivity of the detector (approximately 375 nm–500 nm). Temporal resolution was limited to 10 ns but this was most probably due to the rise time of oscilloscopes at the time. Temperatures of copper from approximately 700 K to 1400 K and errors of $\pm$30 K were reported, however these results assume emissivity had remained the same as during a static, ambient pressure measurement and the emissivity did not vary by more than a factor of 2; there was no experimental evidence these assumptions were justified.

Some practical drawbacks of the diagnostic method reported by Taylor are that, due to the proximity of the PMT to the shock loaded sample, the PMT will be destroyed. Additionally, this approach measures a single wavelength band; additional bands give confidence that measurements are consistent with Planck's Law as illustrated in Figure 2.2.

The first report of a system that used multiple PMTs at different wavelength bands was by Kormer *et al.* in 1965 [65]. The system collected light using free space optics, the light was then collimated and a passed through a beam splitter used to create two beams. The beams were then filtered (478 nm and 625 nm, 10 nm full width at half maximum, FWHM) before reaching PMTs for light measurement. The system was used to investigate the shock temperature of NaCl and KCl at temperatures from approximately 2500 K to 5000 K. The use of two wavelengths helps constrain the variation in emissivity however, it was also determined that the shocked sample is largely opaque as the light output is constant while the shock is in the crystal. The free space coupling of the system is a significant drawback as the destructive nature of the experiment means the collection optics must be 10 m from the sample to avoid destruction which limits the optical efficiency of the coupling.

A system based on silicon PIN photodiodes (PIN is not specifically an acronym but refers to the semiconductor layers in the device: p-type, intrinsic and n-type) was detailed by Lyzenga and Ahrens in 1979 [66]. An array of six photodiodes was individually optically coupled to the sample using a 0.05 numerical aperture (NA) lens and filter system over free space. The rise-time of the detectors was stated to be about 1 ns, although response time of the system was limited to approximately 5 ns due to the oscilloscopes used. The filters in the system had a FWHM of $\sim$9 nm, centred at wavelengths of 450 nm, 500 nm, 550 nm, 600 nm, 650 nm and 800 nm. Of particular relevance to the work presented in this thesis, Lyzenga's thesis contains the first reported results of pyrometry measurements on shocked metals. Results of silver (Ag) with a sapphire anvil (Al_2O_3) shocked to pressures of 185 GPa were reported. An apparent temperature of 5950 K was reported but

various issues that could perturb the measurement such as microscopic interface gaps and heat transport were discussed. The bulk of the materials investigated were NaCl, Mg_2SiO_4. MgO and Al_2O_3. Like the system reported by Kormer, free space coupling results in a system with a low optical throughput so the system is not suitable for low temperature experiments and was fielded on experiments producing temperatures of over 4000 K.

Yoo *et al.* [67] reported, in 1992, the first use of optical fibre to couple light during an experiment that aimed to measure temperature during a plate impact experiment. Although high pressure temperature results are reported, the primary purpose of the paper is to detail a diagnostic technique where the output from an Ar flash lamp is used to diagnose the optical properties of the sample/window assembly under shock loading. Here, just the points relevant to pyrometry will be discussed. The optical system used seven optical fibres; six were arranged, without lenses, to view the shocked sample. One of the fibres was used to couple the light from the flash lamp to illuminate the target. The collection fibres are coupled to three different systems; a time resolved spectroscopy system, a non-time resolved spectroscopy system and a bank of PMTs. Although the research highlighted issues with uncertainties in optical emission of the window material, the optical collection and detection operated as intended, demonstrating the efficacy of optical fibres.

There are numerous practical benefits to the use of optical fibre in pyrometry experiments. First, it is relatively straight-forward to create an optical probe that exploits the full numerical aperture of the fibre. The NA of fibre is usually significantly higher than attainable with free space coupling in the case of destructive shock experiments where a significant stand-off distance is required. Second, optical fibre is also flexible, allowing more experimental configurations. This flexibility is particularly useful in shock experiments where the sample is loaded in a containment vessel which can make free-space optical coupling problematic. An issue with the multi-fibre approach is that each detector collects light from a different location, thus it is difficult to determine the cause of any outlying measurements.

A wide range of detectors were used by Blanco *et al.*[68] in a pyrometer design reported in 2002. An eight channel system using mercury cadmium telluride (HgCdTe) detectors, indium antimonide (InSb) detectors, germanium (Ge) detectors and visible photomultiplier tubes (PMTs) was used to investigate the temperature of shocked metals. Rise times are not quoted but can be derived from the quoted bandwidth. The HdCdTe and InSb detectors are quoted to have a 100 MHz bandwidth implying a rise time of 3.5 ns. A 1 GHz bandwidth is quoted for the Ge detectors and PMTs; this bandwidth implies a rise time of $\sim$0.35 ns. The specific wavelengths used are not listed, only that the spectral range from 0.3 μm to 3.5 μm was covered by the detectors. Light was collected by placing a multi-core optical fibre in contact with the lithium fluoride window.

The multi-core fibre splits into single core fibres which then couple to the detectors. The fibre used is 200 μm diameter, 0.2 NA, infra-red compatible fibre, with a transmission window extending to 4 μm. The need to consider the fibre transmission does highlight one of the drawbacks of using optical fibre, many commonly available fibres have significantly lower transmission at wavelengths longer than 2.5 μm, this can be an issue as at lower temperatures more radiation is emitted at longer wavelengths so measurements at wavelengths above 2.5 μm are required to enable measurements. One solution, used by Blanco *et al.*, is to use specialist fibre although this is often limited in core diameter and numerical aperture. Another solution is to use free-space coupling and accept the attendant fielding difficulties.

Further developing the use of InSb detectors, Seifter *et al.*[69] reported a four channel InSb based detector. A significant improvement was that, although fibre coupled, this system uses just one fibre. Spectral separation was achieved by means of dichroic mirrors which selectively pass or reflect incident light. The bandwidth of the system is quoted as 20 MHz, implying a 17.5 ns rise time. It has also been noted that in single fibre systems use of parabolic mirrors, rather than lenses, is beneficial as reflective optics are not subject to chromatic aberration. It was also noted that large diameter, 1 mm, chalcogonide fibre is unwieldy due to its

low strength and large bend radius making it unsuitable for rugged experimental use. The solution suggested was to move to a multi-fibre assembly consisting of multiple smaller, 200 μm core fluoride glass fibres.

2.3 Pyrometer design discussion

Having reviewed the development of pyrometer designs for plate impact applications the specifics of system design can be discussed. However, an important consideration is the goal of the instrument design. There are two key metrics with regard to pyrometer performance in shock physics applications; temporal response and minimum measurable temperature.

Temporal response has commonly been reported in the literature. A goal of 1 nanosecond rise time will result in a system that is faster than most previous systems and is more than adequate for plate impact experiments. However, it should be noted that increased temporal resolution results in a commensurate increase in measurable temperature due to the reduced signal levels.

With regard to minimum measurable temperature, this is not a metric that is commonly reported in the literature so it is difficult to determine historical performance. However, based on the temperatures that an be reached on single stage gas gun experiments, a minimum measurable temperature of 1000°K is required.

To simplify pyrometer design the system can be logically split into two subsystems that are relatively independent. One is the radiometry system, the purpose of which is to sort, direct and detect incoming radiation. The second sub-system is the probe head; this collects light from the sample and passes it to the radiometry system.

2.3.1 Radiometry system

Detector criteria

One of the most significant factors affecting the performance of a pyrometer are the detectors. A detailed review of the available detector technologies follows.

There are a wide variety of optical detectors that are commercially available; the performance of these detectors is usually described by parameters detailed by the manufacturer or supplier. There are three ways the performance of optical detectors can be parameterised that are particularly relevant to pyrometry; rise time, noise equivalent power (NEP) and active area. These three parameters are now discussed.

Rise time is a measurement of the temporal response of the detector and indicates the time taken for a signal to rise when exposed to an abrupt increase in incident power. To investigate the effect of temporal averaging on pyrometry measurements it was necessary to develop a pyrometer that was capable of nanosecond time-resolution.

Noise equivalent power is a measure of the sensitivity of a detector, allowing the feasibility of a measurement at a specified bandwidth to be quickly assessed. As the name suggests it is the incident power that will produce a signal equal to the power of the noise on the detector (*i.e.* SNR = 1). However, care is required when using NEP because different definitions of noise power are used; usually a bandwidth-normalised value based on a bandwidth of 1 Hz is specified, and is the one used here, but occasionally a specific bandwidth is inferred. In the case of a bandwidth-normalised NEP the value must be multiplied by the square-root of the bandwidth to determine the power required to attain an SNR of 1. Thus NEP is typically specified in Watts per square-root Hertz.

Active area is the area of the detector that is sensitive to light. This is relevant for pyrometry because thermal radiation is incoherent, this incoherence means collected light cannot be focused to a higher intensity than the source, [70, p. 26]. Thus, once intensity has been maximised by focusing the collected light, the collected power is proportional to the collection area.

Three technologies represent the only commercially available products that can measure light levels at the time resolutions ($\sim$ns) required by this project; photo-multiplier tubes, photo-diodes and avalanche photo-diodes, which are now discussed.

Photo-multiplier tubes

The specifics of the operation of detectors is not a primary concern for this review, but the capabilities of various detector technologies is relevant. Photo-multiplier tubes are the most sensitive optical detector able to achieve gains of over 160 dB with minimal noise. In addition to this high gain they are able to operate at high frequencies (rise times of $\sim$ps are achievable) with a large active area (10s mm^2).

The sensitivity of PMTs is not fixed but depends on a number of factors. Defining the charge on an electron as e, dark current as I_d, gain as G, and cathode sensitivity as S, typically the noise equivalent power (bandwidth normalised) of a PMT can be given by the relation [71]:

$$\text{NEP} = \frac{\sqrt{2eI_dG}}{S}.$$

PMTs, however, also have drawbacks. The most relevant drawback in application to shock physics experiments is that they are delicate and cannot sustain the high currents caused by high light levels. This is a particular problem in pyrometry applications for two reasons. One, calibration of a pyrometry system requires illumination with broadband light, typically a blackbody. Such blackbody sources cannot be modulated because they rely on heating of a cavity (which cannot be done quickly). As such to prevent current thresholds from being exceeded PMTs often need to be calibrated at a lower gain than they will be operated in the experiment; this is undesirable as it relies on indirect calibration (for example pulsed laser illumination) where detector response is extrapolated to higher gains. Two, high strain rate experiments are often extremely violent making it likely high intensity flashes will occur. If a PMT is exposed to these flashes the current limits are likely to be exceeded.

The delicate nature of PMTs is exacerbated by their relatively high cost. Thus, not only is it relatively easy to damage a PMT, it also expensive to replace it. Coupled with the high risk of intense light flashes in high strain rate experiments PMTs become a potentially undesirable component.

Semi-conductor Diodes

There are a variety of types of semi-conductor diodes, *e.g.* photo-diodes, photo-transistors. Only photo-diodes react sufficiently rapidly to be used in high strain rate experiments.

Photo-diodes can be operated in two modes, photo-conductive and photo-voltaic. Photo-voltaic mode is typically used when trying to convert light into electrical energy (*i.e.* in solar cells). Photo-conductive mode offers improved linearity and faster response times so is typically the mode used in measurement systems.

Photo-diodes are suitable as optical detectors for pyrometry applications because, in photo-conductive mode, they are highly linear, producing current proportional to the incident light level over many orders of magnitude. Also beneficial, photo-diodes are highly resistant to damage; light levels must be sufficient to damage the semiconductor material to affect their operation ($\sim$100 mW/cm^2).

Finding photo-diodes appropriate for high-speed pyrometry can be challenging as there are a number of conflicting attributes. As discussed, pyrometry collects incoherent light which limits the intensity to which it can be focussed, this makes larger active areas more desirable. However, the capacitance of a photo-diode increases with area. Capacitance is a key variable in determining the rise time of a photo-diode detection system. Thus when trying to attain 1 ns rise times, minimising capacitance is important.

Specifically, assuming the rising voltage, $V(t)$, can be described by the expression,

$$V(t) = 1 - e^{-t/RC}, \tag{2.2}$$

where R is the load resistance, C is the photo-diode capacitance [72], the 10%-90% rise time of a circuit, t_{10-90}, can be described by the equation,

$$t_{10-90} \approx 2.2RC. \tag{2.3}$$

For example, solving the above expression to determine the capacitance required to achieve a 1 ns rise time with a 50 Ω load (typical for high frequency electronics) the maximum capacitance is 9 pF.

Since capacitance, and hence rise time, is linked to active area it is often difficult to find photodiodes that are sufficiently fast and have an optimum active area. The incoherent nature of thermally emitted light means it is not possible to achieve a spot size smaller than the source without losing light. However for fibre based systems the fibre source is likely to be large ($\sim$1 mm diameter) requiring a trade-off between light collection and temporal response.

There are two materials of photo-diode that are of particular interest in high speed pyrometry, silicon (Si) and indium gallium arsenide (InGaAs). These diode materials have relatively low capacitances, allowing nanosecond response times and are sensitive to light from the visible to the infra-red band [73, 74] which are relevant to the temperatures attained in shock physics experiments.

Some typical values for the characteristics of photodiodes that use these materials, the 1.02 mm diameter FDS010 Si photo-diode from ThorLabs has a capacitance of 6 pF. A 1 mm diameter FGA10 InGaAs photodiode, also from ThorLabs, has a capacitance of 65 pF. These capacitance values show that, although some components meet the capacitance requirements, there is not a large margin thus satisfying a nanosecond rise time with photo-diodes is a challenge.

Aside from rise time and active area concerns, Si and InGaAs photodiodes benefit from low intrinsic noise. For examples of typical values a ThorLabs FDS010 Si photodiode has a NEP of 1.2 $\times$ 10^{-13} W·Hz$^{-\frac{1}{2}}$, a ThorLabs FGA10 InGaAs photodiode has a NEP of 2.5 $\times$ 10^{-14} W·Hz$^{-\frac{1}{2}}$.

However, while photo-diodes are low noise detectors their responsivity can be an issue. Photo-diodes can be thought of as light dependent current sources, thus in the simplest applications a resistor is used to create a voltage for measurement. When using a resistor, responsivity (which is wavelength dependent) is a problem because it is typically around 0.1 to 1 A·W^{-1}. The presence of a resistor means it is also necessary to consider thermal or Johnson noise. Thermal noise is described by the equation,

$$v_n = \sqrt{4k_bTR}, \tag{2.4}$$

where k_b is Boltzmann's constant, T is temperature and R is resistance. For a 50 Ω resistor at 300°K, this gives a voltage spectral density of 9 $\times$ 10^{-10} W·Hz$^{-\frac{1}{2}}$, which is often higher than the intrinsic NEP of the detector. To get optimum performance from a photodiode, a custom designed electronic amplifier can increase signal levels with minimal noise. However, a full amplifier design and noise analysis is beyond the scope of this research.

In summary, because low temperature pyrometry needs detectors as sensitive as possible photodiodes are not an ideal choice. However, the robustness of photodiodes do mean they are convenient to use experimentally.

Avalanche photo-diodes

An extension of photo-diodes are avalanche photo-diodes (APD). In addition to the current generated by light interacting with a photoelectric material, a high bias voltage can generate current multiplication due to generation of secondary carriers. APDs are designed to exploit this current multiplication effect which results in higher signal levels for the same light level and active area.

While the high bias voltages in APDs creates additional gain, it does have drawbacks. One, the generation of high voltages ($\sim$250 V) makes circuit design more difficult. Two, the gain in APDs is often highly temperature sensitive which means either temperature control or temperature compensation is required to achieve a reliable responsivity.

A final issue with APDs is simply the smaller selection. Due to their difficulties in implementation there is less demand and hence a smaller market. Thus it can be difficult or impossible to find appropriate components.

Detector Summary

The previous discussion has highlighted that each technology has different issues and benefits. A list of a number of appropriate detectors is shown in Table 2.1. To make some general comments, the high gain, low noise and high active area generally makes PMTs the detector of choice where available. However, PMTs

that are able to detect infrared wavelengths (*i.e.* above 950 nm) are limited to a small range of expensive models (over £10k). Thus for infrared wavelengths photodiodes and APDs were used. In the infrared region, it appears that the low NEP of some APDs offsets the smaller active area available.

2.3.2 Design of radiometry system

The system that filters and measures the intensity of light collected by the optical probe head from the target has been termed the radiometry system. The radiometry system has a number of components that have been chosen to provide the maximum optical throughput to reduce the minimum detectable temperature of the pyrometry system.

- Lenses: A 1" diameter form factor allows access to the widest range of off-the-shelf optics, thus this has been chosen as the lens diameter. Given the requirement to optimise optical throughput, high NA aspheric lens have been chosen.

- Dichroic Mirrors: As shown by modelling described in Chapter 4 it is desirable to collect light over a large a wavelength window as possible and maximise the amount of light collected. A search of suppliers has identified dichroic mirrors with high transmission (above 90%). These are compatible with the filters identified.

- Filters: Again modelling (Chapter 4) indicates that filter widths should be wide enough to reach the low signal-to-noise ratio threshold. In this case it has been chosen to have five bands in the 600 nm to 1700 nm region.

- Detectors: To maximise signal levels at low light levels photo-multiplier tubes have been used as detectors where spectrally available. Outside this area APDs have been identified as the solution that offers the optimum trade-off in noise and active area. Because the APD models have only recently become available (2017), some experiments were performed with amplified photodiodes.

Manufacturer & Part number	Technology	Rise-time	Noise Equivalent Power ($pW \cdot Hz^{-\frac{1}{2}}$)	Active area	Wavelength sensitivity
Hamamatsu H10721-20	Photomultipler Tube	0.8 ns	1×10^{-3}	50.3 mm^2 (⌀8 mm)	230–920 nm
ThorLabs APD430C	InGaAs Avalanche photodiode	1.1 ns	0.45	0.04 mm^2 (⌀0.2 mm)	900–1700 nm
ThorLabs APD430A	Si Avalanche photodiode	1.1 ns	0.14	0.25 mm^2 (⌀0.5 mm)	400–1000 nm
FEMTO HCA-S-400M-SI	Amplified Si photodiode	0.75 ns	40	0.64 mm^2 (⌀0.8 mm)	320–1000 nm
FEMTO HCA-S-400M-IN	Amplified InGaAs photodiode	0.75 ns	24	0.09 mm^2 (⌀0.3 mm)	900–1700 nm
Terahertz Technologies Inc. TIA-525	Amplified InGaAs photodiode	2.7 ns	3	Fibre coupled	900–1700 nm
ThorLabs DET10A	Si photodiode	1.0 ns	0.03	0.8 mm^2 (⌀1.0 mm)	200–1100 nm
ThorLabs DET10C	InGaAs photodiode	10 ns	3	0.8 mm^2 (⌀1.0 mm)	900–1700 nm
Hamamatsu H11526-20	Photomultiplier tube	0.57 ns	1×10^{-3}	50.3 mm^2 (⌀8.0 mm)	230–920 nm

Table 2.1: Table listing some detectors relevant for high speed optical pyrometry including some key characteristics of the detectors.

A single fibre system, using dichroic mirrors to separate the collected light into broad wavelength bands has been constructed; this is similar to that initially proposed by Seifter *et al.* [75]. A single fibre design has two main advantages; every detector senses light from nominally the same region and single fibre systems minimise the number of optical fibres required, which can ease fielding and reduce cost.

A schematic diagram of this arrangement is outlined in Figure 2.3. The layout of the radiometry system is as follows:

1. A lens collects light from the optical fibre which passes light from the experiment to the radiometry system. This lens nominally collimates the light for filtering.

2. Next the light passes through dichoric mirrors to split the beam into separate wavelength bands.

3. After the dichoric mirrors the collimated beam passes through a precisely defined bandpass filter.

4. The collimated beam is then focused to an appropriate size using a lens for detector coupling.

5. The detectors convert the optical signal to an electrical signal which is recorded on an oscilloscope.

2.3.3 Pyrometry probe head

As discussed previously, the probe head is the component that collects light from the sample and couples the light into a system that relays the light to the radiometer sub-system. In the designs discussed here optical fibre has been chosen as the relay system; fibre is convenient for fielding and an appropriate fibre has a high optical throughput. The fibre chosen was a 1 mm diameter, 0.48 NA optical fibre (Low OH). The relatively high diameter and NA give a high optical

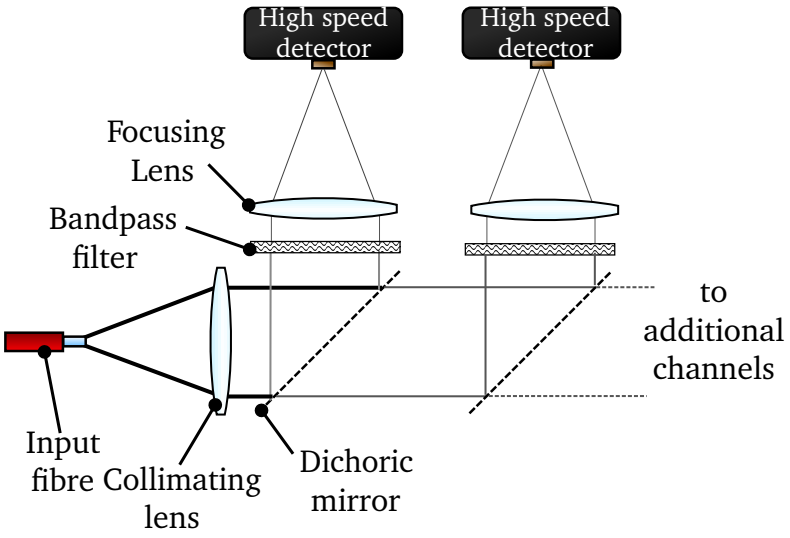


Figure 2.3: Schematic of a single input, multiple channel radiometer systems. The system takes the output from a fibre and directs the light, via filters, to high speed detectors.

throughput and, while larger diameter fibre is available, it is considerably more expensive and of limited benefit due to the active areas of high-speed detectors.

To maximise coupling efficiency probe design must be optimised for the fibre characteristics. Two pyrometry probe heads have been developed. One probe head has a nominally collimated design to maximise light collection. The other, focused configuration, is designed to collect light from a sub-mm diameter spot.

The optical probes have been designed using Zemax Opticstudio and a number of designs have been tested, see Appendix A.5. Figure 2.4 shows a schematic of the collimating probe head. Figure 2.5 shows a schematic of the focusing probe head.

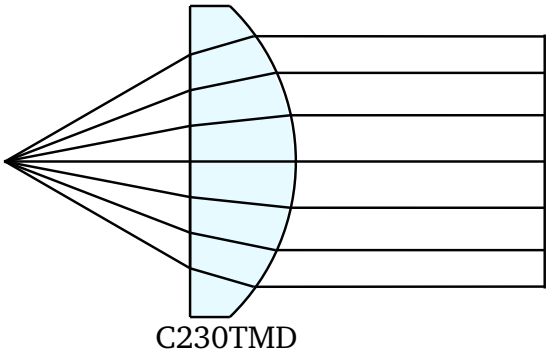


Figure 2.4: A ray diagram of the 'collimating' probe head. A high numerical aperture lens is used to focus light from a sample into an optical fibre.

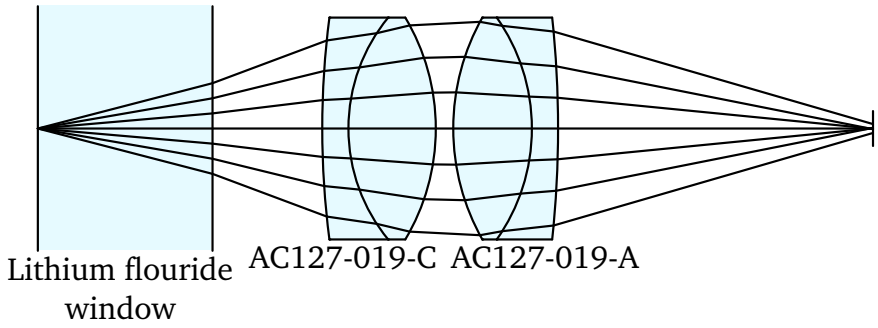


Figure 2.5: A ray diagram of the focusing probe head. Two achromatic lenses couple light from a sample into an optical fibre. The design was optimised using Zemax Opticstudio; the root-mean-squared spot size was 137 μm.

The collimating head is not sensitive to alignment and positioning. However, the focusing head must be positioned with precision. A spacer block was used to ensure that a precise stand-off between the focusing probe head and the target is achieved.

2.4 Laboratory testing

2.4.1 Time resolution

Given the goal to improve time resolution it is necessary to define what is meant by time resolution. When considering analysis of electrical signals a common metric is signal rise time. The rise time is the signal response when the input changes discontinuously from a one value to another, usually this is from zero to a finite value.

A commonly used definition is the 10% to 90% value. This is defined as the time taken for the signal to pass from the 10% steady state value to 90% steady state value, see Figure 2.6.

One issue that complicates the measuring of rise time is that no physical systems are truly discontinuous. However, lack of a discontinuity is acceptable when testing a system provided the transition time of the input is significantly faster than the system under test. For the sub-nanosecond domain, few systems are capable of providing a step function with transitions significantly faster than a nanosecond. Thus an alternative approach is used here.

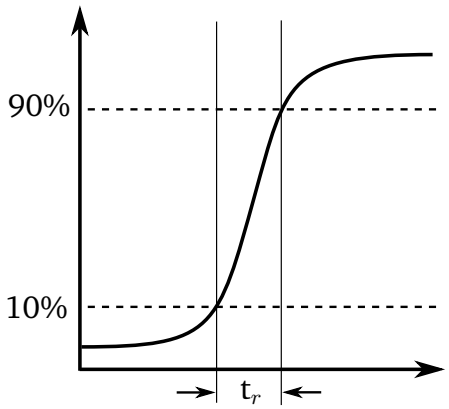


Figure 2.6: Plot showing the definition of rise time using the 10% to 90% criteria.

Rather than applying a step function, a fast pulse is applied. The drawback of this approach is that a steady state is not reached and the signal immediately falls after rising. However the same 10%-90% criterion can be applied to the baseline to peak value.

The system used for these tests was a picosecond laser (PicoQuant LDH-P-C-840). The laser produces pulses a nominally 825 nm wavelength pulse with a full-width half maximum (FWHM) duration of <90 ps; approximately 10 times shorter than the nanosecond time response relevant to the detector testing.

The rise times for a selection of the detectors listed in Table 2.1 were measured. One was an amplified photodiode, FEMTO HCA-S-400M0SI, that is quoted to have a 400 MHz bandwidth (this is equivalent to a 0.88 ns rise time). Two were avalanche photodiodes ThorLabs APD430A and ThorLabs APD430A, also with 400 MHz bandwidth. The other two detectors are photomultiplier tubes. PMTs are less straightforward than amplified photodiodes because the gain and temporal response of a PMT can be varied using a control voltage, characterisation of the PMT response is therefore, necessary.

To characterise the PMT response the detectors were exposed to the picosecond laser pulse with a range of control voltages and the rise times were measured. The results of the rise time tests for both the PMTs and the photodiode are shown in Figure 2.7 and Table 2.2. It can be seen that when using a control voltage greater than 0.4 V the PMT a sub-ns rise time is achieved.

	Rise time / ns			
Control Voltage	PMT(H10721-20)	PD(HCA-S-400M-SI)	APD430A	APD430C
0.3	1.10			
0.4	0.95	0.7	1.2	1.2
0.5	0.85			

Table 2.2: Results of the rise time experiments. The photomultiplier tube (PMT) has a variable control voltage; the photodiode (PD) is not variable.

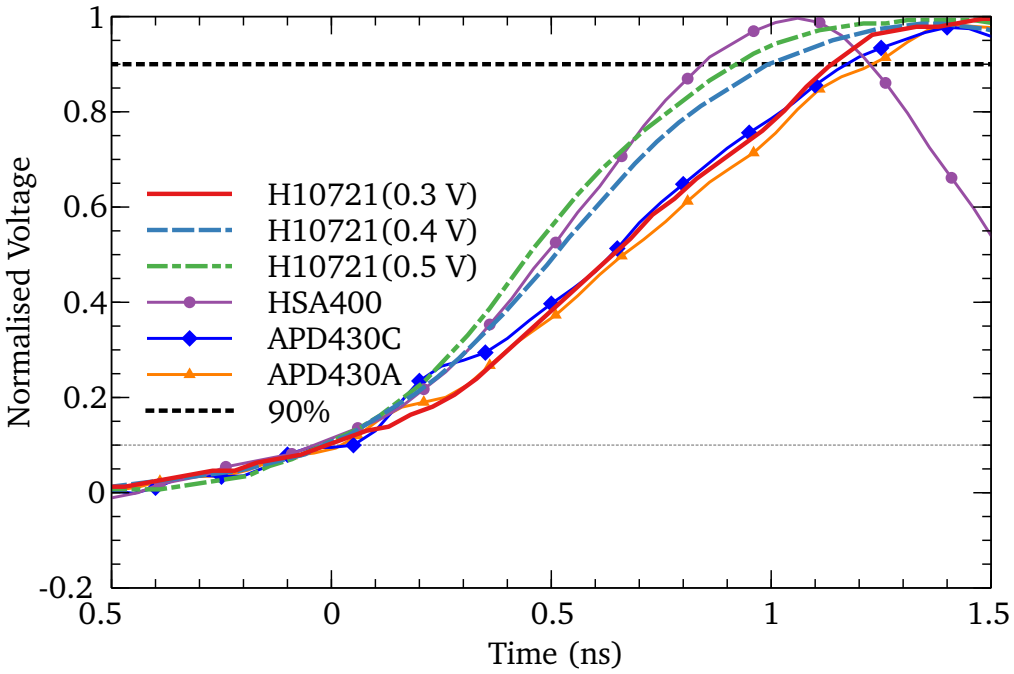


Figure 2.7: Plots showing the response of the H10721-20 photomultiplier tube and the HSA400 photodiode when irradiated with a <90 picosecond (FWHM) laser pulse.

2.4.2 Spatial resolution

The definition of spatial resolution in relation to defining the performance of a collection probe is less straight forward than the definition of rise time. While there are a number of definitions of spatial resolution they are largely formulated for imaging and based of the ability of a system to distinguish between two objects. The issue to be parameterised in this case is more analogous to defining the spot size of a beam, but rather than defining an edge of illumination, it is desired to define the edge of collection.

A common approach for defining the edge of a beam is to use the $1/e^2$ limit

where the 'edge' of the beam is defined as the position where the intensity of the beam falls to approximately 13.5% of the peak value, see Figure 2.8. A similar threshold can be applied to collection with some modifications.

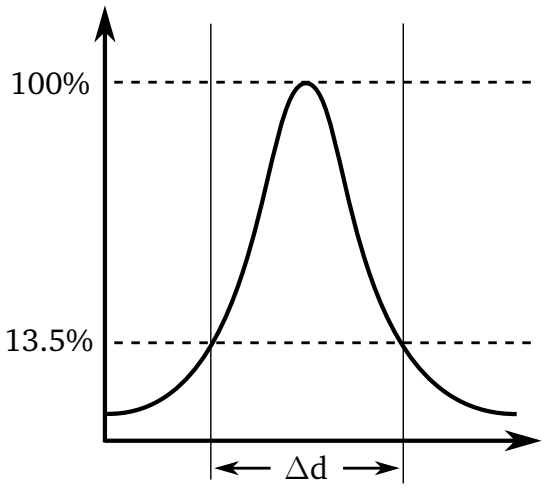


Figure 2.8: Figure illustrating the $1/e^2$ limit for defining spot size; this limit is commonly used for defining beam diameters of lasers.

The $1/e^2$ threshold cannot be simply applied to collection optics because no spot, with a defined intensity profile, exists. However it can be imagined that, if the system is collecting from an ideal source of varying diameter, as the source reaches the collection limit of the optics increases in source diameter produce progressively smaller changes in collected light. A modelling methodology using this approach has been implemented in Zemax OpticStudio.

The approach to determining the collection 'spot size', it to first develop the system in sequential mode in Zemax (see the Zemax manual for a discussion of optical modelling modes [76]). The model is then converted to non-sequential mode for Zemax and a source of varying diameter modelled. The method has been applied to the focussing probe head. The results, shown in Figure 2.9, indicate a collection 'spot size' of approximately 0.64 mm diameter, attained with an effective NA of 0.38.

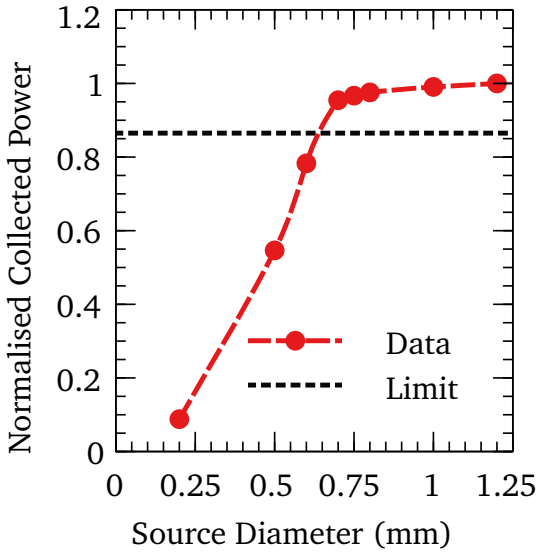


Figure 2.9: Plot of normalised collected power as source diameter was varied, as modelled in Zemax OpticStudio.

2.4.3 Minimum measurable temperature

A number of different configurations of pyrometer were used in the course of the work presented here. To determine the minimum measurable blackbody temperature the output of the calibrated model was used to find the temperature that would generate signal levels of 1 mV, which would be measurable on a high-speed digitiser at 400 MHz bandwidth, results from this calculation are shown in Table 2.3.

Channel	Minimum measurable temperature (K)
1	1207
2	935
3	855
4	809
5	795

Table 2.3: Results from calculation of the minimum measurable temperature for a pyrometry system.

2.5 Summary

The purpose of this chapter has been to provide context for the design and testing of a high speed optical pyrometer. The first step has been to review the existing literature to provide an overview of the systems that have previously been developed. A key outcome of the review was that, while a number of pyrometer designs have been reported, a standardised process for the design of systems has not been established. A standardised process is difficult to develop because pyrometry design requires the balancing of a number of factors and the application that the pyrometer will be used for.

Following the review, a framework that breaks a pyrometry system into sub-systems was introduced. The framework then outlines the key performance parameters of the different sub-systems.

The radiometer sub-system performance metrics have been identified as rise time and the minimum measurable temperature. The probe head can be parameterised by spot size and numerical aperture. Components have been selected or designed for optimal performance against these criteria. The performance of components against these metrics have been demonstrated.

The rise time results show that the detectors tested have rise times either below, or very close to 1 ns. While systems with faster rise times have been reported they did not operate cover the range of wavelengths available with this detector selection, specifically in the infrared region.

The optical probe sub-system performance metrics have been identified as numerical aperture, where the component with the minimum NA is the limiting factor, and collection spot size, a approach for defining collection spot size has been proposed as no definition could be found in the literature. A probe head with an NA of 0.38 and collection spot size of 0.64 mm has been designed. The design should be able to convey approximately 40 times more light in comparison to the design reported by Blanco *et al.*[68].

3

Sources of uncertainty in pyrometry

3.1 Introduction

For pyrometry to fulfil the goal of providing temperature data for the refinement of equations of state it is necessary for the technique to accurately determine the bulk temperature of the material under test. However, the accuracy of pyrometry in determining bulk temperature is limited by a number of uncertainties [77]. The purpose of this chapter is to discuss the most significant sources of uncertainty and assess their impact.

Some of the uncertainties are random uncertainties, for example due to the radiance measurement process, and some are systematic uncertainties. The various uncertainties have been separated into two categories; uncertainties in the determination of the sample's surface temperature and uncertainties due to the difference between the sample's surface temperature and its bulk temperature. These two categories are now discussed in more detail.

3.2 Sources of uncertainty in surface temperature

The sources of uncertainty that affect the determination of surface temperature can be categorised into broadly three areas:

- Uncertainty in the radiance measurement, due to noise in the instrument from shot noise, thermal noise and digitisation noise.
- Uncertainty in the emissivity of the sample.
- Uncertainty in the radiance measurement due to spurious signals created in the dynamic loading of the sample.

3.2.1 Sources of measurement noise

The components of measurement noise and how they may be reduced are now discussed.

Shot Noise

Shot noise is a fundamental source of noise due to the quantisation of light. A light signal is made of photons and while on average the signal will produce a fixed rate of photons, the arrival of each individual photon is independent; the statistics of independent random events are described by a Poisson distribution. The signal levels in pyrometry are usually sufficient for the Poisson distribution to be considered Gaussian, which allows shot noise to be described by the equation:

$$\mathrm{SNR} \propto \sqrt{N}, \tag{3.1}$$

where SNR is the signal-to-noise ratio (*i.e.* signal mean divided by the standard deviation of the signal) and N is the number of events, in the case of light detection that is the number of photons. The relation is proportional, rather than exact, because the conversion of photons to electrical signals is less than unity (although not substantially less in the visible spectrum). For a 650 nm, 1 μW source, sampled for 1 ns, with an ideal detector shot noise is approximately 0.2%.

Due to the fundamental nature of shot noise it is not possible to reduce it on a particular signal but its impact can be minimised by maximising the signal. Shot noise is rarely the most significant source of noise in pyrometry applications but has been included here for completeness.

Digitisation noise

Here the term digitisation noise is used to describe noise that is added due to the process of measurement and storage of a signal. There are two aspects to digitisation noise, the effects of the quantisation process and dither, which is used to counter artefacts of quantisation.

In modern practice, virtually all rapidly varying signals are recorded on high bandwidth digitisers that employ analog-to-digital converters (ADC) to convert signals for storage. The process of digitisation is straight-forward, the signal value is measured at a specific time and, based on the on this measurement, the signal is stored as an appropriate level. However, one of the subtle issues with this process is that not only is each individual measurement limited to the set of quantisation levels but the system is unable to distinguish levels beneath the quantisation resolution. For example, in a 2-level quantisation scheme that varies between 1 and 0, a signal that varies between 0.1 and 0.4 will always produce a level of zero. It is possible to overcome this resolution limitation.

The two step process for improving digitiser resolution is to first (somewhat paradoxically) add random noise ('dither') and second take multiple samples of the signal ('oversample'). The addition of random noise of sufficient magnitude means that, although the outcome of the quantisation process will now have a random component, the mean value will tend to the measurement before quantisation. Over-sampling means that the same temporal resolution can be attained after the averaging process.

The benefits of dithering are widely known and incorporated into most modern digitisers. The optimum amount of dither noise to add is dependent on the bit-depth of the instrument and, assuming unity signal, is determined by the expression:

$$\mathrm{SNR} = \frac{3}{2} 2^{Q} \tag{3.2}$$

where SNR is signal-to-noise ratio and Q is the bit-depth. For an 8-bit digitiser dither noise is approximately 0.3%.

The use of high speed digitisers for the high bandwidth recording of electronic signals is unavoidable in shock experiments so digitisation noise will always be present. However, digitisers of higher bit-depths are being developed which would have reduced dither noise.

Thermal Noise

Thermal noise is also unavoidable, in general, but certain circuit architectures are less noisy. Thermal noise, which is usually most significant in the detection circuit, can be minimised by appropriate choice of detector. This was discussed in Section 2.3.1.

Summary of measurement noise

The combined effect of the shot noise and digitisation noise is an error of approximately 1% in radiance measurement. The effect of thermal noise is less easy to quantify as it acts as a fixed noise threshold dependent on the bandwidth of the measurement. Furthermore, although the threshold is fixed, the wavelength dependence of blackbody emission and the wavelength dependent sensitivity of detectors means defining a quantitative error value due to thermal noise requires numerous parameters to be specified.

To illustrate the behaviour with a representative example consider a 1000 K source, with a 1 mm diameter, 0.3 NA collector into a PMT with 400 MHz bandwidth (NEP of 11 pW·Hz$^{-\frac{1}{2}}$) through a 100 nm width bandpass filter, centred at 600 nm, the optical power that reaches the detector will be 1.29 nW giving a SNR of 117 (or noise fraction of 0.9%). However, it should be noted that with a source just 100 K lower, at 900 K, the optical power on the detector is 90 pW giving a SNR of 8 (or a noise fraction of 12%). Thus thermal noise largely acts as a minimum temperature threshold, below which the uncertainty increases dramatically, however this threshold is a function of numerous parameters.

More generally, when considering the effect of measurement noise, it can be said that, provided the signal is above a certain threshold, the uncertainty due to measurement noise is less significant than other sources of uncertainty.

3.2.2 Emissivity uncertainty

Emissivity is an optical property of a material that parameterises its efficiency in emitting radiation. Emissivity can be affected by the pressure, density or temperature of the material which, as discussed, change drastically in plate impact experiments; emissivity changes is often the most significant source of uncertainty in pyrometry measurements on plate impact experiments. The effect of emissivity on a pyrometry measurement can be seen by re-arranging Planck's Law to allow temperature to be determined from a radiance measurement; doing so leads to the expression,

$$T = \frac{hc}{\lambda k_b \ln\left(1 + \frac{2hc^2}{\epsilon L \lambda^5}\right)}, \tag{3.3}$$

see Equation 2.1 for definition of terms.

From Equation 3.3 it can be seen that it can be seen that, first, emissivity scales radiance and, second, temperature is not linearly dependent on radiance. To illustrate the relation between temperature and radiance Figure 3.1 shows how temperature varies with 650 nm light emitted from a blackbody.

To quantify the effect of radiance uncertainty, and hence emissivity uncertainty, it can be seen that a factor of 10 increase in emitted light is accompanied by a change in temperature of approximately 50 K ($\sim$7%); similarly if emissivity was estimated to be 1 but was actually 0.1 there would be an error of 50 K. By applying a similar analysis it can be seen that, if emissivity is know with an uncertainty of $\pm$50%, temperature can be determined with an uncertainty of 1%.

Emissivity uncertainty can be reduced by measuring emissivity during the experiments. There are numerous aspects to solving the problem of dynamic emissivity measurement, Chapter 8 discusses the topic of determining emissivity be measuring reflectivity in more detail. The discussion above was limited to the effect of emissivity uncertainty on temperature uncertainty.

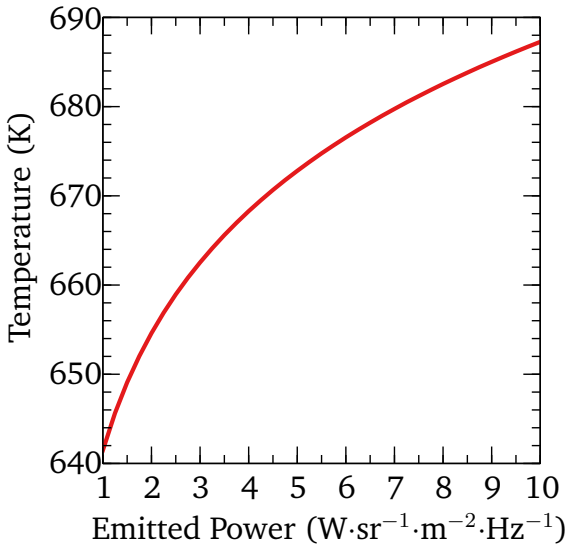


Figure 3.1: Visualisation of how the apparent temperature of a blackbody source varies with emitted optical power as determined using the Planck equation, considering emission at 650 nm.

3.2.3 Non-thermal signals

The presence of non-thermal signals have the potential, in the worst case, to cause complete data loss of pyrometry measurements as they can saturate detector systems and digitisers. Even small amounts of additional light can obscure the underlying temperature signal and mean signal processing techniques, such as temporal averaging, cannot be meaningfully applied. Avoiding the generation and recording of spurious signals can only be addressed through good experimental design. There are a number of features that are known to generate light in shock experiments, these are now listed with potential solutions:

- Air bubbles in the adhesive layer will heat dramatically on shock. These can be avoided with careful assembly of the experiments.
- Excessive surface roughness promotes micro-jetting. This can be avoided by specifying high precision surface finishes on interfaces (i.e. polishing and diamond turning).
- Shock response of adhesive and window materials can lead to emission.

Certain materials such as lithium fluoride and Loctite 326 have been demonstrated as producing minimal emission under shock.

- Shock of window edges is known to cause optical emission. Ideally flyer-sample geometry should be designed to preclude edge shocks, failing that impedance matching fillers can be used.

Furthermore it is prudent to, as much as possible, optically isolate the sample and optical probe from the environment by surrounding the experimental assembly with opaque material.

3.3 Sources of uncertainty due to interface effects

The practicalities of applying pyrometry to shock experiments mean it is inevitable that there will be an interface where the pyrometry measurement is made. The presence of an interface results in various perturbations to the shocked system. It is necessary to understand the effect of these perturbations to accurately determine the sample temperature. The uncertainties that arise in this process can be split into two categories:

- Uncertainty in the physical parameters that affect heat transport at the surface interface. This usually consists of three materials consisting of a sample-adhesive-window layer.

- Uncertainty in the temperature of the low emissivity materials in thermal contact with the surface.

To provide context for this discussion the example of a tin sample with a lithium fluoride window (attached with polymer adhesive) is used, see Figure 3.2. This example has been chosen because it is representative of a number of experiments detailed in later chapters.

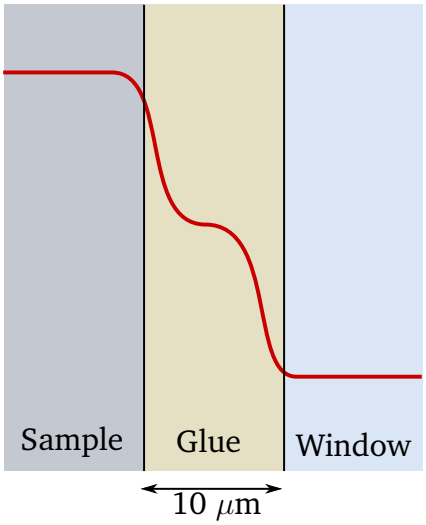


Figure 3.2: Schematic diagram of the sample-glue-window interface during shock loading. The red line indicates the temperature at that position. The passage of the shock initially heats the different components to different temperatures, as time progresses the heat diffuses between the components.

3.3.1 Heat transport at an interface

The opacity of metal samples mean it is inevitable that any measurement of optical emission from a metal sample will collect emission from the surface (specifically the depth will depend on the skin depth of the metal but is typically of the order of nanometres). Furthermore, there will be a systematic difference between the bulk temperature and the surface temperature, unless a material has infinitely high thermal conductivity or it is in contact with a perfect insulator.

Thus to determine the bulk temperature of the sample it is necessary to understand the thermal behaviour of the sample surface. When assembled, the surfaces of the sample and the window are separated from each other by a glue layer, see Figure 3.2. Considering the system immediately after the shock has passed, each element of the system will be in the post-shock state. The thermal evolution can then be described by the heat equation,

$$\frac{\partial T}{\partial t} = \alpha \left(\frac{\partial^2 T}{\partial x^2} + \frac{\partial^2 T}{\partial y^2} + \frac{\partial^2 T}{\partial z^2} \right), \tag{3.4}$$

where T is the temperature, α is the thermal diffusivity, t is time and x, y and z are the spatial dimensions. In many cases it is possible to consider the interface

a 1D system, in this case the equation can be simplified to,

$$\frac{\partial T}{\partial t} = \alpha \frac{\partial^2 T}{\partial x^2}. \tag{3.5}$$

The thermal diffusivity term is further defined as,

$$\alpha = \frac{\kappa}{\rho c_P}, \tag{3.6}$$

where κ is thermal conductivity, ρ is density and c_P is specific heat capacity at constant pressure.

There is extensive literature describing the transport of heat in solids, giving analytical solutions to the heat equation for a number of specific cases. More generally the heat equation can be solved numerically. In the context of shock temperatures, Grover and Urtiew [78] reported a number of expressions describing 1D heat transport at an interface between two media which are relevant to plate impacts. More recently Tan and Dai [79] have derived 1D expressions for three and four layer systems. However La Lone *et al.* [80] have presented results with similar models and regimes to the example here and justify the use of the simplified expression,

$$T_I = T_S - \frac{T_S - T_W}{1 + \left(\frac{\kappa_S \rho_S C_S}{\kappa_W \rho_W C_W}\right)^{\frac{1}{2}}}, \tag{3.7}$$

where T is the material's temperature, κ is the material's thermal conductivity, ρ is the material's density and C is the material's specific heat capacity, with the subscript I,S or W specifying if it is the interface, sample bulk or window bulk respectively.

If the adhesive layer can be considered thermally 'thick' then the two media solution is applicable and this equation can be used to determine the sample's bulk temperature. However, while pyrometry allows measurement of T_I, given the number of terms, it is not possible to solve the two material expression to determine the bulk sample temperature without further information. The two additional parameters that would allow the bulk temperature of the sample to be determined are the ratio of the diffusivity and temperature of the glue. The following sections discuss these parameters.

3.3.2 Uncertainty in diffusivity ratio

The diffusivity ratio is clearly dependent on diffusivity of the two interface materials. While some investigations into thermal transport in shocked materials have been conducted[81], which could determine information on thermal diffusivity, data is limited. However, as noted previously, diffusivity is determined by thermal conductivity, specific heat capacity (at constant pressure) and density, thus the diffusivity ratio can be determined if these three parameters are known.

Density under shock conditions is relatively straightforward to determine as it can be determined to high accuracy from the Rankine-Hugoniot relations. However, thermal conductivity and heat capacity are more complex so are now discussed in more detail.

Thermal conductivity

No general approach for determining thermal conductivity at shock conditions could be identified so it was necessary to consider each material individually. Thus for the purposes of illustrating the analysis and due to their use in later chapters the 'sample' material will be defined as tin and the 'adhesive' defined as Loctite 326.

Measurement of thermal conductivity under shock conditions is challenging, as such there is limited data on thermal conductivity in shock experiments. However there is more data on the variation of material properties at pressures similar to shocks that has been generated using quasi-static laboratory equipment such as diamond anvil cells (DACs). An approach often used, on iron for example [82] (due to its relevance to Earth's core physics), is to:

1. Use the Wiedeman-Franz law to relate thermal conductivity to electrical conductivity.

2. Use literature data to determine the electrical conductivity of the material at high temperatures and pressures.

3. Convert literature electrical conductivity data to thermal conductivity.

This approach was used to determine the thermal conductivity of tin; data on the high pressure resistivity (the reciprocal of conductivity) of tin has been reported by Bridgman [83] and Eiling and Schilling [84]. Although they were only able to measure up to approximately 10 GPa, they also present a theory predicting resistivity at higher pressures.

As discussed the Wiedeman-Franz law is the basis for relating thermal conductivity to electrical conductivity. The relation is given by the expression,

$$\frac{\kappa}{L} = T\sigma, \tag{3.8}$$

where L is the Lorenz number (usually taken to be 2.44 $\times$ 10^{-8} W·Ω·K^{-2}), σ is the electrical conductivity and κ and T are as previously defined. It should be noted that the Weideman-Franz law is an empirical law which applies to metals and its value can vary by up to 30% [85, p.169]. Using this relation, together with the Eiling and Schilling model [84], steps outlined above have been used to predict thermal conductivity at shock pressures, see Figure 3.3.

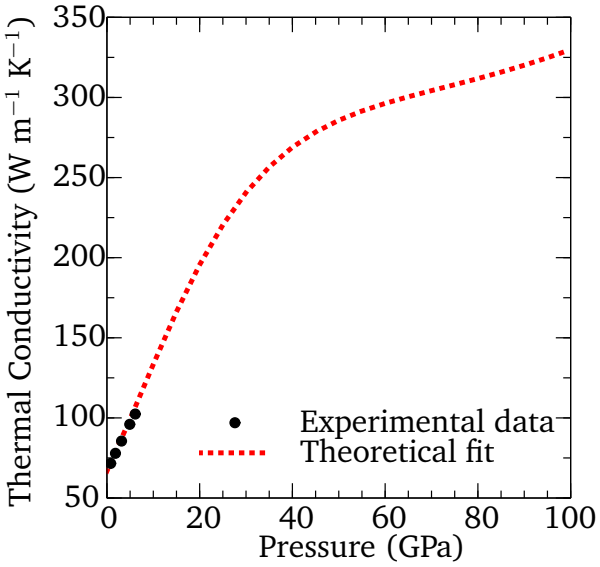


Figure 3.3: Variation of thermal conductivity of tin with pressure. Calculated using data presented by Eiling and Schiling combined with the Wiedeman-Franz Law (assuming a temperature of 300 K).

There is no specific literature discussing the conductivity (thermal or electrical) of Loctite 326 at high pressure however the data sheet details its composition

as 20-40% 2-hydroyethyl methacrylate, 10-20% isobornyl methacrylate and all other constituents are $< 5\%$. Thus a suggested proxy for shock behaviour is poly(methyl methacrylate) (PMMA).

PMMA has been studied in silicon-carbide anvils [86], see Figure 3.4. The study by Hsieh *et al.*[86] described the thermal conductivity of PMMA (as a function of pressure) as,

$$\Lambda_{PMMA}(P) = \Lambda_1 + \Lambda_2\sqrt{P}, \tag{3.9}$$

where P is the pressure, Λ_1 is the low pressure thermal conductivity of PMMA and Λ_2 is a constant that scales the pressure dependence. Λ_1 is determined to be 0.185 $W^{-1}{\cdot}m^{-1}{\cdot}K^{-1}$ and Λ_2 is 0.11 $W^{-1}{\cdot}m^{-1}{\cdot}K^{-1}{\cdot}GPa^{-\frac{1}{2}}$.

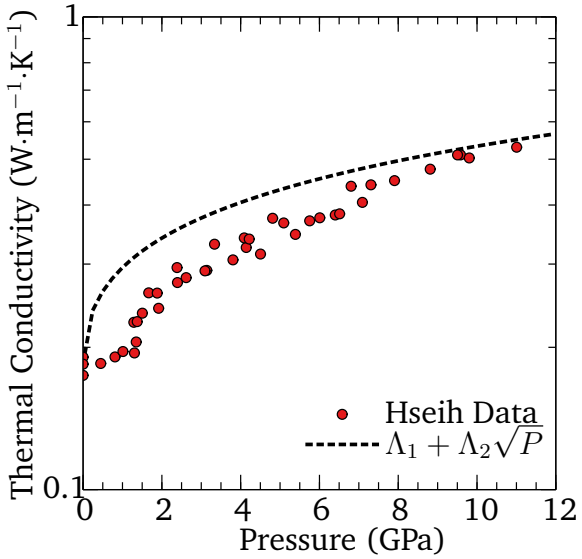


Figure 3.4: Thermal conductivity of poly(methyl methacrylate) at a range of pressures as reported by Hsieh [86]. Results from a theoretical model are also shown.

Heat capacity

Like thermal conductivity, data on the specific heat capacity of materials at shock conditions is limited so to predict specific heat capacity at shock conditions extrapolation from lower pressure experimental data is required.

Developing an approach for tin first; the heat capacity of most elements can be approximated by the Dulong-Petit Law [87], which states the heat capacity

per mole is given by,

$$\frac{c}{N} = 3R. \tag{3.10}$$

Where c is heat capacity, N is the number of moles and R is the gas constant. Thus the heat capacity of tin (Sn) can be expected to remain approximately constant across changes in pressure and temperature at 210 J·kg^{-1}·K^{-1}.

PMMA is not an element so another approach is required; Andersson and Sundqvist present data on the pressure dependence of the specific heat capacity of PMMA up 4 GPa [88]. Determining a value for specific heat capacity at 20 GPa requires extrapolation considerably outside the reported data, however this is necessary given the lack of other high pressure data. The data from Andersson and Sundqvist was fitted with a function of the form,

$$c_p \left(1 - aP^b\right), \tag{3.11}$$

where a and b are arbitrary constants, c_p is specific heat capacity at atmospheric pressure and P is pressure. Figure 3.5 shows a plot of the data and the fitted function.

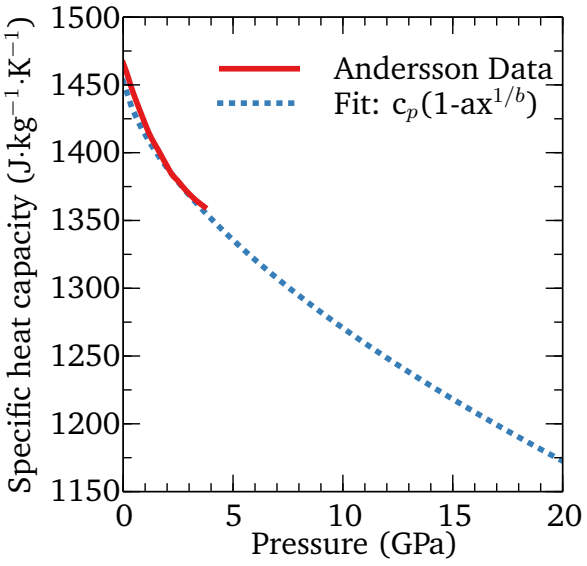


Figure 3.5: Plot showing the variation of specific heat capacity (at constant pressure) of poly(methyl methacrylate) with pressure. Also shown is a model with variables a = 0.00339 and b = 1.69.

3.3.3 Estimate of high pressure diffusivity

It is now possible, based on the preceding sections, to estimate how the diffusivity ratio will vary with pressure at the interface. Predictions for the thermal conductivity and specific heat capacity in tin and PMMA are presented in Tables 3.1 and 3.2. Using these values, the limits of thermal diffusivity were calculated if the underlying parameters varied by $\pm$50% and are shown in Table 3.3. If the central predicted values are used then it can be seen that, from an initial value of 341, the ratio changes to 360 under compression to 100 GPa, which is a variation of just 6%. However, despite a larger difference of approximately 16% from ambient values at 20 GPa, it can be concluded that diffusivity ratio is not a strong function of pressure (assuming constant phase).

To calculate the potential effect on a dynamic temperature measurement, the temperature difference between the surface and the bulk can be calculated with the predicted diffusivity ratios. These values indicate a temperature difference of between 10 K and 70 K at 20 GPa, suggesting an error of approximately $\pm$3%.

Pressure (GPa)	Thermal Conductivity ($J{\cdot}m^{-1}{\cdot}K^{-1}$)			Specific Heat Capacity ($J{\cdot}kg^{-1}{\cdot}K^{-1}$)		
	Lower	Middle	Upper	Lower	Middle	Upper
0		67			210	
20	121	241	362	105	210	420
50	144	286	430	105	210	420
100	165	329	484	105	210	420

Table 3.1: Table of predicted values of thermal conductivity and specific heat capacity of tin based on a number of literature sources.

3.4 Shock state uncertainties

While the shock state of an ideal, two material interface is well defined, the use of optical windows in a shock experiment usually requires adhesive to mount the window. The addition of a thin, low impedance material (the adhesive)

Pressure (GPa)	Thermal Conductivity ($J{\cdot}m^{-1}{\cdot}K^{-1}$)			Specific Heat Capacity ($J{\cdot}kg^{-1}{\cdot}K^{-1}$)		
	Lower	Middle	Upper	Lower	Middle	Upper
0		0.185			1370	
20	0.34	0.68	0.87	550	1100	1650
50	0.48	0.96	1.44	450	900	1350
100	0.62	1.29	1.94	330	660	990

Table 3.2: Table of predicted values of thermal conductivity and specific heat capacity of poly(methyl methacrylate) based on a number of literature sources.

Pressure (GPa)	Diffusivity Ratio		
	Lower	Middle	Upper
0		341	
20	38	288	3500
50	34	300	3600
100	40	360	4420

Table 3.3: Table of upper, middle and lower predicted values for the diffusivity ratio at a range of pressures.

causes uncertainty in the states that all the material near the interface attains after the shock.

The final state of the interface materials is reached via a 'ring-up' process, see Figure 3.6. The ring up process can be modelled as multiple shocks that reverberate between the two high impedance interfaces.

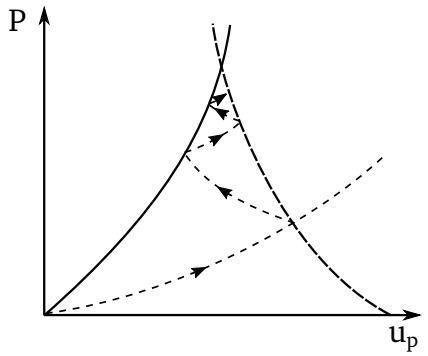


Figure 3.6: Depiction of the 'ring up' of a low impedance layer between two higher impedance layers. The curves show the Hugoniot curves of the three layers in particle velocity-pressure space. While the final state it determined by the two outer layers, the middle layer is shocked multiple times, as indicated by the multiple reflected Hugoniots, until the final state is reached.

To illustrate the potential size of this effect, calculations of the ring-up process, considering a tin-glue-lithium fluoride interface, have been conducted. The most straightforward analysis is to use the results of impedance matching calculations between the tin sample and LiF window. The result of this analysis when the tin is shocked to 18.83 GPa (equivalent to a 1 km·s^{-1} tungsten impact) is the glue would attain a state of 14.15 GPa, 0.530 cm^3·g^{-1} and 2.27 GPa·cm^3·g^{-1}.

However, while the first state of the ring up process is well defined by an impedance matching calculation (because it is on the principal Hugoniot) subsequent shocks are not on the principal Hugoniot, see Figure 3.7, without an EoS to describe off-Hugoniot states there is uncertainty what final state will be reached.

A simple EoS which enables calculation of off-Hugoniot state is to use a Mie-Grüneisen equation of state [49] which uses a linear u_s-u_p Hugoniot to approximate an EoS. Table 3.4 shows the results of a number of calculations for the states that are created in a ring up process using both the ideal shock and Mie-Grüneisen equations of state. It can be seen that the effect of re-centering the Hugoniots and allowing deviation from the principle Hugoniot leads to differences in internal energy of over 10% but differences in pressure and specific volume are smaller, indicating that temperature must be significantly different between the two cases. While a Mie-Grüeisen EoS does provide a solution, the value of the Grüneisen γ parameter is subject to considerable uncertainty itself.

These results highlight an issue with pyrometry in this configuration, not only is there uncertainty in the final state of the material that has rung-up, the ring-up process also affects the sample. In this case the part of the sample in close proximity to the glue (which is the part from which pyrometry data would be collected) undergoes a shock-release process followed by multiple re-shocks. The process is quite complex but was modelled in detail by La Lone *et al.* [80] using the CTH code [90]. The results they reported indicated the relevant region of the sample may be heated by 20–30 K in comparison to the bulk of the material.

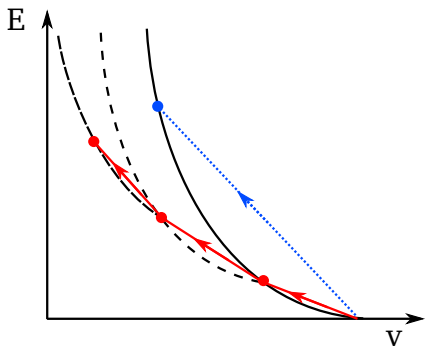


Figure 3.7: Depiction of the 'ring up' of a material in energy-specific volume space. After a shock, the state of the material moves further up the Hugoniot, as indicated by the arrows. However, in the case of multiple shocks the material is in a different state after each shock resulting in a modified Hugoniot. In volume-energy space the final state is not as easily defined in the particle velocity-pressure space.

State	Pressure (GPa)	Pressure' (GPa)	ΔP	Volume ($cm^3 \cdot g^{-1}$)	Volume' ($cm^3 \cdot g^{-1}$)	ΔV	Energy (GPa·$cm^3 \cdot g^{-1}$)	Energy' (GPa $cm^3 \cdot g^{-1}$)	ΔE
0	0.0	0.0		0.843	0.843		0.0	0.0	
1	5.87	5.87	0.0%	0.619	0.619	0%	0.659	0.659	0%
2	10.28	10.16	-1.1%	0.553	0.559	1%	1.177	1.139	-3%
3	12.91	12.79	-0.9%	0.523	0.534	2%	1.511	1.422	-6%
4	13.65	13.59	-0.5%	0.514	0.528	3%	1.631	1.505	-8%
5	13.71	13.66	-0.4%	0.510	0.527	3%	1.694	1.513	-11%
6	13.97	13.94	-0.2%	0.508	0.525	3%	1.714	1.542	-10%

Table 3.4: Table of predicted pressure, specific volume and specific energy states of PMMA using a linear u_s-u_p Hugoniot (determined from fitting Marsh data [89], resulting in constants $c_0 = 2.6811$, $s = 1.4197$) reflection method and the same Hugoniot with a Mie-Grüneisen EoS (denoted by ', $\gamma = 1$) method.

These uncertainties in the state of the materials near the interface mean additional temperature data is less useful for constraining EoS data. Specifically, although the final pressure-particle velocity state is determined by the two outer materials, see Figure 3.6, the final internal energy and pressure (and by extension temperature) are not.

3.5 Predicted measurement effect

To understand the magnitude of the effect of the glue layer and its properties it is insightful to apply the previously discussed models and calculate the resultant

effect on the interface temperature in a specific example.

The example used here is the aforementioned 1 km·s^{-1} test problem. From Table 3.4 it can be seen the state of PMMA is 13.94 GPa, 0.525 cm^3·g^{-1} (ρ = 1.90 g·cm^{-3}) and 1.542 GPa·cm^3·g^{-1}.

Using the approach outlined in Appendix C.3 the temperature on the PMMA adiabat can be calculated. Then using the model for heat capacity and the energy difference between the adiabat and the glue state the temperature of the glue can be calculated. Following this procedure the temperature of the glue has been estimated to be 586 K.

Again the approach outlined in Appendix C.3 can be used to calculate the Sn temperature. It should be noted that the approach does not consider the ring-up interactions; a hydrocode would be the most appropriate way to calculate such effects [80] but the purpose of this analysis is to be representative of the heat transport effects so the simpler model is acceptable. Based on the calculation the bulk tin will attain a temperature 690 K. Using Equation 3.7 it can be calculated that the interface temperature will be 680 K, approximately 10 K less than the bulk temperature; this is a 1.5% difference.

3.6 Summary and conclusions

This chapter has reviewed the causes of uncertainty in pyrometry. Uncertainties can be divided into two categories, those due to uncertainties in the temperature measurement of the emitting surface and those that are due to the physical effects of the interface. Uncertainties in the temperature measurement are considered in more detail in the following chapters, the uncertainties due to the interface have been discussed quantitatively.

With regard to determining bulk temperature from interface measurements uncertainties in the diffusivity ratio are estimated to lead to bulk temperature uncertainties of up to 3% at 20 GPa. However an associated issue is that there is also uncertainty in the states generated in plate impact experiments due to the presence of a glue layer between the sample and the window. Calculations

using different models indicate differences of up to 10% in the internal energy of a shocked material depending on the model used.

There are two key conclusions from these findings:

- The value of a temperature measurement is limited unless the state that is created is well understood thus, to generate data for the constraint of EoSs, temperature measurements need to be made either alongside measurements of other state variables or on previously well characterised states.
- If accurate (<1% accuracy) bulk temperature measurements are desired, further investigations into the thermal transport properties of the interface materials are required. Quasi-static compression with diamond anvil cells is probably the most straightforward approach to get thermal transport properties at high pressure.

While the challenges in determining EoS data are significant to the application of pyrometry data, the remainder of this thesis will concentrate on improvements in the pyrometry measurement itself.

4

Investigation of the effect of filter parameters on pyrometry accuracy

4.1 Introduction

In optical pyrometry, the temperature of a surface is inferred by measuring the light emitted by a sample due to thermal emission over one, or more, spectral bands. There are two potentially significant sources of uncertainty in this process: sample emissivity and the measurement of radiance. Emissivity can vary with state variables; if emissivity is not measured, significant uncertainty can result [91, 92]. Progress in the measurement of reflectivity (and hence its complement emissivity) has been reported in Chapter **??** and the wider literature [80, 93, 94]. However, further understanding of the uncertainty in a radiance measurement is also desirable as the resultant uncertainty in temperature is a combination of both uncertainties. The discussion in this chapter focuses on the uncertainties in a thermal radiance measurement.

To improve understanding of the uncertainty, a model of the system was created and Monte-Carlo modelling used to simulate the effects of noise. The model was validated against an experiment before using the model to investigate the effects of parameter changes. It was found that there are threshold effects when selecting a spectral window.

4.2 Background

Despite the conceptual simplicity of a spectral band pyrometer, there are numerous considerations when configuring the system, these include pyrometer topology, lens selection, detector choices and filter parameters. Consideration of the number of permutations of detectors, filters and lenses indicates it is not feasible to determine the optimum pyrometer experimentally. Furthermore, the increased complexity of an experimental system can obfuscate the effect of changing one component. For example, increasing the centre wavelength of a filter may decrease signal levels due to detector response, despite the increased emittance of a thermal source at longer wavelengths.

Complexities arise even if considerations are limited to which spectral bands to use. For example, moving the wavelength band toward the peak in the emission spectrum will make more light available for detection. However, it has been proposed previously that collection of light at shorter wavelengths allows the temperature to be determined more accurately as, in this section of the spectrum, small changes in temperature result in large changes in spectral radiance [95]. Similarly, it is clear that by increasing the passband of a filter more light will be available to be detected, however it is not clear this increase will reduce the uncertainty in the temperature measurement. The conflicting guidance of these heuristics indicate a complexity that requires deeper investigation to resolve.

Thus a model is needed to investigate the effects of changing individual components to identify the configuration changes that most significantly reduce measurement uncertainty. This chapter focuses on the combined effects of the wavelengths and wavelength ranges at which measurements will be taken as these are a fundamental choice when configuring a spectral-band pyrometer. Even restricted to these two variables it is not trivial to identify the most appropriate choices, and indeed this is a long-standing challenge [96–98]. While the published literature provides useful insights they overlook the requirement for high temporal resolution and are thus not immediately relevant to high strain rate experiments.

In particular, although high strain rate experiments allow extreme states to be reached, these states are only maintained for a short time. Considering plate impact experiments in particular, well defined states are maintained for $\sim\mu$s requiring sub-μs time resolution diagnostics. Correspondingly the high bandwidths required mean it is necessary to consider the effects of noise as this can significantly influence which wavelength ranges are most appropriate.

4.3 Development of a Monte-Carlo model

4.3.1 Calculation of radiance

A model has been developed to provide a quantitative understanding of the aforementioned compromises. The model consists of a source, a filter and a detector. Some limitations on the system being considered have been imposed. First, due to the high radiances at higher temperatures, the trade-offs regarding filter wavelength and passband are particularly relevant at low temperatures where spectral-band pyrometry is the most viable technique. Furthermore the available UK facilities are not able to generate temperatures significantly above 1700°K, see section 5.3 for further discussion. As such analysis shall be restricted to temperatures of less than 2000°K.

The transmission of the filter, $T(\lambda)$, was parameterised by a centre wavelength, λ_c and passband $\Delta\lambda$. It was also assumed the filters used are 'ideal' in that they have 100 % transmission in the passband and 0 % transmission out of band, as specified by the equation,

$$T(\lambda) = \begin{cases} 0, & |\lambda - \lambda_c| > \frac{\Delta\lambda}{2} \\ 1, & |\lambda - \lambda_c| \leq \frac{\Delta\lambda}{2} \end{cases} \tag{4.1}$$

In addition, shock experiments require high speed detectors; such detectors operate predominately in the visible and near-infrared part of the electromagnetic (EM) spectrum. Furthermore, many high speed pyrometry measurements use silica optical fibre, which has high propagation losses at longer wavelengths.

Thus the second limitation was that only centre wavelengths from 300 nm to 2000 nm will be considered.

Finally, to remove the additional uncertainties related to material specific emissivity it was assumed that these measurements are to be made on a blackbody (*i.e.* emissivity of one at all wavelengths). Thus the radiant output of the source is given by Planck's Law,

$$L_\lambda(\lambda, T) = \frac{2hc_0^2}{\lambda^5} \frac{1}{e^{\frac{hc}{\lambda k_B T}} - 1}, \tag{4.2}$$

where L_λ is the spectral radiance, h is Planck's constant, c_0 is the speed of light in a vacuum, λ is wavelength, k_B is Boltzmann's constant and T is temperature of the source.

Monte-Carlo simulations have been performed to investigate the uncertainties of the process of converting radiance to temperatures. The approach proceeds as follows:

1. Planck's law, Equation 2.1, is used to calculate the radiant output of a blackbody emitter viewed by an optical system with a filter specified by λ_c and $\Delta\lambda$ at a range of temperatures.

2. The detection of the light is simulated assuming a detector with an ideal spectral response of 1 V·W^{-1} for all wavelengths. Noise is generated via a Monte-Carlo process and added to the signal to simulate the uncertainties inherent in performing a high speed measurement. The probability distribution of the noise is determined by an appropriate noise model, discussed in §4.3.2.

3. The previously calculated radiance-temperature relation is used to convert the simulated measurement into a temperature. This process is repeated until a statistically reliable value of the uncertainty of the process, parameterised by the standard deviation, is found.

4. The properties (*i.e.* λ_c or $\Delta\lambda$ or both) of the filter are changed and the process repeated.

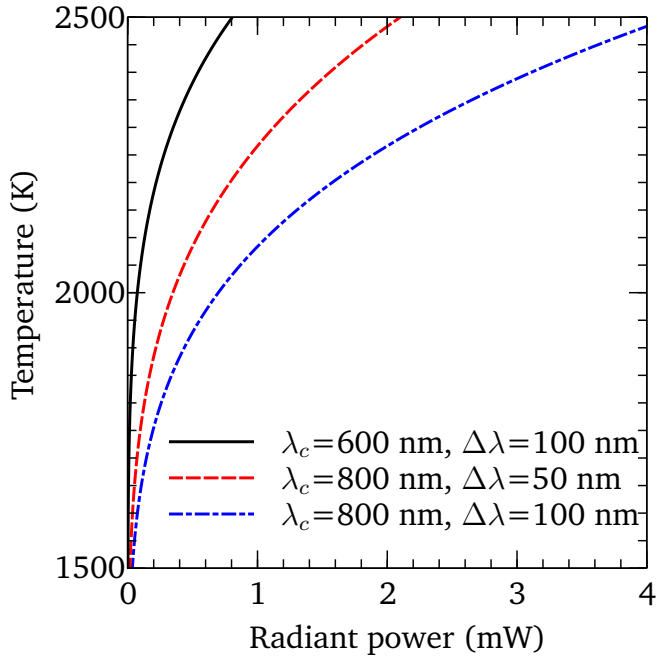


Figure 4.1: A radiance-temperature curve showing how the radiance of a blackbody can be related to its temperature over three filter passbands (light collected from 1 mm diameter spot with 0.2 NA optical system). The legend indicates the filter parameters.

To calculate the energy output from a blackbody over a specific wavelength band it is necessary to integrate Planck's Law over the wavelength range of interest and scale for optical coupling effects. To convert measured radiance, R, to a temperature, T, the reverse process is required but there is no analytical solution for this process. Thus it was necessary to calculate a curve for $R(T, \lambda)$ then invert it numerically to calculate $T(R, \lambda)$. Figure 4.1 shows curves created by this process for a number of filter parameters. It can be seen that in all cases the gradient of this curve is steeper at lower temperatures making the measurement more sensitive. However this is balanced by the correspondingly lower signal levels that mean any measurements in this region are likely to have a larger proportional uncertainty (assuming constant noise). As the accuracy of the measurement is dependent on the noise of the measurement it is necessary to consider an appropriate noise model.

4.3.2 Noise model

The noise model proposed has three components: shot noise, detector noise and digitiser noise. Shot noise is due to the quantised nature of light and is a function of the number of photons collected. This noise is assumed to have a Gaussian probability distribution, p_G, given by,

$$p_G(z) = \frac{1}{\sigma_{shot}\sqrt{2\pi}} e^{-\frac{z^2}{2\sigma_{shot}^2}}. \tag{4.3}$$

Where the standard deviation of the distribution, σ_{shot}, is given by,

$$\sigma_{shot} = \sqrt{\frac{P_{opt}}{h\nu_c B}}. \tag{4.4}$$

The number of photons was calculated using the calculated optical power, P_{opt}, the energy per photon, which assuming the photons are the centre frequency of the filter, is given by $h\nu_c$, and the time interval, which is related to the bandwidth B of the recording system.

Detector noise is a description of the noise inherent in all optical detectors (although not necessarily from the same source) and is specified by the noise equivalent power (NEP) and the bandwidth, B. Like shot noise, detector noise has a Gaussian distribution and is parameterised by its standard deviation σ_{det},

$$\sigma_{det} = \text{NEP}\sqrt{B}. \tag{4.5}$$

Digitiser noise is the noise due to the digital acquisition of the signal and can be approximated as a fixed percentage of the signal. It has two components, quantisation noise and dithering. Quantisation noise is due to the quantisation process which implicitly adds noise [99]. Dithering is noise that is purposely added by digitiser manufacturers to improve resolution when over-sampling [100]. Both are assumed to have a Gaussian distribution and are parameterised by their standard deviations, σ_{qnt} for quantisation noise and σ_{dth} for dithering. The expressions for the standard deviations are,

$$\sigma_{qnt} = \frac{1}{\sqrt{12}} 2^{-Q} \tag{4.6}$$

and

$$\sigma_{dth} = \frac{2}{3}2^{-Q}, \tag{4.7}$$

where, because the noise is related to the minimum resolvable voltage (least significant bit), Q is the bit depth of the digitiser. It is assumed the signal scales to the digitiser input range, thus the previous values are fractions of the recorded value. They can be combined in a single term, σ_{dig}, given by,

$$\sigma_{dig} = P_{opt}\sqrt{\sigma_{qnt}^2 + \sigma_{dth}^2}. \tag{4.8}$$

As these three components of noise are uncorrelated they are added in quadrature to determine the resultant noise on the signal,

$$\sigma = \sqrt{\sigma_{shot}^2 + \sigma_{det}^2 + \sigma_{dig}^2}. \tag{4.9}$$

4.4 Model validation experiments

It is desirable to experimentally validate the approach before using it to systematically investigate system behaviour. To achieve this a calibrated voltage-temperature curve, $V\,(T)$, is required to allow measured radiances to be converted to temperature. The Monte-Carlo model does not produce such a curve due to the noise that is added. Even if the noise component was removed there would be numerous inaccuracies, in comparison to experimental systems, due to the ideal components in the model. Thus to produce the $V\,(T)$ curve a system level model (SLM) which was more representative of a physical pyrometer system was developed. The differences between the SLM and the Monte-Carlo model are as follows:

- Filter bandpass performance is derived from manufacturer supplied data rather than ideal.
- The effects of detector size, spectral and electrical response were derived from manufacturer supplied data rather than ideal.

- Wavelength dependent performance of glass and anti-reflection coating of lenses derived from manufacturer supplied data was included.
- The effects of noise on collected signals was omitted. This allows the $V(T)$ curve to be generated directly.

The SLM is similar to the first step of the Monte-Carlo model, discussed previously, which can be broken down into the following steps:

1. A blackbody curve is generated for a specified temperature, T.
2. The curve is then scaled to account for the collection optics.
3. Transmission through the various optics is calculated.
4. The spectrum of light reaching the detector is multiplied by the detectors spectral response and integrated to calculate a photocurrent.
5. The electrical gain of the detector system is used to produce a voltage-temperature point.
6. The process is repeated for a range of temperatures.

Despite the increased detail of the system level model there remain some factors that are not included, for example, errors due to chromatic aberration of the lenses and reproducibility of the filters. Due to these omissions it is still necessary to calibrate the pyrometer to accurately interpret measurements.

The calibration was conducted as follows. First, voltages were recorded when the collection fibre was viewing the blackbody source at known temperatures. By comparing the voltage measurements with those predicted by the SLM a calibration curve can be produced. This curve, together with the output from the SLM, allows voltage data to be converted directly to temperature. The calibration data indicated that due to losses in the experiment (due to component imperfections and sub-optimal alignment) radiance levels were 0.75 that predicted by the SLM.

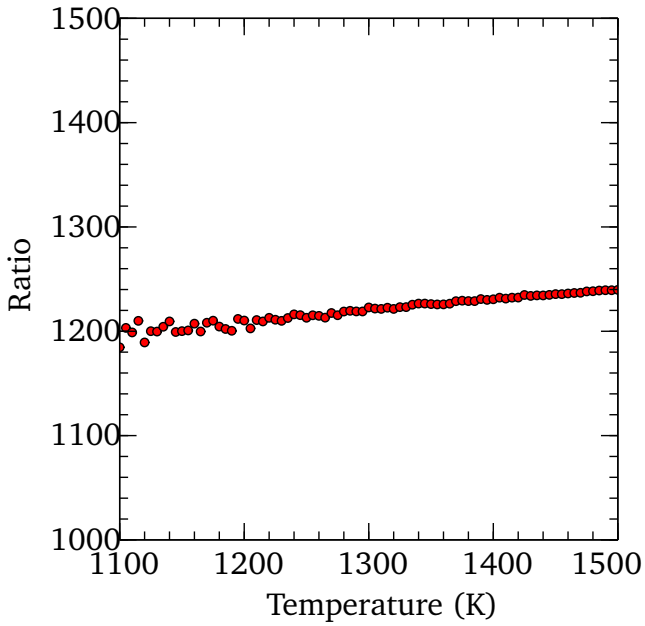


Figure 4.2: A plot of the ratio of the mean output of the Monte-Carlo model to the SLM output from 1100°K to 1500°K. The SLM model uses the Semrock FF01-794-32 filter, the Monte-Carlo model used an ideal filter window with a 32 nm passband centred at 800 nm.

The final step in validation is to relate the Monte-Carlo model to the SLM model. As discussed there are numerous factors that differ between the models. However, if the ratio of the mean output of the Monte-Carlo model to the SLM output is constant, the models would be equivalent apart from this scaling factor. Figure 4.2 shows the ratio of the Monte-Carlo to the SLM over a range of temperatures. It can be seen that variations of up to 2% occur, indicating the models are largely consistent but not exactly equivalent, thus the Monte-Carlo model results are comparable to the experimental results.

The most straightforward experiment that would generate data that was readily comparable to the Monte-Carlo model was measuring the effect of changing the filter passband. Three commercially available filters, of approximately equal centre frequency with different passbands, were used for the measurements.

The experimental system used to acquire the data collected light from a blackbody source (LAND R1200P) using a 1 mm diameter, 0.48 NA optical fibre (Thorlabs^{TM} BFL48-1000). A lens system collected the light emitted from the

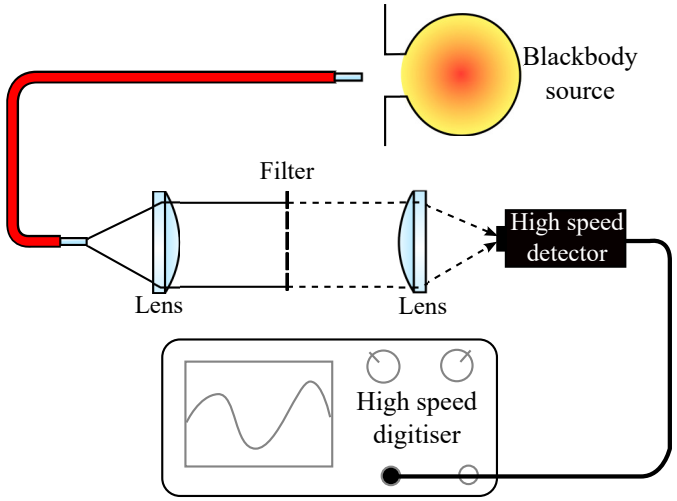


Figure 4.3: Schematic diagram of the filter test setup. Light is collected from a blackbody source using an optical fibre. Light from the fibre is collimated, filtered then focussed onto a detector. The output from the detector is recorded on a high speed digitiser.

fibre and directed the light, via a bandpass filter, to an amplified photodiode (FEMTO HCA-S-400M, a NEP of 68 pW·Hz$^{-\frac{1}{2}}$ was assumed), see Figure 4.3. The output of the detector was recorded with an 8-bit high speed digitiser (Tektronix^{TM} DPO7254) at 1 GS·s^{-1} (*i.e.* a bandwidth of 5×10^8 Hz).

To perform the analysis approximately 3,000 points of voltage data (at each temperature) were converted to temperature using the SLM and calibration data. The mean and standard deviation of the dataset were calculated, yielding the results shown in Table 4.1.

Source Temperature (°K)	Filter	Mean Measured Temperature (°K)	Standard Deviation (°K)
1425	FF01-800-12	1425	39
1425	FF01-794-32	1423	17
1425	FF01-795-150	1420	5

Table 4.1: Results from the system level model. All filters were obtained from Semrock.

When using the Monte-Carlo model to calculate uncertainty, the modelled signal levels had to be adjusted to ensure appropriate noise scaling. Thus the 0.75 scaling factor determined in calibration was applied to the radiance levels in the Monte-Carlo model to account for optical inefficiencies. Experimental mea-

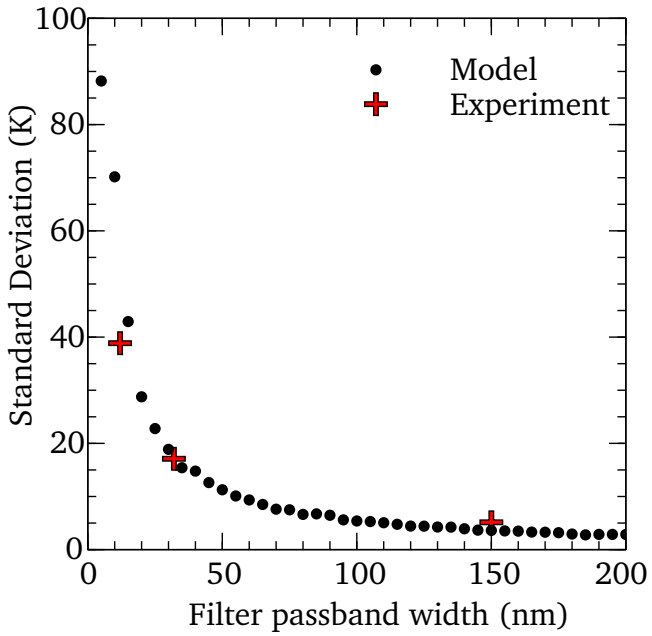


Figure 4.4: A plot comparing the results from the Monte-Carlo model to experimentally obtained data viewing a blackbody source at 1425°K.

surements are compared with results from the Monte-Carlo model in Figure 4.4. While the output of the simple model does not perfectly describe the experimental results, the fit is sufficient to validate the Monte-Carlo model for investigation of the effect of filter parameters on pyrometer performance.

4.5 Monte-Carlo Model Results

4.5.1 λ_c variation

Following validation, the ideal model was used to investigate the effects of varying λ and $\Delta\lambda$, assuming the NEP of the detector was 50 pW·Hz$^{-\frac{1}{2}}$, the data is recorded on an 8-bit digitiser and the blackbody radiant source was 1 mm in diameter with light collected from a 0.25 numerical aperture. Figure 4.5 shows the effect of altering the centre wavelength of the filter while maintaining a passband of 100 nm at temperatures of 1250°K, 1500°K and 1750°K. It can be seen that as the centre wavelength increases, the uncertainty decreases. Also noticeable is a transition where the uncertainty drops rapidly; this transition occurs at higher wavelengths for lower temperatures. In addition, there are diminishing returns

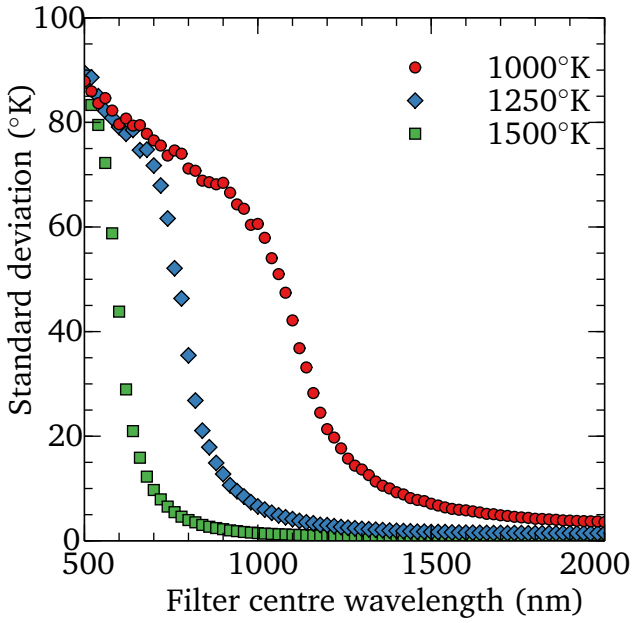


Figure 4.5: A plot of calculated temperature uncertainty for a range of filter parameters. Assuming a blackbody source, centre wavelength is varied and while maintaining a passband of 100 nm.

to increasing the centre wavelength after the transition; subsequent increases in centre wavelength produce progressively smaller improvements in accuracy.

The response of the system to centre wavelength variation can be accounted for if the noise model is considered. Shifting the centre wavelength of the collection band to longer wavelengths leads to an increase in the amount of light reaching the detector resulting in a decrease in uncertainty. The noise model also accounts for the transition in uncertainty as the detector noise component is constant thus will be the dominant component at low signal levels but, once overcome, digitisation noise becomes the most significant source of noise. Digitisation noise is a fixed percentage of the signal so has a constant effect.

It is suggested that the system is configured so the centre wavelength is beyond the transition value. While a general expression for the transition value could not be determined analytically, an approach that may approximate the location of the transition is discussed in Section 4.5.4.

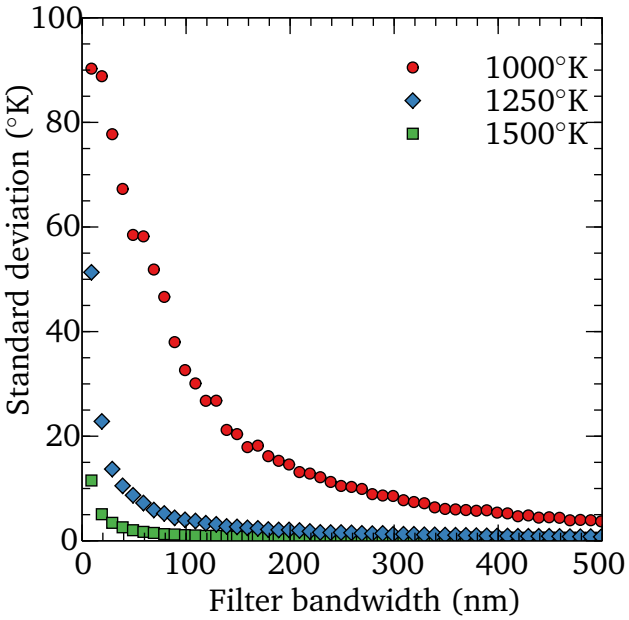


Figure 4.6: A plot of calculated temperature uncertainty for a range of filter parameters. Assuming a blackbody source, passband width and temperature was varied while a centre wavelength of 800 nm was maintained.

4.5.2 $\Delta\lambda$ variation

Figure 4.6 shows the effect of altering the width of the passband of the filter while maintaining a centre wavelength of 800 nm. Increasing the width of the passband increases the signal level which improves the accuracy of the temperature measurement. As with moving the centre wavelength the benefit of increasing the signal level continues until the most significant source of noise becomes digitisation noise. Again, there are diminishing returns; increases in bandpass width produce progressively smaller benefits. Changes to bandpass width produce a similar response to change to centre wavelength as the response is determined by the noise model and the same noise model was used. It can be observed that the wavelength uncertainty due to increasing the passband has a smaller effect than the benefits of increased signal level.

Thus it appears increasing the filter bandpass width is beneficial, however, when considering the pyrometry system as a whole, there are drawbacks. First, a wide bandpass excludes the possibility of additional bands in that spectral region. Combining multiple measurements can be beneficial, leading to a reduction in

uncertainty. This is where the noise component becomes critical, if the noise scales such that a relatively large passband increase only produces small improvements in uncertainty it maybe preferable to add another measurement band rather than continue to extend a single filter passband. Second, there are practical considerations, filters with extremely wide passbands are difficult to obtain and detectors often have limited spectral responsivity so the width of the passband cannot be increased arbitrarily.

4.5.3 Multiple passbands

The benefit of adding an additional measurement channel can be assessed by quantifying the effect of the change. The combination of the uncertainties from multiple measurements is given by Equation 4.10,

$$\sigma_{\Sigma}^{2} = \frac{1}{\sum_{i=1}^{n} \sigma_{i}^{-2}}, \tag{4.10}$$

where σ_{Σ} is the resultant uncertainty and σ_i is the i^{th} uncertainty from a set of n measurements,

A specific example is instructive when considering multiple bands. Using Equation 4.10 the uncertainty from combining two measurements for filters centred at 600 nm and 800 nm viewing a 2000°K source with increasing passbands was calculated, Figure 4.7. It can seen that once the passband of the 800 nm filter reaches ∼100 nm there is a greater reduction in uncertainty due to adding another spectral band compared to increasing the passband to 200 nm. Thus adding an extra measurement channel is a better use of the available spectrum.

4.5.4 Simultaneous variation of λ_c and $\Delta\lambda$

In addition to investigating the effect of individual changes in centre wavelength and bandpass width, the idealised model was used to explore simultaneous variations in these parameters for a single passband system. If both parameters are varied a 2D surface of uncertainty is generated. An example of the results of this process (from a 1250°K source) are shown in Figure 4.8.

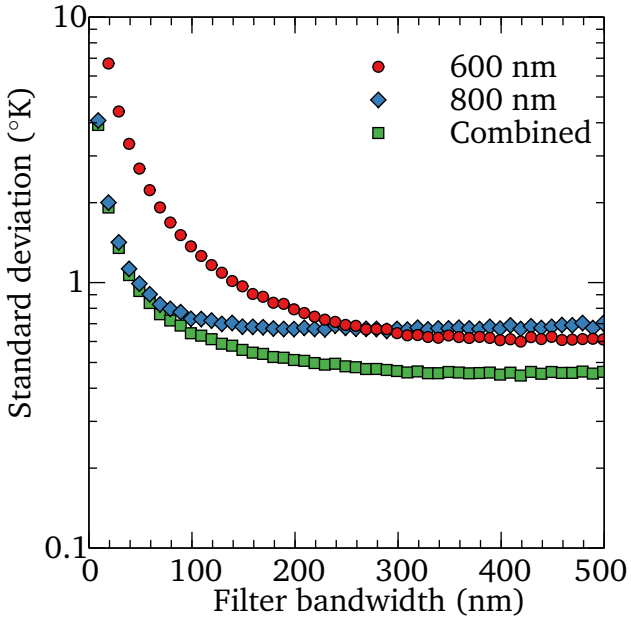


Figure 4.7: A plot of the standard deviation of model results as bandpass width is varied for filters centred at 600 nm and 800 nm viewing a 2000°K blackbody. In addition the standard deviation calculated when the measurements are combined is shown.

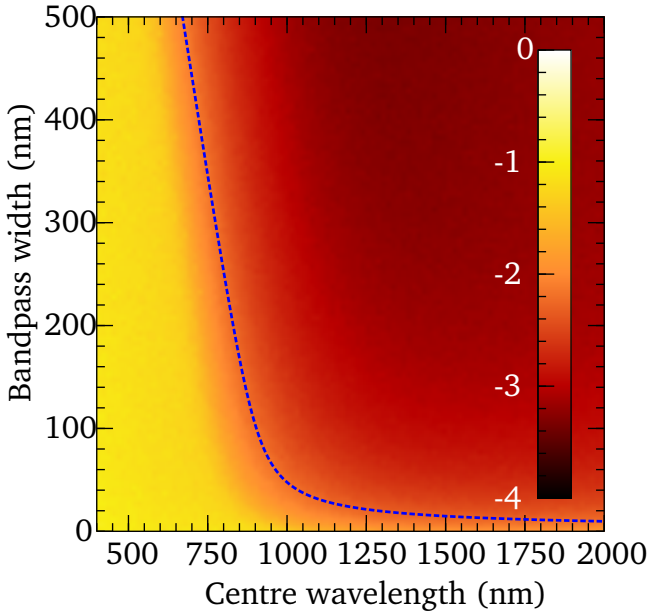


Figure 4.8: A 2D image of the log of the normalised standard deviation (σ/T) for a 1250°K blackbody source with a detector with 50 pW·Hz$^{-\frac{1}{2}}$ noise equivalent power and 500 MHz bandwidth. A line indicating the 1 % uncertainty level has been added determined by fitting the location of data points within in the range 0.9 % and 1.1 % with a sum of a linear function and an hyperbolic function, $f(x) = \left(\frac{a}{x}\right)^n$.

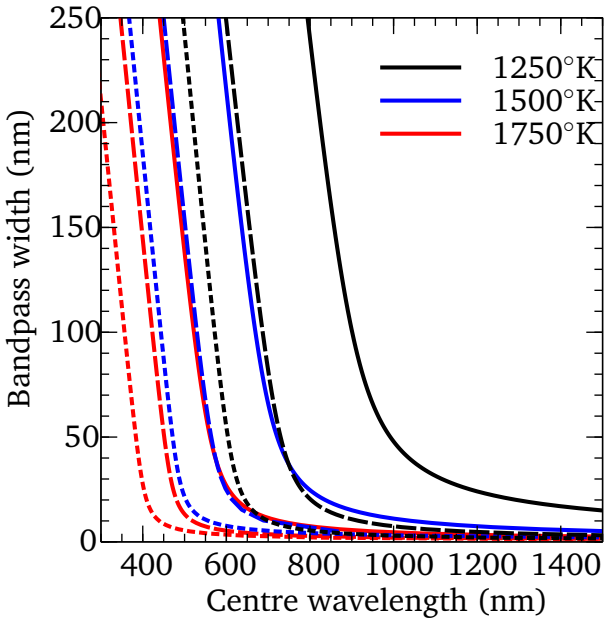


Figure 4.9: Plot of uncertainty contours of 1 % for blackbody source temperatures of 1250°K, 1500°K and 1750°K. The same uncertainty contours for the same temperatures with detector noise values of 50 (solid), 5 (dashed) and 0.5 (dot-dash) pW·Hz$^{-\frac{1}{2}}$ are also plotted.

These data can be analysed to determine uncertainty 'contours' where a range of centre wavelengths and bandpass widths satisfy a specified uncertainty. A 1 % uncertainty contour is shown as the line on Figure 4.8.

A benefit of reducing the data to contour lines is that it allows for easier comparison of the effect of changing other model parameters. Figure 4.9 shows the 1 % uncertainty contour for temperatures of 1250°K, 1500°K and 1750°K with detector noise, σ_{det}, varying between 50, 5 and 0.5 pW·Hz$^{-\frac{1}{2}}$.

An empirical expression that approximates contour location has been determined. The expression specifies the centre wavelength (in nm) required to attain 1 % error, $\lambda_{c1\%}$, for a defined bandpass width, temperature and noise level. Using variables defined earlier in this paper, the expression is,

$$\lambda_{c1\%} = -0.5\Delta\lambda + \left(-0.071 \cdot ln\left(\text{NEP}\sqrt{B}\right) - 1.66\right) T + 7930 \cdot \left(\text{NEP}\sqrt{B}\right)^{0.11}. \quad (4.11)$$

The lines generated by the above expression are generally in good agreement with results from the simulations, however the results diverge at lower bandpass

widths, see Figure 4.10. The lower bound (in nm) for the region where Equation 4.11 is a good approximation for the contour locations can be approximated by the equation:

$$\Delta\lambda_{NA} < 0.16\lambda_c - 60. \tag{4.12}$$

While the approximation for the 1 % contours (Equation 4.11) is somewhat unwieldy to manipulate algebraically, it can be solved numerically for any of the variables (given the other parameters). For example, the expression was solved numerically to calculate the bandpass width required for a 650 nm centred filter with a 1500°K source using a 500 MHz bandwidth detector with 50 pW·Hz$^{-\frac{1}{2}}$ NEP, resulting in a bandpass width of 152 nm. This solution is displayed on Figure 4.10. This value is above the limit set by Equation 4.12 so approximates a point on the associated simulation contour.

While Equation 4.11 can be used to give an indication of suitable filter parameters (for given experimental conditions). It is important to consider the limitations of the model, to give two examples; one, the idealised model has assumed the source is a blackbody emitter; deviation from this condition will reduce signal levels, changing the filter parameters. Two, the idealised model results considered temperatures under 2000°K, the approximation is likely to fail if used outside this temperature range. Thus, to ensure the most appropriate filter choice, it is suggested that the insights discussed here be used to down-select potential components for testing in a system level model that contains component level models. The system level model, together with forward modelling to estimate temperature, can then be used to optimise the configuration of the optical components.

4.6 Conclusions

A Monte-Carlo model has been developed and validated to investigate the performance of a pyrometry channel viewing a blackbody source while the characteristics

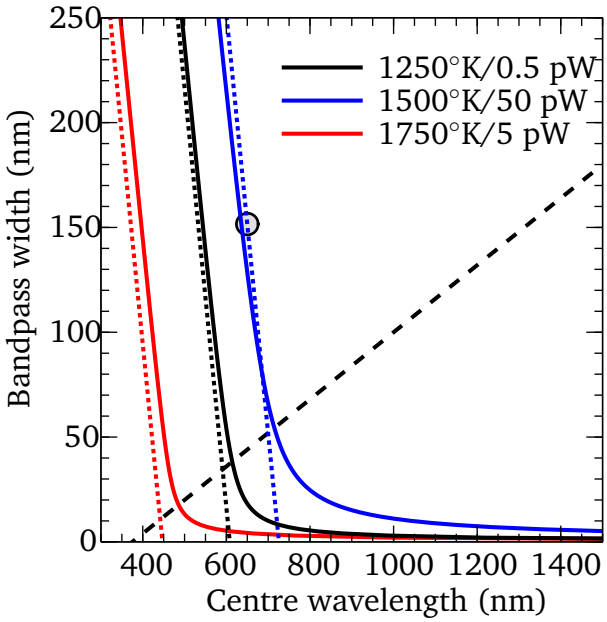


Figure 4.10: Plot of contours of 1 % uncertainty at selected blackbody source temperature and noise powers with associated fitted curve (dotted). The region below the dashed line indicates where results diverge from the fitting function. The circled point illustrates a solution obtained by numerically solving the fitting expression to determine the bandpass width required for a 650 nm centre wavelength filter.

of its associated filter are varied. The model was used to investigate the effect of individual variations in centre wavelength and passband width of a filter. Further investigation was conducted by considering variation of both parameters allowing the effect of varying a noise source to be investigated.

An important finding, that has not been reported in any of the previous literature, is that there is a marked transition in uncertainty when varying centre wavelength. Below this transition wavelength uncertainties are large but above the transition wavelength uncertainty drops rapidly. However, increasing the centre wavelength significantly above the transition wavelength produces little reduction in uncertainty. Thus, if signal levels are high, it is usually desirable to reduce the spectral range of the filter passband and add another spectral band for measurement. The location of the transition is dependent on the filter parameters, noise levels and the temperature that is to be measured.

Increases in filter bandpass width generally increase signal levels thus reducing uncertainty. However as the bandpass gets wider the benefit diminishes. In some

cases it may be better to add additional spectral bands for additional measurements rather than continue to increase bandpass width; a mathematical framework for making this assessment is shown in Equation 4.10

It is also observed that the increased wavelength uncertainty created by increasing the passband of filters is not noticeably detrimental to resultant uncertainty within the ranges modelled here. There is a caveat that, if the passband becomes sufficiently wide, spectral variation issues (*e.g.* emissivity, detector response) become significant, which would affect measurements, but these effects have not been considered in the work reported here.

While not entirely straight-forward, due to the requirement for Monte-Carlo simulations and a potentially large parameter space, the framework developed here captures the relevant complexity of a physical pyrometer system. The framework enables a system to be developed using a few, readily accessible, parameters, saving the time and expense of procuring and testing components. Previous approaches in the literature were not sufficiently defined to allow assessment of components so this is a significant development.

To simplify component assessment further, resultant uncertainties from varying both bandpass and centre wavelength have been fitted over a range of temperatures and noise levels. This has allowed an expression to be determined that approximates the bandpass width required to attain 1% uncertainty given the remaining variables (Equation 4.11); this expression reduces even further the cost of assessing component changes. However at lower bandpass widths the approximation becomes inaccurate so cannot be applied; an expression describing this transition has also been determined.

5
100 mm bore plate impact experiments

5.1 Introduction

While the previous chapters have reported work regarding the modelling of various aspects of pyrometer performance (which has been validated with static measurements) it is desirable to evaluate the performance of the pyrometer by measuring the apparent temperature of a sample shocked to high pressure in an experiment.

However, before discussing the details of the experiment it is helpful to have a detailed discussion of the practicalities of plate impact experiments. This chapter begins by giving a generic overview of plate impact experiments then discusses the detailed design of the plate impact experiment used to test the pyrometer's dynamic performance.

5.2 Plate impact overview

Plate impact experiments, where a flat plate impacts a flat sample, are widely used in the shock physics field to create well defined quasi-static high pressure states. There are a number of methods to accelerate an impactor plate to high

speed however, in the course of this research, high pressure gas has been used to provide the driving force. The facility used to both accelerate the impactor and contain the energy and debris created by the impact is known as a 'gas gun'.

In a typical gas gun-driven plate impact experiment, a projectile assembly (consisting of a sabot and an impactor plate) is accelerated into a target assembly (consisting of a sample and a window). When the impact plate hits the sample a shock is induced in the sample and the impact plate. A forward travelling shock progresses through the sample and then the window; a backwards travelling (w.r.t to the interface) shock progresses through the impact plate. When the forward shock wave reaches the sample-window interface the diagnostic probes measure the change in state and transmit the data to a recording system. Due to the violence of the events the impact is usually contained within a chamber. A schematic diagram of a plate impact experiment is shown in Figure 5.1. While the duration of the experiment depends on numerous factors, the shock state is usually maintained for approximately 1 μs.

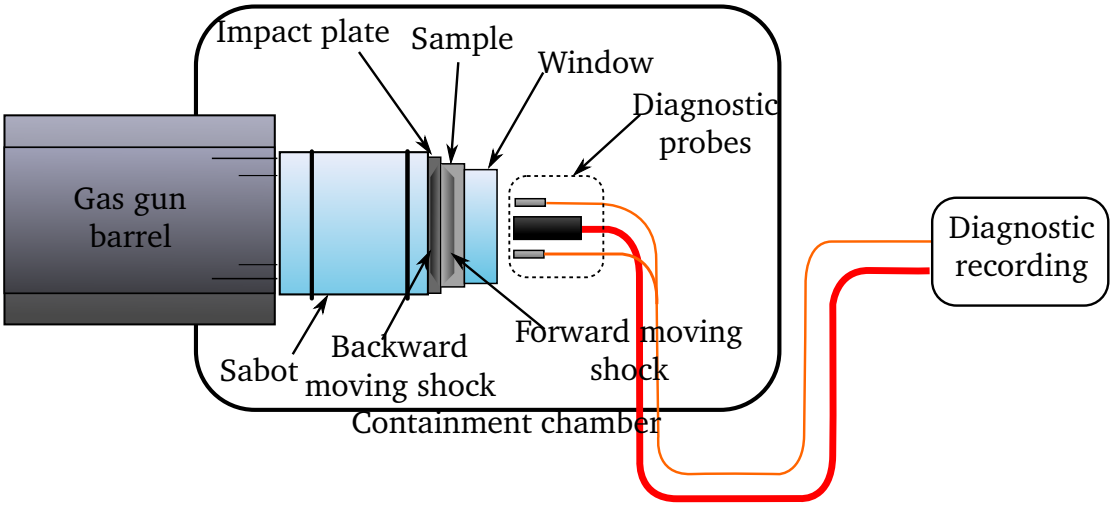


Figure 5.1: Schematic of plate impact experiment. The time just after impact is depicted. The projectile (formed of the sabot and impact plate) has been accelerated by the gas gun and has just impacted the rear of the sample. The impact has created a shock in the sample and the impact plate. When the forward moving shock reaches the sample–window interface the diagnostic probes will register the change in state. The impact takes place in a containment chamber to contain the energy and debris created.

An important factor is the pressure requirements of the experiment. While

high velocity is a key factor in generating high pressures, impactor material and sample material should also be considered. Generally, high shock impedance materials (shock impedance is the product of density and sound speed) will generate higher pressures. However, obviously higher density materials also add mass to the projectile which can limit the achievable pressure. When designing temperature experiments, the achievable pressure is critical as temperature is highly dependent on pressure and unless the temperature is sufficiently high the sample will not emit a measurable level of light.

One of the benefits of plate impact experiments is that they can create a well-defined state, however, care is required to ensure the state lasts for the required duration. As discussed in Chapter 1.1, a shock can be considered a one dimensional (1D) state, where material properties in front of the shock can be related to those behind it. However, there are two phenomena that can disrupt this state causing this relation to breakdown. First, there are 'lateral releases', shocks can only be supported in a material–an edge can cause the shock state to release to zero pressure causing a low pressure release wave to enter the material. Second, there are 'rarefaction' waves, these release waves occur when the backward (w.r.t target) travelling shock reaches the rear of the impactor plate. Again the interface causes a release wave, in this case the release travels faster than the shock, eroding the duration of the shock over time. A more detailed discussion of 1D state is presented in Appendix C.2.

There are two measures that can increase 1D time. Increasing the diameter of the components means lateral release waves must travel further before reaching the centre of the target which can increase 1D time. Increasing the thickness of the impactor plate delays the onset of the rarefaction wave.

Finally, the purpose of experiments is to generate data; diagnostics are crucial to data collection so are an important consideration. While each experiment has unique requirements it is important to consider how the data will be used. For example, temperature data has more value when collected with velocity data as the accompanying pressure state can be determined with higher accuracy. More

generally, determining one variable to high accuracy at the expense of another can reduce the value of both measurements.

5.3 Experiment design

The design of a plate impact experiment requires a number of factors to be considered. The factors, and the optimum way to balance them, depends on the purpose of the experiment. For these experiments the purpose of the experiment is to generate a measurable temperature, however, it is not possible to determine the temperature that will be generated without first selecting a sample material, impactor material, window material and projectile velocity. Because the temperature generated depends on these four parameters it is helpful to simplify the problem to avoid a large number of calculations.

The first step to simplifying this problem is to understand that generating a higher pressure will generate a higher temperature; therefore the factors that generate the highest pressure will also give the upper temperature limit regardless of the other factors. The next step is to understand that a higher projectile velocity generates a higher pressure. Thus to determine the factors that will achieve the highest pressures it is only necessary to calculate the pressure states generated at the maximum attainable velocity. The pressure states that can be generated by an impactor plate at a given velocity can be described by the equation,

$$P = \rho_0 \left(u_p - u_i\right) \left(c_0 + s \left(u_p - u_i\right)\right), \tag{5.1}$$

where P is the generated pressure, ρ_0 is the initial density of the impactor, c_0 is the ambient sound speed on the material, s is the experimentally determined slope of the Hugoniot, u_i is the impactor velocity and u_p is the particle velocity. Using Equation 5.1 to plot pressure as a function of particle velocity allows a number of material options to be compared.

However, before the calculations to determine the optimum impactor material can be undertaken it is necessary to understand the performance of the facility that will launch the projectile. At the time this experiment was conducted the 100 mm

bore gas gun at the Institute of Shock Physics (at Imperial College London) was the fastest plate impact facility in the UK, hence it was the facility of choice for these experiments. A gas gun's performance can be characterised by a mass-velocity curve; this curve determines the maximum velocity achievable (*i.e.* using the gun at maximum pressure) for a given projectile mass. The mass-velocity curve of the gas gun based at the ISP is shown in Appendix D.1. Thus, if the projectile mass is known, the projectile velocity can be predicted; projectile mass is the sum of the sabot mass and the impactor plate mass. The following sections discuss aspects of the projectile mass.

In addition to testing the pyrometer and window size effects, a development to plate impact pyrometry experiments has also been explored. As discussed in Chapter 3, the drawback of using a window in a plate impact experiment is that measurements at the sample-window interface are of material that has been shocked then partially released. Because the loading path does not go directly to the measured state there is additional uncertainty in any EoS parameters that can be derived from the interface measurements. To give further insight into the loading path the sample undergoes, the experiment was designed to also measure the initial shock state of the sample. Specifically, diagnostics to determine the shock speed in the sample were added.

5.3.1 High speed sabot

As discussed in the previous section, it was desirable to maximise the projectile velocity for these experiments. Because projectile velocity depends on the projectile mass, reductions in sabot mass or impactor plate mass will increase the maximum achievable velocity. The existing design for the gas gun sabot was a 100 mm long, polycarbonate sabot with a mass of approximately 930 g. A number of potential strategies for reducing sabot mass were investigated including construction from alternative materials, novel geometries and shortening of the sabot. A shortened sabot (50 mm length compared to 100 mm) was determined to be the most practical, resulting in a sabot of approximately 465 g mass.

Material	Density (g cm^{-3})	Projectile Velocity (m s^{-1})
Tungsten alloy*	18.1	1470
Tantalum	16.7	1480
Copper	9.0	1555
Tin	7.3	1575

Table 5.1: Table of predicted projectile velocities for a range of impactor plate materials given a 100 mm diameter, 2 mm thick impact plate and a sabot of 465 g mass. * – *Wolfmet 395*

The primary drawback of reducing the length of the sabot is that it increases the variation in tilt that occurs during the plate impact experiment. Tilt is undesirable because it reduces the accuracy of the 1D assumptions that much of the analysis in relies upon. However experiments using the 100 mm sabot had resulted in tilts of between $\pm$5 mrads, the effect of halving the sabot length can be anticipated to increase tilt by approximately a factor of of two. A tilt of $\pm$10 mrads was deemed acceptable.

Now sabot mass has been defined the remaining variable in determining maximum projectile velocity is the impact plate, which we now discuss.

5.3.2 Impactor material selection

The mass of the impactor plate is given by the product of its volume and density and thus, as the sabot mass is fixed, the maximum velocity is dependent on the impactor plate dimensions and the material choice. The projectile mass was calculated (from the previously mentioned mass–velocity curve) assuming impactor dimensions of 100 mm diameter and 2 mm thickness for a variety of commonly available materials, see Figure 5.2. The resultant projectile velocities are shown in Table 5.1.

The calculated projectile velocities where then used to generate the pressure–particle velocity Hugoniot curves (using Equation 5.1 and parameters from Marsh [89]) which are plotted in Figure 5.2. The result of this analysis was that tungsten heavy alloy (WHA) was determined to be the optimum material as it generates the highest pressures, and hence the highest temperatures, of the materials considered.

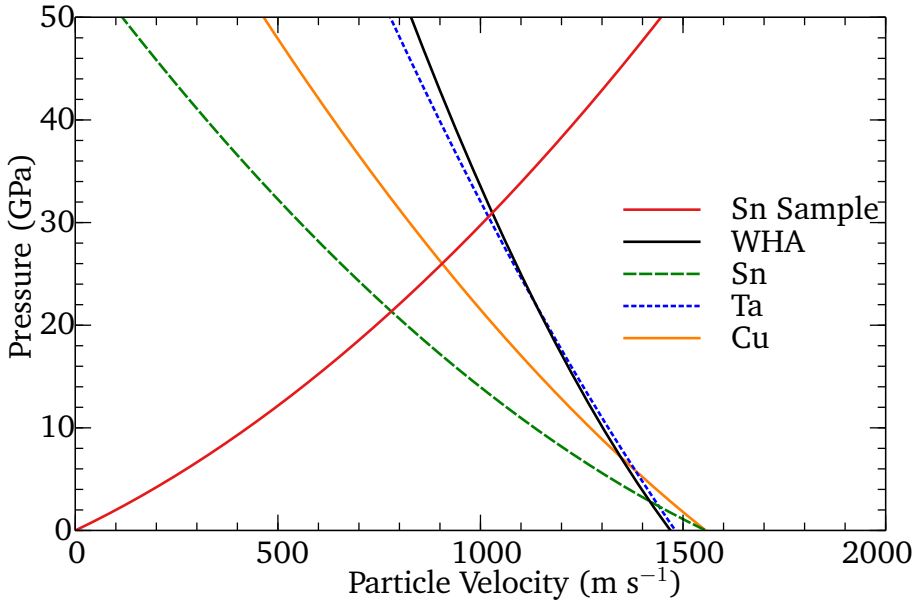


Figure 5.2: Hugoniot crossing analysis to determine achievable pressures with the 100 mm bore gas gun. The resultant pressure is determined by the intersection of the sample line with the other material. Tungsten (W) produces the highest pressure.

Because all the relevant parameters have now been determined, it is insightful to calculate the energy delivered in these experiments. From the parameters presented it can be calculated that the kinetic energy of the projectile at impact is 0.81 MJ, for comparison that is equivalent to a small car travelling at 90 mph. As such, plate impact experiments on this facility were highly destructive events; the combination of high precision experiments which require extensive clean up meant only a limited number of experiments are possible within the time and funding constraints of a doctorate project.

5.3.3 Window material selection

The purpose of the window is to prevent the target sample from releasing; the more a material releases, the more it undergoes adiabatic cooling which is undesirable if higher temperatures are desired. Thus, for the goal of maximising the temperature generated in a plate impact pyrometry experiment, it would be preferable to select a window material based on the material shock properties that minimise release effects. However, there are other—more significant—factors to consider when selecting a window material for a plate impact pyrometry experiment.

The factors that can be important when selecting a window material for a plate impact experiment are, for example, transparency, shock properties and existing characterisation data. While an obvious requirement for a window is that it be transparent this is not entirely straightforward as many materials transparent at standard conditions become opaque at the elevated pressures and temperatures in shock experiments (for example PMMA is opaque over $\sim$22 GPa [101]). Additionally as pyrometry is a broadband optical measurement it is important the window material should not produce light, which interferes with the pyrometry diagnostic, when shocked. Work by Partouche-Sebban *et al.* [50] has shown sapphire produces significant light in the pressure ranges achievable on single-stage gas guns. A final factor is that it is desirable that a window material is well characterised. When these factors are considered lithium fluoride (LiF) stands out as the most desirable window, despite its sub-optimal shock properties (its properties result in release to lower pressures than sapphire) and is a widely used window material for pyrometry.

However, recently reported issues regarding luminescence on shock release of LiF [52] suggests there may be issues using LiF in plate impact experiments with pyrometers. On balance, despite the luminescence issue, LiF remains the most desirable window material for plate impact experiments as it has been used for many experiments in the past and it is not clear if other materials have less significant issues.

Furthermore, due to the widespread use of LiF in the literature and the relatively limited information on the luminescence issue, it was desirable to investigate the phenomenon. The aspect investigated here is how a larger window size affects the collection of emitted light.

5.3.4 Sample material selection

Having selected a impactor material, calculated the associated projectile velocity and selected a window material the choice of sample material was investigated. The sample material can have a significant effect on the resultant temperature and

Material	Release Temperature (K)
Copper	583
Lead	1720
Tin	1217

Table 5.2: Table of predicted temperatures for materials shocked by a 1500 m·s^{-1} WHA impactor with a initial temperature of 300 K.

a number of materials were considered. To inform this decision, predictions of the material temperature were conducted using the analysis given in Appendix C.3. These calculations of temperature assumed a 1500 m·s^{-1} impact by a tungsten heavy alloy impactor with a lithium fluoride window to tamp the release, Table 5.2 shows the results of these calculations.

The conclusion from the shock temperature calculations was that tin is an appealing pyrometry target sample material because, of the commonly available metals, it undergoes significant heating under shock loading. While lead (Pb) would reach a higher temperature in the same experimental configuration, lead is toxic and the gun facility was not equipped to deal with the waste that would be produced. Thus a tin target sample was used for these experiments.

The key elements of the experiment have now been selected: the impactor material is tungsten heavy alloy, the sample material is tin and the window material is lithium fluoride. The next step is detailed design of the experiment.

5.3.5 Pyrometer system

As highlighted at the start of the chapter one of the goals of these experiments was to try to demonstrate the pyrometry system in a dynamic application. There are aspects of the pyrometer that affect aspects of the detailed experiment design. The pyrometer is split into two components; the radiometry system and the optical probe, these are now discussed.

The radiometry system was designed using the principles discussed in Chapter 2. The system consisted of a single input from an optical fibre. The input was split into four paths using dichroic mirrors; each path was directed to a detector by a

Channel	Nominal wavelength band (nm)	Detector
1	600–700	Hamamatsu H10721-20
2	750–850	Hamamatsu H10721-20
3	875–1250	FEMTO HCA-S-400M-SI
4	455–550	Hamamatsu H5783-20

Table 5.3: Table summarising the configuration of the radiometry system for the second experiment.

Channel 1	Channel 2	Channel 3	Channel 4
FF875-Di01	*FF875-Di01*	FF875-Di01	FF875-Di01
FF735-Di02	FF735-Di02	*Edmund 1200 LP*	Edmund 1200 LP
FF02-650-100	FF02-795-150	None	FF01-535/150

Table 5.4: Table summarising the filters in place on each channel in the radiometer system. Italics are used for filters that are reflected from, rather than transmitted through the filter.

lens. Specifically, three channels were dedicated to pyrometry while a dynamic reflectivity diagnostic was implemented on a fourth channel (discussed further in Chapter 8). The nominal wavelength bands and detector configuration are shown in Table 5.3 with the details of the filters shown in Table 5.4. A schematic of the layout of the radiometry system is shown in Figure 5.3.

The configuration of the radiometry system was changed for the second experiment due to issues that arose during the first experiment (this is discussed further in Section 7.3.4). The dichoric mirror associated with the reflectivity diagnostic was removed. Thus the first dichoric mirror (Semrock FF875-Di01-25x36) splits the light into above and below 875 nm. Each path is further split by a dichoric mirror (Semrock FF735-Di02-25x36 and Edmund 1300LP). While the light was further constrained for the PMTs (Semrock FF01-650/100-25 and FF01-795/150-25) no additional filtering was applied for the photodiode based channels. This deployed configuration is shown in Table 5.6 and 5.7 summarises the configuration.

The radiometer was calibrated before each experiment with the optical head that was used. The procedure for calibration is discussed in Appendix A.1.

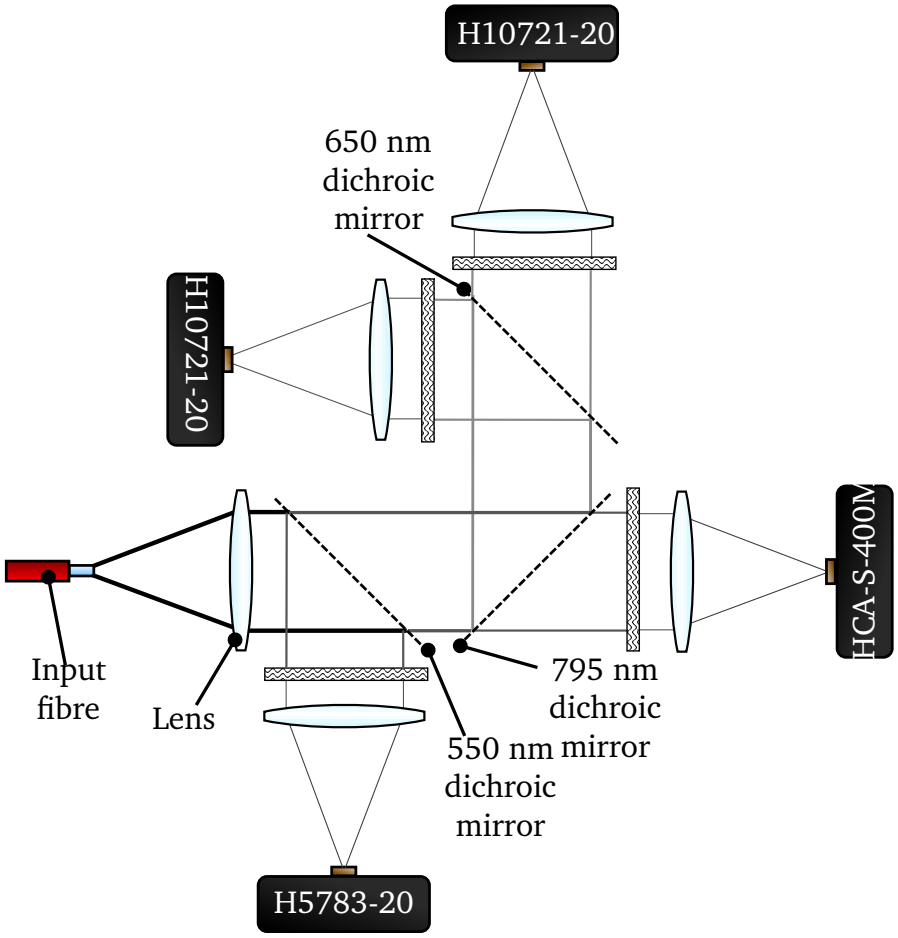


Figure 5.3: Schematic of the radiometry system used for the first initial experiment.

For the purpose of detailed experiment design it is relevant to note that the pyrometry system collects from a circular region, which is dependent on the optical probe used; the maximum size of this region is 12 mm diameter. The size of the optical probe head creates a footprint, 19 mm diameter, in which no other probes can be placed.

5.3.6 PDV diagnostic

Shock arrival time and particle velocity measurements employed a photonic Doppler velocimetry (PDV) system (also known as heterodyne velocimetry, HetV) [102]. PDV uses the velocity dependent Doppler shift of light to measure the velocity of a surface illuminated by laser light. The Doppler shift is measured by mixing the reflected light with a known reference, where the beating of the

mixed waves indicates the velocity. The relation between the beat frequency, f_b, and the velocity, v is described by the expression,

$$f_b = 2f_0\frac{v}{c_0}, \tag{5.2}$$

where f_0 is the initial laser frequency and c_0 is the speed of light.

Because these experiments used a window it was also necessary to correct for changes in apparent velocity due the refractive index changes caused by the shock [103, 104].

For this specific implementation of PDV the output from a single laser was split across the eight probes 'arms'. Each arm consisted of an non-reciprocal device called an optical circulator, to which the probe was attached. The circulator passes the light that enters the input port to the probe—where the light is emitted—but light that is collected by the probe is directed to a third port. From the third port the collected light is combined with a reference.

Two configurations for the combination were used; combination with the source laser (homodyne) and combination with a separate reference source (heterodyne). A heterodyne system has the benefit that a sample with zero velocity creates a finite frequency signal which can make analysis easier; the drawback is that it requires an additional laser. For these experiments a heterodyne configuration was only available for four of the channels.

Following the combination of the two signals they are passed to a detector and recorded on a digitiser. A schematic of the PDV system is shown in figure 5.4.

The recorded signals were analysed using short-time Fourier transforms (STFT); using STFT analysis it was possible to determine velocity with a time resolution of a few nanoseconds [105, 106].

The nominal positions of the probes is shown in Figure 5.5. The arrangement of the PDV probes meant that the time-of-arrival of the shock at the WHA surface and the tin-window surface could be determined. Furthermore, because time-of-arrival was measured at multiple locations, tilt could also be determined. Light was delivered and collected using collimated probes with a 90 mm working distance (AC Photonics 1CL15P090LCGS1/CPT2).

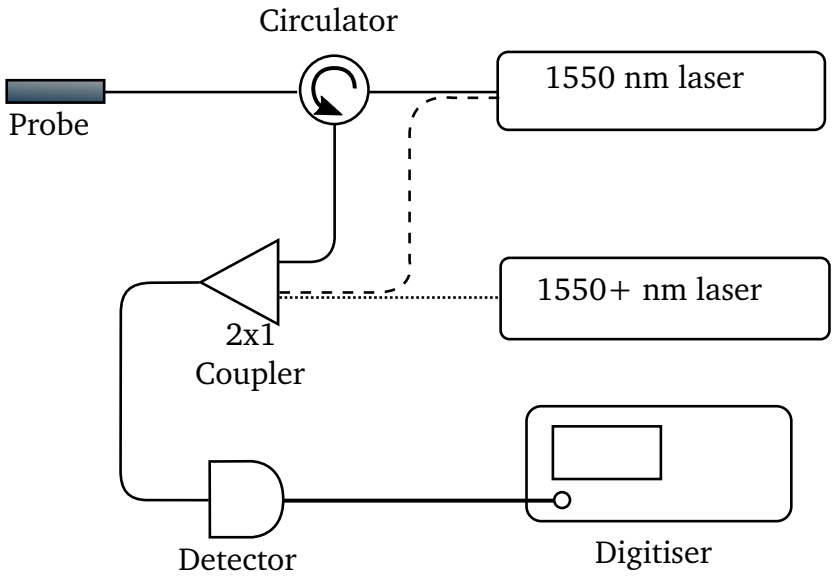


Figure 5.4: Schematic diagram of the velocimetry system(s) used for the experiments. Dotted lines indicate the configuration during heterodyne operation; the dashed line indicates the homodyne configuration.

5.3.7 Triggering

A clear trigger event was required to ensure that the diagnostic recording systems are operating at an appropriate time. The trigger event in these experiments was provided by a Dynasen piezo probe that was mounted through the WHA transmitter plate and extended a short distance from the plate surface, see Figure 5.5. The piezo probe produces a voltage when impacted by the face of the sabot.

5.3.8 Target geometry

The geometry of the target design was a balance of numerous factors which shall now be described.

The first consideration was how the target assembly would be mounted. Given the design of the the gun fixture, the use of a 120 mm diameter WHA disc was an appropriate way to allow the target assembly to be mounted. The WHA disc provides a rigid platform for mounting the target and, as it is impedance matched to the flyer, efficiently transmits the shock produced from the flyer impact into the target.

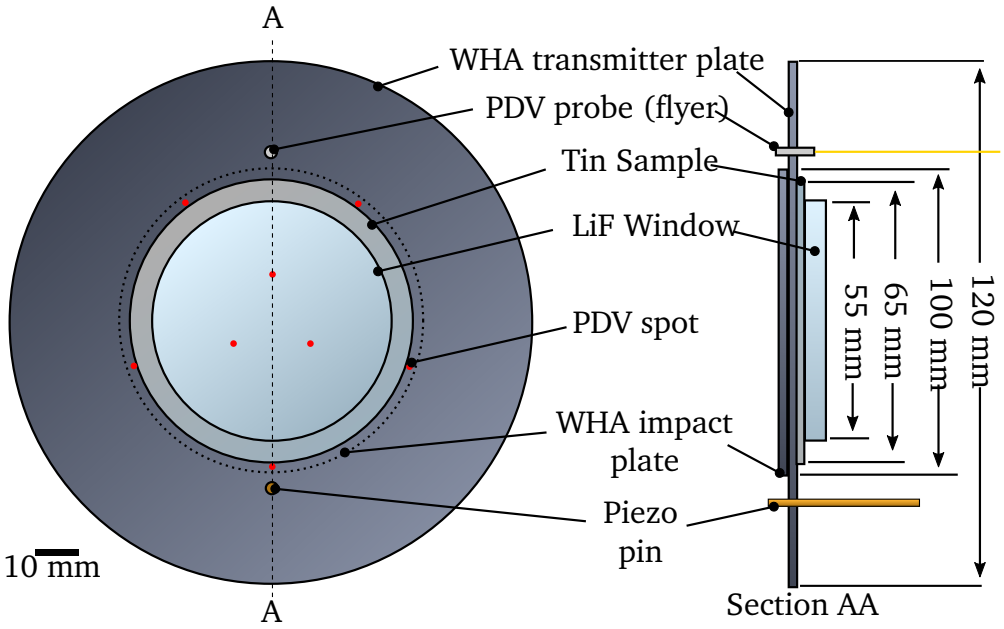


Figure 5.5: Scale drawing of the target layout (flyer plate at impact time is also shown). The black dotted line shows the pyrometry collection area. Red spots indicate PDV measurement locations. The white line indicates the flyer footprint on the target.

The process to design the geometry of the target assembly was as follows. First, the required 1D diameter (see Appendix C.2) was determined from diagnostic capabilities. Second, the required window diameter was determined. Next, the sample diameter was determined and finally the impactor plate diameter chosen.

The meaning of '1D region' is a region where the assumptions of the Rankine-Hugoniot relations are valid. A more detailed definition is outlined in Appendix C.2 but for the purposes of the discussion here the relevant details are that the 1D region will have a finite width and persist for a finite duration. Because the purpose of this experiment is to understand diagnostic performance, the required width and duration depend on the diagnostic capabilities.

With regard to the 1D width required the initial consideration is that the pyrometry system collects from a circular region, and although the diameter is dependent on the optical probe used, the maximum diameter is 12 mm. Additionally, the optical probe head has a footprint, 19 mm diameter, in which no other probes can be placed. This is relevant because, to measure the interface pressure and tilt, PDV probes need to measure velocity in a 1D region. Given a

PDV probe has a nominal collection diameter of 0.5 mm and a footprint of 2 mm, a 1D region with a diameter of 23 mm was required.

The next factor that affects the acceptable window size is the minimum acceptable 1D duration; this was defined as 500 ns which, given the rise time of the detection system is of order nanoseconds, allows sufficient time for a steady state to be reached and numerous measurements of the 1D state to be made. Using Equation C.4 and parameters from Marsh [89] it was calculated the shock in the LiF will travel at 6900 $m \cdot s^{-1}$; a LiF thickness of 5 mm was chosen to give a 1D duration of approximately 700 ns. It was assumed lateral releases travel inward at 45 degrees [107], thus a window section of at least 33 mm diameter would ordinarily be required.

However, due to recently reported issues regarding luminescence on shock release of LiF [52], the LiF window was oversized compared to the calculated requirement. LiF luminescence creates light which interferes with pyrometry measurements. Increasing the size of the LiF window moves the window edges further outside the solid angle of collection of the optics. In the hope that the collection of spurious light from luminescence would be prevented or reduced the window size was increased to 55 mm.

To simplify the gluing of the target sample and window it is desirable the sample should be a slightly larger diameter than the window. A difference of 5 mm ensures that the escape of glue is well controlled when the sample and window are compressed together. As such the tin sample was chosen to have a 65 mm diameter.

The geometry of the window, sample and transmitter plate have now been defined, only the impactor plate needs to be defined. The factors relevant for the impactor plate geometry are that its size need to be minimised (to conserve projectile weight) and it needs to produce a shock with sufficient 1D diameter.

The factor that determines the impactor plate diameter is that, to enable the shock speed through the sample to be determined, the time of shock arrival at the transmitter plate–sample interface needs to be measured. The arrival time will be measured with PDV probes—the same as at the sample–window interface.

Because the transmitter plate thickness is 2 mm, the 45° release assumption means the impactor plate needs to be 69 mm diameter to create a 1D region the same diameter as the sample. An additional 1 mm diameter should provide a 1D region that PDV probes can measure shock arrival from.

Finally, there are two factors that determine the thickness of the impactor plate, the required 1D duration and the need to minimise thickness (and hence weight). The thickness of the impactor plate affects the 1D duration because releases from the rear of the flyer plate erode the high pressure state. Because the shock must travel from the impact face to the rear of the impactor before the release begins, the duration is approximately twice the shock transit time. In this case the shock transit time for a 2 mm thick impactor plate has been calculated to be 0.45 μs giving a 1D duration of about 0.9 μs. The outcome of the preceding analysis is that the impactor plate is 70 mm diameter and 2 mm thick. This arrangement is shown in Figure 5.5.

It should be noted that it has been possible to reduce the impactor plate size from the initial assumptions used to select the impactor plate material (from 100 mm diameter to 70 mm diameter). As a result of the reduced mass the maximum projectile speed has been increased to approximately 1600 m·s^{-1}. An impedance matching calculation shows that with the flyer velocity and target configuration described above a ∼34 GPa shock was generated in the target, releasing to a ∼24 GPa pressure state at the Sn-LiF interface, see Figure 5.6. A shock speed in the tin sample of 4,150 m·s^{-1} is predicted.

The predicted temperature for a 1600 m·s^{-1} impact was 1,380 K, using the approach outlined in Appendix C.3. The improvement in projectile velocity results in an increase in target temperature of over 200 K in comparison to the initial configuration. The increase in temperature results in an increase in signal level at some wavelength bands of over 20 times.

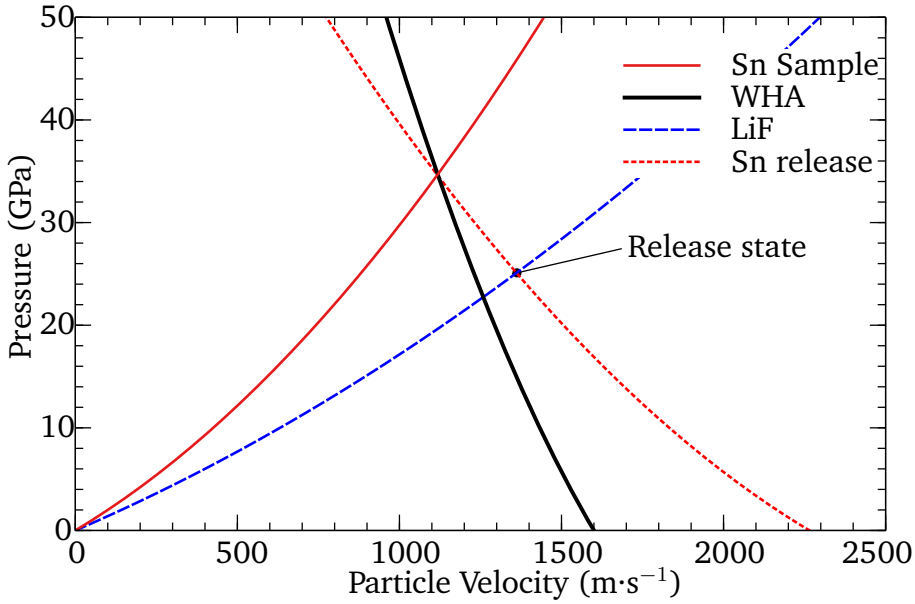


Figure 5.6: Result of Hugoniot crossing calculations of a WHA flyer impacting a tin target, constrained by a LiF window.

5.3.9 Target assembly process

The tin target and lithium fluoride window were bonded together first using the Loctite 326 adhesive. A 2 kg weight was applied to the discs during adhesive setting. Next Loctite 3421 was used to bond the tin to the tungsten transmitter plate; again a 2 kg weight was applied to the discs.

The rear surface of the tin target had a diamond turned surface finish. The surface finish was measured using a Zygo whitelight interferometer. The arithmetic mean deviation parameter, *Ra* [108], of the surface roughness was 0.1 μm.

To prevent any flashes external to the target assembly from compromising the pyrometry data blackout foil was added around the pyrometry head and window.

5.4 Results

Two experiments were completed as part of this series, the configuration and impact velocities are summarised on Table 5.5.

Experiment	Impact velocity ($m \cdot s^{-1}$)	Interface velocity ($m \cdot s^{-1}$)	Interface pressure (GPa)
1	1566 ± 2	1376 ± 1	25.4 ± 0.1
2	1575 ± 5	1381 ± 4	25.5 ± 0.1

Table 5.5: Table summarising result from the WHA/Sn/LiF plate impacts in this series. Interface pressure has been calculated using the principal Hugoniot parameters reported by Marsh [89].

5.4.1 Experiment 1

The flyer velocity measured in experiment 1 by the PDV diagnostic was 1566 ± 2 m·s^{-1}. The results from the three PDV channels viewing the sample-window interface are shown in Figure 5.7a). It can be seen that the velocity of the interface is as expected with a fast rise followed by a plateau.

The output from the pyrometry channels is shown in Figure 5.7b). All channels appeared to be corrupted by extraneous light. The radiance signals do not plateau at the times indicated by the velocity data and light levels are much higher than expected from the calibration procedure, exceeding the digitiser scale at times.

5.4.2 Analysis of experiment 1

The PDV results from experiment 1 indicate a plateau velocity of 1376.4 ± 0.3 m·s^{-1}. Using the Marsh parameters for the Hugoniot of LiF [89], the interface pressure is calculated as 25.4 ± 0.1 GPa.

As discussed the pyrometry channels were contaminated by extraneous light. The most probable source for this extraneous light is the luminescence of LiF upon release from the shocked state. Nevertheless, temperature analysis has been conducted using the procedure outlined in Appendix A. The results from this analysis are shown in Figure 5.8.

The expected plateau region is not seen on the 600–700 nm channel and the pulsed reflectivity signal is completely obscured by the extraneous light. The 750–850 nm channel does have a short plateau region (from ∼250 ns to ∼350 ns) but this is eventually lost when this channel also detects a relatively large light

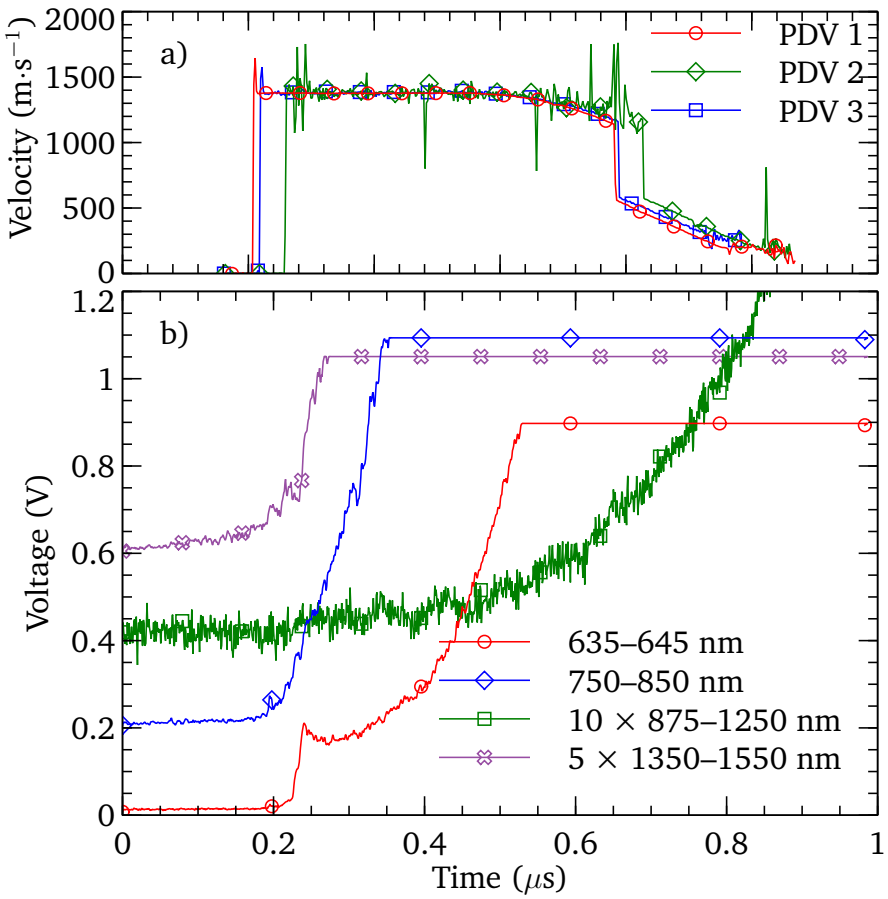


Figure 5.7: a) Plot of particle velocity data at the tin-lithium fluoride interface from experiment 1. The velocities are corrected using a window correction factor [103]. b) Plot of raw output from the detectors in the radiometer downsampled to 1 ns intervals. Voltages are scaled (see legend) and offset (0.2 V) for clarity.

signal. Finally the 875–1000 nm channel appears to detect a signal but this is similar in magnitude to the inherent noise on the channel.

The luminescence also caused the loss of the reflectivity data. The reflectivity diagnostic was operated in the green spectral region as it was anticipated very little light would be produced in this part of the spectrum. Unfortunately the luminescence signal levels overwhelmed that from the reflectivity diagnostic meaning no data was collected.

Tilt analysis

Tilt can be estimated using probe position data, shock arrival time and projectile velocity provided at least three measurements of shock arrival time are made at

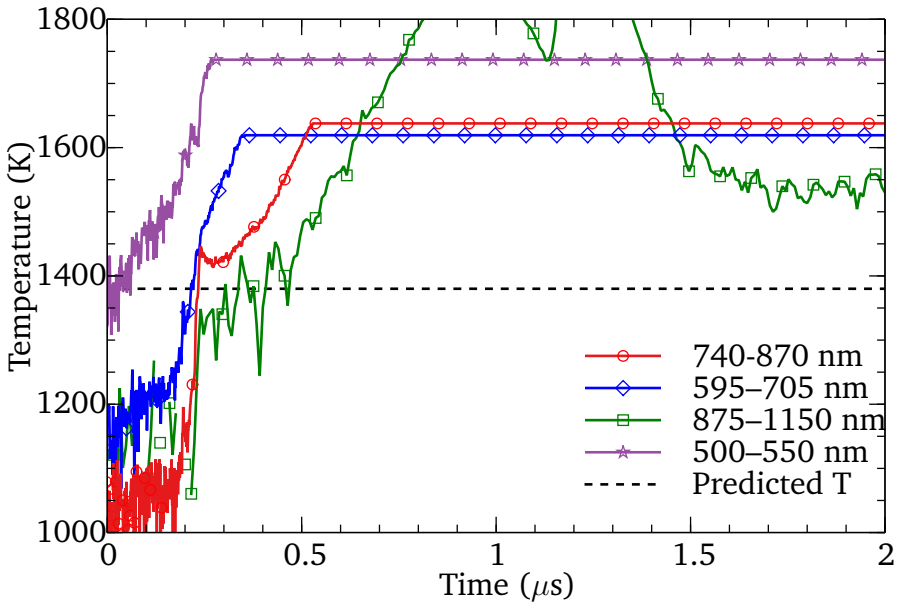


Figure 5.8: Plot of apparent temperatures recorded during experiment 1. It was calculated that the temperature would rise quickly then plateau at approximately 1,400 K. Here all channels saturated very quickly.

different positions. The difference in shock arrival times measured at the various PDV positions, see Figure 5.7a), multiplied by the projectile velocity gives the spatial separation of the impactor plate and sample, normal to the target plane. Combined with the probe position data (determined using laser marker paper) the tilt of the impactor plate relative to the target assembly was determined.

Analysis of the WHA plate shock break out times indicated a tilt of 2 mrad. Applying the same analysis to the Sn breakout times results in a tilt of 3 mrad. The difference in tilt can be attributed to imperfections in the components and build.

Shock speed

Analysis of the shock speed through the sample has been conducted. To calculate the shock speed, the breakout times at both the WHA and tin surfaces are fitted with a sinusoidal function (required due to the effect of tilt on arrival time). The mean difference between the two functions gives the transit time from one surface to the other, the data and the fitted functions are shown in Figure 5.9. The shock transit time determined from the transit time analysis is 0.49 ± 0.02 μs. Prior to the experiment, thickness measurements of the transmitter plate and

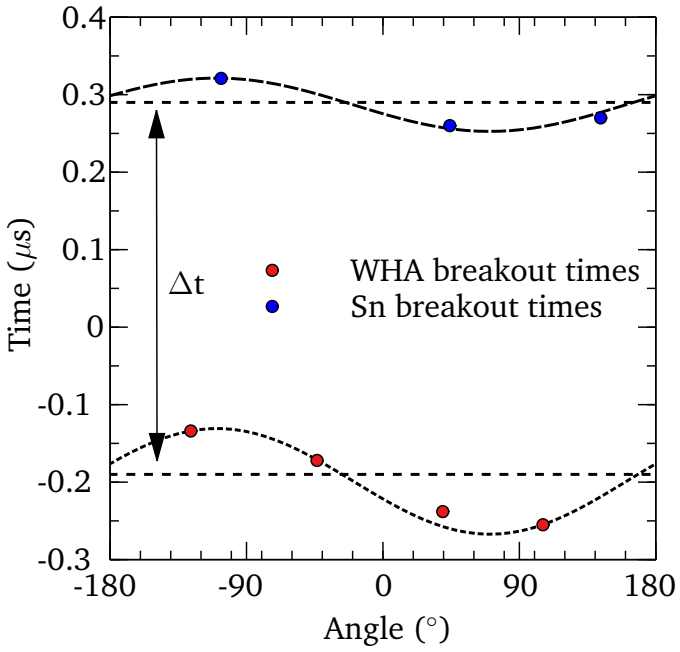


Figure 5.9: Plot of the shock breakout time data and fitted sinusoid function from initial experiment 1.

sample assembly were made, see Appendix B.1. The mean difference between the two surfaces was 2.042 mm. The standard deviation of the difference between the two fitted sinusoidal functions was used to infer an error. The result of this analysis is that the shock speed was 4100 $\pm$ 200 m·s^{-1}. Re-arranging Equations 1.5 and C.4 gives,

$$P = \rho_0 u_s \left(\frac{u_s - c}{s} \right), \tag{5.3}$$

which, assuming ρ_0 is 7.287 g·cm^{-3}, c is 2.58 km·s^{-1} and s is 1.49 [89], can be used to calculate the pressure induced in the tin as 30 $\pm$ 5 GPa which is consistent with predictions.

5.4.3 Experiment 2

Given the extraneous light issues with experiment 1, experiment 2 was configured to both verify that this was a repeatable phenomenon and further investigate the nature of the extraneous light. Specifically, the previous results suggested that light emission reduced at higher wavelengths. To investigate if this trend

Channel	Nominal wavelength band / nm	Detector
1	645–655	Hamamatsu H10721-20
2	720–870	Hamamatsu H10721-20
3	1050–1150	FEMTO HCA-S-400M-SI
4	1200–1300	Experimental InGaAs

Table 5.6: Table summarising the configuration of the radiometry system for the second experiment.

Channel 1	Channel 2	Channel 3	Channel 4
FF875-Di01	*FF875-Di01*	FF875-Di01	FF875-Di01
FF735-Di02	FF735-Di02	*Edmund 1200 LP*	Edmund 1200 LP
FF02-650-100	FF02-795-150	None	None

Table 5.7: Table summarising the filters in place on each channel in the radiometer system. Italics are used for filters that are reflected from, rather than transmitted through the filter.

continued the configuration of the radiometry system was modified to replace the green reflectivity channel with a 1350–1600 nm channel using a prototype InGaAs detector.

As a result of the extraneous light issues in experiment 1 some measures to suppress emission from the LiF edges were applied. Specifically, Apiezon clay was used to surround the edge of the LiF window and black foil was used around the probe end to try prevent the collection from external light sources.

The measured flyer plate velocity was 1575 ± 5 m·s^{-1}. The PDV results from experiment 2 were very similar to experiment 1, indicating the impact occurred as intended. The PDV results from experiment 2 are shown in Appendix B.1. The unprocessed radiance voltages are shown in Figure 5.10 and again there seems to be extraneous light issues.

5.4.4 Analysis of experiment 2

The same analysis procedures were applied to the data from experiment 2. The PDV results indicate a interface velocity of 1381 ± 4 m·s^{-1}, resulting in an interface pressure of 25.5 ± 0.1 GPa. The results of temperature analysis are shown in

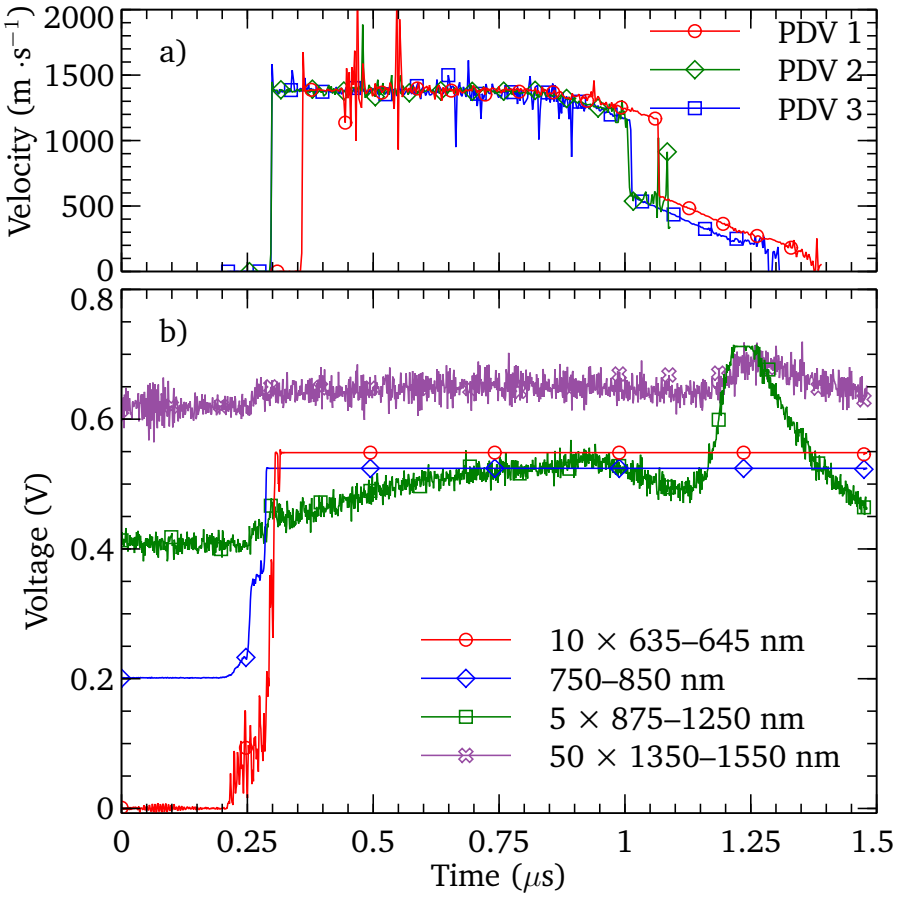


Figure 5.10: Plot of raw output from the detectors in the radiometer. Voltages are scaled (see legend) and offset (0.05 V) for clarity.

Figure 5.11. It can again be seen that the channels are affected by extraneous light and did not produce light levels consistent with thermal radiation. The result of the shock speed analysis was a velocity of 4200 ± 70 m·s^{-1} or 33 ± 2 GPa. The WHA plate shock break out times indicated a tilt of 3 mrad; the Sn breakout times indicated a tilt of 3 mrad.

5.5 Conclusions

These experiments have demonstrated the capability to make window interface particle velocity measurements and sample shock velocity measurements independently and simultaneously. The ability to make these measurements allows two EoS points to be determined in a single experiment. The measurements of interface velocity and shock velocity were consistent with the predicted values.

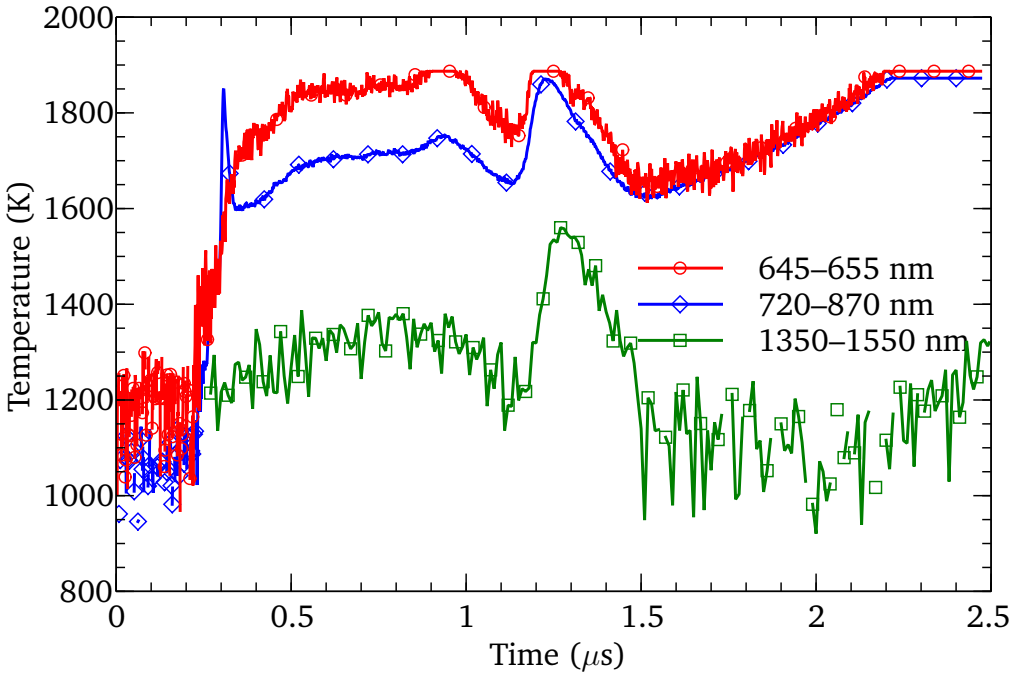


Figure 5.11: Plot of apparent temperatures recorded during experiment 1. It was calculated that the temperature would rise quickly then plateau at approximately 1,400 K. Here all channels saturated very quickly.

However, the EoS data would have been more valuable if the temperature measurement had been successful. As discussed in Section 1.3 accurate temperature data allows EoSs to be constrained much more tightly but it has not been possible to measure temperature in these experiments.

Temperature measurement was not possible because spurious light corrupted channels operating in the visible region of the spectrum. The most probable cause for this light is luminescence due to the shock-release process that occurred at the edge of the LiF window. The window was oversized to mitigate the emission, but these results make it clear that oversizing an optical window is not a solution to LiF luminescence.

A potential explanation for the significant levels of luminescence is that, although increasing window size increases the distance between the edge and the probe collection area (which can be expected to reduce optical coupling), it also increases the perimeter of the window, so although less light from a given section of the window is collected, this is compensated by the longer perimeter. The exact

scaling of the relationship between these two factors is not clear.

The radiance results also highlight one of the benefits multiple pyrometry channels; it is easier to distinguish between non-thermal interference and unexpected temperature results as the different channels can be compared for consistency. The results here are not consistent with radiation of thermal origin hence must come from a non-thermal source.

The nature of the luminescence is not well understood but it may have been a particular issue due to low radiance from the sample. The use of a lead sample would have increased the temperature achieved by approximately 350 K; combined with lead's higher emissivity the resultant signal levels would be approximately 25 times higher. If the luminescence phenomena is not dependent on the sample material the emitted luminescence would have been insignificant in comparison to the sample emission.

The luminescence also caused the loss of the reflectivity data so it is not possible to comment on the performance of the dynamic reflectivity diagnostic. However, it should be noted that, if the reflectivity illumination system had been sufficiently bright, a reflectivity measurement would have been possible despite the luminescence. Thus the ability to have a reflectivity diagnostic able to reach high brightness is desirable.

6

Comparative experiments on a 100 mm bore gas gun

6.1 Experiment Overview

In the work presented in this chapter, data is compared from large bore gas gun experiments acquired simultaneously using three different pyrometers, which have different temporal, spatial resolutions and operate at different wavelength bands. This appears to be the first time such comparisons have been made as none have been reported in the literature. Given the specialist nature of high speed pyrometers it was necessary to engage multiple teams from institutions with interests in shock experiments, specifically, in addition to the development done as part of this thesis, a US team from Los Alamos National Laboratory and Nevada National Security Site and a UK team from the Atomic Weapons Establishment.

The rationale for comparative experiments arises because the design choices made when constructing a pyrometer instrument result in specific performance attributes that must be individually investigated and understood. A consistent issue during pyrometer development is benchmarking the dynamic accuracy and uncertainty performance of a particular system. While theoretical treatments can be helpful for developing understanding [95–98, 109], experimental validation is desirable; a well-established method to calibrate a pyrometer is to use a

blackbody standard. Unfortunately blackbody sources are typically static systems that rely upon thermal equilibrium and therefore cannot be used to test the instruments at the rapid timescales inherent to high strain rate experiments. The ideal solution would be to test the systems under dynamic conditions against a known temperature standard; however, at present there is no well-established temperature standard that operates within the desired timescales. Another option is to compare results from multiple pyrometers of differing designs (each initially calibrated using a blackbody), and field them on the same dynamic experiment to provide a relative comparison of temperature measurement.

While repeating a single target experiment with different diagnostics is one option for a comparison test, it is challenging to achieve high repeatability in shock physics experiments. A potential solution is to use a large bore gas gun; the large shocked area on a large bore gas gun means it is possible to conduct experiments with multiple samples shocked by the same impact plate in a single shot. Because all the samples are hit by the same impact plate the sample-to-sample variation is reduced in comparison to multi-shot experiments.

A further complication to the accurate measurement of temperature using optical pyrometry is that the emissivity of the sample must be known. For multi-spectral band pyrometry knowledge of the spectral variation in emissivity is required to determine a consistent temperature, otherwise variations in emissivity will cause deviations in measured radiance resulting in inconsistent temperatures. The approach used here to account for emissivity is discussed in detail in Section 6.5. Alternative solutions have been reported in the literature. One option is to conduct each experiment twice; the first experiment measures thermal radiance, while the second experiment deduces the spectral emissivity [80, 93]. Methods to measure emissivity simultaneously with pyrometry are nascent [110, 111].

6.2 Pyrometer systems

Three pyrometry systems were used for the simultaneous measurements performed in this work. While all systems exploit the same fundamental principles to infer

temperature, i.e. Equation 2.1, there was significant variation in their design. The strengths and weaknesses of each instrument are discussed and conclusions made about relative error and absolute accuracy of each system. Finally, the effects of different methods for inferring spectral emissivity upon the final calculated temperatures are compared. A short description of each system follows.

6.2.1 Pyrometer 1

The first pyrometer to be discussed, pyrometer 1, is the product of the development activities that have been reported in previous chapters. It is a development of the system in Chapter 5 and uses dichroic mirrors to separate the collected light from a single optical fibre input into broad wavelength bands; this is similar to that initially proposed by Seifter [75] Light from the broad wavelength bands is further filtered using bandpass filters and focused onto detectors. The detectors used were two photomultiplier tubes (PMTs, of type Hamamatsu H10721-20) and two amplified photodiodes (a FEMTO HCA-S-400M-IN and a FEMTO HCA-S-400M-SI). A schematic of the configuration of the filtering and detection system is shown in Figure 6.1. Summaries of the filtering components in each channel are shown in Table 6.1 and a summary of the resultant wavelength bands are shown in Table 6.3. Light is collected from the target using a single aspheric lens (Thorlabs AL1210) mounted in a $\frac{1}{2}$" diameter lens tube to focus nominally collimated light onto a 1 mm diameter core, 0.48 NA optical fibre (Figure 6.2). The detectors in the pyrometer systems produce voltage outputs, voltage data from pyrometer 1 were recorded on digitizers with a 40 Giga-samples per second ($GS{\cdot}s^{-1}$) sampling rate and 16 GHz bandwidth,

6.2.2 Pyrometer 2

The second pyrometer system, pyrometer 2, was constructed at AWE a number of years ago and consisted of three indium-antimonide (InSb) photodiodes (Judson J10D-M204-R01M-60) with associated amplifiers (FEMTO DCHPA-100). Light emitted by the target was coupled to each detector via dedicated optical fibres

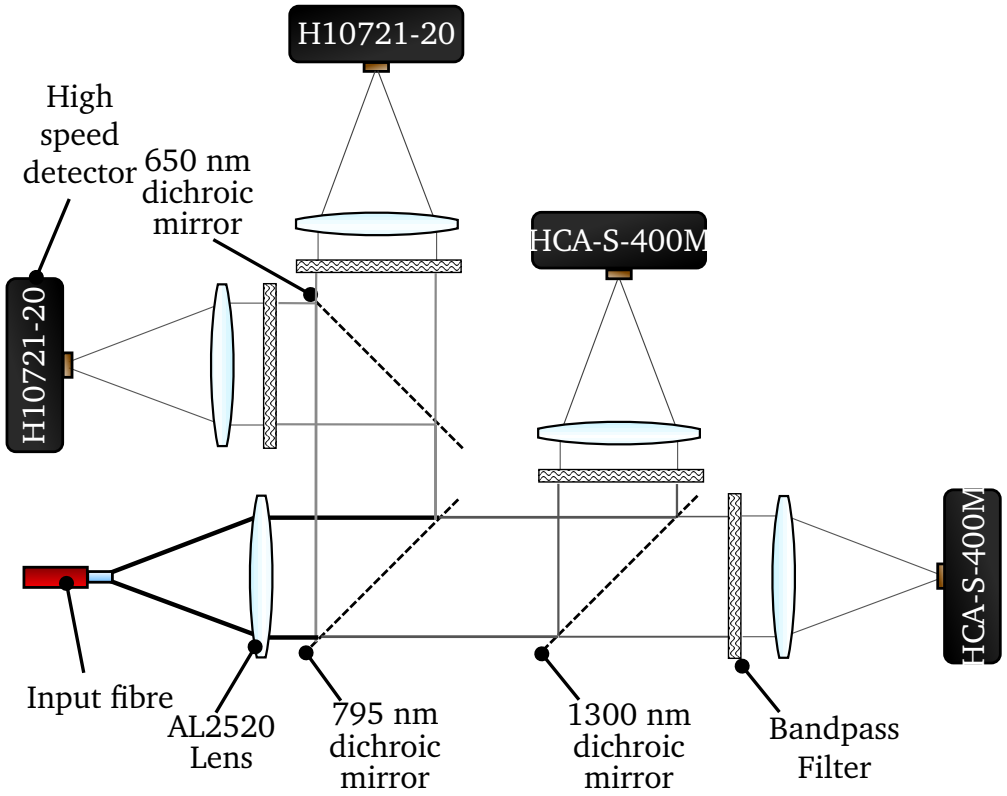


Figure 6.1: Schematic diagram of the enhanced pyrometer system. The system has a single input fibre with a number of dichroic mirrors to separate the collected light and direct it to detectors.

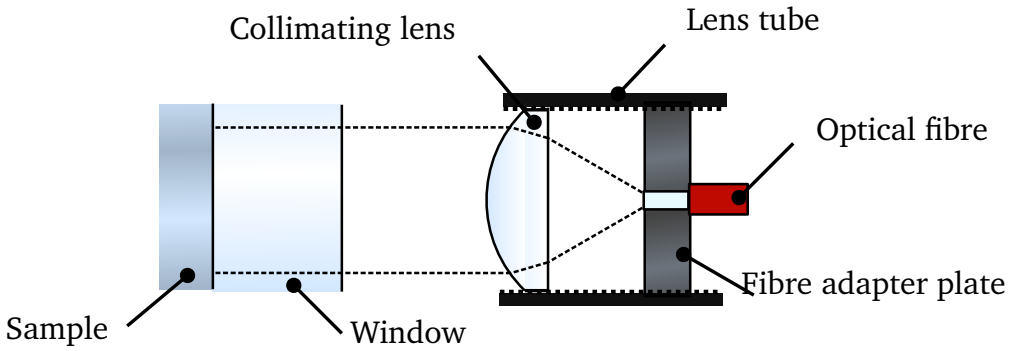


Figure 6.2: Schematic of the optical collection head used to couple light into pyrometer 1. A single aspheric lens (Thorlabs AL1210) collects nominally collimated light from the sample and couples the light into a single, 1 mm diameter core, 0.48 NA, optical fibre.

(1 mm diameter core, 0.48 NA). Prior to reaching the detector the light was first collimated and passed through a bandpass filter. A schematic of the pyrometer configuration is shown in Figure 6.3. More detailed information on the bandpass filters was not available but the effective wavelength bands are summarised in

Table 6.2. Light was collected from the target using a 1” diameter plano-convex lens (ThorLabs LA1805) contained within a 1” diameter lens tube; the lens collected nominally collimated light from the target and focused it on to an array of 1 mm core, 0.48 NA optical fibres positioned at the focal point. Because the optical head associated with this pyrometer collects nominally collimated light, each fibre does view a slightly different region of the sample. However, due to the proximity of the fibres there is significant overlap between the regions. A schematic of the light collection optics is shown in Figure 6.4. Data from pyrometer 2 were recorded by 4 GS·s^{-1} sampling rate and 1 GHz bandwidth digitisers.

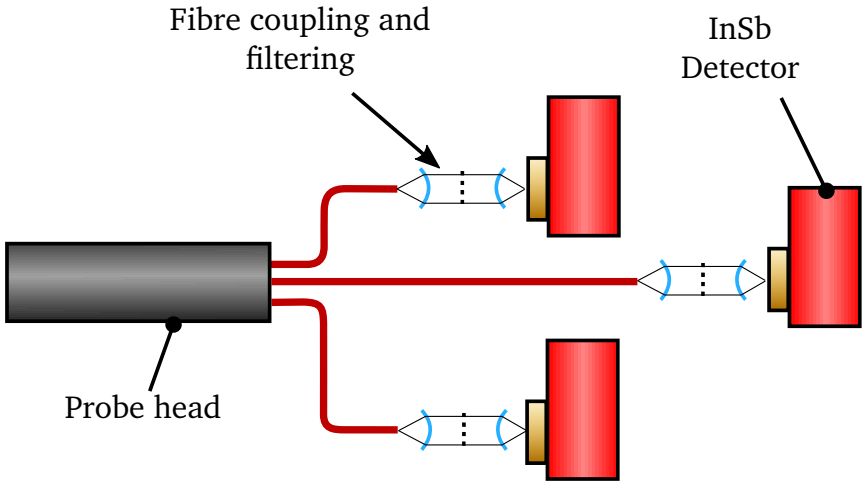


Figure 6.3: Schematic diagram of the antecedent pyrometer system. Each of the three channels has an associated fibre, filtering optics and detector.

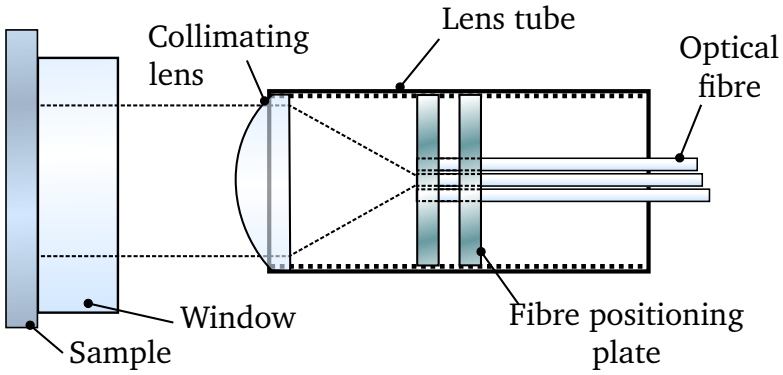


Figure 6.4: Schematic of the optical collection head used to couple light into pyrometer 1. A single aspheric lens (Thorlabs AL1210) collects nominally collimated light from the sample and couples the light into a single, 1 mm diameter core, 0.48 NA, optical fibre.

Channel 1	Channel 2	Channel 3	Channel 4
FF875-Di01	*FF875-Di01*	FF875-Di01	FF875-Di01
FF735-Di02	FF735-Di02	*Edmund 1200 LP*	Edmund 1200 LP
FF02-650-100	FF02-795-150	FF01-1001-234	FF01-1538-82

Table 6.1: List of band pass filters and dichroic mirrors used in each channel within pyrometer 1. The filters were manufactured by Semrock except for those highlighted as being supplied by Edmund Optics. Italics indicates that light is reflected, rather than transmitted, by the filter.

6.2.3 Pyrometer 3

The third pyrometer, pyrometer 3, was designed and built as a collaboration between Mission Support and Test Services, (MSTS) and Los Alamos National Laboratory (LANL). The MSTS/LANL Pyrometer collects light from its sample through a focused probe assembly. The probe has a pair of doublets that focused light from a small area of the surface onto an angle-polished, close-packed optical fibre bundle with seven 300 μm core multimode fibres and three 9 μm core PDV fibres. The 'rosette' fibre bundle then splits, with the PDV fibres routed to a PDV system and the seven 300 μm fibres couple to a 1 mm diameter optical fibre that runs to the pyrometer, see Figure 6.5. The pyrometer collimates the light out of the 1 mm fibre and then uses a system of dichroic mirrors and bandpass filters to select an optical band-pass for each of six detectors, see Figure 6.6.

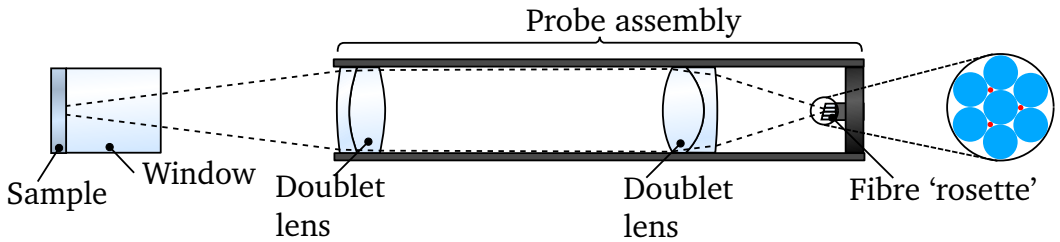


Figure 6.5: Schematic of the optical collection head used to couple light into pyrometer 1. A single aspheric lens (Thorlabs AL1210) collects nominally collimated light from the sample and couples the light into a single, 1 mm diameter core, 0.48 NA, optical fibre.

The MSTS/LANL pyrometer uses four Hamamatsu R943-02 PMTs for optical wavelength detection. The PMTs have a bandwidth of ~300 MHz and the capability to detect single photons when operated at high gain. Two TTI TIA-525

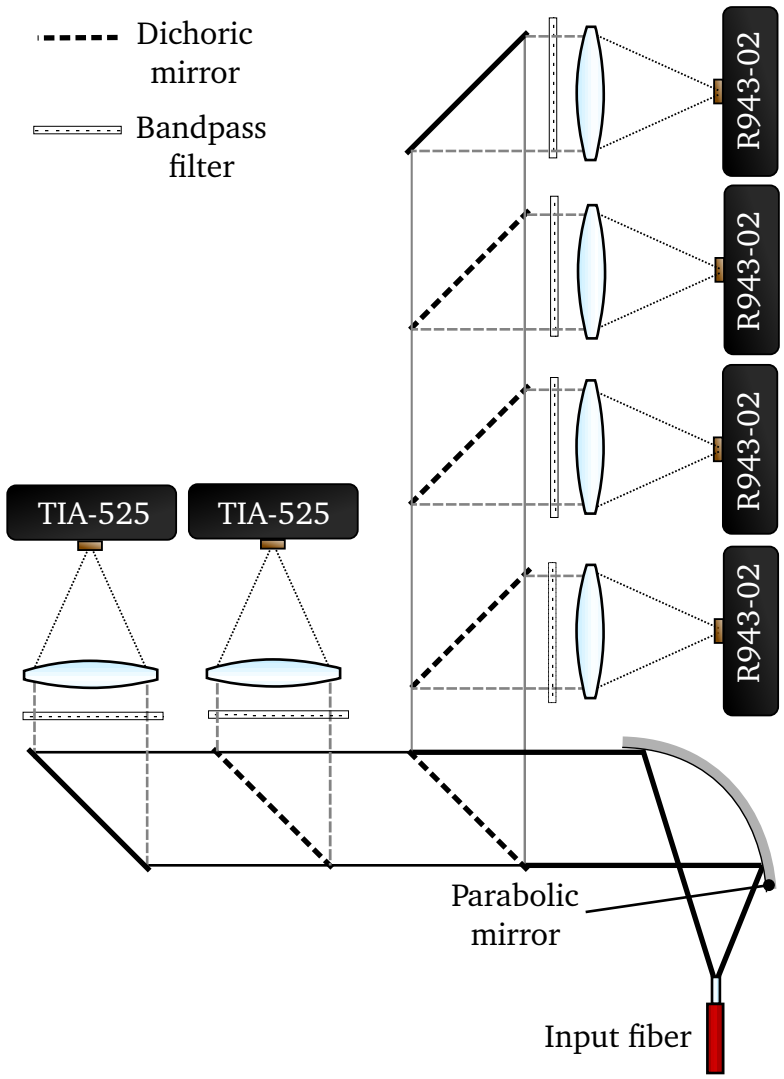


Figure 6.6: Schematic diagram of the MSTS/LANL pyrometer system. The system has a single input fibre with a number of dichroic mirrors to separate the collected light and direct it to detectors.

photodiodes provide collection in the infrared spectrum with a bandwidth of ∼70 MHz. The pass-band and optics associated with each channel are described in Table 6.2. The MSTS/LANL system used 10-bit digitzers with 1 GHz bandwidth measuring at 4 GS·s^{-1}.

Channel 1	Channel 2	Channel 3	Channel 4	Channel 5	Channel 6
FF875-Di01	FF875-Di01	FF875-Di01	FF875-Di01	*FF875-Di01*	*FF875-Di01*
Edmund 1200 LP	*Edmund 1200 LP*	*FF875-Di01*	*FF757-Di01*	*FF660-Di02*	*FF552-Di02*
	FF01-1001-234	FF02-809/81	FF01-708/75	FF01-609/54	FF01-510/42

Table 6.2: List of channels and optical elements in the MSTS/LANL pyrometer system. All filters were obtained from Semrock except those obtained from Edmund. Italics indicates that light is reflected, rather than transmitted, from the filter.

Channel	Pyrometer 1	Pyrometer 2	Pyrometer 3
1	595–700	1725–1775	1207–1630
2	740–870	1925–1975	928–1206
3	880–1120	2323–2373	764–852
4	1490–1590	–	667–740
5	–	–	579–640
6	–	–	486–534

Table 6.3: Summary of wavelength bands of the channels on the three pyrometer systems used. All wavelength bands are in nanometers.

6.3 Experimental Design

6.3.1 Sample material selection

Tin was selected as the sample material due to its: wide availability, existing shock temperature literature [80, 94, 112], relatively large heating under shock loading, and low toxicity. A lithium fluoride, LiF, window was used as a shock anvil to prevent the tin target fully releasing and thus keeping the target at an elevated temperature. A tungsten heavy alloy, WHA, flyer plate was used in the experiments to maximise the generated pressure state. Due to the multi-sample configuration of these experiments the full 100 mm of the large-bore gun diameter is required; for a 100 mm diameter, 2 mm thick impactor plate the fastest impact velocity that can be achieved on the gas gun facility at the Institute of Shock Physics, Imperial College London, was 1450 $m{\cdot}s^{-1}$. A Hugoniot crossing [112], see Figure 6.7, shows that the tin will be shocked to a pressure of approximately 31 GPa before releasing into the LiF window, to a pressure of approximately 23 GPa.

A temperature prediction was calculated by using a tin EoS [40] and the shock

and release pressures predicted by Hugoniot crossing; a temperature of 1200°K was predicted. Hydrocode modelling (using AWE's CORVUS code) was also done and showed a shock plateau duration of approximately 500 ns was expected.

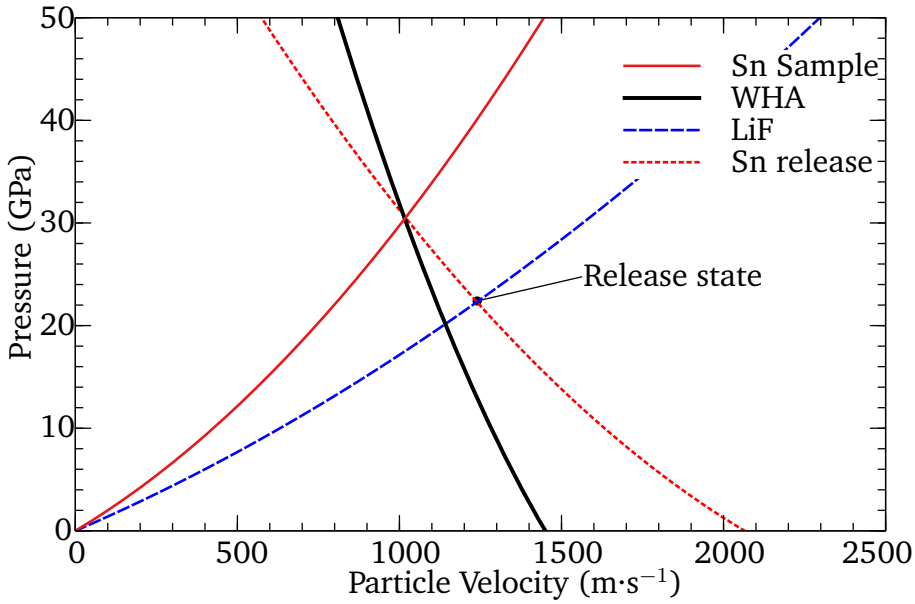


Figure 6.7: Impedance matching analysis of the shock state generated by the impact of tungsten heavy alloy (WHA) at 1450 m·s^{-1} into a tin sample with a lithium fluoride window.

6.3.2 Target configuration

A multi-sample target was assembled to achieve simultaneous shock loading on three tin samples. Each tin sample was 45 mm diameter and 3 mm thick and each had a 40 mm diameter, 10 mm thick LiF window attached to it with Loctite 326 (the glue thickness was measured using a white light interferometer and found to be between 2 μm and 21 μm). The three samples were mounted equally spaced within a 100 mm diameter region, centred on a 120 mm diameter WHA transmitter plate, see Figure 6.8. Each of the three samples was identical within construction tolerances.

Previous experiments have revealed that there are issues associated with non-thermal emission from LiF, which were attributed to the LiF edge releases [52]. Several measures were taken to reduce edge emission. First, the circumferential

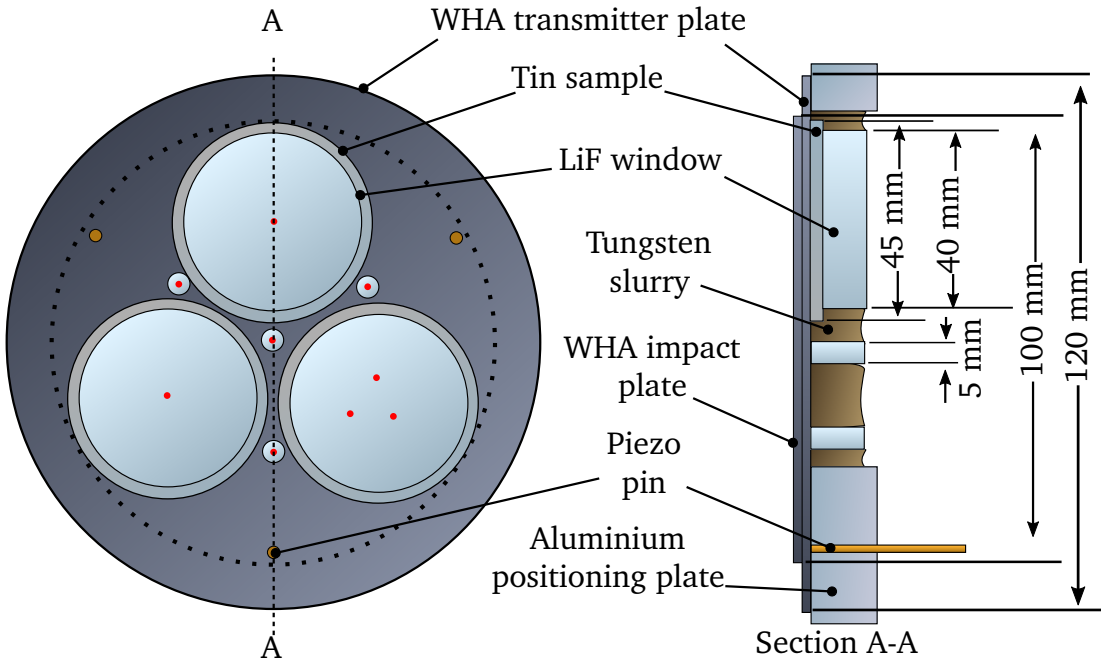


Figure 6.8: Scale diagram of the triple sample assembly. Three nominally identical tin samples, glued beneath lithium fluoride (LiF) windows, were mounted on a tungsten alloy transmitter plate. The LiF windows were surrounded by a shock impedance-matching slurry compound.

edges of the LiF window were polished until optically smooth during manufacture and then coated with an opaque layer of chromium. Second, the space around the circumference of the LiF was filled with an impedance-matching slurry (a silicone polymer solution loaded with powdered tungsten) to mitigate reflected waves propagating back into the LiF window. Finally, the entire target assembly was enclosed within a light-tight assembly to prevent light from the target chamber from contaminating the pyrometer measurements.

6.3.3 Velocity Diagnostics

12 channels of photonic Doppler velocimetry (PDV) were fielded on each experiment to determine shock arrival times and particle velocities. PDV measurements were made at multiple locations indicated as red spots in Figure 6.8. Four channels were used to determine the shock breakout time on the WHA surface, the arrangement of the PDV measurement points allowed the tilt of the shockwave to be determined. The tin sample associated with the pyrometer 2 had a single

PDV probe positioned at the side of the optical probe. The sample associated with the pyrometer 1 had three PDV probes arranged around the optical probe, again to allow tilt to be determined. Finally, the sample associated with the US system had three PDV fibres embedded in the optical fibre used for pyrometry, see Figure 6.5; three fibres were used in case of failure of one or more fibres.

6.3.4 Calibration

Although the basis for all pyrometry analysis is Planck's Law, see Equation 2.1, there are numerous approaches for the conversion of pyrometry data to temperature data. One area of significant variation is the treatment of calibration data; the different approaches to calibration are now discussed.

Broadly, the pyrometer 1 and pyrometer 2 used a system level model to create a model voltage-temperature curve and calibration was used to determine an appropriate voltage scaling factor. The first step was to model the light collected by each pyrometer's optical probe (using Zemax OpticStudio) to calculate the coupling efficiency into the fibre from the sample. The next step was to model the expected signal levels for each detector; this was carried out as follows:

1. A blackbody curve is generated for a specified temperature, T, using Planck's Law, Equation 2.1.

2. The curve was then scaled to account for the coupling efficiency of the collection optics (determined from the Zemax modelling).

3. Transmission through the various optics was then calculated using the highest fidelity data (usually manufacturer provided data).

4. The spectrum of light reaching the detector, determined via step 3 was multiplied by the detectors spectral response and integrated to calculate a photocurrent.

5. The photocurrent was then converted into an expected voltage using the electrical gain of the detector system. This step produced a voltage-temperature point.

6. The process is repeated for a range of temperatures to generate a voltage-temperature curve.

Despite the level of detail in the system level model there remain discrepancies between measured and predicted voltage levels. Discrepancies could arise for a number of reasons such as misalignment or part-to-part variation; notably, because the discrepancies will vary between experiments (different collection optics and optical fibres are used each time), the pyrometers were calibrated before each experiment.

The calibration procedure was conducted by using an optical chopper to periodically interrupt the light path of the pyrometry system while the system was viewing a blackbody. It was necessary to use a fast shutter (actuating in less than 2 ms) in addition to the optical chopper, to allow a single 'chopped' light pulse to be selected, this prevented saturation and droop effects that are associated with the use of PMTs. The associated voltage pulse was analysed to determine a single voltage value when the pulse was incident upon each detector. The pyrometers were calibrated using radiance levels that were approximately equivalent to those expected during the experiment (calculated using the predicted temperature and sample emissivity).

The procedure for pyrometer 3 accomplished the same outcome using a different approach. Prior to an experiment, each pyrometer pass-band was tested with a monochromator to produce a measurement of relative detector output as a function of light input to the pyrometer as a function of wavelength. The system was then calibrated by measuring the radiance of a blackbody calibration standard through the same optical fibre path and probe that was to be used in the experiment. Although the same process was used to measure blackbody radiance, rather than produce a voltage-temperature curve, the radiance of the blackbody

standard is multiplied by the measured optical response of each channel to produce a total radiance throughput on that channel. The channel's recorded voltage response is paired with this information to produce a set of discrete radiance-voltage points. The points are fit with a linear function that closely approximates the detector response within its linear dynamic range. The calibration is then slightly adjusted, as a function of wavelength, to account for the difference in transmission of the optical components in the black body calibration in comparison to the components used in the dynamic experiment.

6.4 Results

In total four experiments were performed at similar shock conditions, a summary of the impact velocities and associated interface conditions is listed in Table 6.4. Example velocity-time traces (from the PDV data) from the tin/LiF interface for each target are shown in Figure 6.9. The velocimetry results from each target on each experiment showed that the impact state generated within different three separate samples was similar during each experiment. Furthermore, the results showed good agreement with hydrocode modelling of the system.

Experiment	Impactor Velocity ($m \cdot s^{-1}$)	Pyrometer 1		Pyrometer 2		Pyrometer 3	
		Velocity ($m \cdot s^{-1}$)	Pressure (GPa)	Velocity ($m \cdot s^{-1}$)	Pressure (GPa)	Velocity ($m \cdot s^{-1}$)	Pressure (GPa)
1	1481 ± 8	1295 ± 5	23.6 ± 0.1	1294 ± 5	23.6 ± 0.1	1293 ± 4	23.5 ± 0.1
2	1481 ± 9	1289 ± 6	23.4 ± 0.1	1293 ± 5	23.5 ± 0.1	1296 ± 4	23.6 ± 0.1
3	1476 ± 8	1289 ± 8	23.4 ± 0.1	1287 ± 4	23.4 ± 0.1	1282 ± 4	23.3 ± 0.1
4	1481 ± 5	1292 ± 7	23.5 ± 0.1	1293 ± 2	23.5 ± 0.1	1290 ± 3	23.5 ± 0.1

Table 6.4: Table summarising the impact velocities for each experiment, along with the measured sample-window interface velocities and pressures (determined using lithium fluoride Hugoniot data).

Examples of unprocessed radiance results are shown in Figure 6.10 and illustrate the signal levels and signal-to-noise levels achieved.

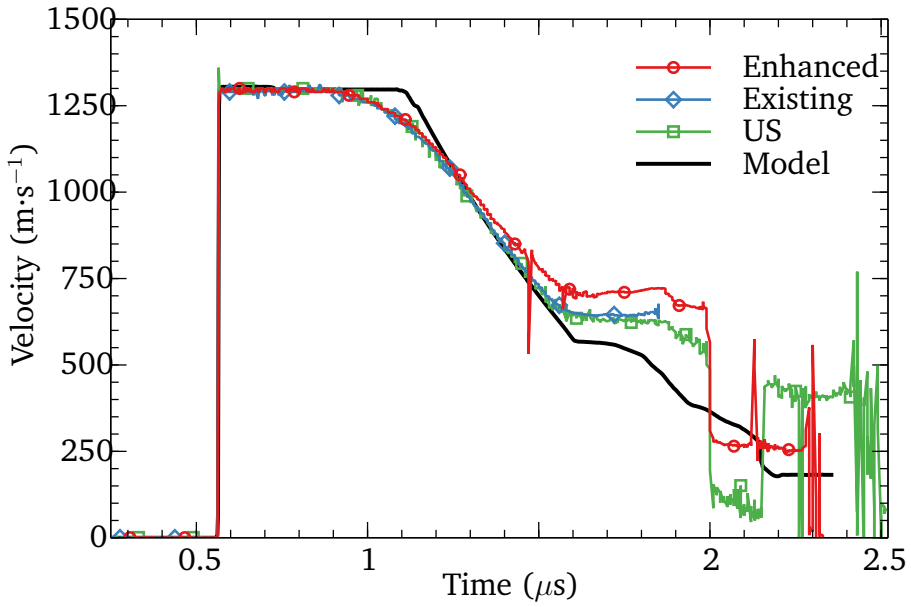


Figure 6.9: Velocity-time data from three different samples in experiment 2 compared with model data from a hydrocode.

6.5 Sample emissivity

The calculation to convert voltage data into temperature data requires a value for emissivity, however, spectrally resolved emissivity data was unavailable so another approach was required. One possible method of data analysis is to assume that the emissivity of the material is one; this method produces the minimum possible temperature, known as a radiance or colour temperature. Another method is to calculate temperature based upon several different possible emissivity values, usually in the range [0.1–1.0] [92]. A further approach taken by some investigators is to assume a range of emissivity values for each channel of a pyrometry measurement and then find the common temperature range; this approach partially addresses the issue of change in spectral emissivity under shock conditions by accommodating a range of possible emissivity values. In this work, the different pyrometry systems used different methods to account for uncertainty in the spectral emissivity of the target. The different methods are now described.

The analysis used for pyrometer 1 and pyrometer 2 used two assumptions to account for emissivity. The first assumption was that the optical properties reported in the literature were an adequate description of the optical properties of the tin

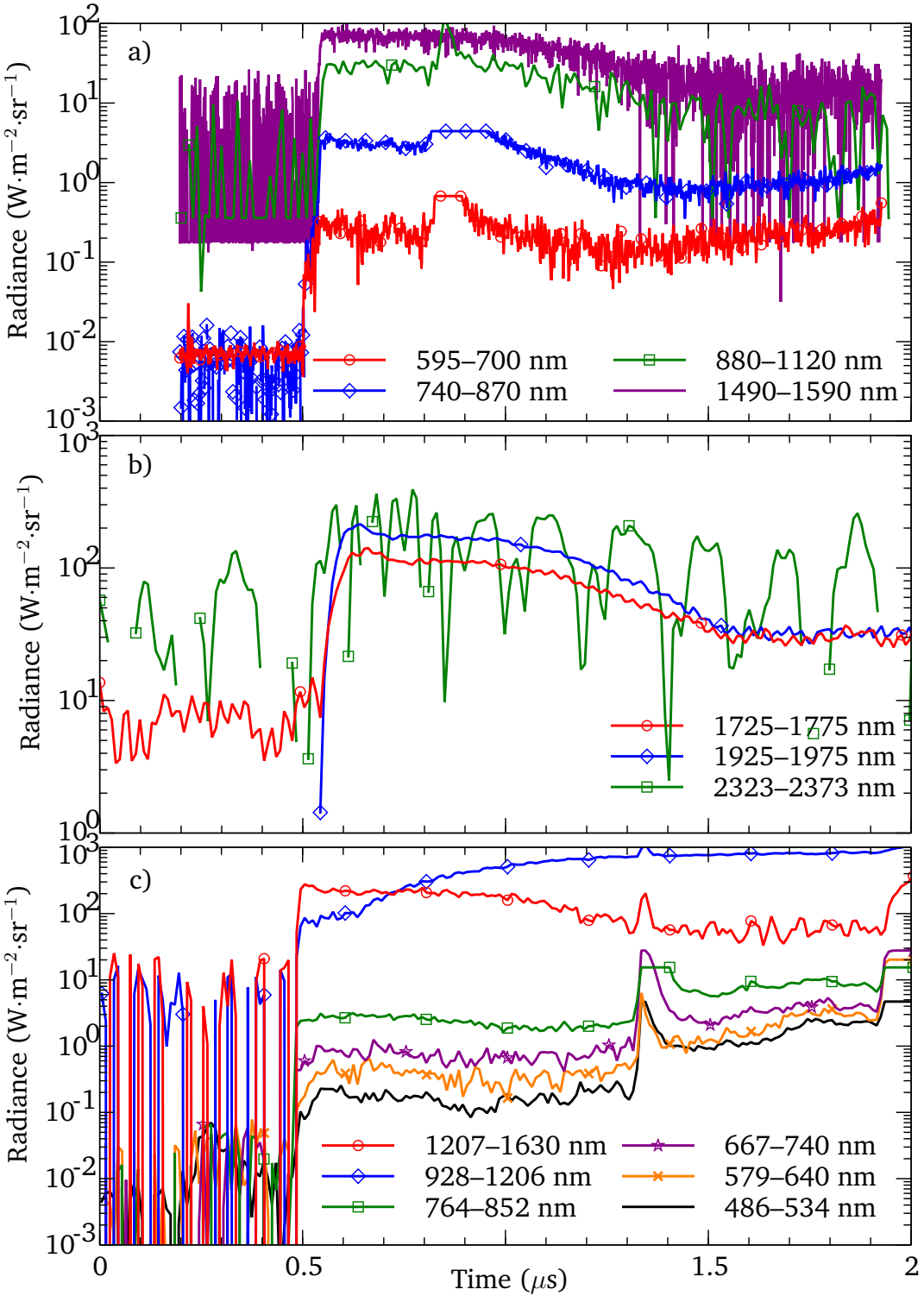


Figure 6.10: Plot of time-voltage traces from all pyrometers. a) data from pyrometer 1 on experiment 2. The shock arrival just after 0.5 μs is clearly visible; a non-thermal radiance 'spike' occurs at approximately 0.8 μs. b) data from pyrometer 2 on experiment 2. c) data from pyrometer 3 on experiment 1. A non-thermal radiance 'spike; occurs at approximately 1.3 μs.

samples used. For opaque materials, such as metals, reflectivity is the complement of emissivity hence a simplified version of Kirchhoff's Law can be applied,

$$\epsilon = 1 - r, \tag{6.1}$$

where ϵ is emissivity and r is reflectivity. The second assumption was that the uncertainty in the reflectivity of shocked tin was $\pm$10% of the data literature (based on measurements of the reflectivity of shocked tin reported in the literature[80, 93, 94, 113]). Due to non-linearities in the analysis process a Monte-Carlo based analysis method was used to calculate the resultant uncertainty in temperature measurements.

The Monte-Carlo procedure first generated a set of voltage traces for each channel with a standard deviation determined by the standard deviation of the voltage measurement in the plateau on the corresponding channel. Next a set of emissivity values was generated using the literature values with a 10% uncertainty, creating a set of voltage-emissivity pairs. The voltage-emissivity pairs were then converted into a set of temperature values (using the calibration data) for each channel, an example is shown in Figure 6.11. Each set of temperature values is fitted with a Burr distribution (this distribution was chosen by trial-and-error) and, finally, all the distributions from each channel combined to give a temperature probability distribution function (PDF) for the pyrometer, see Figure 6.12. The temperatures quoted from this analysis are the most probable temperature (i.e. the peak of the PDF) and the $\pm 1\sigma$ equivalent confidence interval (i.e. 64.2% probability that the temperature is in that range). A disadvantage of the above approach is that, as a statistical approach, it is not possible to create time resolved errors, so time resolved temperature data has been calculated using unchanged emissivity values from the literature.

6.6 Temperature analysis

The temperature analysis of data from pyrometer 3 began with spectral reflectivity values measured at standard temperature and pressure in the lab [114]. A

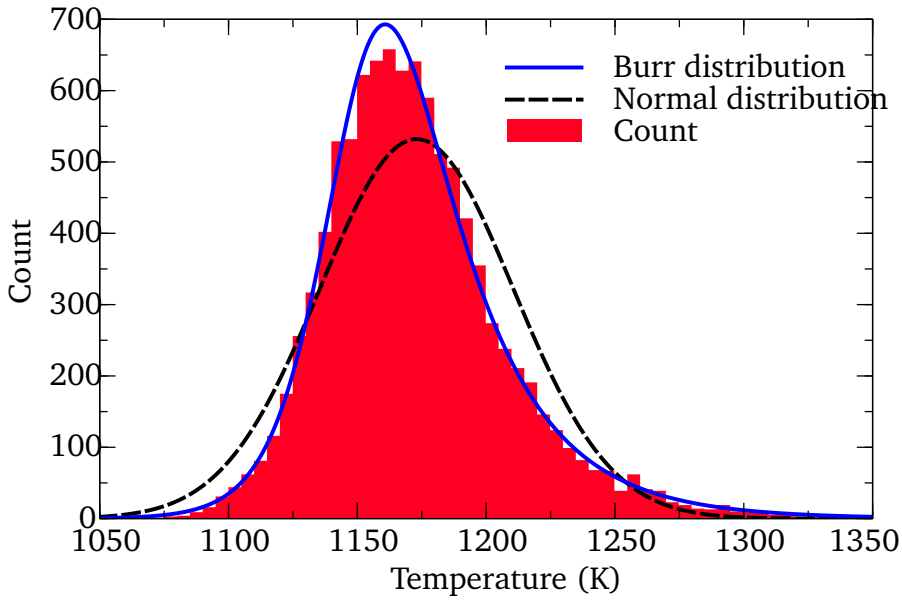


Figure 6.11: Distribution of temperature values generated from a Monte-Carlo simulation of one channel 10,000 times. A Burr distribution was used to describe the distribution of the values created; a normal distribution was not an adequate fit.

monochromator system paired with an integrating sphere measured absolute reflectivity of the material as a function of wavelength, see Figure 6.13. Over the wavelengths measured here, it can be seen the reflectivity of tin does not vary by more than 0.002 per nm, so over a particular wavelength band in the pyrometer a single emissivity value can be assumed. For each pyrometer band, a minimum and maximum allowable emissivity is then defined. Since spectral emissivity is known to change under shock conditions [80, 93, 94], the range of allowable values is relatively broad, approximately ± 0.1–0.2 for the reflectivity values measured and the bounds inferred for pyrometer 3 in this work.

Using the emissivity windowing scheme described above, along with judicious choice of pass-band wavelengths for a given temperature, a combined multi-channel analysis can constrain a pyrometric temperature measurement far better than the individual emissivity uncertainty of a single channel. Further, the comparison of the temperature range as a function of time recorded by each channel can be used to look for obvious transients or patterns of non-thermal light falling into a single channel.

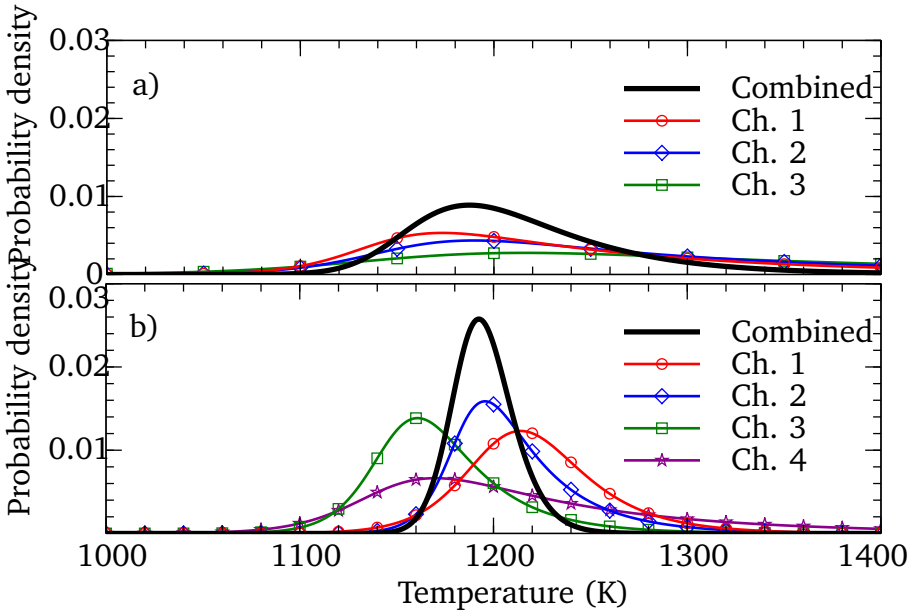


Figure 6.12: Plot illustrating the temperature distributions derived from Monte-Carlo analysis. Results from each channel are combined to give an overall temperature probability distribution. a) results from pyrometer 2 on experiment 2 b) results from pyrometer 1 on experiment 2.

The above spectral analysis for non-thermal light shows that, despite our measures to prevent it, contamination of the thermal radiance by non-thermal backgrounds was still observed. On each experiment, one or more channels were contaminated by a non-thermal signal. Non-thermal radiance was identifiable on the multi-channel system as the measured radiance spectrum violates any blackbody curve distribution. An example of identifiable non-thermal radiance is shown in Figure 6.10a; note that while Channel 2 sees a non-thermal signal for an extended duration, most of the channels see a non-thermal 'spike' at 1.35 μs. The identification of non-thermal radiance allows the data to be discarded for the purposes of temperature determination.

The cause of the non-thermal optical emission remains unclear. The emission did not consistently appear at a specific time, on specific experiments or have a specific temporal profile. It is noted that no non-thermal radiance signals were detected on channels sensitive to wavelengths of 1490 nm and above. The lack of consistency means it has not been possible to form a meaningful hypothesis for how to reduce the emission further.

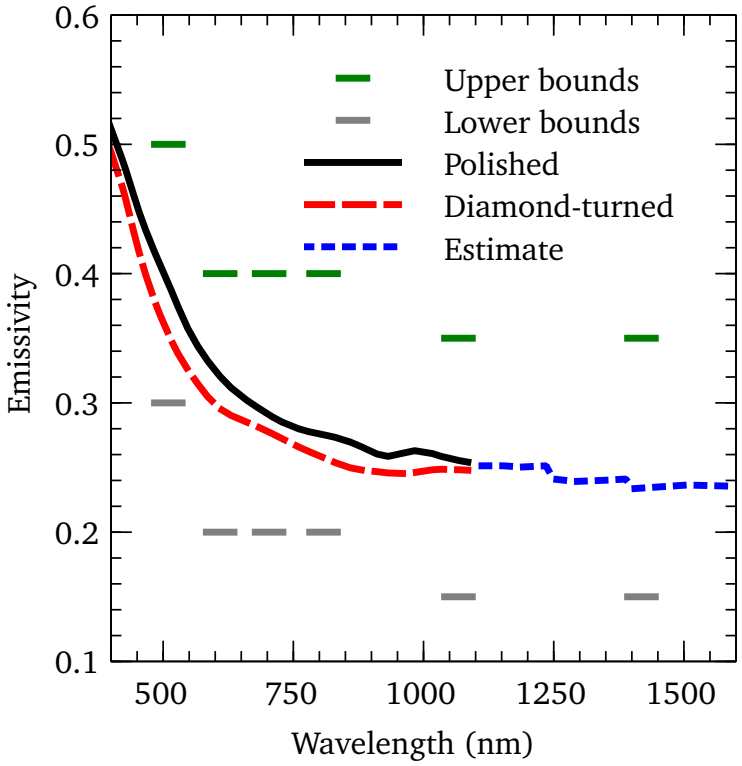


Figure 6.13: Measured tin emissivity (black, red curves), assumed emissivity (dashed gray curve), and chosen emissivity bounds (green and grey lines) for each NSTec/LANL pyrometer band, as a function of wavelength.

A selection of the clearest time resolved temperature data, calculated using the analyses discussed above, are shown in Figure 6.15, Figure 6.14 and Figure 6.10. Before conversion to temperature, the data from pyrometer 1 was down sampled to 1 ns resolution and band reject filtering was applied to data from pyrometer 2. A summary of the measured plateau temperatures for each system on every experiment is shown in Table 6.5.

	Temperature (K)		
Experiment	Pyrometer 1	Pyrometer 2	Pyrometer 3
1	1192 (1176–1208)	1214 (1150–1258)	1190 (1170–1230)
2	1197 (1179–1214)	1189 (1127–1234)	1200 (1170–1240)
3	1178 (1152–1204)	1163 (1110–1206)	1190 (1130–1250)
4	1224 (1210–1239)	1171 (1111–1213)	1180 (1150–1220)

Table 6.5: Summary of plateau temperatures determined during this set of experiments.

A summary plot showing the measured pressure and temperature points

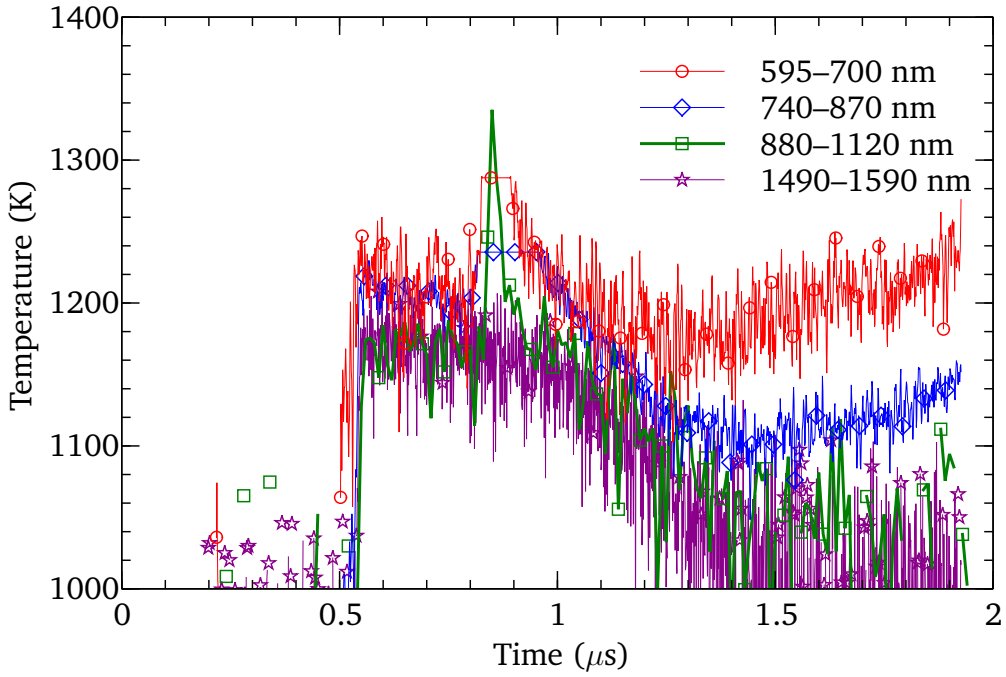


Figure 6.14: Time resolved temperature on experiment 2 from pyrometer 1 using literature emissivity values.

alongside the modelling results are shown in Figure 6.17. It can be seen that the measured temperatures appear to be approximately 55°K below that predicted by modelling.

6.7 Conclusions

Four multi-sample plate impact experiments have been conducted to compare the results of three different pyrometry systems simultaneously, a summary of the different capabilities of these systems is shown in Table 6.6. The results of the three systems agree within the uncertainty bounds of the systems. There was good agreement between the three systems despite significant differences in their spatial resolution, temporal resolution and system design. The agreement between the three systems should improve confidence in the technique of optical pyrometry in shock experiments.

It is noted, however, that the uncertainties of the three systems are not similar. Specifically, pyrometer 1 has a significantly lower uncertainty than the other

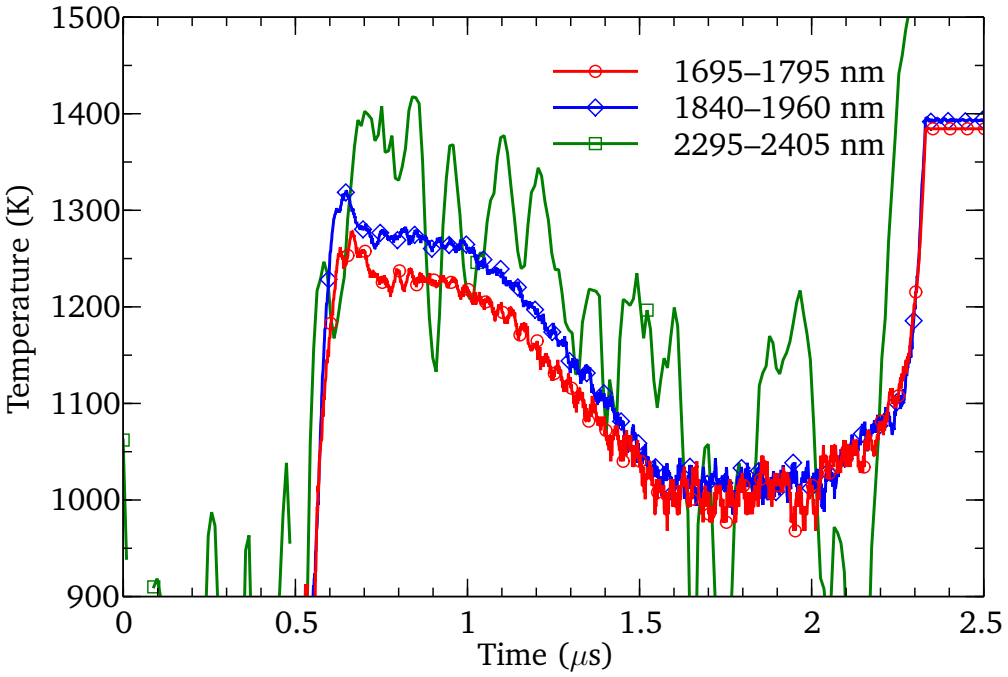


Figure 6.15: Time resolved temperature results from pyrometer 2 using literature emissivity values.

	Pyrometer 1	Pyrometer 2	Pyrometer 3
Spatial resolution (spot size)	10 mm	20 mm	2 mm
Detector bandwidth	400 MHz	100 MHz	300 MHz
Emissivity method	Monte-Carlo	Monte-Carlo	Windowed emissivity
Collection probe optics	Collimated	Collimated	Focused
Absolute error (K)	$\pm$ 19	$\pm$ 55	$\pm$ 35
Relative error (%)	$\pm$ 1.5	$\pm$ 5	$\pm$ 3

Table 6.6: Summary of selected capabilities of the different pyrometry systems.

systems. Pyrometer 1 was the system that was the culmination of the research and modelling discussed in the previous chapters. The superior performance provides validation of the value of the frameworks, models and experiments that have been presented.

The higher uncertainties of the other systems have been attributed to a number of causes. The higher uncertainty of pyrometer 2 has been attributed to the emissivity assumptions for the wavelength bands of that system; because emissivity is assumed to be lower at the wavelength bands used by pyrometer 2 the uncertainty in reflectivity results in a higher emissivity uncertainty (in percentage

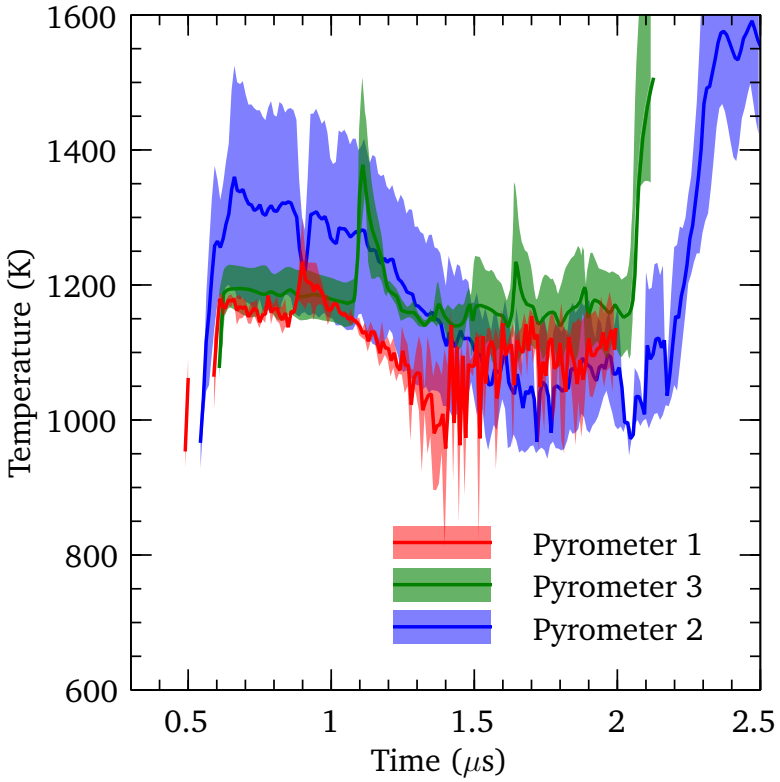


Figure 6.16: The calculated windowed temperature from three individual pyrometer bands produced by pyrometer 3, using measured emissivity values.

terms, see Appendix C.4). The higher error reported by pyrometer 3 is attributed to a more pessimistic approach to uncertainty analysis, however the confidence interval has not been specified. Given both the improved uncertainty and more rigorous understanding of the resultant uncertainty the Monte-Carlo approach is a helpful development to the application of pyrometry to shock experiments.

The variation in uncertainty between the three pyrometry systems was caused primarily by the emissivity assumption used. The analysis approaches detailed required various assumptions to be made about the emissivity of the sample and while it was felt that the assumptions can be justified, it is desirable to develop a way to measure emissivity dynamically to remove the need for these assumptions and reduce the uncertainty of the temperature measurements.

In addition to comparing the different systems, the results were compared with modelled temperature data. The comparison showed model temperatures were approximately 55°K above the average measured temperature. The uncertainties

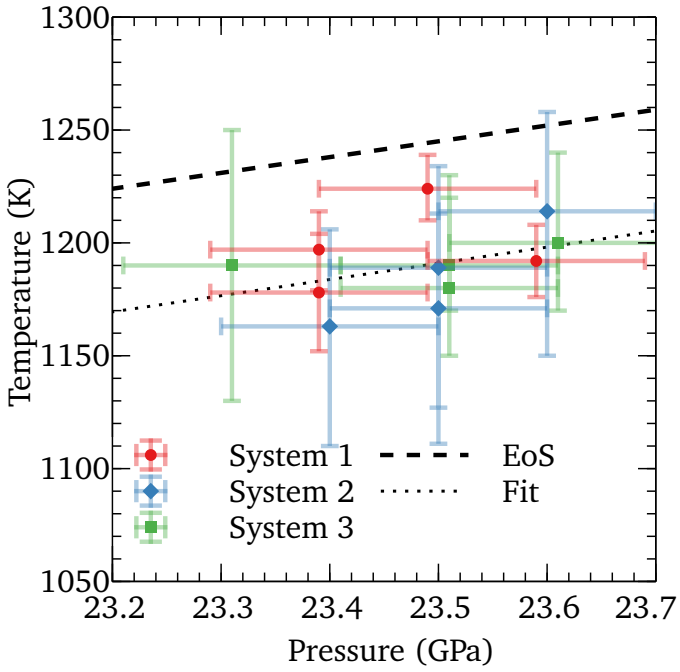


Figure 6.17: Summary plot showing all pressure and temperature results. The following offsets were applied to the pressure data for visual clarity: Pyrometer 1: –0.01 GPa, Pyrometer 3: +0.01 GPa. The fit was a linear regression applied to all points with no consideration of uncertainties.

associated with the measurements indicate that this difference is statistically significant. There are three previously discussed sources of error that could cause the difference:

- Errors in the emissivity assumptions could cause a systematic error with effects up to approximately ±20°K from bulk temperature.
- Thermal transport from the sample to the glue layer probably results in a discrepancy of approximately –10°K from bullk.
- Interface interactions between the sample and glue probably results in a discrepancy of +20°K from bulk.

In combination the sum of these effects does not appear to completely account for the difference between the model results and the experiment so the underlying cause of the discrepancy is not clear. It is possible that the assumptions these

perturbations are based on are incorrect, alternatively there could be inaccuracies in the equation of state.

The effects of non-thermal radiance (probably from the lithium fluoride window) remained an issue during this series of experiments, with a number of artefacts compromising a number of channels in each experiment. The cause of non-thermal emission remains uncertain as there appears to be little consistency in non-thermal emission behaviour despite high target-to-target and shot-to-shot repeatability. The measures taken to limit the production of non-thermal emission during these experiments did however reduce its effect sufficiently that meaningful temperature measurements were possible on most pyrometer channels.

7

Radiance measurements of lead (Pb) during plate impact

7.1 Introduction

Much of the previous research presented has focussed on understanding and validating a pyrometry diagnostic. The outcome of that research has validated the system that has been developed so an appropriate progression was to use the diagnostic to explore material behaviour. This chapter discusses the application of the diagnostic to measurements of a lead sample in plate impact experiments. Following an overview of the experimental details, temperature results using emissivity assumptions are presented. The results are potentially consistent with phase changes occurring during the experiment.

7.2 Experiment overview

Lead (Pb) is a material of interest for pyrometry applications because it undergoes amongst the most heating of a pure metal under shock compression. Lead also undergoes both a solid-solid phase change and solid-liquid phase change at pressures readily accessible to plate impact experiments on single-stage gas guns. Furthermore there is limited shock-temperature data on lead reported in the

literature and recent work reported by Mabire and Héreil[115] noted anomalous radiometry results. The radiometry results they reported were from a single experiment where lead was shocked to ∼50 GPa and released to ∼30 GPa. The measured radiometry profiles did not have stable post-shock plateaus. A number of potential explanations were suggested, with emissivity changes due to a phase change being a credible explanation. If a phase change was the cause the results may give insight into phase kinetics as the non-steady nature of the radiance data could indicate a phase transition occurring over timescales comparable to the plateau duration.

The purpose of these experiments was to collect more data on lead during plate impact loading at different pressures to gain further insight into the anomalous behaviour of lead.

7.2.1 Experiment design

The purpose of these experiments was to explore the temperature of lead under shock loading. This series of experiments used the 100 mm bore light gas gun at ISP to conduct plate impact experiments. The data that were desired from these experiments were simultaneous measurements of time-resolved apparent temperature and particle velocity from a single sample allowing determination of the state of the sample during shock plateau and release. The approach that was used to design this series of experiments is now discussed.

As with previously discussed experiments (see Chapters 5 and 6) lithium fluoride was chosen as the window material due to its well established suitability for pyrometry experiments.

For the impactor plate material tungsten heavy alloy was chosen as it is a material that can generate amongst the highest pressures on this facility, as discussed in previous chapters. Figure 7.1 shows $P-u_p$ projections of the Hugoniot curves for the relevant materials. The impact plate velocities chosen for these experiments were approximately 1450 m·s^{-1} and 1250 m·s^{-1}. As shown in Figure

7.1 this will create shock states of ∼35 GPa and ∼30 GPa, respectively, and release states of ∼23 GPa and ∼19 GPa.

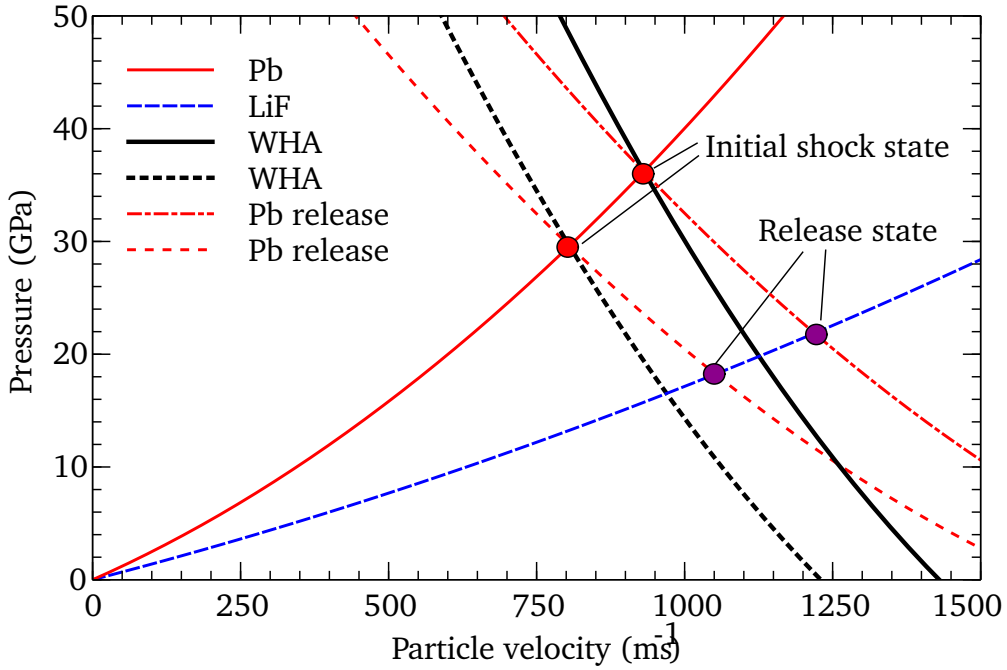


Figure 7.1: Impedance matching analysis to determine shock and release pressures when tungsten heavy alloy (WHA) impacts a lead–lithium fluoride target. The resultant pressure is determined by the intersection of the sample line with the other material.

In addition to the impedance matching calculations, temperature calculations have also been conducted using the approach described in Appendix C.3. The predicted temperatures for these impacts were 1620°K for 1450 m·s^{-1} and 1260°K for 1250 m·s^{-1}. Combining the impedance matching calculations and temperature calculations allows the states that occur in the experiment to be shown in temperature-pressure space, see Figure 7.2.

In addition to the P-T states generated in the experiment, the locus of P-T states has been calculated using a linear fit to the Hugoniot in Marsh [89]. Similarly the locus of shock-release states using the Hugoniots of lead and lithium-fluoride in Marsh [89] has been calculated; both the shock Hugoniot and shock-release states have been added to Figure 7.2. Additionally, the melt curve [116] and solid-solid phase boundary (face-centered cubic to hexagonal close-packed) [117, 118] have been added to Figure 7.2. It can be seen that both the shock and

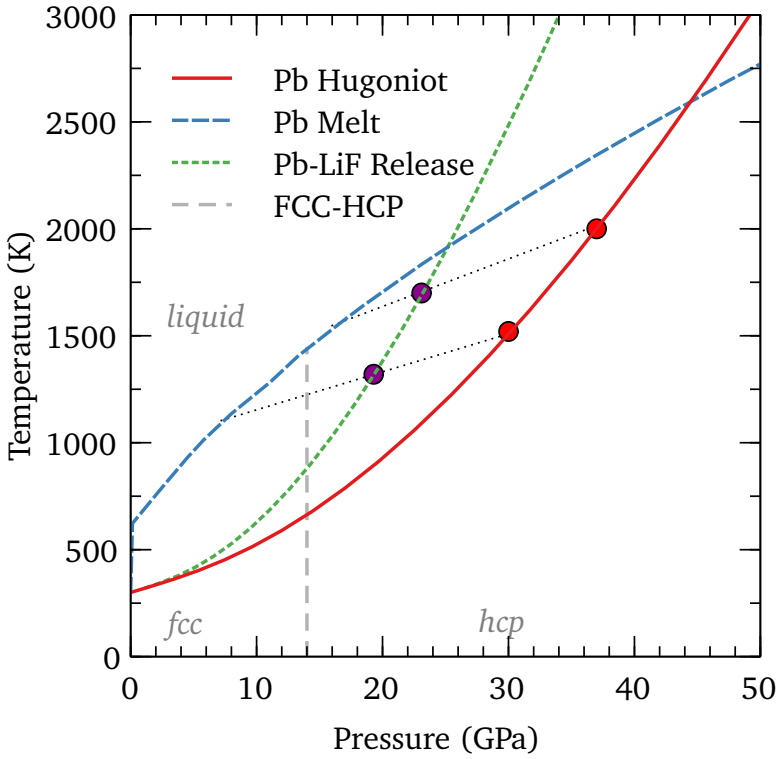


Figure 7.2: Pressure-temperature phase diagram for lead in the region of the states expected to be generated in this experimental series. 'Pb Hugoniot' was calculated from the Marsh[89] linear fit Hugoniot. 'Pb Melt' used data from Cricchio *et al.*[116]. 'Pb-LiF Release' was the locus of release states using linear Hugoniots of Pb and LiF in Marsh[89]. 'FCC-HCP' is the phase boundary reported by Kuznetsov *et al.*[117]

plateau release states are expected to be in the h.c.p phase. However, during the slower release rate phase the higher states generated by the higher velocity impact will release to the melt boundary but the lower velocity states will pass though the solid-solid phase change.

An aspect that is not indicated on Figure 7.2 is the time scales over which the material's state changes. For example, the transition from the Hugoniot state to the release state occurs almost instantaneously as the shock in the lead reaches the Pb-LiF interface. In contrast, release below the interface pressure occurs at a release rate of approximately $\sim$20 GPa$\cdot\mu s^{-1}$ because it is due to rarefaction waves from the rear of the impact plate.

A complication to the use of lead as a target material is that it is toxic, thus various containment measures were necessary to conduct the experiments safely.

Specifically, the containment tank was enclosed in an additional tent to prevent the escape of lead particulate which poses a poisoning risk. Furthermore any ports in the containment tank were modified to seal under internal pressure (previously only a vacuum seal had been required). To demonstrate the correct implementation of these various measures a non-toxic test shot was required; a preliminary experiment with tin as the sample material was used for this demonstration.

7.2.2 Target geometry

The geometry of the target design was a compromise between numerous factors. The lead sample was chosen to be 65 mm diameter, 3 mm thick with a LiF window 40 mm diameter, 5 mm thick. The lead target was held onto the gun fixture using a 120 mm diameter Al disc; the Al disc provides a rigid platform for mounting the target. As in the comparative plate impact experiments, tungsten slurry was used to suppress lithium fluoride luminescence, see Section 6.3.2. This arrangement is shown in Figure 7.3.

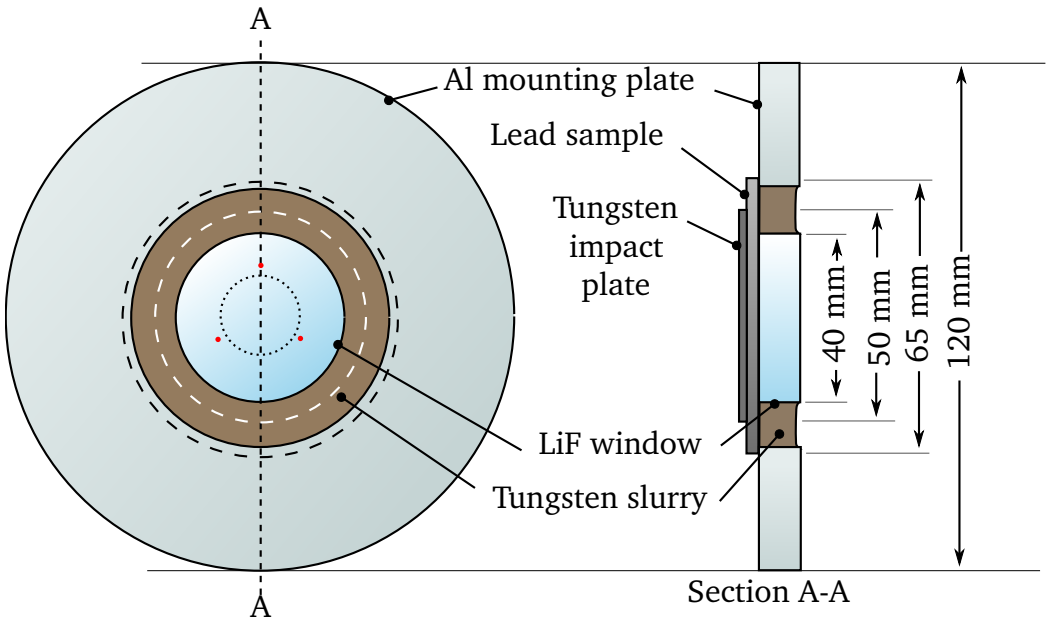


Figure 7.3: Scale drawing of the target layout (flyer plate at impact time is also shown). The black dotted line shows the pyrometry collection area. Red spots indicate PDV measurement locations. The white dashed line indicates the flyer footprint on the target.

The impactor plate was 50 mm diameter, 2 mm thick. The trigger event in these experiments was provided by a Dynasen piezo probe that was mounted to be in contact with the rear surface of the tungsten slurry.

It was relevant to consider the 1D duration due to lateral releases because results during the release stage of this experiment are of interest. The pyrometry collection area is approximately 20 mm diameter so the perimeter of the collection is 10 mm from the LiF window edge. Of the interface materials LiF has the highest acoustic wave speed so, assuming a release travels at the longitudinal sound speed of 6.56 mm·μs^{-1} [119], the collection area should be unperturbed for a duration of 1.52 μs.

The tin preliminary experiment was a similar configuration but the sample was 50 mm diameter, 3 mm thick with a 25.4 mm diameter, 10 mm thick LiF window.

7.2.3 Target assembly

The samples and lithium fluoride window were bonded together using the Loctite 326 adhesive. A 2 kg weight was applied to the discs during adhesive setting. Next Loctite 3421 was used to bond the sample to the aluminium mounting plate; again a 2 kg weight was applied to the discs.

It is not possible to use diamond turning machining processes on lead, so high precision machining was used to create a surface as smooth as possible. However, this surface was not optically smooth and had visible machining marks.

To prevent any flashes external to the target assembly from compromising the pyrometry data blackout foil was added around the pyrometry head and window.

7.2.4 PDV diagnostic

Shock arrival time and particle velocity measurements were implemented using a photonic Doppler velocimetry (PDV) system. The nominal positions of the probes are shown in Figure 7.3. The arrangement of the PDV probes meant that the time-of-arrival of the shock at the sample-window surface could be determined. Furthermore, because time-of-arrival was measured at multiple locations, tilt

could also be determined. Light was delivered and collected using collimated probes with a 90 mm working distance (AC Photonics 1CL15P090LCGS1/CPT2).

7.2.5 Radiometry system

The radiometry system design was further developed prior to these experiments. Specifically, the availability of avalanche photodiodes allowed the sensitivity of three channels to be increased. The nominal wavelength bands and detector configuration are shown in Table 7.1 with the details of the filters shown in Table 7.2. A schematic of the layout of the radiometry system is shown in Figure 7.4. The radiometer was calibrated before each experiment with the optical head that was used for that experiment, as described in Appendix A.1.

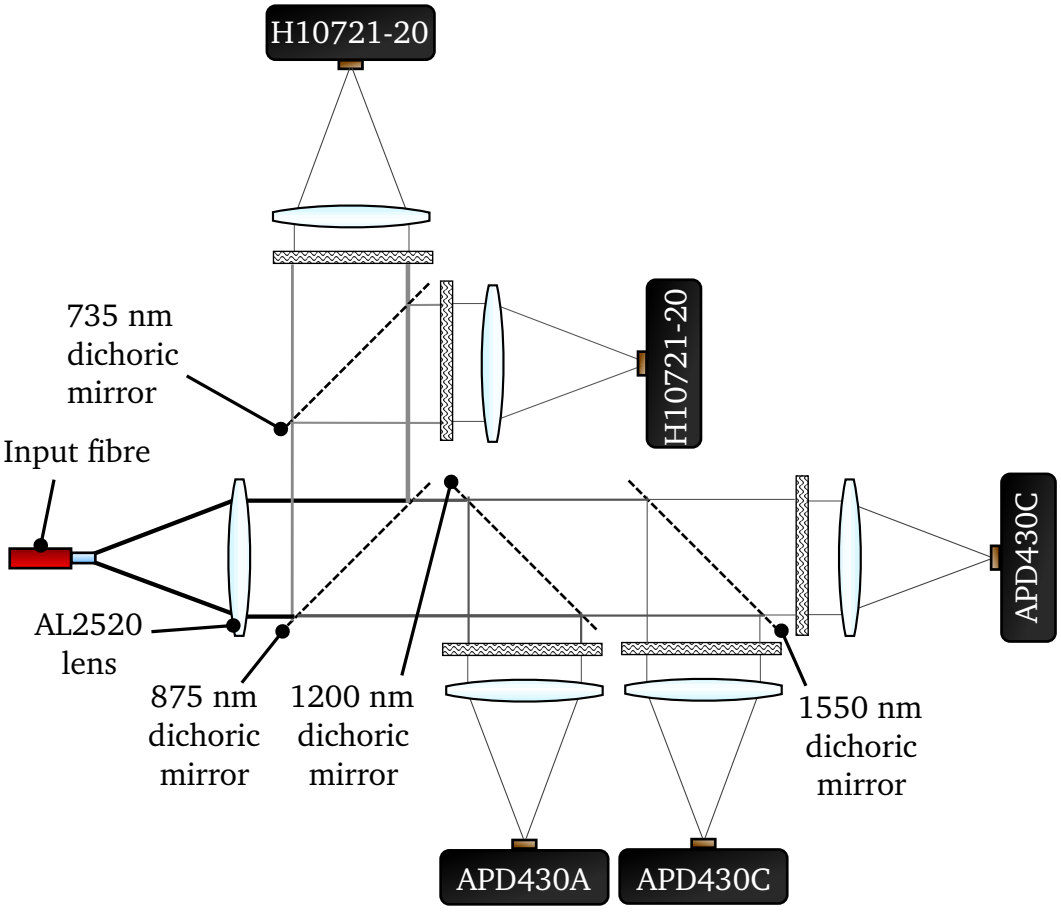


Figure 7.4: Schematic of the radiometry system used for the lead experiment series.

Channel	Nominal wavelength band (nm)	Detector
1	600–700	Hamamatsu H10721-20
2	720–870	Hamamatsu H10721-20
3	884–1118	ThorLabs APD430A
4	1250–1550	ThorLabs APD430C
5	1582–1684	ThorLabs APD430C

Table 7.1: Table summarising the configuration of the radiometry system for the second experiment.

Channel 1	Channel 2	Channel 3	Channel 4	Channel 5
FF875-Di01	*FF875-Di01*	FF875-Di01	FF875-Di01	FF875-Di01
FF735-Di02	FF735-Di02	*Edmund 1200 LP*	Edmund 1200 LP	Edmund 1200 LP
FF02-650-100	FF02-795-150	—	*ThorLabs BLP01-1550R*	ThorLabs BLP01-1550R
—	—	—	—	FF01-1538-82

Table 7.2: Table summarising the filters in place on each channel in the radiometer system. Italics are used for filters that are reflected from, rather than transmitted through the filter.

7.3 Results

A summary of the experiments in the series with sample material, projectile velocity, interface velocity and pressure are shown in Table 7.3.

7.3.1 Experiment 1, Sn sample, 1556 m·s^{-1} impact

The first experiment used a tin sample and was primarily to demonstrate the efficacy of the containment measures that had been implemented to allow the use of lead. In this respect the experiment was a success, no substantial issues

Experiment	Sample material	Projectile velocity (m·s^{-1})	Interface velocity (m·s^{-1})	Interface pressure (GPa)
1	Tin	1556 ± 6	1376 ± 1	25.4 ± 0.1
2	Lead	1433 ± 3	1274 ± 1	23.1 ± 0.1
3	Lead	1233 ± 2	1103 ± 3	19.3 ± 0.1

Table 7.3: Table showing the sample materials and projectile velocities in the lead series of experiments.

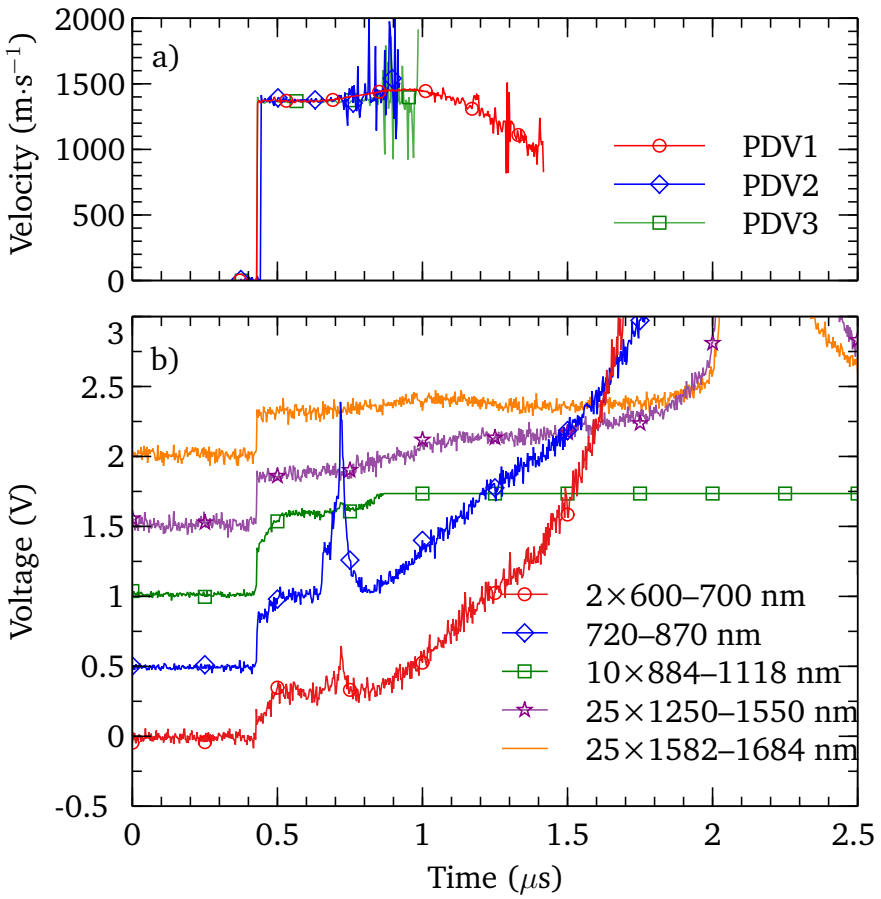


Figure 7.5: a) Plot of particle velocity data at the tin-lithium fluoride interface from experiment 1. The velocities are corrected using a window correction factor [103]. b) Plot of raw output from the detectors in the radiometer. Voltages are scaled (see legend) and offset (0.2 V) for clarity.

with the containment systems were found.

The results from the three PDV channels viewing the sample-window interface are shown in Figure 7.5a. It can be seen that there is a prompt rise in velocity at shock breakout followed by a plateau of approximately 300 ns duration. Two of the channels then drop out and channel 1 shows an increase in velocity. Based on the flyer and window thickness it could be expected that the velocity profile should be a plateau followed by a release however, due to the small diameter of the LiF window, lateral releases obscure the expected behaviour.

The output from the pyrometry channels is shown in Figure 7.5b. Three of the channels (600–700 nm, 720–870 nm and 884–1118 nm) reveal a rise in signal following shock breakout believed to be due to extraneous light . Also visible on

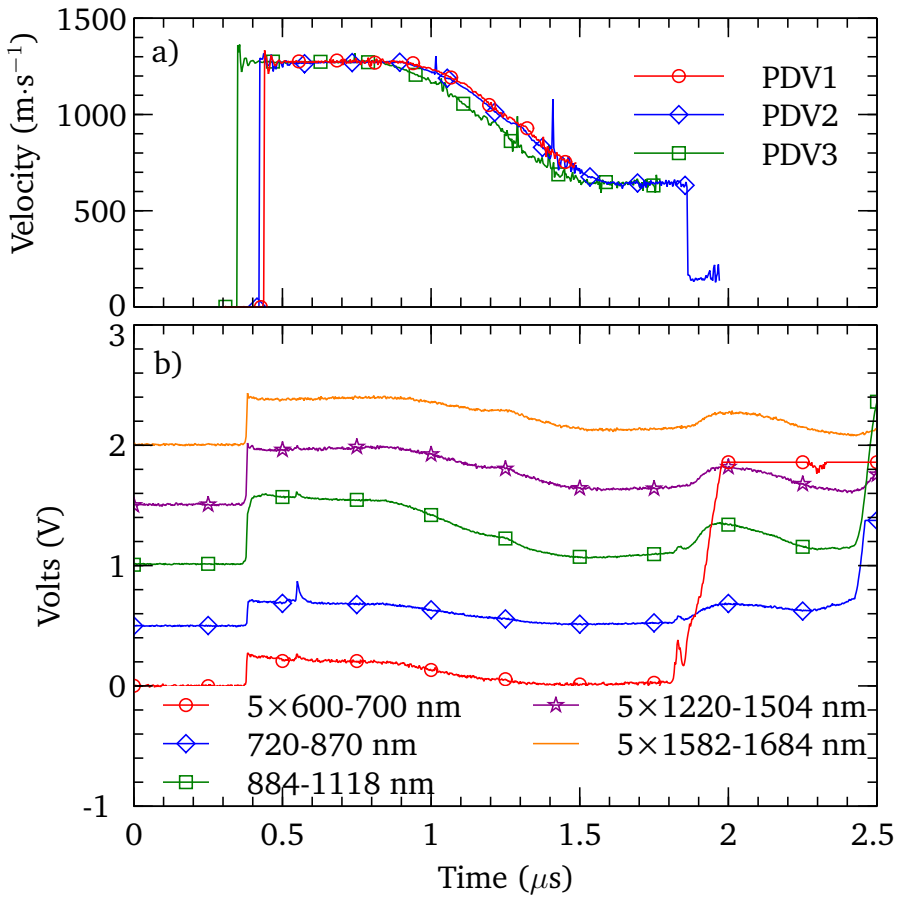


Figure 7.6: a) Plot of particle velocity data at the lead-lithium fluoride interface from experiment 2. The velocities are corrected using a window correction factor [103]. b) Plot of raw output from the detectors in the radiometer from experiment 2. Voltages are scaled (see legend) and offset (0.5 V) for clarity.

the 600–700 nm and 720–870 nm is an intensity 'spike' approximately 200 ns after shock breakout. These features are unsurprising as they were seen in the comparative plate impact experiments and the same experimental procedures were followed for these experiments.

7.3.2 Experiment 2, Pb target, 1433 m·s^{-1} impact

Following the successful demonstration of the lead containment system, it was possible to safely conduct the plate impact experiments with lead. The PDV results from the experiment are shown in Figure 7.6a. The results show a sharp rise at shock breakout followed by a 400 ns plateau with a smooth release from the rear of the impact plate, consistent with expectations.

Voltage data from the five radiometer channels are shown in Figure 7.6b. The voltage profiles appear largely consistent, although the 884–1118 nm channel appears to have an artefact shortly after shock breakout which produces an apparent slow in rise-time. Intensity spikes are also visible on the three lowest wavelength channels, although due to the higher signal levels they are less noticeable than on the previous tin experiment.

7.3.3 Experiment 3, Pb target, 1233 m·s^{-1} impact

PDV results from the experiment are shown in Figure 7.7a. The results show a sharp rise at shock breakout followed by a 400 ns plateau with a smooth release from the rear of the impact plate—consistent with expectations.

Voltage data from the five radiometer channels are shown in Figure 7.7b. The two shortest wavelength channels saturated the digitiser leading to data loss immediately after shock break-out, however the channels subsequently recover to record data. Despite this, the voltage profiles appear largely consistent with a general downward trend. Significant intensity spikes are not visible.

7.3.4 Analysis of experiment 1

PDV results from experiment 1 indicate a plateau velocity of 1376 $\pm$ 1 m·s^{-1}. Using the Marsh parameters for the Hugoniot of LiF [89], the interface pressure is calculated as 25.4 $\pm$ 0.1 GPa.

Temperature analysis of experiment 1 was conducted using the assumption that the emissivity of tin at room temperature and pressure were representative of the high pressure state. The results of temperature analysis are shown in Figure 7.8.

The temperature data reflects the extraneous light seen in the unprocessed voltage data. The three shortest wavelength channels have higher apparent temperatures, do not appear to remain a constant value during the plateau and, furthermore, the temperatures are not consistent. The two longer wavelength channels appear to agree with each other and show an approximately constant temperature for the duration of the plateau. Given the inconsistent radiance

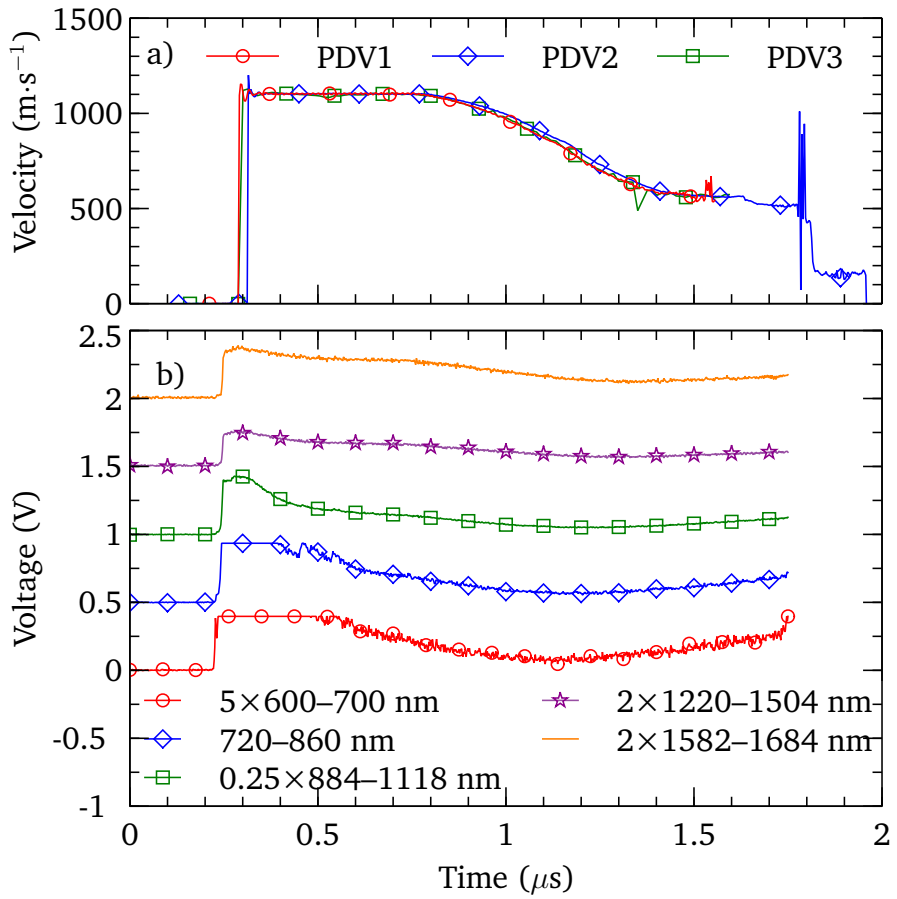


Figure 7.7: a) Plot of particle velocity data at the lead-lithium fluoride interface from experiment 3. The velocities are corrected using a window correction factor [103]. b) Plot of raw output from the detectors in the radiometer from experiment 3. Voltages are scaled (see legend) and offset (0.5 V) for clarity. The flat features on the 720–860 nm and 600–700 nm channels are due to digitiser saturation.

results and the safety validation nature of the experiment no further analysis has been conducted.

7.3.5 Analysis of experiment 2

The interface pressure and apparent temperature are shown in Figure 7.9. The temperature calculation of the sample assumed the emissivity of the sample is given by liquid lead [120].

As seen in other experiments an intensity spike causes an increase in apparent temperature on shorter wavelength channels approximately 200 ns after shock breakout. Particularly notable is that the plateau region is not flat, furthermore

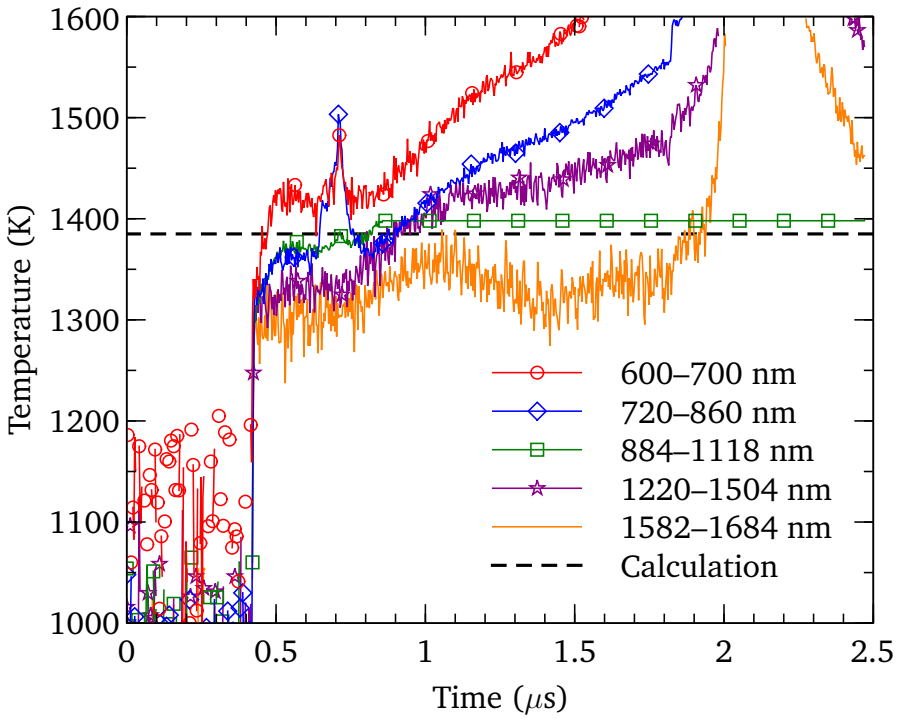


Figure 7.8: Plot of apparent temperatures recorded during experiment 1. It can be seen shock breakout causes a sharp increase in apparent temperature. The apparent temperatures are not consistent due to LiF luminescence. The calculated temperature of 1,385 K is also shown.

the gradients of the different wavelengths are different, some are positive, some are negative. Clearly differing gradients of temperature, on the same sample, are not physically consistent and no constant emissivity assumption will be able to reconcile the temperatures calculated from the different channels. It is believed the most plausible explanation is that the emissivity of the sample is changing during the measurement. Additional evidence for this explanation is that the multiple traces appear to converge over time. The convergence of the traces could indicate that, while initially the emissivity assumption is incorrect, the emissivity of the sample changes to those of molten lead over the course of the experiment.

Also notable is the convergence occurs at approximately the same time as an inflection point in all the temperature traces. The velocimetry data indicates that pressure is dropping during the plateau which would be expected to result in adiabatic cooling unless a phenomenon such as a phase change is occurring.

The apparent temperature was also calculated using an assumed emissivity

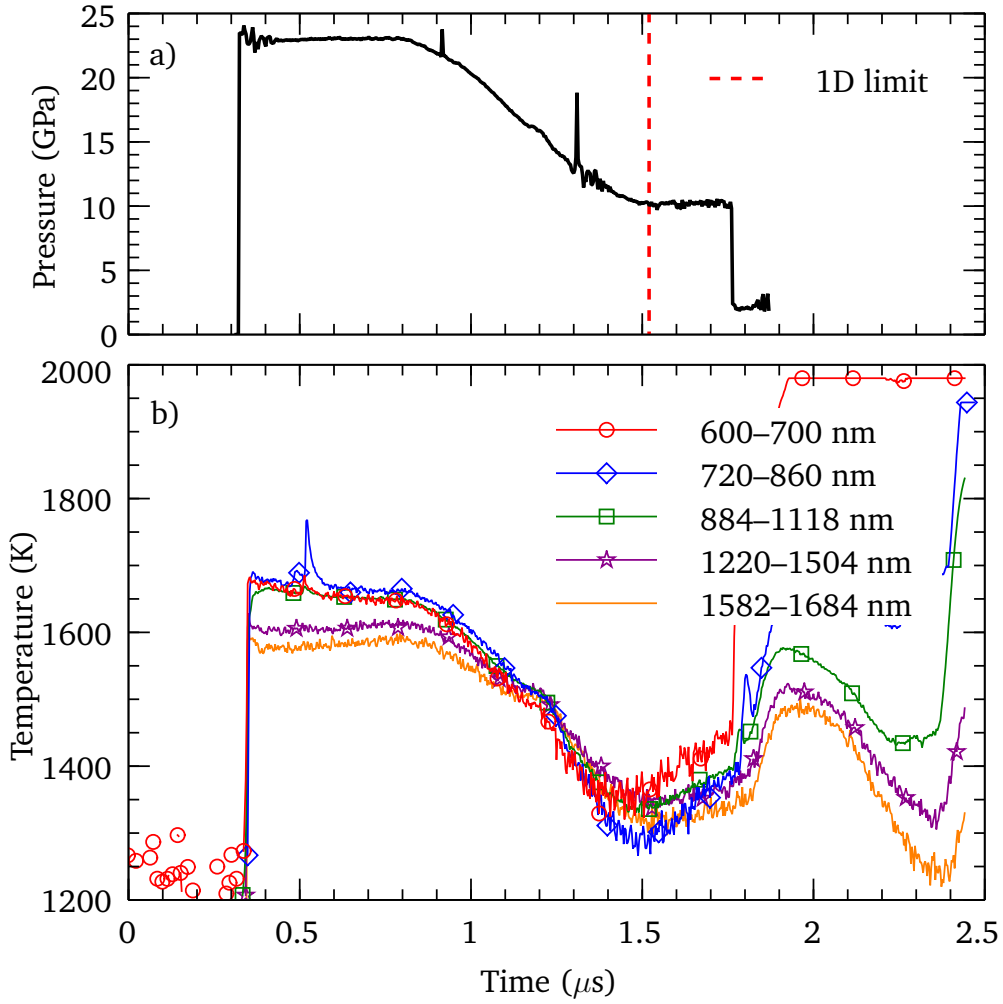


Figure 7.9: a) Plot of time-resolved pressure data derived from LiF EoS [89] and interface velocity data. b) Plot of apparent temperatures recorded during experiment 2 using the assumption that emissivity is given by molten lead [120].

given by solid lead, see Appendix D.3. It can be seen that the apparent temperatures produced are highly inconsistent, see Figure 7.10a. Another calculation using an arbitrary emissivity assumption, which ensures each channel has the same temperature shortly after shock breakout, is shown in Figure 7.10b. It is clear that, despite the initial agreement, the results diverge. Using an arbitrary emissivity to generate matching temperatures also shows that, within broad limits, any desired temperature can be attained with an appropriate emissivity assumption, thus while it is possible to generate dynamic emissivity values if these are unconstrained the results will not produce meaningful insight.

Another possible explanation for the differing apparent temperatures between

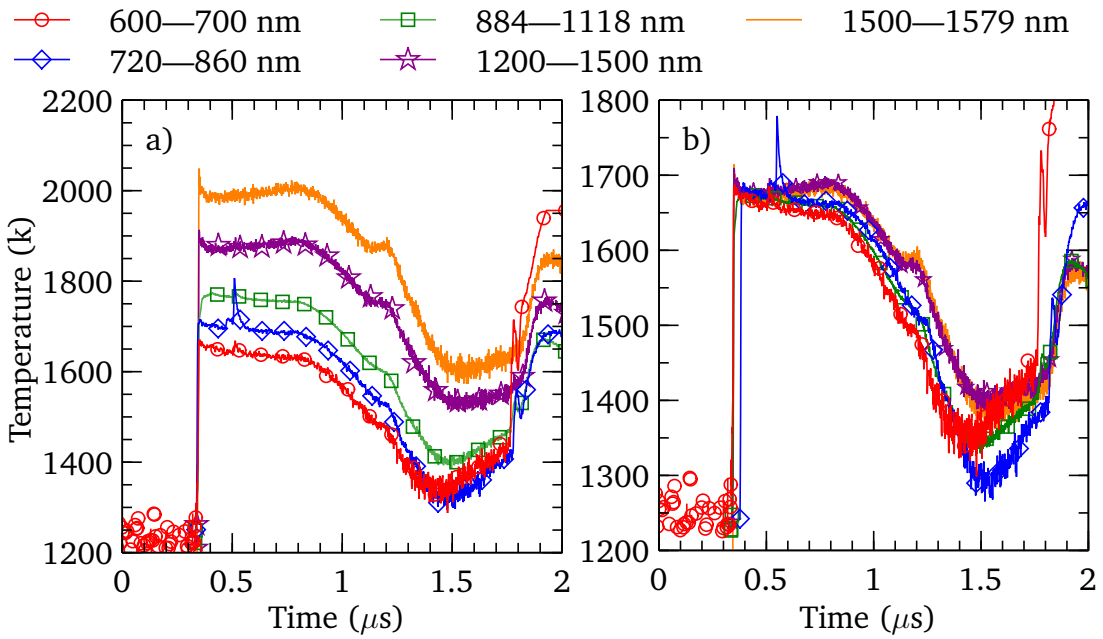


Figure 7.10: a) Plot of apparent temperatures recorded during experiment 2 using the assumption that emissivity is given by solid lead, see Appendix D.3 b) Plot of apparent temperatures recorded during experiment 2 using an arbitrary emissivity assumption that gives matching temperatures shortly after shock breakout.

the wavelengths is that extraneous light is responsible for the difference, although it is unlikely the extraneous light would have the required spectral and temporal profile to cause the discrepancy.

An estimate of the effects of heat transport and the glue interface were not calculated as they are relatively minor in comparison to the 150°K span of apparent temperatures in the plateau region.

7.3.6 Analysis of experiment 3

The apparent temperature of the lead-LiF interface was calculated using the assumption of a sample emissivity equivalent to solid lead at room temperature and pressure, these results are shown in Figure 7.11. It should be noted this is a different assumption to that used in experiment 2 (where liquid emissivity properties were assumed). Following inspection of the results of the temperature analysis, two points are apparent:

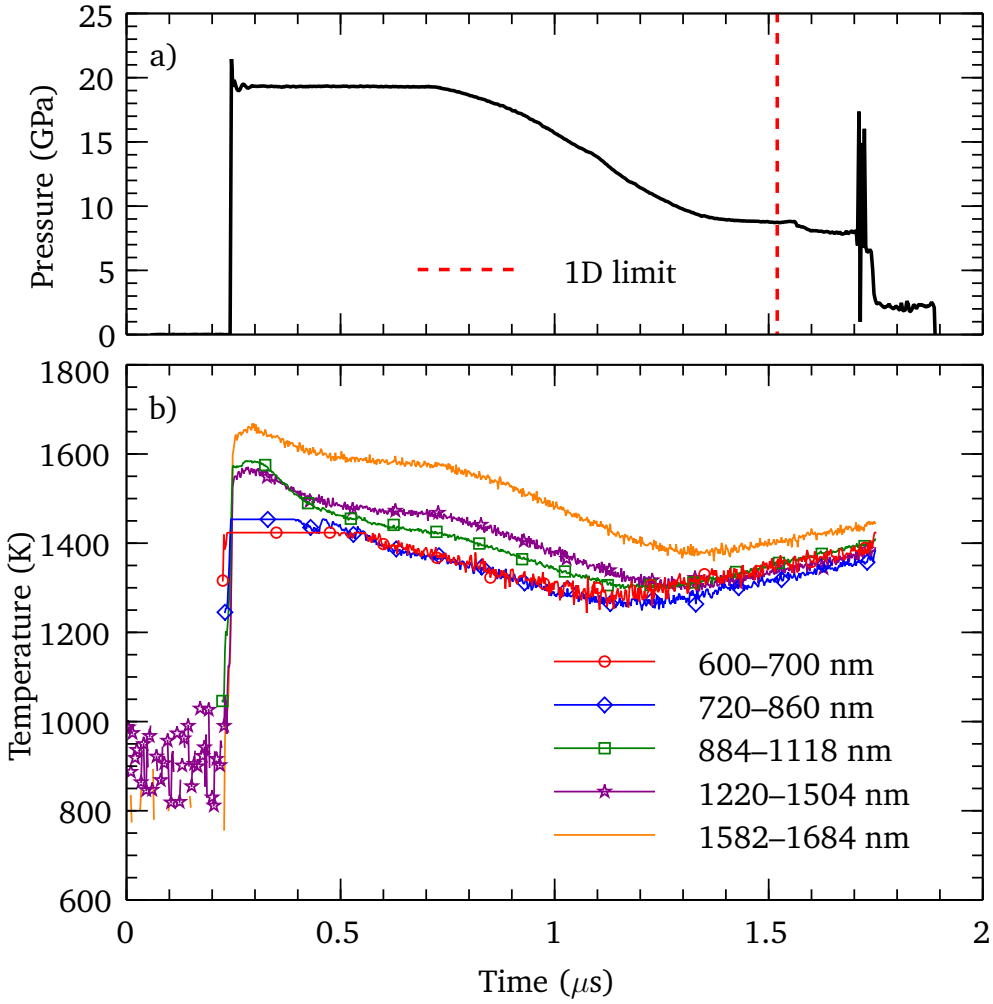


Figure 7.11: Plot of apparent temperatures recorded during experiment 3. It was calculated that the temperature would rise quickly then plateau at approximately 1,400 K. Here all channels saturated very quickly. Solid emissivity.

- If the 1582–1694 nm channel is ignored, the temperature results appear to show initial agreement, followed by a divergence before re-converging.
- The apparent temperature does not reach a steady state and is continuously changing.

A potential explanation for this diverging and converging behaviour is that the sample undergoes a phase change, with associated changes in emissivity, before returning to the initial phase. The convergence during the release coincides with a pressure of approximately 14 GPa (where the phase change has been reported in DAC measurements), furthermore there is potentially a 'kink' in the

PDV data that coincides with this pressure (modelling is required to determine the cause of this feature).

The lack of a stable plateau is compatible with the phase change explanation. If the kinetics of the phase change mean it is not abrupt, the emissivity and apparent temperature could be varying over the time scale of the plateau.

7.3.7 P-T phase diagram

An alternative way to visualise the results from the experiments is to plot the range of temperatures measured in the experiment across all channels against the interface pressure, as determined using PDV data and the LiF equation of state. This visualisation of the data is shown in Figure 7.12. Based on this analysis it appears that there is some discrepancy between the literature data and the measurements in these experiments. The results from experiment 2 show a temperature lower than predicted, but there is a visible kink at approximately 16 GPa in the release path that appears to transition from following the release adiabat to the melt line. There are also discrepancies with experiment 3, the temperature appears higher than expected and appears to cross the melt boundary.

7.4 Summary

Pyrometry measurements of lead samples undergoing shock compression in plate impact experiments have been made. The temperatures inferred from the thermal emission of the samples are not consistent when emissivity values for lead at standard temperatures and pressures are used. Furthermore, despite the relatively small range of pressures investigated in this experimental series, constant emissivity values that result in consistent temperatures could not be identified.

Temperature analysis has been conducted using literature emissivity values but due to the uncertainty in the actual emissivity values, a conservative approach to estimate uncertainty has been used. Specifically, temperature has been calculated using literature emissivity assumptions with a $\pm 10\%$ scaling and the emissivity

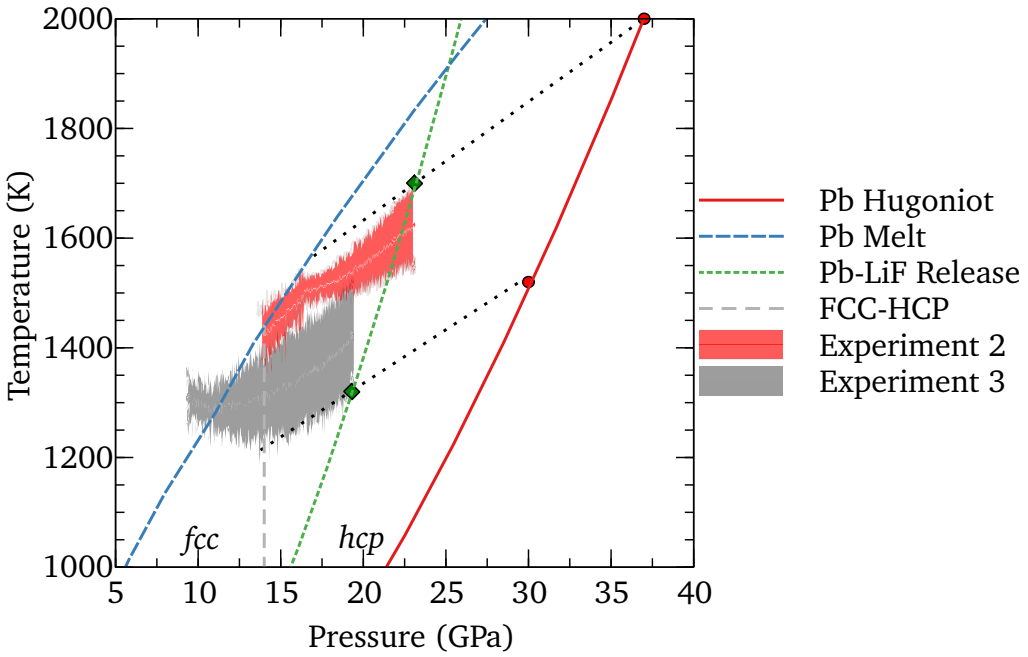


Figure 7.12: Apparent temperature ranges (*i.e.* maximum and minimum temperatures across all channels) recorded during experiments plotted against interface pressure from experiments 2 and 3. Red dots indicate the predicted shocked state of the material. Green squares indicate predicted equilibrium release state.

Experiment	Interface pressure (GPa)	Temperature (K)
2	23.1 ± 0.1	1610 ± 100
3	19.3 ± 0.1	1340 ± 120

Table 7.4: Table showing lead temperatures measured during the plateau region of the experiment. The emissivity was assumed to be the literature values scaled by ±10%, with the result which produced the widest range of temperatures being used.

values that produce the largest range of temperature used. The results of this analysis are shown in Table 7.4.

The lack of consistency between channels viewing the same target may be indicative of phase changes in lead that result in changes in the emissivity of the sample. Some key data that would improve understanding of the radiance data presented here would be measurement of the optical properties of the h.c.p. phase of lead; no data in the present literature could be identified.

8

Measurement of reflectivity at high strain rate

8.1 Overview

This chapter first discusses the importance of reflectivity measurements to support pyrometry measurements. Potential solutions for the measurement of reflectivity are discussed before reporting results from laboratory and dynamic tests. Ultimately, reflectivity was successfully measured in a dynamic experiment.

8.2 Importance of emissivity measurements

In Chapter 2 an equation describing Planck's Law was introduced (Equation 2.1). That statement of Planck's Law is strictly only true for a blackbody; for most cases it is necessary to consider the emissivity, ϵ, of the emitting material. A blackbody is an ideal emitter with an emissivity of 1; for most materials the emissivity is usually lower. When the effect of emissivity is included, Planck's Law is modified as follows:

$$L_\lambda(\lambda, T) = \epsilon(\lambda, T, P)\,\frac{2hc_0^2}{\lambda^5}\frac{1}{e^{\frac{hc}{\lambda k_B T}} - 1}. \tag{8.1}$$

From Equation 8.1 it can be seen that emissivity acts to scale the blackbody emission. To fully understand the effect of emissivity on the light emitted by

a hot material, and hence how to accurately determine temperature from a radiance measurement, it is necessary to know how emissivity varies with a number of parameters.

The most relevant parameters that affect emissivity, in the context of applying spectral band pyrometry to high strain rate experiments, are wavelength, pressure and temperature. It is clear from emissivity measurements of various materials that, for the vast majority of materials, emissivity varies with wavelength, see Appendix D.2 and D.3 for some examples. Specifically, given the wavelength ranges used in the systems developed here (approximately 1000 nm range in the visible/infrared portion of the spectrum) emissivity is expected to vary significantly between spectral bands.

Furthermore, the emissivity of a material, at a fixed wavelength, is a function of both the pressure and temperature state of the material. As both pressure and temperature will change significantly in high strain rate experiments it is difficult to justify an assumption that the emissivity will remain the same value as that measured at room temperature and pressure. Given the importance of emissivity to the pyrometry technique, measurement of emissivity is essential to reduce systematic errors.

A straight forward approach to determine the emissivity of a material is to employ Kirchhoff's Law of thermal radiation [121] which states that the emissivity of a surface is equal to it's absorbance. Defining absorbance as the complement of reflectivity it follows that for a opaque material (where transmittance is negligible) reflectivity, r and emissivity are related by the simple relation:

$$r = 1 - \epsilon. \tag{8.2}$$

Thus in an experimental setting measuring reflectivity can be the easiest way to determine emissivity. In the simplest case, of a static environment, reflectivity can easily be determined by illuminating the target surface then measuring the intensity of light reflected from the surface. Any changes in the light measurement

can be used to deduce a relative change in reflectivity. Independent measurement of sample reflectivity during pyrometry measurements is not a new idea. Commercially available pyrometers have offered this feature for many years (Pyrofiber E10). However both the commercially available systems and most of those reported in the literature are unsuitable for the rapidly evolving, high speed conditions present in high strain rate experiments. The primary issues are insufficient time resolution and inability to consistently measure a dynamically evolving sample.

For high strain rate experiments sub-μs time resolution is required; this time resolution should be attainable as high speed optical detectors are readily available. Consistent dynamic measurements are more complex. It is inevitable that when objects undergo high strain rate loading changes in tilt and surface finish can occur. Furthermore, emissivity is a function of surface finish as well as the intrinsic material properties. Thus a system that rigorously measures reflectivity must be able to function under these non-ideal conditions.

There are relatively few reports in the literature of relevant reflectivity diagnostics despite the significant improvement in confidence a reflectivity measurement would add to high-speed optical pyrometry.

8.3 Review of high speed reflectivity literature

Some of the earliest attempts to determine the reflectivity of shocked surfaces used the assumption that drops in signal in existing optical diagnostics, such as Fabry-Perot, were due to changes in the reflectivity of the material. While the measured drop in signal level did fall with increasing shock pressure the mechanism for this is not entirely clear. Although a reduction in material reflectivity could explain a drop in the collected signal, such decreases could also be attributed to variations in tilt or surface finish or both.

More recent measurements of reflectivity in shock experiments have attempted to address these issues in a couple of different ways. One popular solution is to use an integrating sphere to minimise any issues due to changes in the

geometry of the target (including tilt, bending and surface finish). The first reports of using an integrating sphere to measure reflectivity during a shock experiment were by Partouche-Sebban and Pélissier [122]. While this technique provides high confidence that changes in signal level are due to changes in sample reflectivity rather than ancillary experimental effects there were some issues in the implementation reported.

One of the most significant issues with Partouche-Sebban and Pélissier's approach are the relative wavelengths of the pyrometry and reflectivity measurements. The pyrometry measurements use a range from 0.4 μm to 4 μm, while the reflectivity measurement is made at 0.532 μm. The reflectivity of bismuth varies by up to 0.2 over the wavelength range of the pyrometry measurements [123]. While the wavelength dependent emissivity is addressed by means of an analytical model, which shows good agreement at 0.532 μm and produces self consistent results, there is no data at longer wavelengths to validate the model predictions.

More recent work by Seifter *et al.*[124] has attempted to address this by making reflectivity measurements at a range of wavelengths, again using a integrating sphere to ensure that the changes in measured intensity are due to changes in surface reflectivity. The method consists of using a well characterised 'glower' (a metal coil heated by means of a electric current) to illuminate the integrating sphere. By ensuring that the signal level from the glower is sufficiently high the radiance from the sample can be ignored. This is an extremely thorough approach to measuring emissivity but suffers from the drawback that the technique precludes pyrometry-based temperature measurement.

The approach reported by Partouche-Sebban and Pélissier has been expanded by La Lone *et al.*[80], who have made both reflectivity and pyrometry measurements with a similar system. The only criticism of this approach is that separate experiments are required for each measurement thus the system relies on good shot-to-shot repeatability and also requires, at least, two experiments for each measurement.

One solution that would enable reflectivity and pyrometry on a single experiment is to trigger the light source so that it quickly illuminates the sample in the 1D period but after sufficient time has passed to enable a pyrometry measurement to be made. Such an approach was reported by Poulsen and Hare [125] where a Xenon flash-lamp was used. The system they report does not employ a integrating sphere, rather the sample is illuminated by optical fibres coupled to the flash-lamp; separate optical fibres collected the light emitted. It was reported that the main issue with this approach was that the system did not appear to reach a quasi-static state after shock arrival, this made it difficult to extract the reflectivity signal particularly given the long duration of the flash illumination ($\sim$10 μs).

A sensible development of a reflectivity based approach is to use an illumination source that could be modulated at high speed; this would allow illumination pulses both pre-shock and post-shock and should make separation of the reflectivity and pyrometry signal simpler. While this appears straight-forward in principle there are a number of practical issues that need to be resolved. The primary issue is the creation of light at a wide range of wavelengths. The traditional source used to create a well defined, broad band spectrum (for pyrometer calibration *etc.*) is a black body cavity; unfortunately high speed switching of these is impossible. Another commonly used source is a heated filament bulb, for example Tungsten, however while these can be switched relatively quickly (approximately 1 ms) they cannot reach the sub-μs regime required for shock experiments.

The development reported in this thesis chose to use modulated LED sources and began in 2016. However a recent paper by Liu *et al.*[110] used a similar approach. The paper reported simultaneous pyrometry and reflectivity results using an integrating sphere with a 800 mW, 1064 nm laser light source. The stated accuracy of the reflectivity measurement was $\pm$15%. Two temperature analysis methods, one using a grey-body assumption and another using the measured reflectivity were applied. The approach that used the measured reflectivity produced a temperature that was consistent with a published EoS but the grey-body derived temperature was not.

Three drawbacks of the method used by Liu *et al.* have been identified. Firstly, the reflectivity measurement was at a single wavelength; there is no physical reason that reflectivity changes would not vary with wavelength so assumptions are required to extrapolate the result to other wavelengths. Secondly, the illumination laser used would be rated as a Class 4 laser device in the UK; as PDV is also used in these experiments there are potentially practical difficulties with the use of multiple laser wavelengths. Finally, the method used integrating spheres which are destroyed in the experimental process. Integrating spheres are costly items so the use of these devices would increase the cost of the experiments.

Another method that offers the potential for tilt and surface finish insensitivity is ellipsometry. The basis for ellipsometric methods is that the complex refractive index of a material can be used to calculate its reflectance. Ellipsometry can derive the complex refractive index of a material from the change in polarisation state of light incident on a sample. Thus ellipsometry can be used to measure the reflectance of a sample and, given the high speed response of optical detectors, can make measurements at high sampling rates. Seifter *et al.*[124] reported application of the ellipsometry technique to copper and tin samples with a variety of surface finishes. While the technique showed promise there is one significant flaw, the complexity of ellipsometry increases significantly when multiple layers are involved. In shock pyrometry experiments the standard practice of gluing a lithium fluoride window to prevent immediate release creates a complex layered system that is not easily amenable to ellipsomteric analysis [126, Ch.4].

8.4 Laboratory measurements of reflectivity

Static measurement of reflectivity is valuable in understanding how sample oxidation and attachment of a window (and the associated glue) can affect reflectivity. Thus the capability to perform laboratory reflectivity measurements has been developed. Two techniques have been used to determine sample reflectivity, an integrating sphere and spectroscopy of light reflected from the sample.

An integrating sphere is a hollow sphere with an inner surface coated with a highly reflective, but diffuse, material. The sphere also has a number of ports for sample interfaces, illumination and detection. In an ideal integrating sphere any light entering the sphere will be reflected until it reaches one of the ports. Assuming ideal function it is obvious that, if a sample is presented at one of the ports, any changes in the light level in the sphere can be attributed to the reflectivity of the sample. Thus the integrating sphere offers a way to measure the absolute reflectivity of a sample independent of the surface finish of the material (assuming the surface finish does not affect reflectivity).

Due to the non-ideal nature of laboratory integrating spheres the measurement of reflectivity is often accomplished using comparison with a known sample. Comparative reflectometry is the technique used here. First, using an illumination source, a baseline light intensity measurement (with no sample) was made. Next, a mirror was placed in the sample position and an intensity measurement made. Finally, the sample was placed at the port and another intensity measurement made, see Figure 8.1.

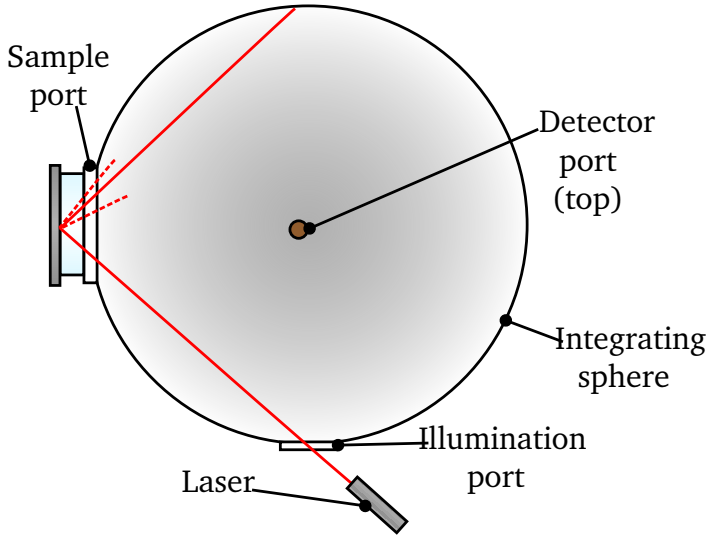


Figure 8.1: Schematic diagram of the measurement of the effect of a sample on the light level within an integrating sphere.

The sample of interest was a 45 mm diameter tin target with a 40 mm diameter, 10 mm thick LiF window attached using Loctite 326 glue. This is not ideal for

an integrating sphere measurement as, ideally, the reference sample would be in an identical geometry to the sample but such a sample was not available. To compensate for the stand off between the tin sample and the sphere introduced by the window, a spacer was used for measurements with the reference mirror. The spacer was the same radius and depth as the LiF window but hollow and coated with a white paint/barium sulphate mixture. A schematic of the various arrangements is shown in Figure 8.2.

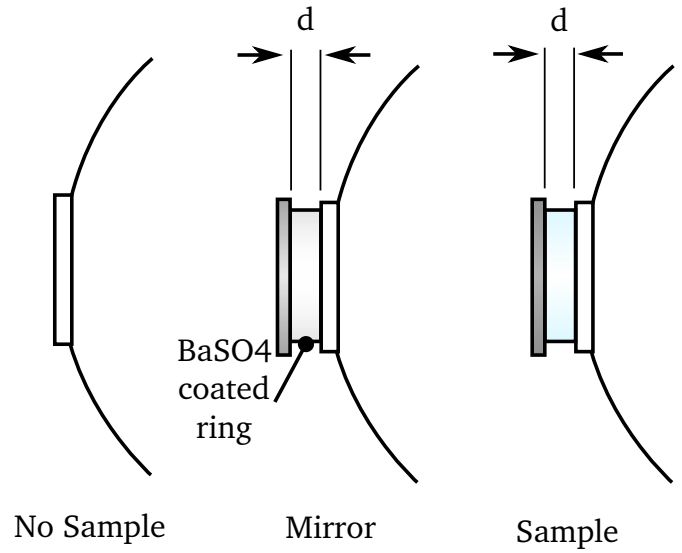


Figure 8.2: Schematic diagram of the configuration used for the measurement of the reflectivity of a windowed sample. To compensate for the stand-off of the sample due to the window, a spacer of matching dimensions is required when using a reference mirror.

While the arrangement described was adequate for the measurement of reflectivity when the sample was illuminated with a laser, there were a limited number of laser wavelengths available limiting the number of measurements that could be made. A number of LEDs were available at a range of wavelengths, so a procedure to measure reflectivity with LED illumination was developed.

The key challenge with LED illumination was that the baseline light level, when no sample is present, is much higher due to the diffuse nature of the illumination. This made differentiation of the effect of placing a reference or sample at the port much more difficult. To enable the difference in light level to be resolved it was necessary to modulate the LED and average over multiple measurements.

8.5 Potential reflectivity diagnostic solutions

8.5.1 Initial reflectivity diagnostic concepts

The success of integrating spheres in the dynamic measurement of emissivity shows that the problem is tractable. There are, however, some problems with the integrating sphere approach. One, it is difficult to use in conjunction with other optical techniques as it must, by definition, obscure the target. Two, integrating spheres are a relatively expensive optical component which then require further customisation for use in plate impact experiments. Thus the cost of employing integrating spheres is relatively high. Considering the underlying reasons for the success of integrating spheres allows some simplifications to be made.

The most significant benefit of an integrating sphere is that it is largely insensitive to the geometry of the optics. Variations in tilt, surface finish and surface curvature all have minimal effect on the signal allowing measurements to be made for a significant duration in high strain rate experiments. The insensitivity of integrating spheres may, however, be of limited value in experiments such as windowed plate impact experiments where variations in geometry are minimised.

The integrating sphere approach could be considered 'over-engineered' for reflectivity measurements in plate impact experiments. The tilt in plate impact experiments should not exceed a few mrads in a high quality experiment, surface curvature should be negligible and the use of an optical window suppresses changes in surface finish. These characteristics indicate that it may be possible to create optical systems that are simpler than an integrating sphere. While, ideally, absolute reflectivity would be measured there is also benefit to measuring the relative reflectivity at multiple wavelengths.

One potential solution uses the idea of a inverse integrating sphere, in this concept, rather than collecting all light from the surface the surface is uniformly illuminated from all angles and light collected from a single view point. This can be simplified further when the range of possible conditions is limited, as in a plate impact experiment. Thus the range of angles the target is illuminated from

can be decreased and 'uniform' illumination can be reduced to a number of points, see Figure 8.3.

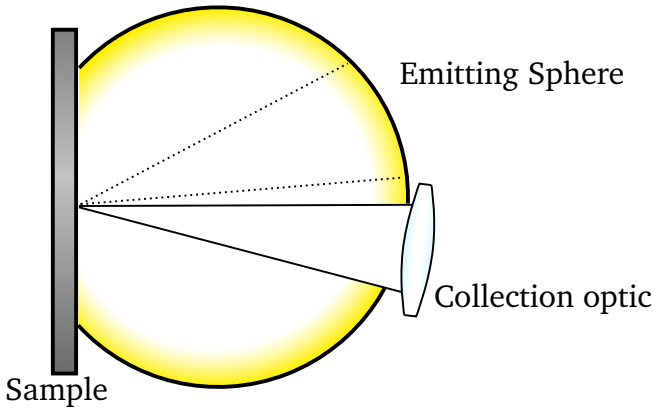


Figure 8.3: Conceptual diagram of a 'illuminating sphere' where a sample is illuminated over a wide range of angles.

Another potential solution is based on using under-filled optics so that there is unused solid angle in the collection optics that is available to collect light in the case of tilting or diffuse reflections. For the collection optical design, having a large optical throughput is consistent with other optical requirements, so this is not an issue. However the illumination optic needs to be well collimated with a small spot size; given the reciprocal nature of most optical systems this is not straight-forward. One type of optical system that is compatible with optical injection is where focusing is split between two lenses; one lens nominally collimates collected light, the other focuses it. A possible solution arises if the light could be 'injected' into the optical path after one lens. A schematic of this solution is shown in Figure 8.4.

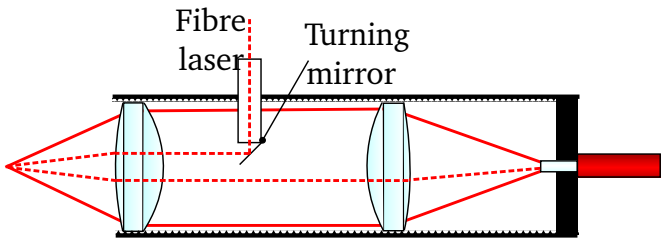


Figure 8.4: Conceptual diagram of an insertion probe.

While the 'optical injection' solution is not likely to be as robust to changes in tilt and surface finish as diffuse illumination, it is compatible with focused collection

and may be sufficiently robust for application to plate impact experiments.

8.5.2 Laboratory testing of reflectivity diagnostics

The 'inverse integrating sphere' diagnostic concept was initially implemented in static laboratory tests to investigate performance. The benefits of such an approach are that:

- it is compatible with simultaneous measurement of radiance and reflectivity, provided the illumination sources can be modulated sufficiently rapidly.
- it can be designed to be low cost.
- it should retain much of the insensitivity to tilt of the integrating sphere approach.
- it allows the radiance collection area to be the same as the reflectivity measurement area.

However, the approach has the following drawbacks:

- it is sensitive to surface finish
- the addition of two signals onto a single channel reduces data quality
- the illumination source usually has some limitation in optical power which, as sufficiently high sample radiance, cannot be resolved against the thermal emission background which limits the upper temperature of the approach.

An initial prototype for the diffuse illumination was developed using a rapid prototype collar. Three 1 mm holes were drilled into the collar; 1 mm thickness of rapid prototype was left at the base of the hole. Three 4 m long, 1 mm diameter plastic optical fibres (Avago HFBR-RLS001Z, polished with 1 μm) were inserted into the holes to illuminate the target with light produced by light emitting diodes (LEDs). The output of the LEDs were coupled to the optical fibres by pushing the fibres as close as possible to the LED die.

The arrangement of the diffuser and fibres was designed such that the light was emitted over a wide range of angles, this was to reduce the diagnostic's sensitivity to tilt and surface finish. The optics used to collect the light reflected from the surface are the same as those used to measure the light radiated by the target. A schematic of the system is shown in Figure 8.5.

Laboratory tests were conducted to investigate the response of the system to sample stand-off distance, target sample material and sample tilt. To test the response to variations in stand-off distance, collected light level was measured as stand-off distance was varied; both a mirror sample and a diffuse (paper over a mirror) sample were used. The results of this are shown in Figure 8.6. It can be seen that at a stand-off of approximately 11 mm the system is insensitive to surface finish.

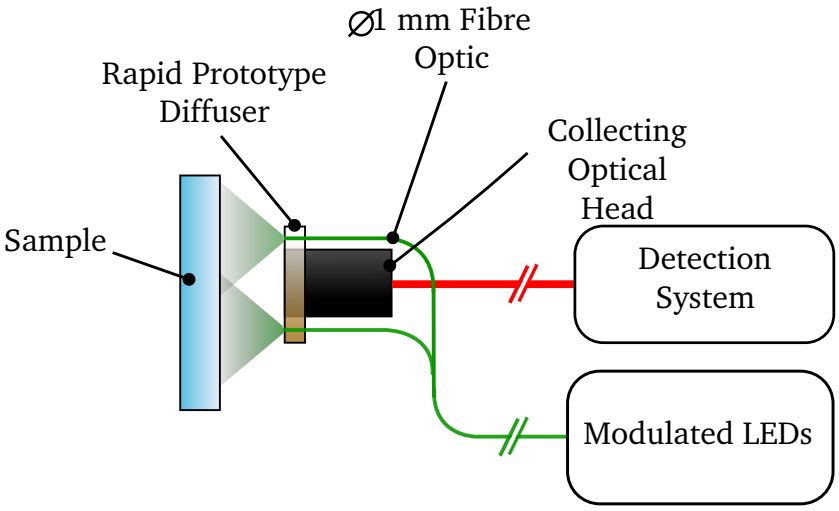


Figure 8.5: Schematic of the reflectance measurement system. Optical fibres illuminate the surface over a wide area and angle. The pyrometry head is used to collect the reflected light.

With a diffuse sample, tilt will not be a significant issue. However if the sample is mirror-like, as was fielded, there was concern tilt would significantly affect the collected signal. To test sensitivity to tilt with a mirror-like sample a mirror was mounted in a kinematic mount (ThorLabs KM200) and collected power measured at a range of angles. The results, shown in Figure 8.7, indicated that tilt under 20 mrads has a less than 1% effect on the collected light level.

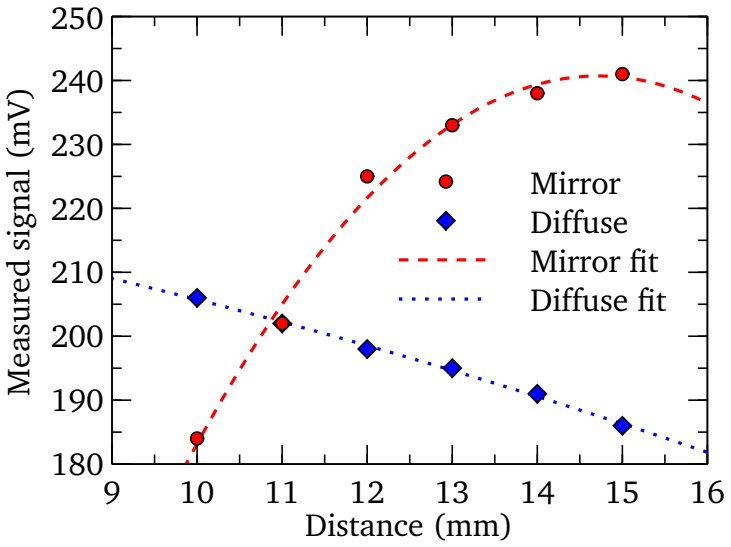


Figure 8.6: Results from a laboratory experiment showing the collected signal as a function of stand-off distance. Squares indicate results from a diffuse reflector; diamonds indicate results from a mirror.

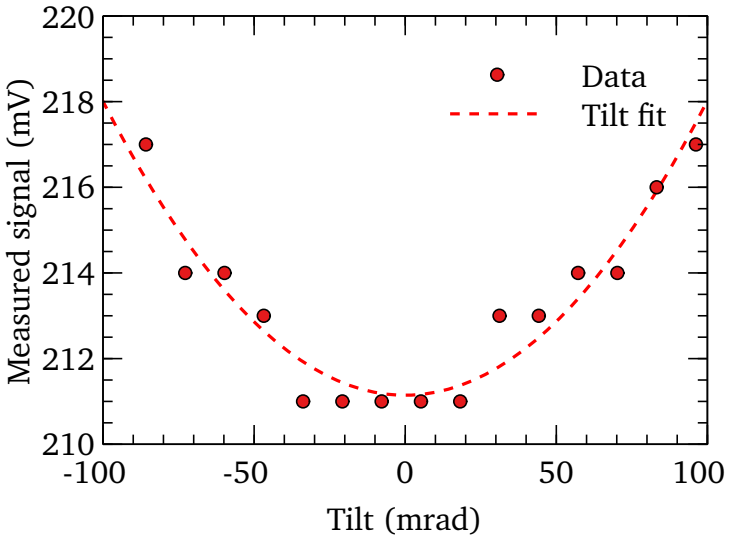


Figure 8.7: Results from a laboratory experiment showing change in collected signal as a function of target tilt.

In addition to the requisite optical performance it was desirable the illumination system was modulated to allow reflectivity measurements to be taken at a specified bandpass while also measuring the sample radiance for pyrometry over the same bandpass. Due to the short timescales of plate impact experiments, it is necessary to modulate the signal at greater than 2 MHz to ensure the associated radiance measurement is not obscured. It is also highly desirable

that the illumination system reduces to zero light output during it's duty cycle.

A drawback to modulation is that it does make analysis more complex because it is necessary to separate two signals that have been added to a single channel.

To achieve this light emitting diodes (LEDs) have been used as the illumination sources as they are cheap and can be modulated at high speeds. A simple MOSFET based circuit (Figure 8.8) is used to modulate the LEDs while supplying high power. The maximum achievable modulation speed is dependent on the LED used. Modulation frequencies of approximately 100 MHz were achieved using an OSRAM TOPLED (Osram Opto LT G5AP-CZEX-36). The drive signal was provided by a Stanford DG645.

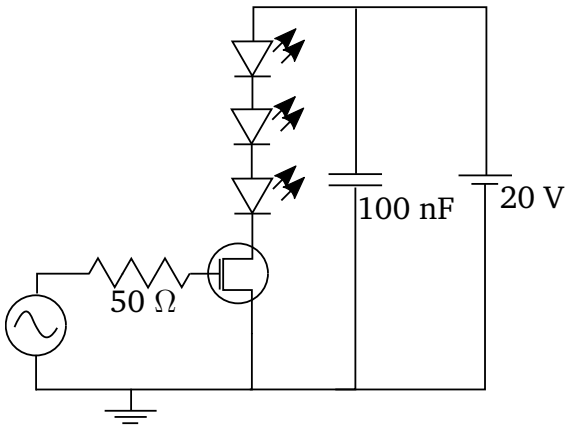


Figure 8.8: Circuit diagram of the LED driver circuit. The signal generator rapidly switches the MOSFET between conducting and non-conducting states, this modulates the LEDs.

8.5.3 Dynamic testing of a reflectivity diagnostic

While the laboratory testing indicated that the reflectivity diagnostic can be made relatively insensitive to conditions of varying surface finish and tilt it was not compatible with a simultaneous radiance measurement at the illumination wavelength. To achieve this the LED sources were modulated at high speed. This multiplexes the reflectivity signal onto an associated radiance measurement channel; in this case a 650 nm centred LED was used for illumination. A plate impact experiment was used to test the dynamic performance of the reflectivity diagnostic.

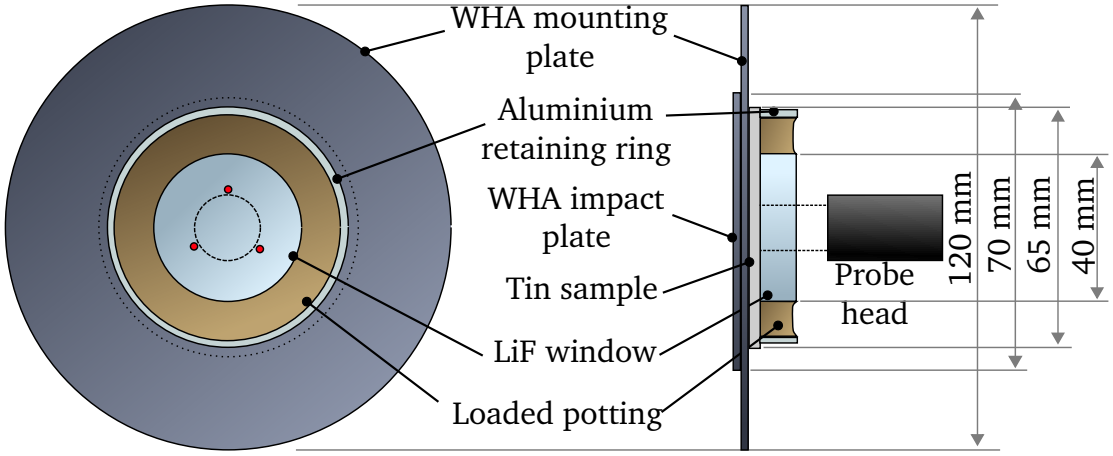


Figure 8.9: Schematic diagram of the target configuration for the plate impact experiment. The red dots indicate PDV probe positions, the dotted circle indicate the pyrometry probe collection area.

The experiment was similar to the experiment reported in Chapter 5 and consisted of a 50 mm diameter, 3 mm thick tin sample, mounted on a 120 mm diameter, 2 mm thick tungsten heavy alloy (WHA) plate. A 70 mm diameter, 2 mm thick WHA plate impacted the WHA mounting plate at approximately 1550 $m{\cdot}s^{-1}$. The significant difference was that a window of different dimensions was used, specifically a 40 mm diameter, 10 mm thick lithium fluoride (LiF) window. To prevent luminescence of the edges of the LiF the window was surrounded with a tungsten loaded Sylgard potting. The target arrangement is shown in Figure 8.9.

In addition to the reflectivity measurement a three channel, spectral band pyrometer was used to measure the thermal radiance of the sample. Three PDV probes measured the sample-window interface velocity and shock arrival times. The position of the probes, indicated on Figure 8.9, allowed tilt to be determined.

The configuration of the pyrometer is shown in Figure 8.10. The reflectivity signal was multiplexed onto the 600–700 nm channel.

8.5.4 Initial dynamic reflectivity results

Two plate impact experiments were conducted. The interface velocities and interface pressures, calculated using the LiF Hugoniot [89] are shown in Table

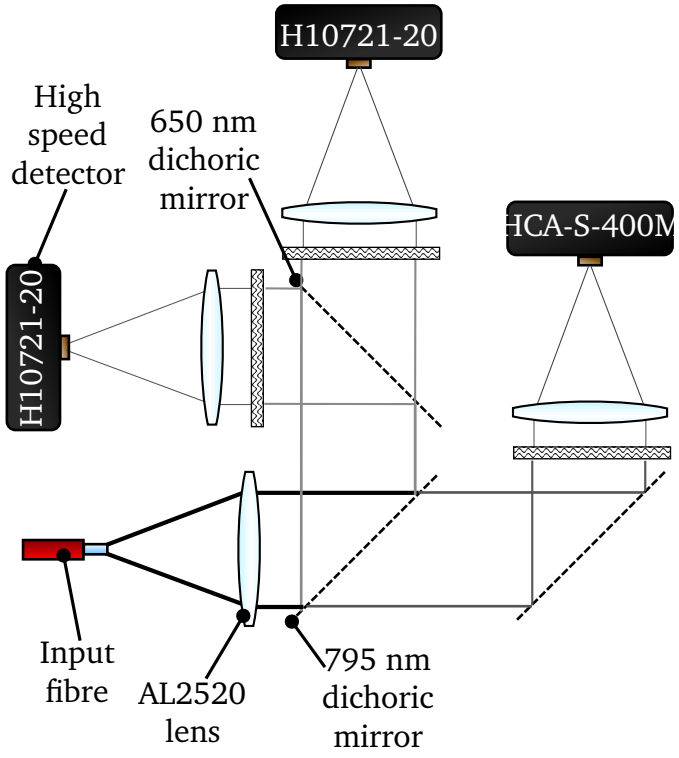


Figure 8.10: Schematic diagram of the radiometer sub-system used in the initial dynamic reflectivity experiments.

8.1. Unprocessed radiance data is shown in Figures 8.11 and 8.12.

Table 8.1: Interface velocities as measured by PDV and inferred interface pressures.

Experiment	Interface Velocity ($m \cdot s^{-1}$)	Interface Pressure (GPa)	Tilt (mrad)
1	1373 ± 5	25.37 ± 0.3	7
2	1373 ± 3	25.37 ± 0.7	5

To determine the reflectivity it is necessary to analyse the multiplexed signal from the 600–700 nm channel. Determining the change in the reflectivity signal is not straight-forward as the underlying radiance signal is complex. However, using both the static reflectivity signal and the spectrally closest radiance channel as references, the change in reflectivity was determined. The first point to note is that from the 750–850 nm channel we can infer that, after a spike in intensity,

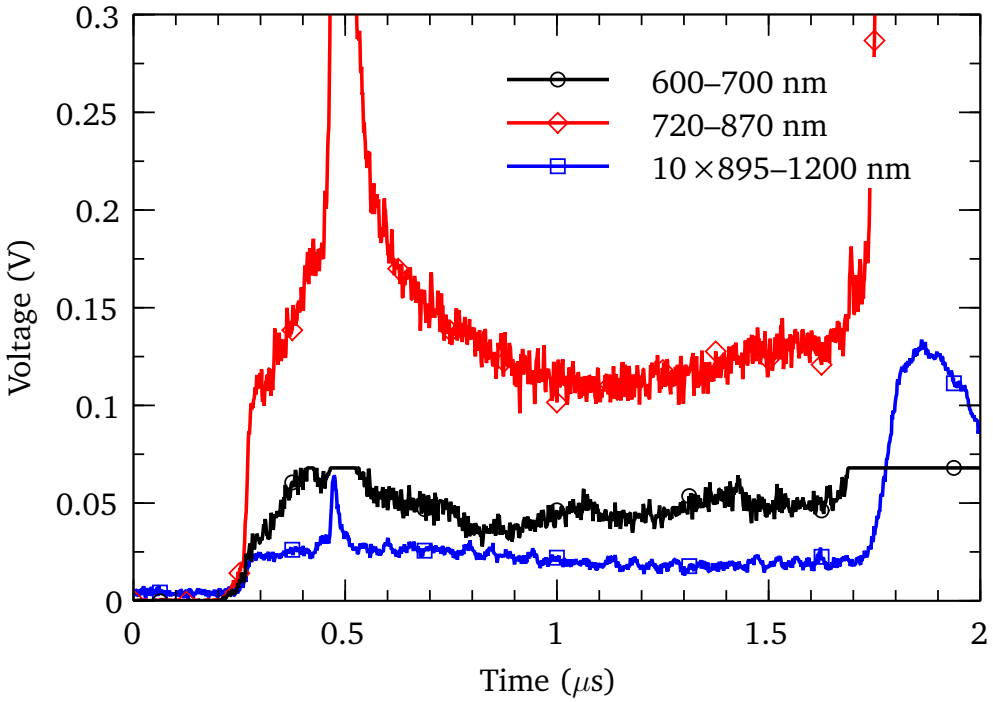


Figure 8.11: Radiance-time data from the first dynamic test of the reflectivity system.

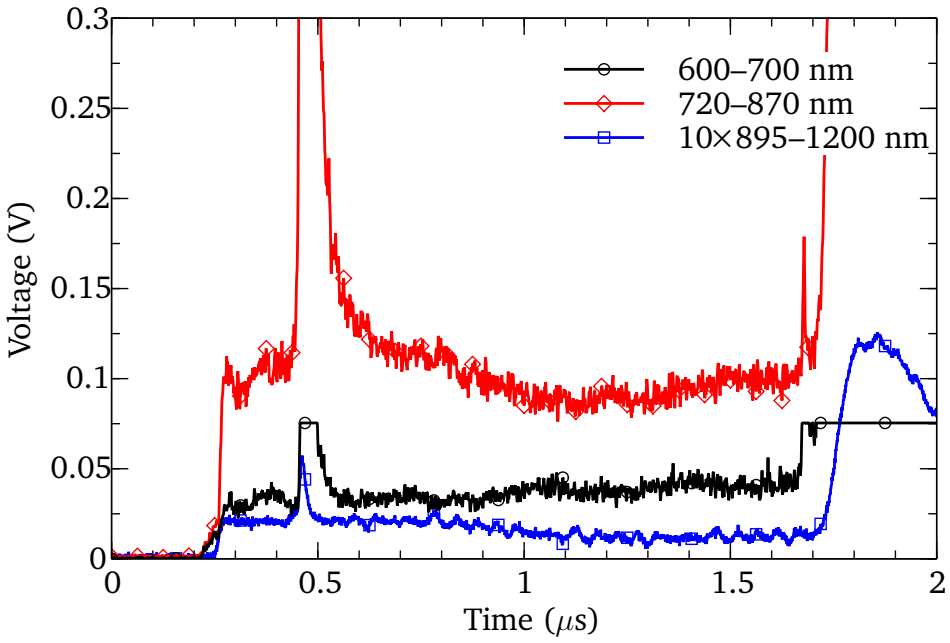


Figure 8.12: Radiance-time data from the second dynamic test of the reflectivity system.

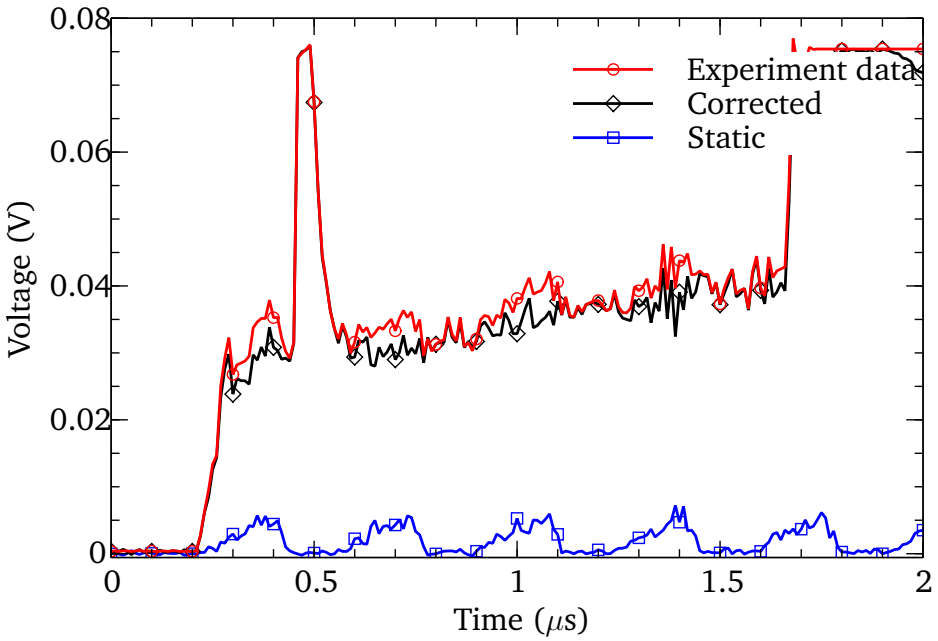


Figure 8.13: Plots of the dynamic and static reflectivity signals. Also shown is the dynamic signal with the reflectivity signal removed using the determined parameters.

the radiance varies smoothly. Using this the following process was used to determine the reflectivity signal:

1. the dynamic signal was down-sampled to reduce noise.
2. the static signal was time-shifted and amplitude-scaled and the shifted signal down-sampled to the same time points as the dynamic signal.
3. the difference between the two signals was calculated.
4. the difference was fitted with a 2^{nd}-order polynomial and the mean residual between the difference and fitted curve calculated.
5. steps 2 to 4 are repeated until the mean residual between the difference and fitted curve is minimised. The amplitude scaling factor indicates the change in reflectance.

An example of the results of this process are shown in Figure 8.13. Reflectance results from both experiments are shown in Table 8.2. It can be seen that the

Experiment	Relative reflectivity
1	0.70 ± 0.05
2	0.55 ± 0.05

Table 8.2: Measurements of reflectivity determined by the dynamic reflectivity diagnostic.

results are not consistent. The cause of this is unclear; potential explanations include lack of repeatability in the pulse intensity, incorrect alignment and real shot-to-shot variation.

Due to the inconsistent reflectivity results conversion of voltage to temperature analysis was conducted using both literature emissivity values and emissivity values scaled using the measured relative reflectivity. The results of the analysis of experiment 1 are shown in Figure 8.14. There are two notable features, first not only is there a radiance 'spike' at 0.4 μs there also appears to be non-thermal radiance during the entire release-equilibrium duration on channels 1 and 2. Second, using the scaled emissivity data makes agreement between the channels and with the predicted temperature worse than using the literature data.

The results of the analysis of experiment 2 are shown in Figure 8.15. While there is also a radiance 'spike' at 0.4 μs the additional non-thermal radiance is less apparent. Again using the scaled emissivity data makes agreement between the channels worse. However, due to the better quality radiance data it was possible to apply the Monte-Carlo error analysis outlined in Section **??**. The result of this analysis was that, assuming literature emissivity values, the temperature during the plateau was 1398 (1379–1418)°K.

There were two key conclusions from these results. First, due to the lack of clear cause for the inconsistent reflectivity measurements, further investigations into the application of dynamic reflectivity measurements needed to be conducted to understand potential causes for the errors in the reported measurements. Specifically, ensuring the system was capable of reflectivity measurement immediately before shock arrival was of high importance. Second, the large uncertainty about

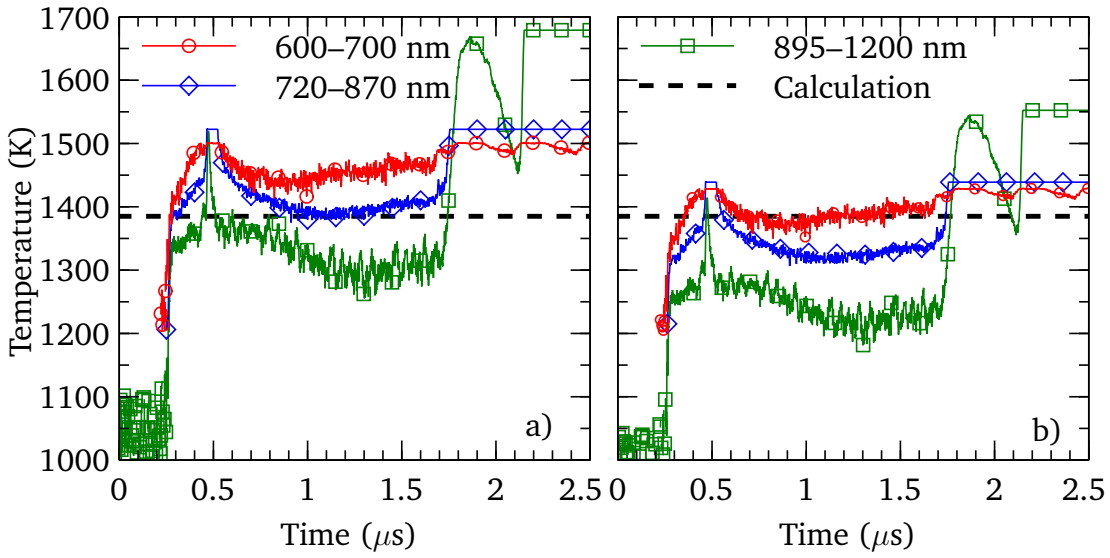


Figure 8.14: Temperature results from experiment 1 of the initial dynamic reflectivity experiments. a) shows results using literature values of emissivity. b) shows results when these values are scaled by the measured reflectivity value.

the applicability of a reflectivity measurement in one wavelength band to other wavelength bands highlighted the need for multi-wavelength measurements.

8.5.5 Dual wavelength testing

While some success was achieved with the fibre based illumination system an issue with a single wavelength measurement is that any functions used to describe wavelength dependent changes in reflectivity are poorly bounded, relying on data at a single wavelength band. To address this it was desirable to measure reflectivity at multiple wavelengths.

Initial testing of available infrared LEDs showed that, given the optical output power of the LEDs combined with the sensitivity of available detectors, a fibre coupled system was not feasible as the signal from an LED could not be detected after passing through the fibre. However, it was noted that if an LED was placed in the location of the fibre output a detectable signal was generated. A system based on mounting LEDs next to the optical probe head was then developed.

To illuminate the target two sets of three LEDs were arranged as close to the collection lens as possible. The LEDs were spaced on an equal radius at 60 degree

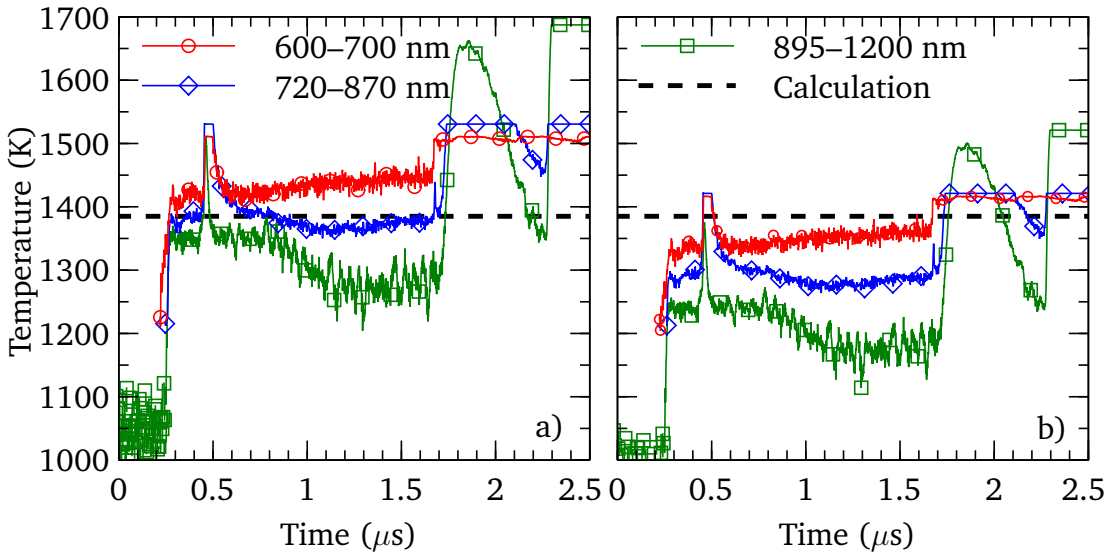


Figure 8.15: Temperature results from experiment 2 of the initial dynamic reflectivity experiments. a) shows results using literature values of emissivity. b) shows results when these values are scaled by the measured reflectivity value.

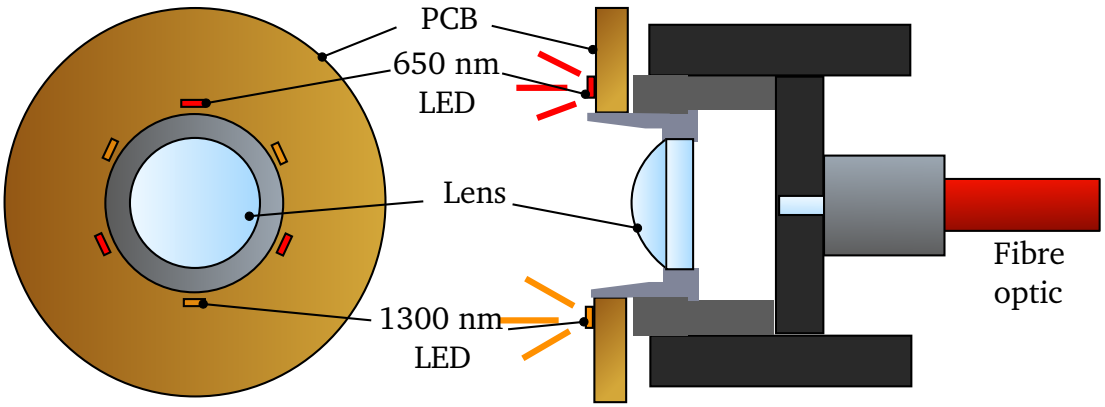


Figure 8.16: Schematic diagram of a dual wavelength, combined reflectivity and pyrometry probe.

intervals, alternating between 640 nm LEDs and 1300 nm LEDs, see Figure 8.16.

As with the fibre-based version, the principle behind the optical design of the reflectivity diagnostics is the balancing of the specular and diffuse components of the light reflected from the sample. Laboratory measurements highlighted two issues with the system that was developed. First, the balance point between the specular and diffuse samples varied slightly for the two illumination wavelengths, see Figure 8.17. To resolve the issue of differing balance points a compromise

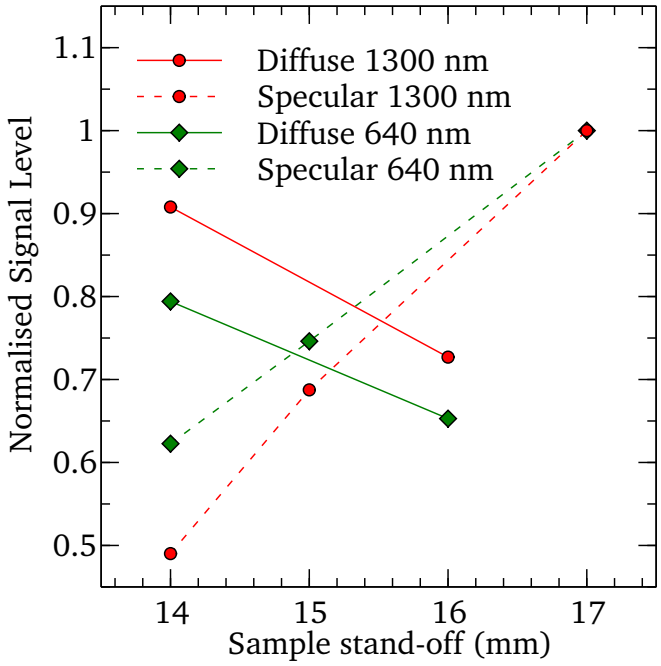


Figure 8.17: Plot of normalised signal level for both illumination wavelengths of the dual-wavelength reflectivity diagnostic at a range of stand-off distances.

stand-off distance was chosen, in between the two balance points, which adds some sensitivity to surface finish; based on the measurements this could lead to variations of up to 10%. Second, the addition of an optical window affected the system sufficiently that the distance at which the two components are balanced is different than when no window is present, so the stand-off distance was determined using measurements where a window was in place. The next step in demonstrating the diagnostic was to perform a dynamic test.

A plate impact experiment was designed to test the diagnostic. The sample was a 30 mm diameter, 0.5 mm thick copper foil, with a 25.4 mm diameter, 10 mm thick LiF window. The impact plate was a 24 mm diameter, 1 mm thick tungsten heavy alloy, see Figure 8.18. The diameter of the impact plate was chosen to be smaller than the window diameter to avoid LiF luminescence effects.

Experiment 1 used a nominally polished sample. The sample in experiment 2 was roughed using 1200 grit sandpaper.

The radiometer used for these experiments was a single fibre, five channel

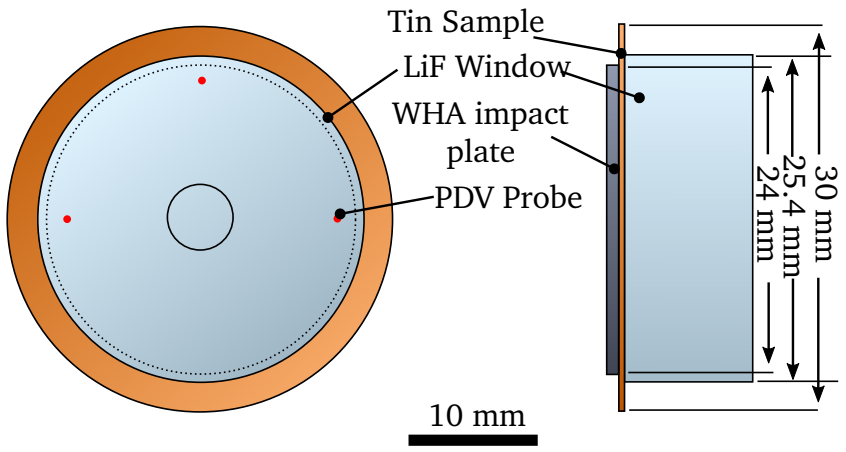


Figure 8.18: Scale diagram of the target configuration for the dual channel reflectivity experiments. Red dots indicate PDV probe positions. The solid circle indicates the pyrometer collection area.

Channel 1	Channel 2	Channel 3	Channel 4	Channel 5
FF875-Di01	*FF875-Di01*	FF875-Di01	FF875-Di01	FF875-Di01
FF735-Di02	FF735-Di02	*Edmund 1200 LP*	Edmund 1200 LP	Edmund 1200 LP
FF02-650-100	FF02-795-150	FF01-1001-234	DMSP1500R	*DMSP1500R*
				FF01-1538-82

Table 8.3: Table summarising the filters in place on each channel in the radiometer system. Italics are used for filters that are reflected from, rather than transmitted through the filter.

system. Table 8.3 shows that configuration of the dichoric mirrors and filters on the channels. Table 8.4 shows the detectors on each channel and the bandpass the channel operated at.

Channel 1	Detector	Wavelength band
1	Hamamatsu H11536-20 PMT	595–700 nm
2	Hamamatsu H11536-20 PMT	740–870 nm
3	ThorLabs APD430A	800–1120 nm
4	ThorLabs APD430C	1215–1500 nm
5	ThorLabs APD430C	1500–1585 nm

Table 8.4: Table summarising the detectors and wavelength bands on each channel.

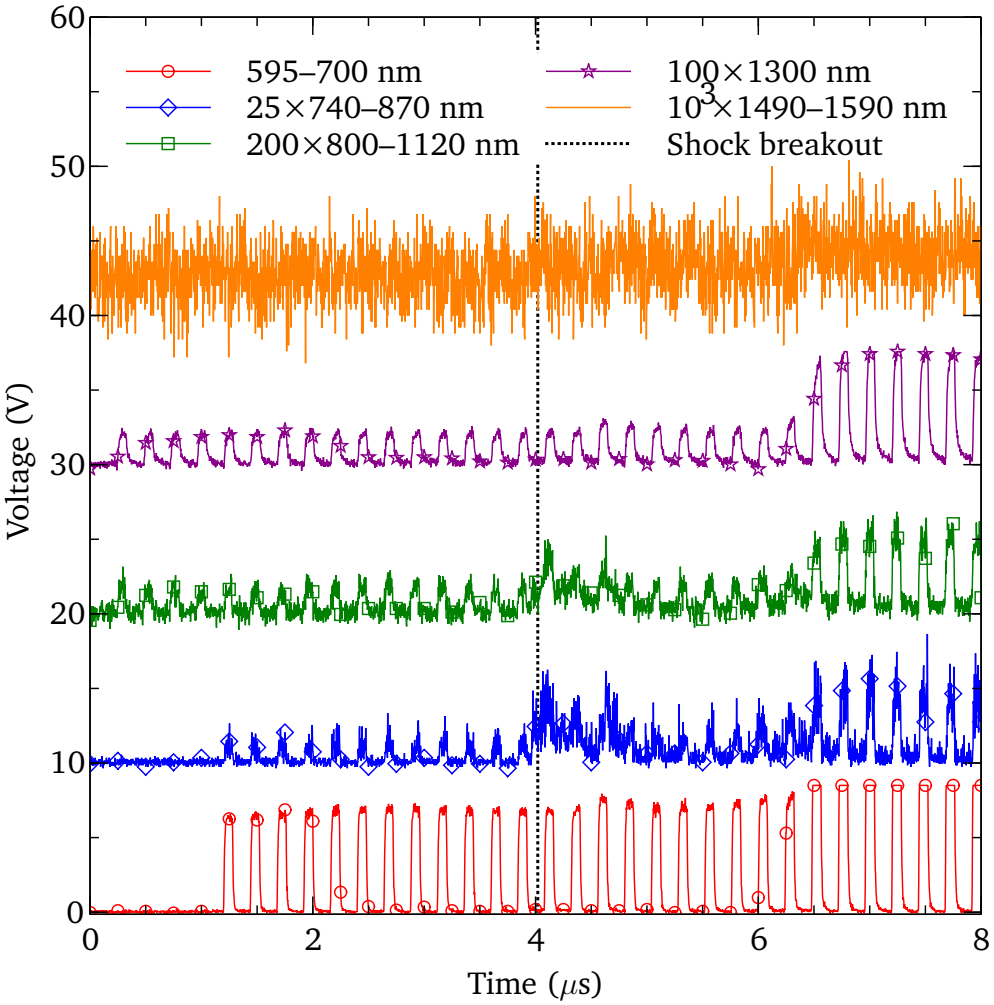


Figure 8.19: Plots of the dynamic reflectivity signals from the first dynamic test of the dual-wavelength reflectivity diagnostic. Weak, modulated reflectivity signals can be seen on channels that were not intended to collect them.

8.5.6 Results and analysis

Two dynamic experiments were conducted. The outputs of the detectors during the experiment are shown in Figures 8.23 and 8.24. A few points are notable from these figures. First, it can been seen that modulated signals appear on four of the five channels rather than the two channels that are indicated by the LED wavelengths, this has been attributed to wideband emission of the LEDs. Second, during the shock plateau there is minimal change in the collected signal, indicating minimal changes in reflectivity. Third, approximately 2 μs after impact the collected signal increases considerably on all channels.

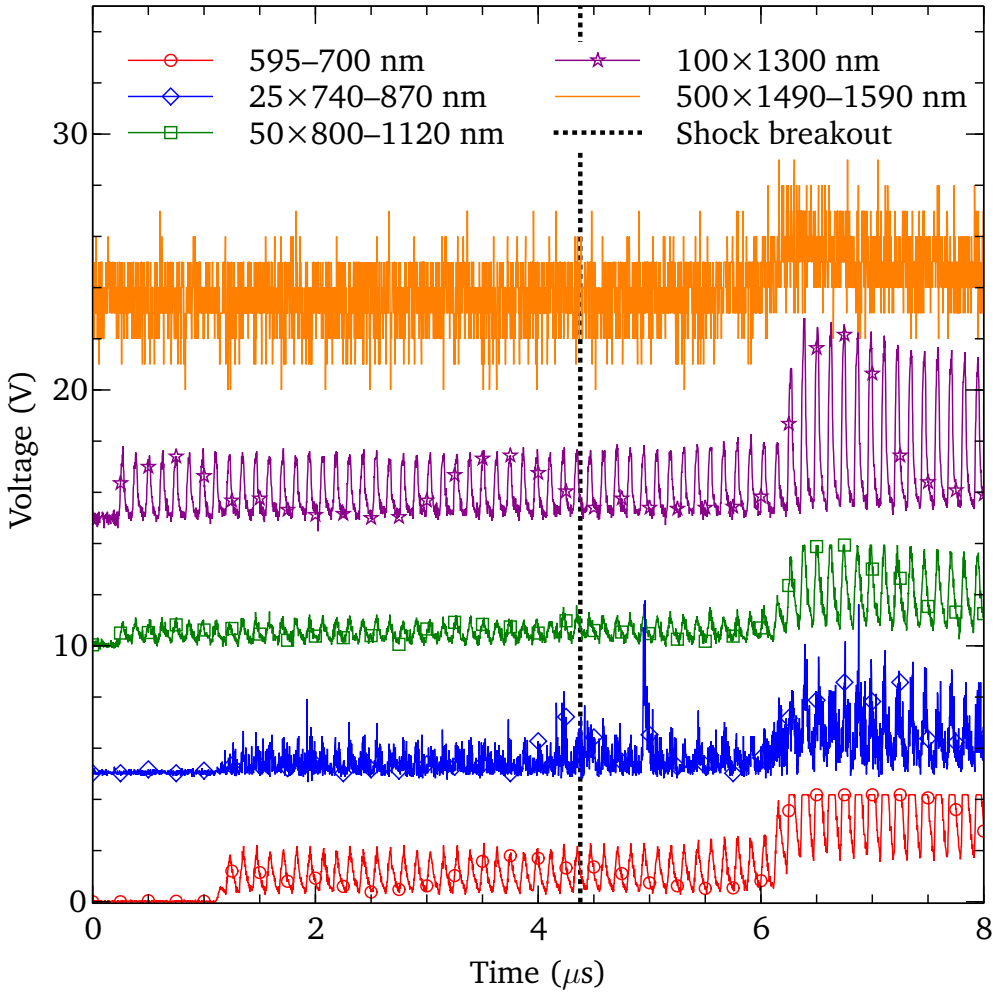


Figure 8.20: Plots of the dynamic reflectivity signals from the second dynamic test of the dual-wavelength reflectivity diagnostic.

While some qualitative conclusions can be deduced from the appearance of the results, for quantitative understanding a more rigorous approach is required. To extract time resolved reflectivity measurements from the pulsed data the following analysis procedure was used:

1. Isolate approximately five pulses before the shock and fit with a switched RC curve.

2. For the entire trace, down-sample to reduce noise and select data that occurs when fitted is less than 5% the peak value. Fit this data with cubic spline to calculate underlying baseline.

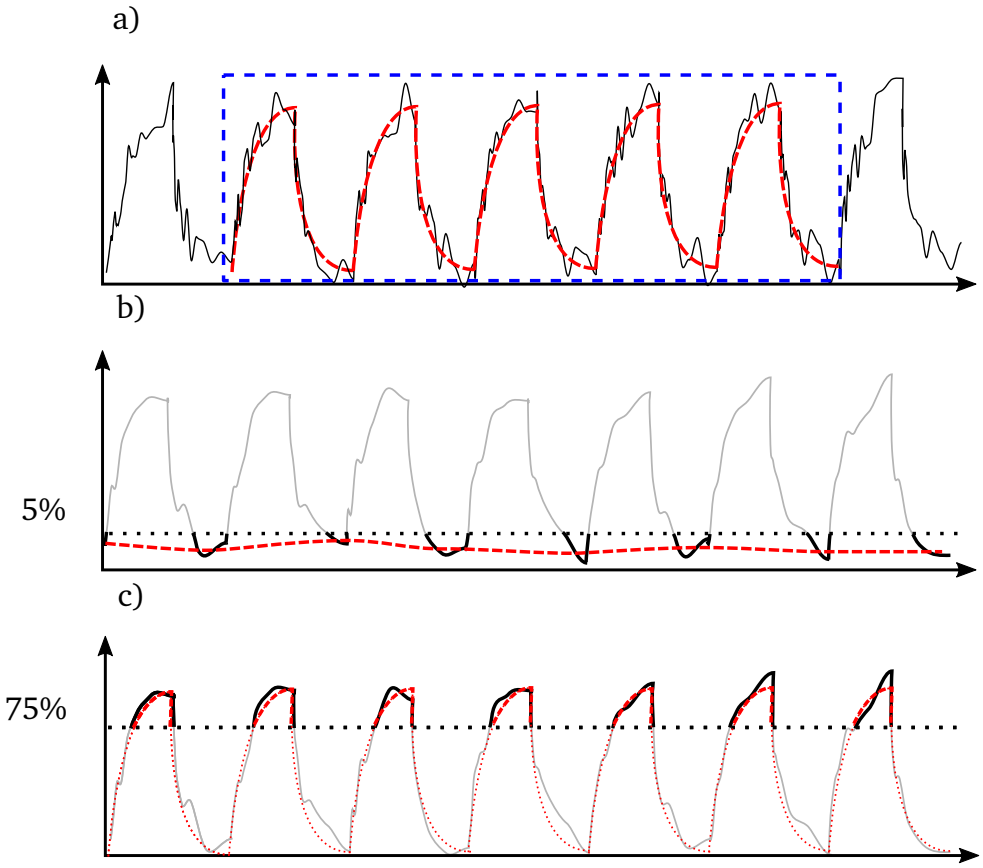


Figure 8.21: Illustration of the steps used to analyse pulsed reflectivity data. a) Shows fitting of raw data. b) Shows baseline fitting. c) Shows selection of high signal data used for calculation of reflectivity.

3. Remove baseline and calculate relative reflectivity by dividing data by fitted function considering only data that coincides with fitted signal levels of more than 75%.

Figure 8.21 illustrates the above steps.

An RC curve was chosen to describe the LED emissions as it is the anticipated behaviour of a capacitive load (such as an LED) driven by a square wave. Figure 8.22 shows an example RC waveform, Equation 8.3 provides a mathematical description of such a waveform.

$$V(t) = \begin{cases} \dfrac{1 - e^{-R_1 C_1 t}}{1 - e^{-R_1 C_1 t_1}}, & t_0 \geq t > t_1. \\ \dfrac{e^{-R_2 C_2 (t - t_1)} - e^{-R_2 C_2 (t_2 - t_1)}}{1 - e^{-R_2 C_2 (t_2 - t_1)}}, & t_1 \geq t > t_2. \end{cases} \tag{8.3}$$

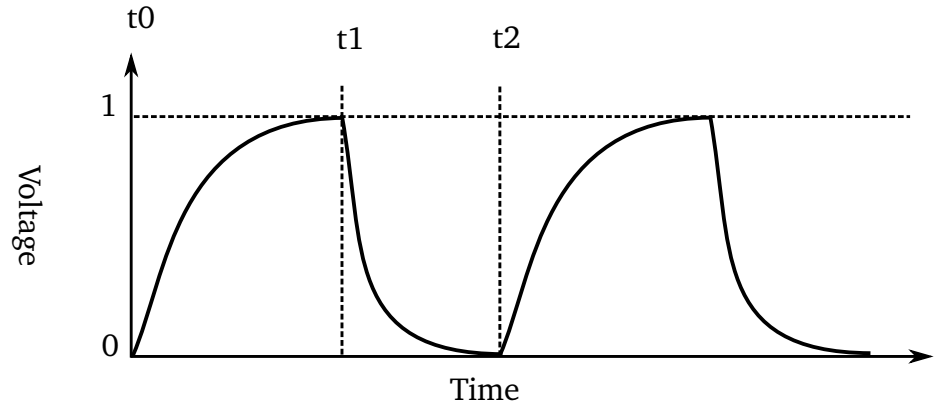


Figure 8.22: Illustration of the piecewise RC function. Each pulse is comprised of an rising RC pulse and a falling RC pulse. The time constants of the two components may differ.

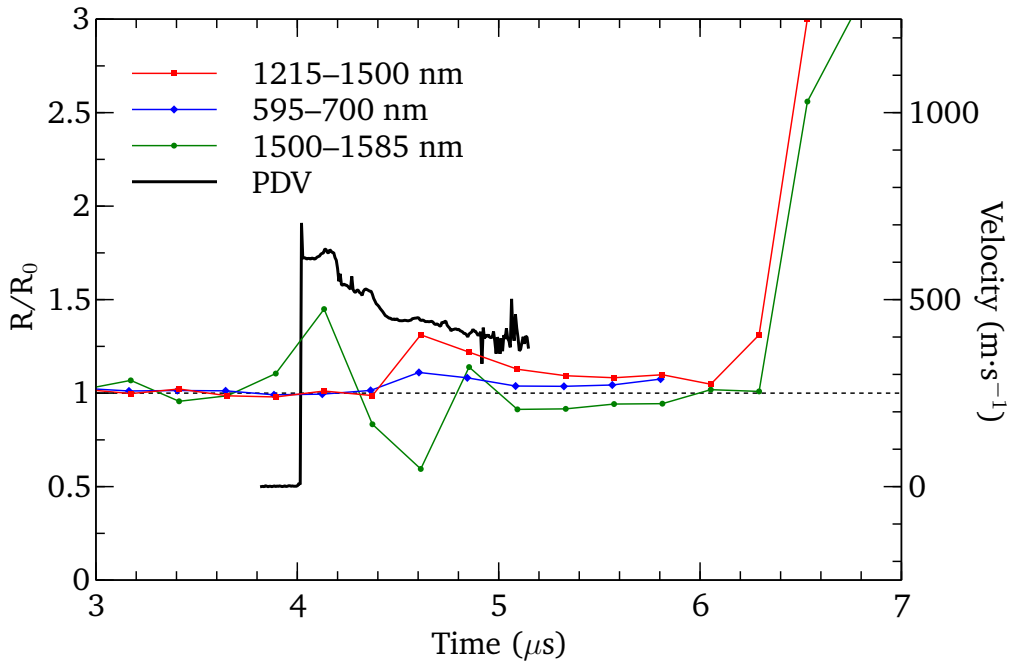


Figure 8.23: Plot of the results of dynamic reflectivity analysis applied to experiment 1 of the dual reflectivity channels. The sample surface was a specular reflector. Reflectivity data uses the left axis, PDV data uses the right axis.

The results of applying this analysis are shown in Figures 8.23 and 8.24.

It can be seen that on both experiments no significant change in reflectivity is measured during the plateau of the shock wave. While it is possible that the sample's intrinsic reflectivity is changing at the same time as the sample's surface

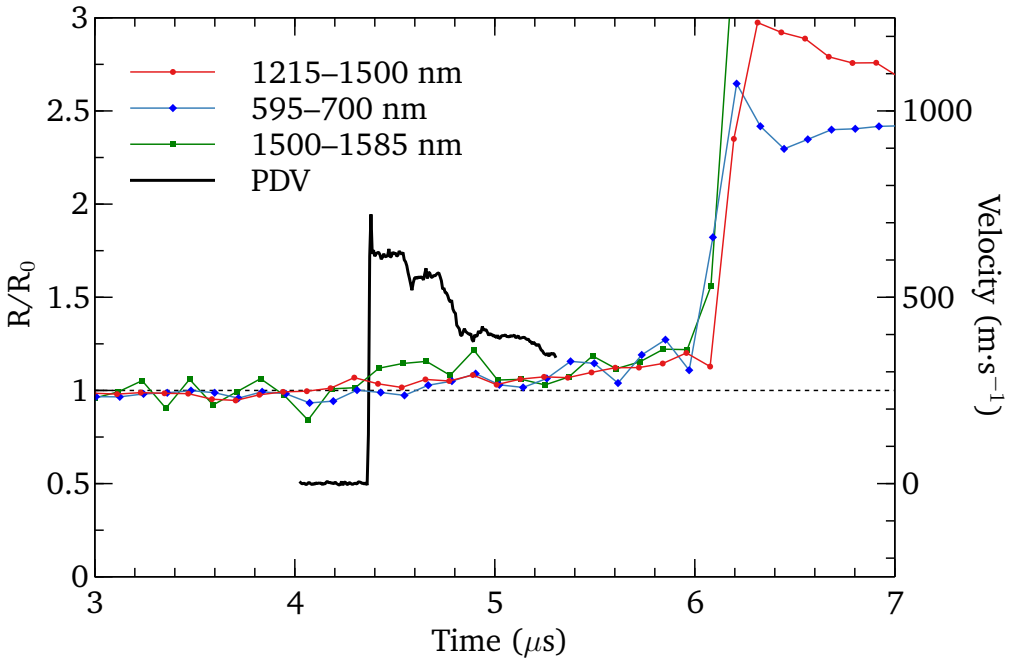


Figure 8.24: Plot of the results of dynamic reflectivity analysis applied to experiment 2 of the dual reflectivity series. The sample surface was a diffuse reflector. Reflectivity data uses the left axis, PDV data uses the right axis.

finish, and that the effects are cancelling each other exactly, it is much more likely that both are unchanged.

It is interesting to note that an increase in apparent reflectivity is seen with the specular target (at approximately 4.3 μs) after the interface pressure has reduced following the shock, Figure 8.23, however this is not seen on the diffuse target. A possible interpretation of this difference is that the specular sample becomes more diffuse after release. The same may happen to the diffuse sample but, because it is already diffuse, no change in signal is observed.

8.5.7 Conclusions

A review of reported dynamic reflectivity measurements identified that relatively few approaches to dynamic measurement have been tested. Only the recent work of Liu *et al.* [110] reported measured reflectivity on the same sample and experiment as the pyrometry measurement. Furthermore the results from the different approaches are not consistent. To address these issues, a new reflectivity

diagnostic has been developed that is able to measure reflectivity and thermal radiance on the sample and experiment.

The new diagnostic can be described as using multiple sources, with large solid angle emission, close to the optical head used for pyrometry to illuminate the sample. The pyrometry optics collect the illuminated light, which is in the same wavelength band as the pyrometry channels, and is measured by the same detectors; to enable measurements on the same experiment alongside a pyrometry measurement, the illumination sources are modulated at high speed.

Laboratory testing of the reflectivity measurement system indicates the system measures similar signals with both specular and diffuse samples. The first iteration of the system was developed that used a single illumination wavelength. While initial dynamic testing successfully collected results, they appear inconsistent. The cause of this inconsistency is unclear particularly because the system only operated after shock break out, so it is not possible to determine precisely when changes in signal level occurred, which would help identify the underlying cause.

Following the first iteration an integrated pyrometry and reflectivity system was developed that measures sample radiance at five wavelengths and reflectivity at two wavelengths. The system has been tested on a plate impact experiment where it has been tested on samples with specular and diffuse surface finishes.

Results suggest that the system works as intended and is able to make reflectivity measurements with both specular and diffuse targets. The results also suggest that the surface finish at the sample-window interface is not significantly perturbed during the plateau duration. If correct this is significant as changes in surface finish are a major concern in dynamic reflectivity measurements. Unfortunately, due to facility availability the impact speeds used in the dual wavelength tests are not fast enough to induce measurable radiance, thus simultaneous pyrometry measurements were not possible. However, the system does appear compatible with simultaneous measurements.

Ideally the next step in the development of the dual wavelength reflectivity system would be to apply it to an experiment with a sample material and

shock conditions comparable to results in the literature. This would enable a simultaneous reflectivity and pyrometry measurement with published results for validation.

It is believed that there may also be some straight forward enhancements of the illumination system possible. The multi-component function used to model the temporal illumination profile requires a complicated analysis procedure; it is anticipated that a sinusoidal waveform would be simpler to analyse. There are also some changes to the drive circuit design that may be able to speed up the modulation of the course LEDs [127].

9
Summary and conclusions

The broad goal of this thesis and the associated research has been to enhance ultrafast temperature measurement in high strain rate experiments. Specifically, this research has focused on the temperature measurement technique of optical pyrometry and its development. Five significant contributions have been achieved:

- A systematic and rigorous approach to the modelling of pyrometer systems has been developed. The capability to model pyrometer systems reduces trial-and-error in instrument design and has allowed outstanding questions, highlighted in the literature, to be answered, see Chapter 4.

- A pyrometer system of superior performance to existing systems has been designed, implemented and demonstrated. The pyrometer was designed using the aforementioned models so the performance of the system validated the value of the approaches used.

- Increased confidence in pyrometry for shock experiment applications. The high degree of agreement seen when comparing results from multiple pyrometer systems on a single experiment is a demonstration that results from different systems are comparable, see Chapter 6.

- A multi-wavelength dynamic reflectivity diagnostic, that can be applied simultaneously with pyrometry, has been developed and demonstrated. Emissivity uncertainty is one of the most significant sources of uncertainty in pyrometer measurements. As the complement of emissivity, measurement of reflectivity allows temperature analysis to employ measurements and reduce dependence on assumptions. The ability to dynamically measure reflectivity at a number of wavelengths provides additional confidence that the spectral dependence of reflectivity is well constrained, see Chapter 8.

- Additional shock temperature data on tin and lead has been obtained. While shock temperature measurements have been reported in the literature, they are limited in number so the additional data should significantly contribute to developing and understanding the EoS of these materials.

A more in-depth discussion of the contributions follows.

9.1 Advances in radiometer design

While pyrometry has been used for high strain rate applications for many years there had not previously been a systematic review of the most appropriate components and how they should be configured. Chapter 2 details a systematic review of relevant systems that have been reported in the literature. While the optimal design varies depending on the specific application, the review does highlight the advantages and disadvantages of various approaches.

Supporting the review of the literature, a review of commercially available detectors has also been conducted. Detectors and their capabilities are a key limiting factor in the minimum measurable temperature and the time resolution of systems so the data presented in Chapter 2 provides researchers with a rapid assessment of the feasibility their desired measurements. Detector technology develops relatively slowly so it is hoped this review will remain relevant for some time.

The literature review identified an inconsistency in the literature regarding the optimum choice of bandpass filter. Specifically much of the literature did

not take the effects of random noise (such as thermal noise and shot noise) into account; for high bandwidth applications, such as those discussed in this document, noise is a significant factor in system performance. To try to resolve this inconsistency, a model of the system was created and various parameters investigated using a Monte-Carlo approach. Results from the model were validated against experimental measurements, agreeing within 30%, which is reported in Chapter 4. The results of the subsequent numerical investigation clearly layout the trade-offs that are required when selecting bandpass filter parameters. The veracity of the principles used to design the pyrometer are validated by the success of the pyrometry measurements in the dynamic tests discussed in Chapters 5–8.

The information described above will allow any future research in high speed pyrometry to significantly speed up the design of a radiometer system, based on the requirements. Furthermore, using the frameworks developed it should be straightforward to assess the value of new components as they become available.

9.2 A high performance pyrometer

As a practical demonstration of the improved pyrometer design principles, a pyrometer was designed and assembled based on the principles developed. The performance of the pyrometer was demonstrated in a number of laboratory experiments, discussed in Section 2.4 as well as dynamic tests, Chapters 5 and 6.

The system produced has a limiting bandwidth of approximately 400 MHz ($\sim$1 ns rise time) which is 100 MHz more that the highest similar system. Using an optical head discussed in Section 2.4.2 a collection spot size of 0.64 mm has been attained. Finally, when applied to a dynamic experiment the system was able to produce measurements with an uncertainty of $\pm$ 1.5%, approximately half produced by a similar system.

9.3 Improved confidence in shock pyrometry

One of the outstanding issues with the application of pyrometry to shock experiments was that there was a lack of confidence that pyrometry measurements using different systems were comparable. This lack of confidence arose for two reasons. Firstly, high speed pyrometers are not mass produced, they are complex devices with multiple high precision components constructed to meet specific requirements. It was not clear that the various systems that have been created were equivalent. The second reason—the lack of a high speed standard—exacerbates the uncertainty around the equivalence of the systems. Usual practice for calibration of a pyrometer is to use a blackbody standard. An issue with blackbody sources is that they cannot be modulated at high speed. This means it is generally not possible to test a high-speed pyrometer at the timescales that occur in an experiment and, additionally, no high-speed standard has been established meaning validation of high-speed pyrometry measurements has no defined process.

To address the comparison issue, three pyrometry systems were applied simultaneously to a plate impact experiment. This configuration meant each pyrometer measured conditions that were as similar as is possible to achieve experimentally. The results from the three systems were consistent within the uncertainties of the measurements and, due to the configuration differences between the systems, the results demonstrate that results from different pyrometry systems are comparable.

9.4 Integrated reflectivity measurement

Emissivity remains one of the most important sources of error in pyrometry measurements and measurement of reflectivity remains a promising approach for determining emissivity. While a few methods to measure reflectivity dynamically have been developed and reported in the literature, no approach has become dominant as each approach has different advantages and disadvantages. In

Chapter 8 the development and testing of a novel method to measure reflectivity dynamically has been described.

The motivation for developing an alternative system for reflectivity measurements was that a review of the existing approaches highlighted that none were compatible with pyrometry measurements at the same wavelengths and on the same experiments.

The system developed was able to operate on the same experiment and sample as pyrometry and was also relatively insensitive to tilt, somewhat insensitive to surface finish, could be modulated at ~10 MHz and was low cost. The system does have the drawback that it is not completely insensitive to surface finish.

Following two initial dynamic experiments, which highlighted a number of potential improvements, a further two dynamic experiments were conducted using an improved dual wavelength system. The results with the improved system were mutually consistent and in line with expected results. The results from the improved system demonstrate the system could be used for simultaneous reflectivity and shock temperature measurements provided measurable thermal radiance is produced, which was not present.

Results have given further insight into the issues of dynamic reflectivity measurement. Specifically, the results indicate that surface finish does not change significantly during the shock plateau, this is valuable as variation in surface finish is a concern for many reflectivity measurement approaches. The improvement in results between the iterations of the reflectivity diagnostic also illustrates how desirable it is to have a reflectivity diagnostic that operates both immediately before and during a dynamic loading event.

The ideal next step for the combined pyrometry and reflectivity system would be to apply the system to a plate impact experiment which generates pressure and temperature conditions similar to previous literature data. This would allow the system to be validated against a different system.

With regards to the wider development of reflectivity diagnostics, there may be some possible refinements to the system. In particular, given the increasing

availability of rapid prototyping technology it may be possible to develop integrating spheres that are of significantly reduced cost. These low-cost spheres could then be illuminated with pulsed LEDs to allow simultaneous radiance and reflectivity measurements.

9.5 Additional shock temperature data

Although the primary goal of this research has been the development of temperature diagnostics the dynamic experiments that have been conducted in the course of this development have generated material data that have not been reported elsewhere. Specifically novel shock temperature data on tin and lead have been collected.

9.5.1 Tin data

Tin has been the sample material primarily used in the shock experiments during this project and, while there is substantial literature data on shocked tin, there are not extensive temperature results. In the course of the experiments conducted as part of this research additional data on the temperature of tin has been collected. The measurements reported in Sections 6.4 and 8.5.4 have measured tin temperature data at two equilibrated shock-release states, see Table 9.1 and extend the pressure-temperature space over which such results have been reported.

Due to the large number of results obtained in the collaborative experiments it appears possible to determine a small but statistically significant difference between the temperature predicted by a model based on the linear Hugoniot approximation, as shown in Figure 6.17. The difference indicates that the model is not sufficiently accurate to describe the temperature generated from the shock-release process.

The high temporal resolution of the diagnostics has also allowed temperature measurement during the dynamic 'release' period of the plate impact experiments. When combined with high temporal resolution interface velocity measurements a pressure-temperature 'release path' can be determined. The results of this analysis

are shown in Figure 9.1, alongside similar P-T path data from La Lone *et al.*[81] and shock-release equilibrium measurements by previous researchers[94, 112]; it can be seen results are consistent with previous results.

Table 9.1: Tin (Sn) shock temperature data.

Shock Pressure (GPa)	Interface Pressure (GPa)	Temperature (K)
33.4 ± 0.1	25.3 ± 0.1	1398 ± 21
26.1 ± 0.1	23.6 ± 0.1	1197 ± 18

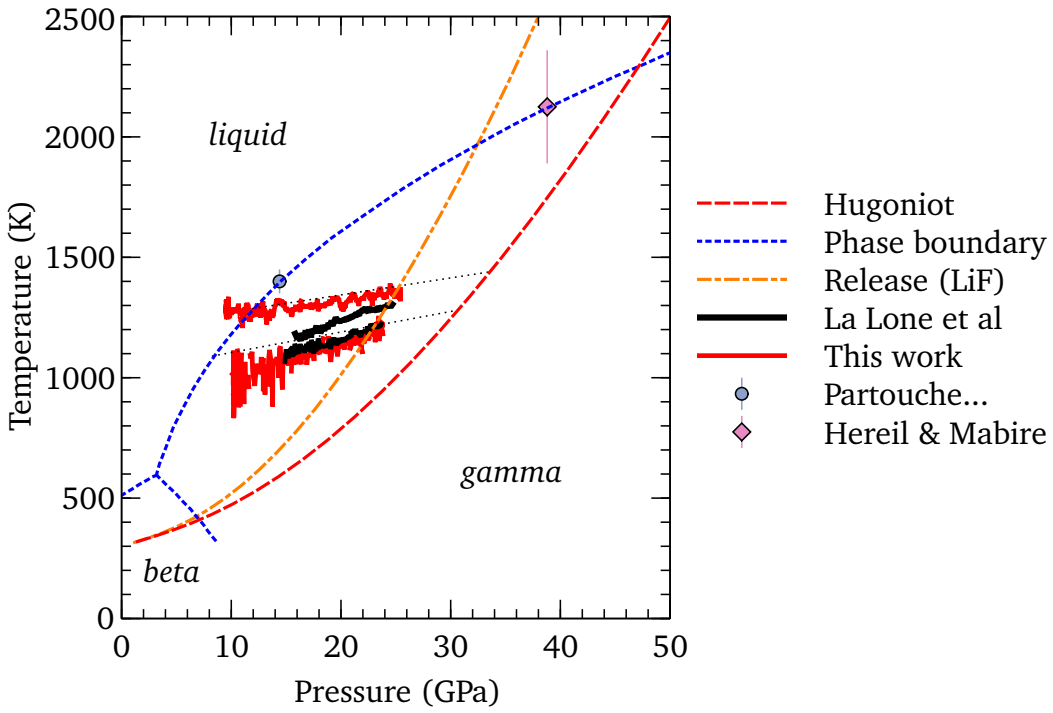


Figure 9.1: Summary of shock temperature measurements of tin reported in the literature. The measurements attributed to this work are from both Section 6.4 and Section 8.5.4. The dotted black lines indicate approximate release paths.

9.5.2 Lead data

Temperature data on shocked lead has also been obtained. Only a limited amount of shock temperature data on lead had been reported, as discussed in Chapter 7, so additional data is highly valuable for EoS development and improving the

Interface pressure (GPa)	Temperature (K)
23.1 ± 0.1	1610 ± 100
19.3 ± 0.1	1340 ± 120

Table 9.2: Table showing lead temperatures measured during the plateau region of the experiment.

understanding of the shock behaviour of lead. Furthermore, the time-resolved results reported in the literatures indicated a number of unexplained features.

Consistent with literature results, the results from the two lead experiments reported here also have a number of unexplained features. Specifically no constant emissivity values could be identified that would give consistent temperatures across both the experiments despite the relatively similar shock conditions and, additionally, there is unexplained temporal variation. Ultimately, temperature analysis was conducted using different emissivity assumptions for each experiment, see Table 9.2. The time resolved results have also been converted to pressure-temperature, a plot is shown in Figure 9.2.

The temporal variation is intriguing because, due to the nature of the relative variation of the different channels, such variations are indications of emissivity changes occurring over the duration of the experiment; the variations are on relatively slow timescales ($\sim$100 ns). Given the multiple phases in the P-T space explored by the experiments it is likely that phase-related emissivity changes would explain the features; time-resolved reflectivity measurements would be an appropriate way to investigate the emissivity changes.

9.6 Additional information on LiF luminescence

An important consideration when applying pyrometry to plate impact experiments is the potential data loss due to non-thermal emission. Luminescence of lithium fluoride has been reported in the literature as a particularly problematic source of non-thermal emission. The issue was replicated on plate impact experiments, Chapter 5, and the emission did result in data loss. To mitigate the risk of data

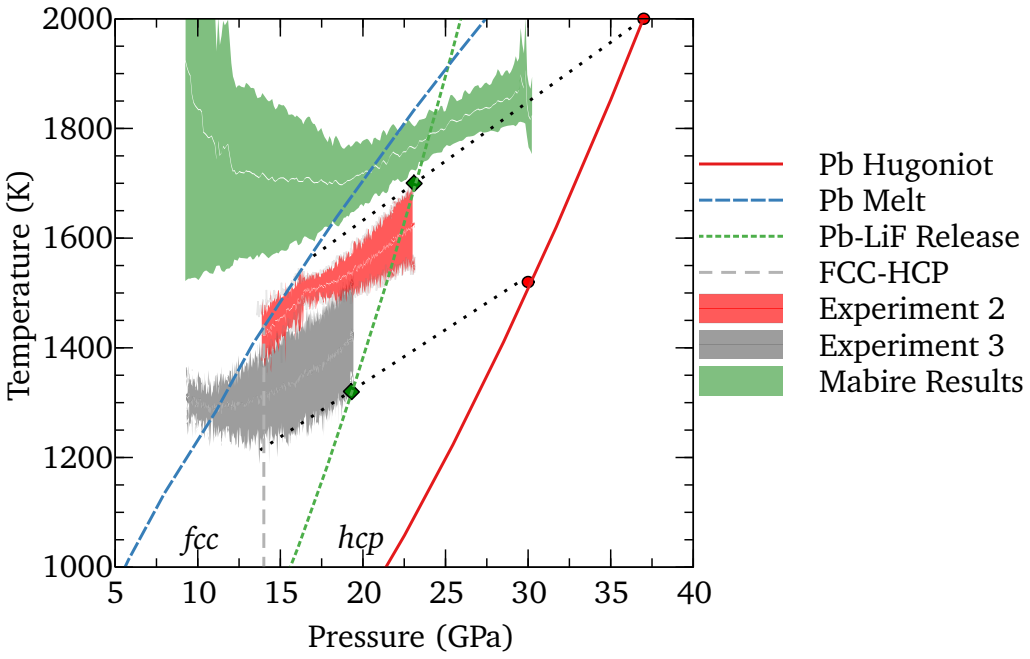


Figure 9.2: Apparent temperature ranges (*i.e.* maximum and minimum temperatures across all channels) recorded during experiments plotted against interface pressure from experiments 2 and 3. Red dots indicate the predicted shocked state of the material. Green squares indicate predicted equilibrium release state. Also shown is the data reported by Mabire [115]

loss measures to prevent or reduce LiF luminescence have been developed, tested and validated on subsequent experiments.

The efficacy of tungsten slurry, in conjunction with various other measures, has been investigated. While the slurry significantly reduced the magnitude of the emitted light, spurious emission was still observed on some channels but temperature measurements were successfully made. Very little spurious emission was detected in the infrared part of the spectrum suggesting it may be possible to avoid the phenomena by appropriate selection of wavelength measurement bands.

The physical mechanism that generates the emission is not well understood. It has previously been attributed as related to release (and limiting release did reduce emission in the experiments here) but the temporal distribution of emission on the latest experiments raises further questions if this is the only mechanism.

To summarise, lithium fluoride luminescence remains an issue but there are partial solutions in many applications. Increasing window size to larger than the

impact plate appears to resolve the issue, if this is not possible, using a slurry and infrared wavelengths enables measurements to be made. Finally, increasing sample radiance (*e.g.* higher temperatures) helps reduce the impact of any emission.

9.7 Future work

There are a number of areas where further research would improve pyrometry measurements.

One of the challenges to designing high speed radiometer systems is the small number of high speed detectors that operate in the infrared, thus the development of high sensitivity, high speed detectors that operate above 1700 nm would be beneficial. Specifically, high speed detectors sensitive to longer wavelengths would allow systems with reduced minimum detectable temperature.

One of the sources of uncertainty in determining bulk temperature with pyrometry is uncertainty in thermal transport at the observable interface, the measurement of thermal transport properties at high pressure and temperature would reduce this uncertainty. Furthermore, the development work required is minimal as diamond anvil cells allow pressures over 100 GPa to be accessible, along with temperatures up to 2000°K, and the measurement of thermal conductivity of a metal in a DAC has been reported[82].

A number of the experiments reported here have been affected by spurious signals from lithium fluoride luminescence due to the choice of window. Furthermore, although the issue was significantly reduced, minor artefacts persisted despite a number of modifications to prevent the issue. There are two potential solutions to the issue, one, an increased understanding of the mechanism of luminescence may allow the phenomenon to be prevented. Two, if alternative shock windows materials can be found that are compatible with pyrometry measurements, experiments could use those materials but without a better understanding of the light generation mechanism a similar issue cannot be ruled out.

As discussed, emissivity uncertainty is a significant issue thus any developments that improve reflectivity diagnostic techniques would be highly valuable. A

particular area of benefit may be brighter modulated sources, for pyrometry measurements at higher temperatures the source radiance increases significantly. High source radiance means that any reflectivity diagnostic needs to use a source that is, at least, a significant fraction of the radiance of the source.

Appendices

A

Calibration and analysis

A.1 Calibration procedure

For the experiments presented here the pyrometer systems were calibrated before use. The calibration method is described in the following section.

For this method it has been chosen to use a 'blackbody' source as the calibration reference. A black body source operates by heating a cavity to a specified temperature. Pyrometry signals generated during high speed plate impact experiments are expected to consist of a fast rising ($\sim$10 ns), short duration ($<$1 μs) pulse. The response of PMTs to such pulses is not necessarily well defined by laboratory experiments using continuous illumination. As such it is preferable to create signals that are as close as possible to those generated by shock. It is not possible to rapidly modulate the temperature of a blackbody thus another method is required to modulate the light collected from the blackbody. The system used here is a combination of an optical chopper and a high speed shutter, see Figure A.1.

An optical chopper is a rotating slotted disc; this modulates the light by periodically allowing light to pass. Using an optical chopper a minimum pulse length of 10 μs is achievable for a 1 mm diameter source. However, the shortest pulses are achieved at the highest rotational speeds, resulting in a relatively high pulse rate. This high rate can mean the average optical power is sufficient

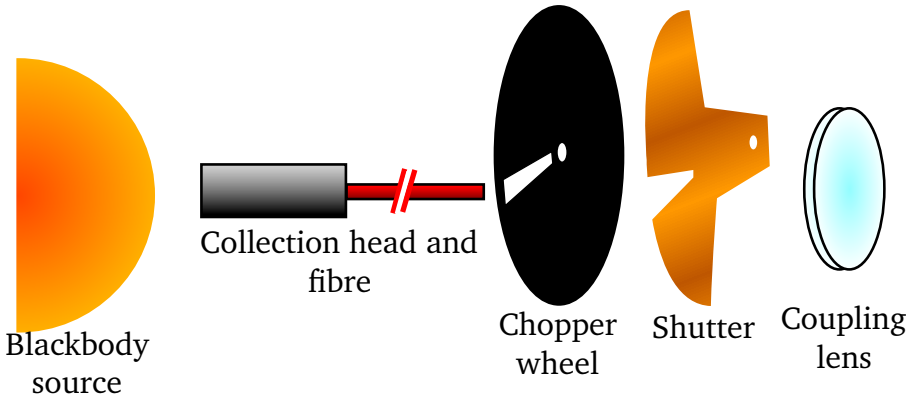


Figure A.1: Schematic diagram of the optical pulse forming system used to modulate the emission from the black body.

to affect the response PMTs. To prevent multiple pulses an optical shutter is used to select a single pulse. The shutter consists of a slotted foil attached to an actuating arm (see Figure A.1).

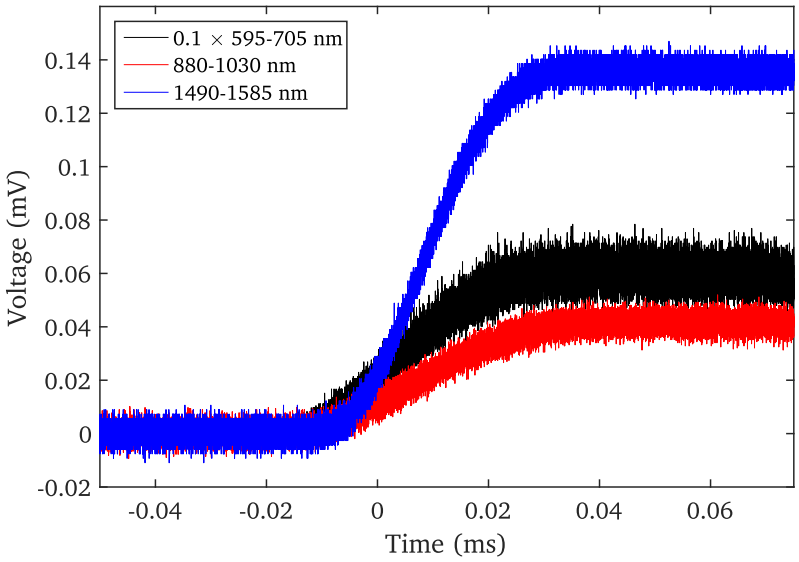


Figure A.2: Voltage output from the radiometry system viewing a 1017 K temperature blackbody.

The calibration procedure consists of setting the blackbody source to a series of temperatures and taking radiance measurements with the pyrometry system. This procedure creates a number of temperature-voltage pairs. While technically, a series of temperature-voltage pairs is all that is required to measure temperature an additional step is used.

A model of the pyrometer system has been developed; the models contains the following details:

- Spectral emission of a blackbody
- Detector active area, responsivity (including any gain)
- Probe collection efficiency
- Manufacturer reported spectral response of filters and dichroic mirrors

Rather than use the voltage-temperature pairs alone, the measured voltage-temperature pairs are compared to predicted voltage-temperature pairs. It has been found that usually the discrepancy between the experimental data and the model can be described by a single scaling factor. Figure A.3 shows a comparison between a series of measurements and a the associated model prediction.

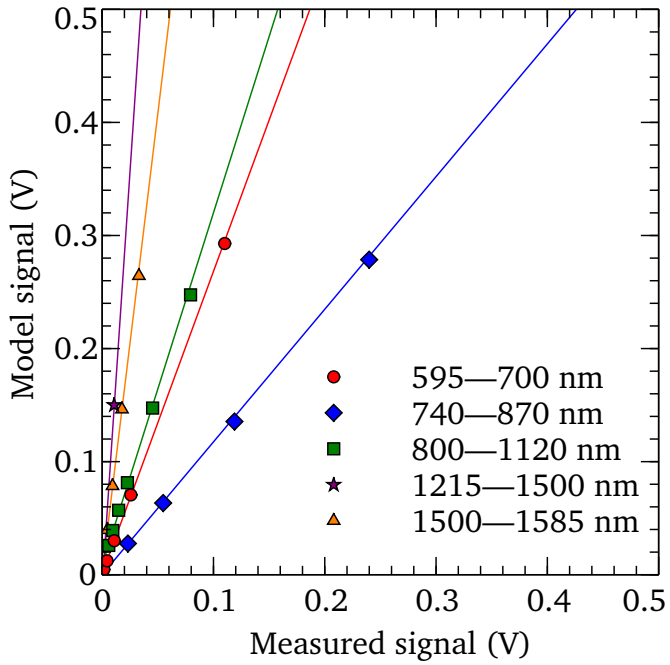


Figure A.3: Plot of predicted voltages against calibration measurements at a number of temperatures.

A.2 Analysis

The calibrated voltage-temperature model can be used to convert voltage to temperature for a blackbody source, however, in all the experiments presented here the sample was not a blackbody. To account for the non-ideal emissivity of the samples further analysis was required.

Specifically, emissivity was calculated by taking the mean emissivity of the sample over the wavelength interval associated with the bandpass of the channel. The emissivity was based on literature data, but scaled if a dynamic measurement of reflectivity was available. The voltage data is then divided by the mean emissivity to calculate the blackbody equivalent voltage (because emissivity is always unity or below, the value of the voltage data increased).

There is a final step to allow the blackbody equivalent voltage data to be converted to temperature. This step is required because although a calibrated temperature-voltage model has been defined, the model calculates voltage from temperature - not visa versa. To allow voltage to temperature conversion the calibrated model is used to generate a range of voltages for corresponding temperatures, typically an interval of 5°K was used here. To convert a blackbody equivalent voltage to a temperature the voltage-temperature range is interpolated to allow any voltage within the created range to be converted to a temperature.

A.3 Voltage to temperature analysis script

MATLAB code for the analysis of voltage data.

```
%% Ch1 Temperature Calc
% Temperature analysis script
% requires:
% remove variables from workspace
clear modelVolts volts
% downsample voltage data
data = decimate(-s02.ch1.v, 40);
% correct any zero offset in data
data = (1/(1-0.75))*(data - mean(data(1:50)));
```

```
% downsample time data
time1 = decimate(s02.ch1.t, 40);
% set range of temperatures and interval for array
t0 = 900;
t1 = 2500;
dt = 5;
% create model voltage output for range of temperatures
for i = 1:(t1-t0)/dt,
    ans = filterInputDeckFuncEOS(t0 + dt*i);
    output(i) = ans(1);
end
% get data for fitting (from calibration)
temps = [0; 1173; 1173; 1223; 1273; 1323; 1373; 1373; 1423; 1473];
volts = [0; 4.11E-02; 3.98E-02; 7.82E-02; 1.41E-01; 2.34E-01; ...
3.05E-01; 4.08E-01; 6.11E-01; 9.07E-01];
% create model data at temperatures of calibration
for i = 1:length(temps),
    funcOut = filterInputDeckFuncEOS(temps(i));
    modelVolts(i, 1) = funcOut(1);
end

% fit calibration data with ax + b form to determine scaling factor
corrFacCoeffs = polyfit(volts, modelVolts, 1);
% plot calibrated results against model results with fit
figure(1)
plot(volts, modelVolts, 'o', volts(1):1e-4:volts(end), ...
    polyval(corrFacCoeffs, volts(1):1e-4:volts(end)))
% convert each voltage point to a temperature
for j = 1:length(data),
    ch1TempOut(j) = threePtInterp(polyval(corrFacCoeffs, data(j)),...
     output, t0+dt:dt:t1);
end
% plot temperature data
figure(2)
plot(ch1TempOut, '.')
```

A.4 Filtering of radiance data

A number of data channels were corrupted with periodic noise, see Figure A.4. To attempt to improve the quality of the data some filtering techniques were applied to the data. The filtering technique used was the 'windowed sinc' filter, described by Smith [100].

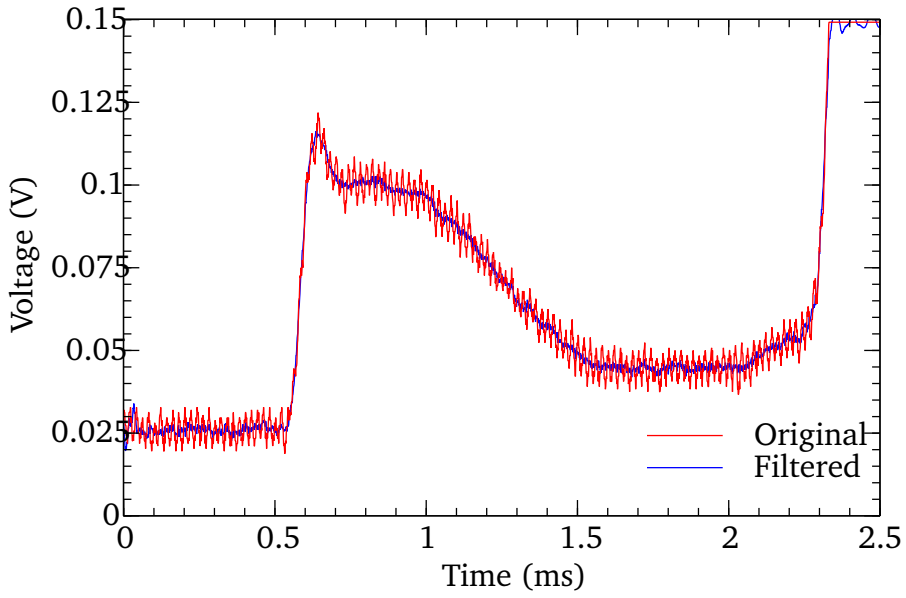


Figure A.4: Filtered and unprocessed voltage trace from channel 2 of the pyrometer 2 system on experiment 2, reported in Chapter 6.

Applying the filter as a low pass filter requires convolving the data with a kernel given by the expression,

$$K\frac{\sin\left(2\pi f_c\left(i-M/2\right)\right)}{i-M/2}\left[0.42-0.5\cos\left(\frac{2\pi i}{M}\right)+0.08\cos\left(\frac{4\pi i}{M}\right)\right], \qquad \text{(A.1)}$$

where K is a normalisation constant, f_c is the cut-off frequency and M defines the 'sharpness' of the filter. This approach can be used to generate a high pass filter by inverting the kernel before the convolution operation.

For this application a 'band reject' filter is required that removes signals in the small bandwidth associated with the periodic noise. To create a band reject filter, the signal is low pass filtered to the start of the rejection band and high pass filtered to the end of the rejection band. The sum of the resultant signals is the filtered data. An illustrative example is helpful in understanding this process.

A.4.1 Filtering example

The original data was filtered in a number of locations periodic noise was identified. Periodic noise is seen as spikes in the power spectrum of the signal, see Figure A.5. Unwanted periodic signals were identified in regions 0.032–0.064 GHz,

0.080–0.112 GHz and 0.508–0.494 GHz. These were removed using the process detailed above. The recovered signal is shown in Figure A.4.

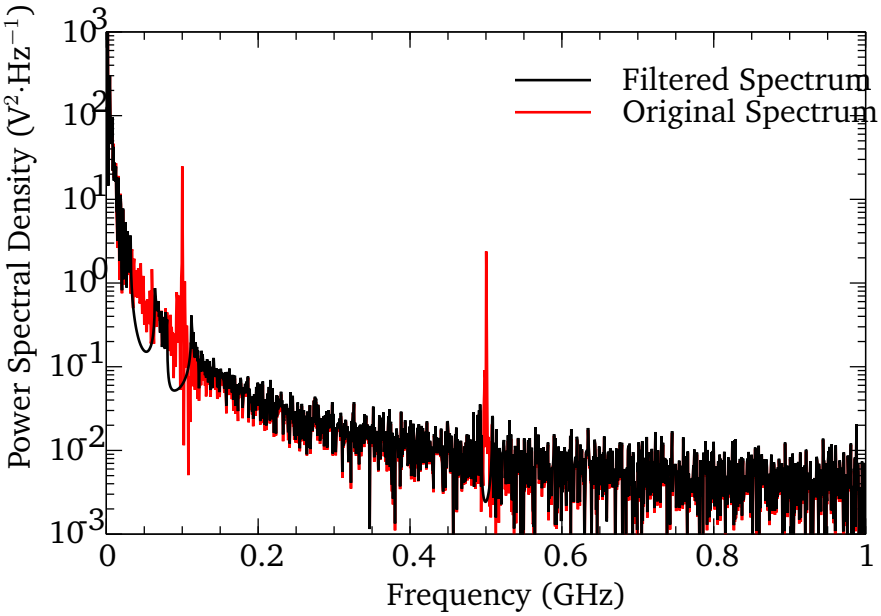


Figure A.5: Power spectral density of the unprocessed voltage trace and the spectrum of the filtered voltage trace.

A.5 ZEMAX probe modelling

It is not obvious what the most appropriate design for a focussing probe should be, the specific challenges for a component in a plate impact experiment are that:

- A numerical aperture of as close to 0.48 is required to match the optical fibre.
- The optical system needs to operate over a wide spectral range (design wavelengths of 0.7 μm, 1.2 μm and 1.7 μm were used).
- The system needs to be relatively low cost due to the destructive nature of the experiments.

Three designs have been considered, using plano-convex, achromats and aspherical lenses.

Lens Type	RMS Spot size (μm)	
	Field 1	Field 2
Achromat	95.9	93.3
Asphere	178	210
Plano-convex	450	479

Table A.1: Table showing the calculated spot size from a range of optical probe designs.

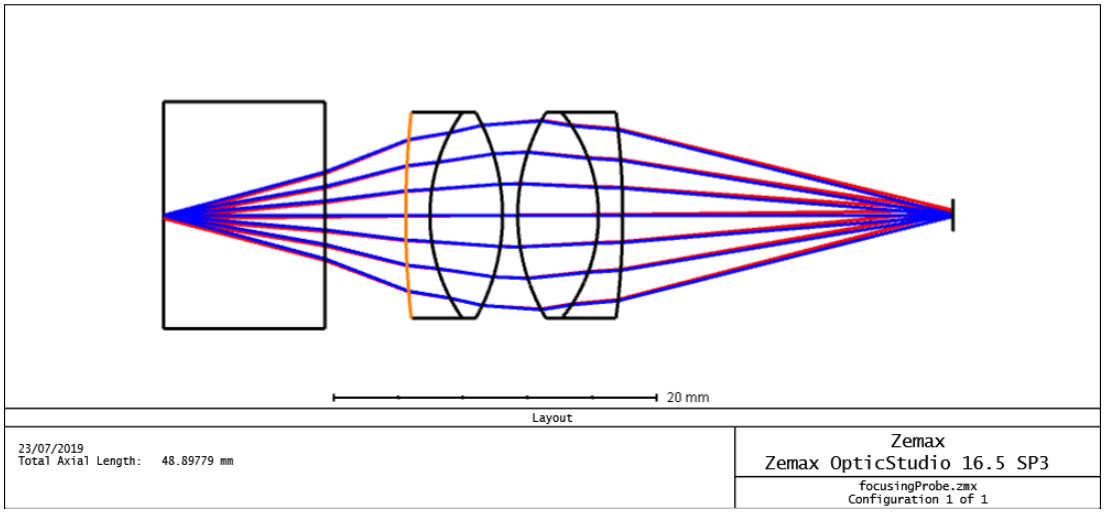


Figure A.6: Ray trace diagram of the focusing probe based on achromat lenses.

The procedure for designing the probes systems is to create the optical system. Then optimise the layout using a default merit function.

The key metrics for performance were spot size.

A.6 STFT Analysis

Photon Doppler velocimetry (PDV) is based on the Doppler effect. Changes in the wavelength due to reflection from moving objects can be related to velocity using the expression,

$$v = \frac{\lambda_0}{2}\Delta f, \tag{A.2}$$

Where v is velocity, λ_0 is the illuminating wavelength and Δf is the change in frequency of the signal.

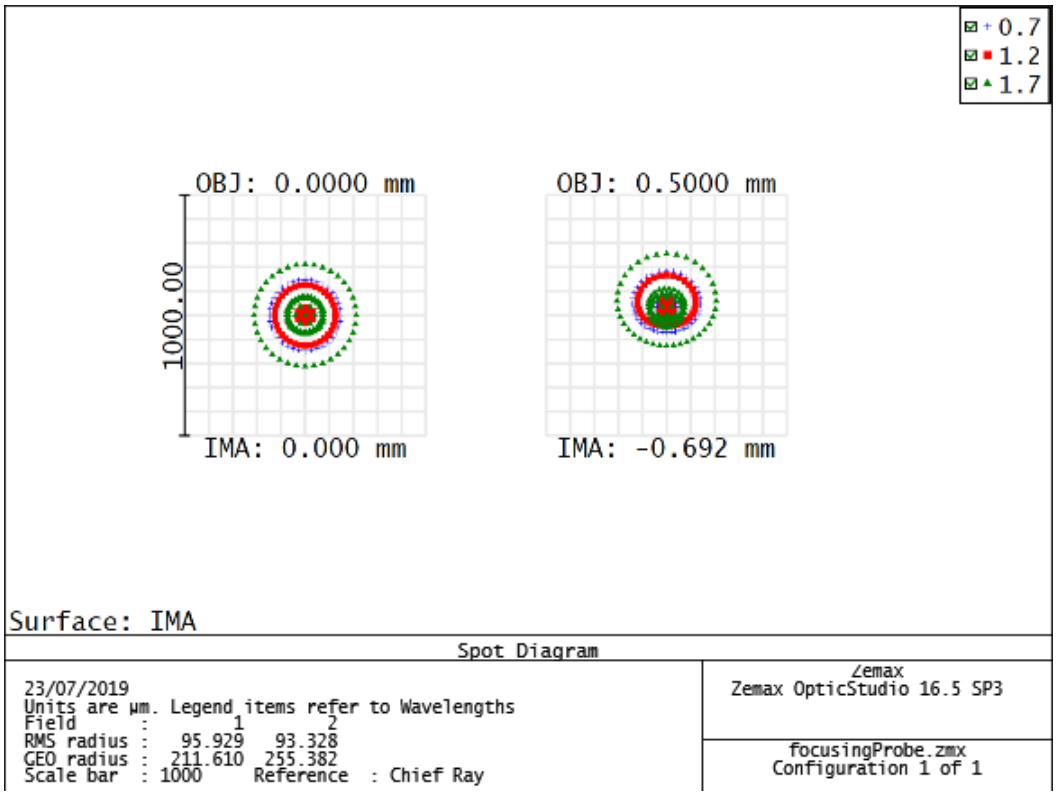


Figure A.7: Spot size diagram of the focusing probe based on achromat lenses.

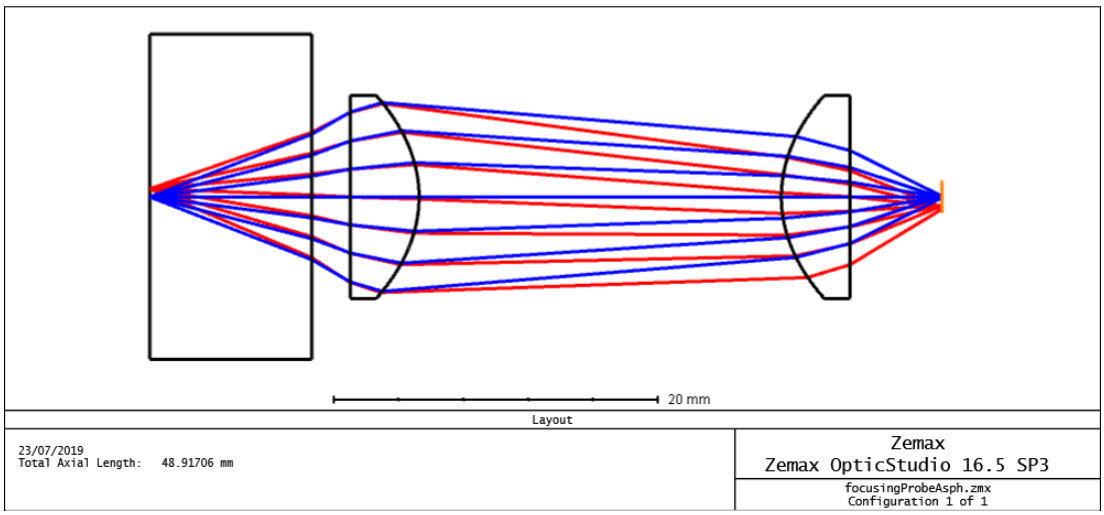


Figure A.8: Ray trace diagram of the focusing probe based on aspheric lenses.

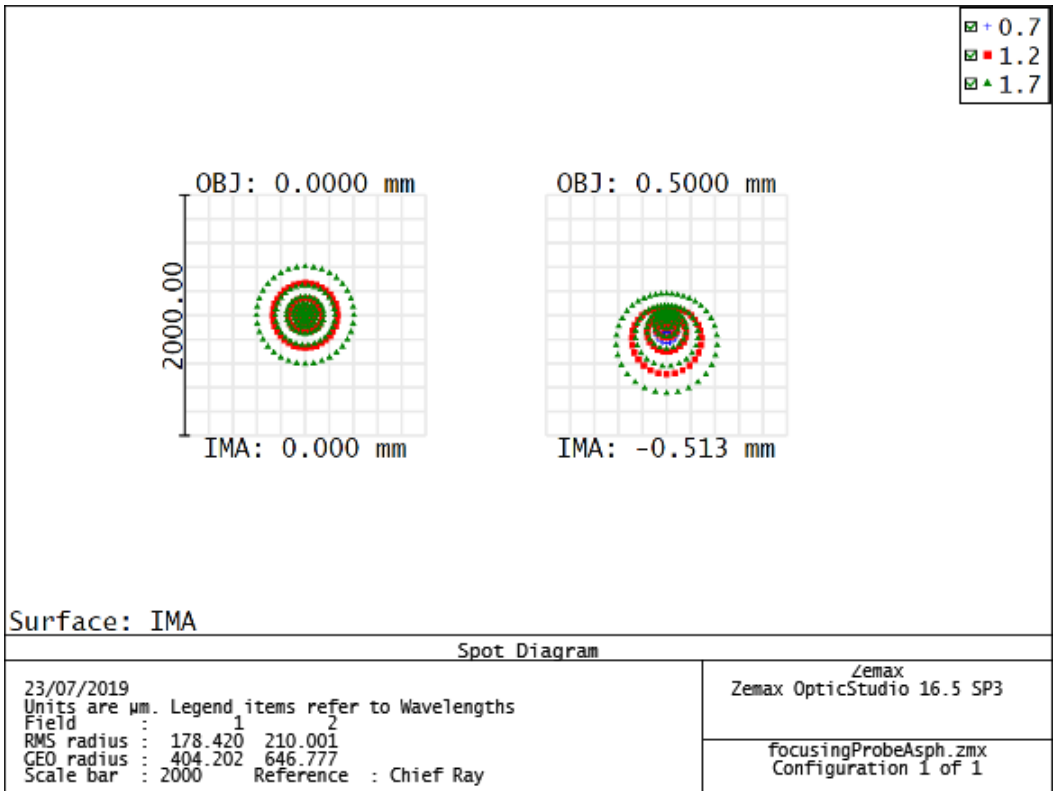


Figure A.9: Spot size diagram of the focusing probe based on aspheric lenses.

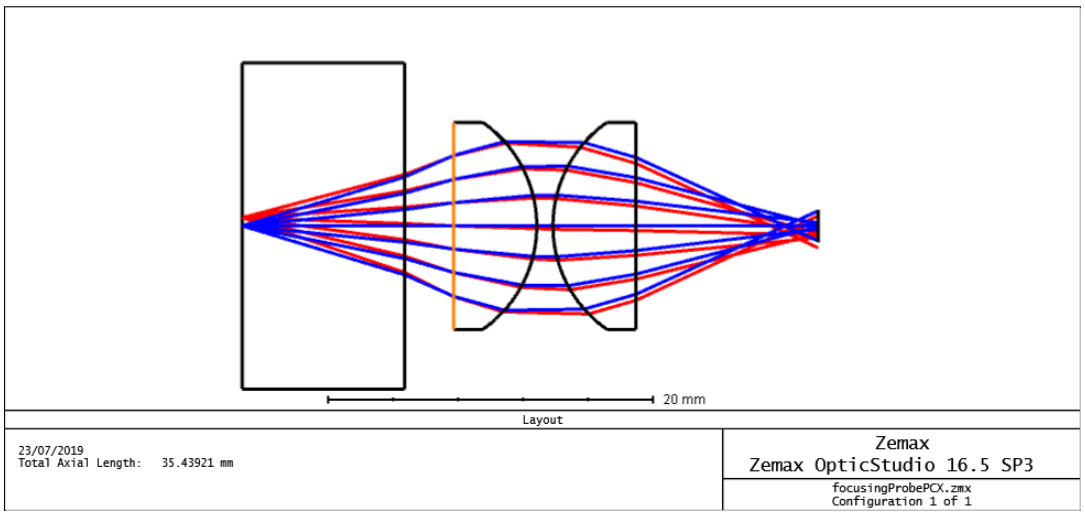


Figure A.10: Ray trace diagram of the focusing probe based on plano-convex lenses.

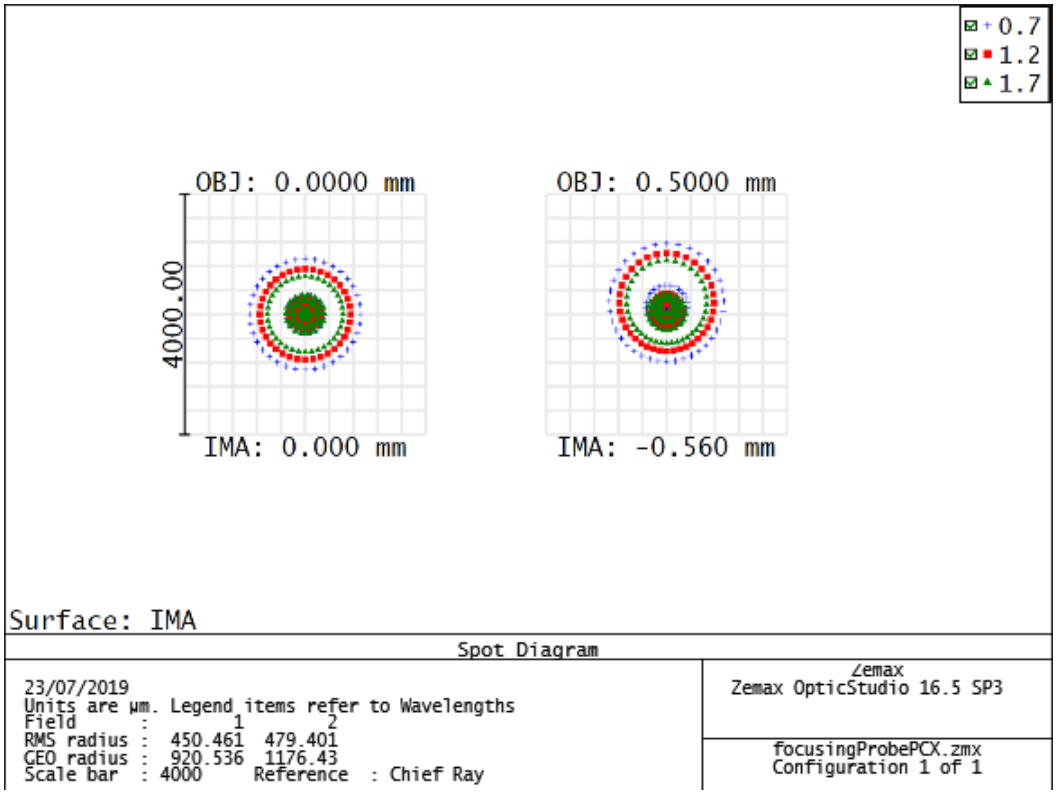


Figure A.11: Spot size diagram of the focusing probe based on plano-convex lenses.

The analysis of photon Doppler velocimetry (PDV) data has been conducted using the short-time Fourier transform (STFT), combined with a peak interpolation algorithm to determine frequency peaks (which are then converted to velocity).

The procedure for analysis is as follows:

1. A small section of the signal is selected from the data trace (typically a few ns).

2. A window function is applied to the section (see [105, 106], usually Hamming).

3. The discrete Fourier transform (DFT) of the windowed section is calculated (using MATLAB 'fft' function). A zero pad value of 4 times the initial data length was used.

4. The process of creating DFT data for a small section is repeated for multiple sections.

5. A region of interest (a wavelength range in each DFT section) is chosen by calculating the logarithm of the absolute values and then visualising the data in 2D. Regions are then chosen using prior knowledge to select the areas where signals of interest are present.

6. For each DFT region of interest the logarithm of the values are taken. The peak value is found and a quadratic interpolation based on the peak value and two neighbouring values determined (this is equivalent to fitting a Gaussian in non-logarithm values [128]).

This analysis process produces a velocity value at each time period that corresponds with the short time associated with the initial section of the data.

B

Supplementary experimental results

B.1 Initial 100 mm bore plate impact experiments

X Position (mm)	Y Position (mm)	Breakout Time (μs)
20.58	25	-0.238
-18.53	19.55	-0.172
13.96	14.4	0.260
-15.96	-4.80	0.321
36.83	-10.25	-0.255
-25.00	-18.65	-0.134
16.23	-22.05	0.270
7.64	-37 .00	-

Table B.1: Table summarising break out times measured in experiment 1 of the initial 100 mm bore plate impact experiments.

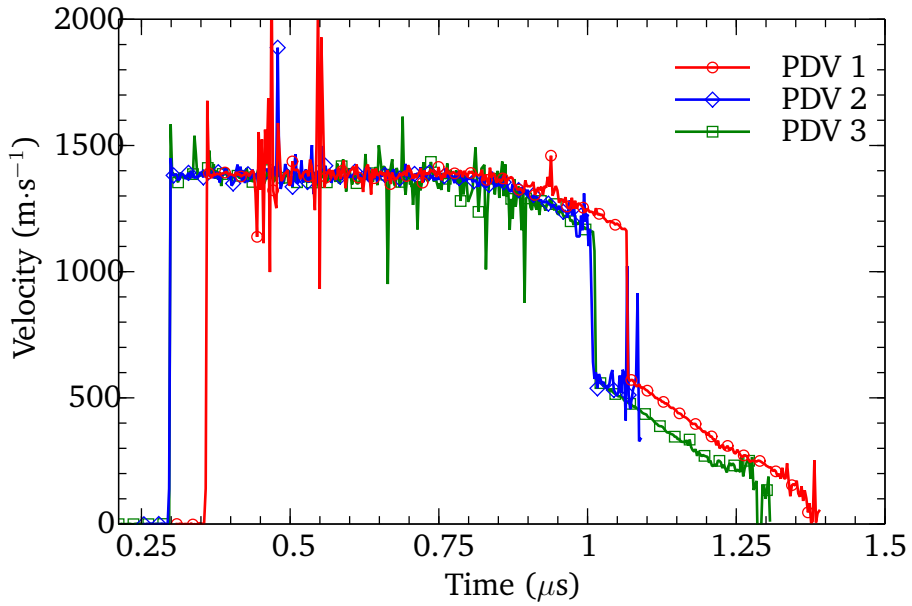


Figure B.1: Plot of particle velocity data at the tin-lithium fluoride interface from experiment 1. The velocities are corrected using a window correction factor [103].

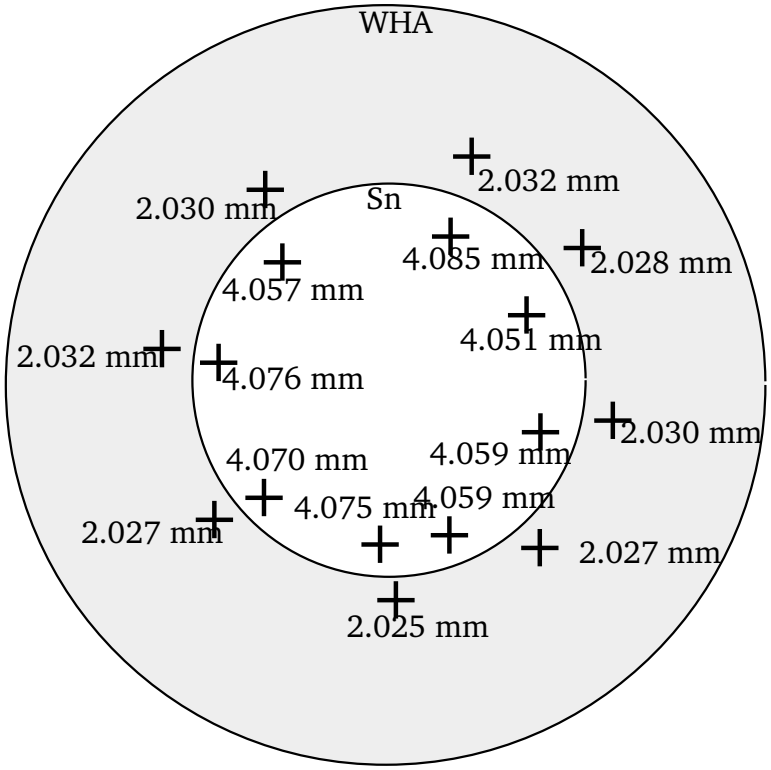


Figure B.2: Thickness of tin target from initial experiment 1 as measured using a micrometer.

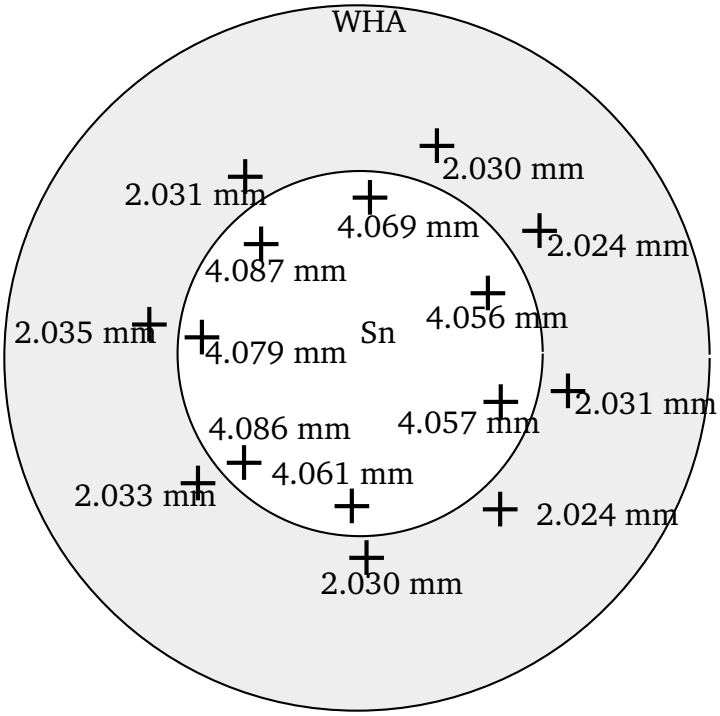


Figure B.3: Thickness of tin target from initial experiment 2 as measured using a micrometer.

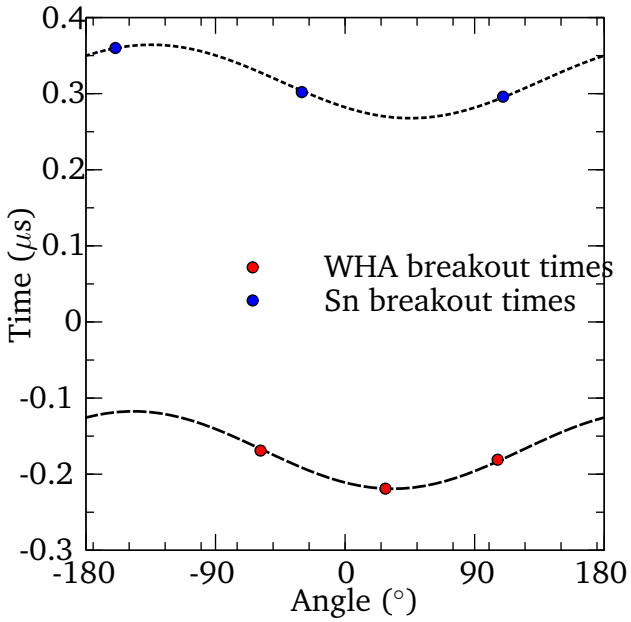


Figure B.4: Plot of the shock breakout time data and fitted sinusoid function from initial experiment 2.

B.2 Glue thickness measurements for collaborative experiments

Target	Thickness Notes
2	6 μm, Imperial S1
5	15 μm in centre (worst point), Imperial S4
6	8 μm (worst), 3 μm in centre, AWE S1
7	13 μm (in centre), 24 μm at one edge, AWE S4
8	16 μm (in centre), 6 μm at edges, US S4
9	4 μm (in centre), 4 μm at edges, US S1
10	3 μm, AWE S2
11	2-4 μm, US S2
12	2.5 μm, Imperial S2
13	2 μm (or better), US3
14	7 μm centre, 3-4 μm edges, Imperial S3
15	7.5 μm centre, 3-8 μm edges, AWE S3

B.3 Reflectivity experiments

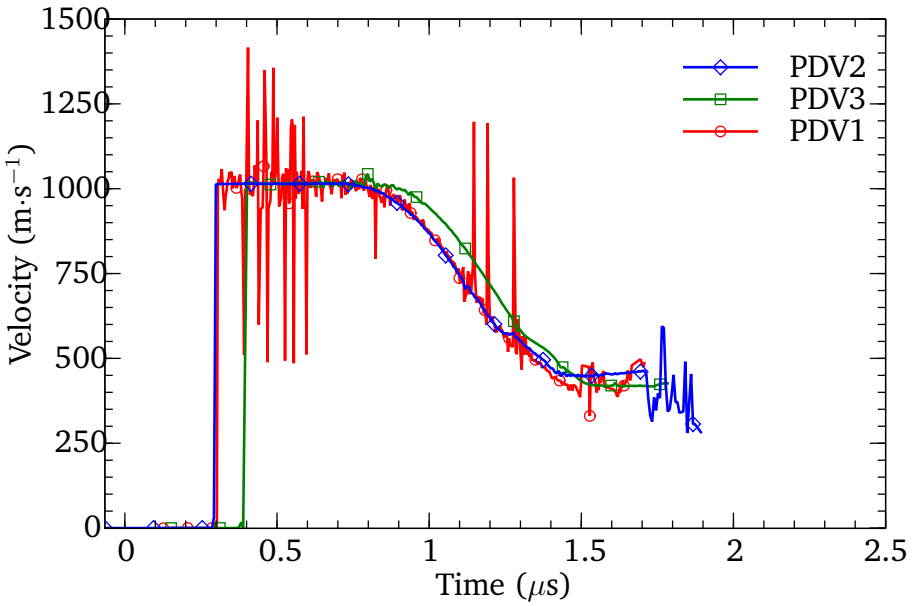


Figure B.5: Plot of particle velocity data at the tin-lithium fluoride interface from experiment 1. The velocities are corrected using a window correction factor [103].

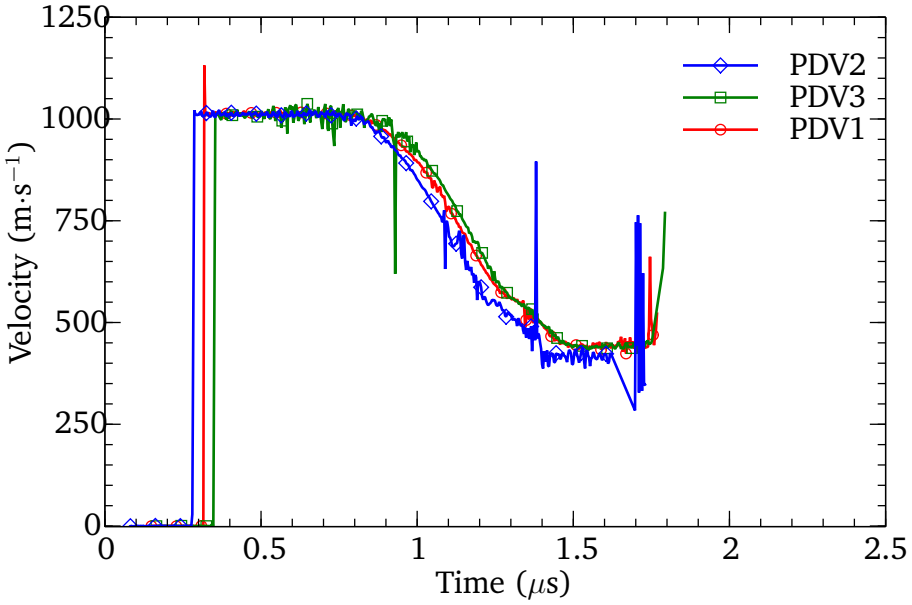


Figure B.6: Plot of particle velocity data at the tin-lithium fluoride interface from experiment 2. The velocities are corrected using a window correction factor [103].

C
Derivations

C.1 Rankine Hugoniot relations

As a shock wave progresses through a medium, Figure 1.4, it is possible to relate the properties on one side of a shock to those on the other. The relationship between the the states ahead and behind the shock are known as the Rankine-Hugoniot equations which are derived from conservation laws.

From conservation of mass it can be determined that,

$$\rho_1 u_1 = \rho_2 u_2, \tag{C.1}$$

where ρ and u are the density and particle velocity and the subscript denotes whether the variable is ahead, denoted 1, or behind the shock, denoted 2.

From conservation of momentum, it can be determined that,

$$\rho_1 u_1^2 + p_1 = \rho_2 u_2^2 + p_2, \tag{C.2}$$

where, in addition to the previously defined variables, p is pressure and the subscripts are as above.

Finally from conservation of energy, it can be determined that,

$$\rho_1 u_1 \left(e_1 + \frac{1}{2} u_1^2 + \frac{p_1}{\rho_1} \right) = \rho_2 u_2 \left(e_2 + \frac{1}{2} u_2^2 + \frac{p_2}{\rho_2} \right), \tag{C.3}$$

where, in addition to the previously defined variables, e is internal energy and the subscripts are as above. It should be noted that as there are four variables, ρ, u, p and e and three equations it is not possible to solve these expressions without further information.

A commonly used relation that has been found empirically and allows calculations to be completed is that shock speed is linearly dependent on particle velocity through the relation,

$$u_s = c + su_p, \tag{C.4}$$

where u_s is the shock velocity, u_p is the particle velocity, c is a constant (often close to the sound speed in the material) and s is a proportionality constant.

Starting with Equation C.2 and setting the initial pressure to zero we have,

$$p_1 = 0, \tag{C.5}$$

$$u_1 = u_s, \tag{C.6}$$

and

$$u_2 = u_s - u_p. \tag{C.7}$$

Resulting in,

$$p_2 = \rho_1 u_s u_p \tag{C.8}$$

Using Equation C.4 we get,

$$p_2 = \rho_1 u_p \left(c + su_p\right) \tag{C.9}$$

Typical applications of the Rankine-Hugoniot relations are to determine the density of the shocked state using the difference between the speed of the shock and the shocked particles and the initial density.

From

$$\rho_1 u_s = \rho_2 \left(u_s - u_p\right) \tag{C.10}$$

define $v = 1/\rho$:

$$\frac{u_s}{v_1} = \frac{u_s - u_p}{v_2} \tag{C.11}$$

Rearrage to:

$$u_s = \frac{u_p v_1}{v_1 - v_2} \tag{C.12}$$

Using Equation C.4:

$$\frac{u_p v_1}{v_1 - v_2} = c + s u_p \tag{C.13}$$

$$\frac{v_1}{v_1 - v_2} - s = \frac{c}{u_p} + s \tag{C.14}$$

$$u_p = \frac{c\left(v_1 - v_2\right)}{v_1 - s\left(v_1 - v_2\right)} \tag{C.15}$$

Using $P = \frac{u_s u_p}{v_1}$

$$P = \frac{1}{v_1}\frac{u_p v_1}{v_1 - v_2} u_p \tag{C.16}$$

$$P = \frac{c^2\left(v_1 - v_2\right)}{\left[v_1 - s\left(v_1 - v_2\right)\right]^2} \tag{C.17}$$

Thus assuming the linear relationship between shock velocity and particle velocity allows an equation of state that describes the relationship between pressure and volume to be created. Furthermore using Equation C.3 we can express the energy as:

Combine conservation of mass and conversation of momentum:

$$p_2 - p_1 = \rho_1 u_1^2 - \rho_2 u_2^2 \tag{C.18}$$

$$p_2 - p_1 = \rho_1 u_1^2 - \frac{\rho_1^2 u_2^2}{\rho_2} \tag{C.19}$$

$$p_2 - p_1 = u_1^2 \frac{\rho_1}{\rho_2}\left(\rho_2 - \rho_1\right) \tag{C.20}$$

$$u_1^2 \frac{\rho_1}{\rho_2} = \frac{p_2 - p_1}{\rho_2 - \rho_1} \tag{C.21}$$

Also rearrange conservation of momentum equation:

$$\rho_1 u_1^2 + p_1 = \rho_2 u_2^2 + p_2 \tag{C.22}$$

$$u_2^2 = \frac{\rho_1}{\rho_2} u_1^2 + \frac{p_1}{\rho_2} - \frac{p_2}{\rho_2} \tag{C.23}$$

Combing Equation C.23 and the energy equation:

$$e_1 + \frac{1}{2}u_1^2 + \frac{p_1}{\rho_1} = e_2 + \frac{1}{2}\frac{\rho_1}{\rho_2}u_1^2 + \frac{1}{2}\frac{p_1}{\rho_2} - \frac{1}{2}\frac{p_2}{\rho_2} + \frac{p_2}{\rho_2} \tag{C.24}$$

Collecting terms:

$$e_1 + \frac{1}{2}u_1^2 - \frac{1}{2}\frac{\rho_1}{\rho_2}u_1^2 + \frac{1}{2}\frac{p_1}{\rho_1} = e_2 + \frac{1}{2}\frac{p_1}{\rho_2} + \frac{1}{2}\frac{p_2}{\rho_2} \tag{C.25}$$

Substitute Equation C.21 :

$$e_1 + \frac{1}{2}\frac{\rho_2}{\rho_1}\frac{p_2 - p_1}{\rho_2 - \rho_1} - \frac{1}{2}\frac{p_2 - p_1}{\rho_2 - \rho_1} + \frac{p_1}{\rho_1} = e_2 + \frac{1}{2}\frac{p_1}{\rho_2} + \frac{1}{2}\frac{p_2}{\rho_2} \tag{C.26}$$

$$e_1 + \frac{1}{2}\frac{p_2 - p_1}{\rho_2 - \rho_1}\left(\frac{\rho_2}{\rho_1} - 1\right) + \frac{p_1}{\rho_1} = e_2 + \frac{1}{2}\frac{p_1}{\rho_2} + \frac{1}{2}\frac{p_2}{\rho_2} \tag{C.27}$$

$$e_1 + \frac{1}{2}\frac{p_2 - p_1}{\rho_2 - \rho_1}\frac{1}{\rho_1}(\rho_2 - \rho_1) + \frac{p_1}{\rho_1} = e_2 + \frac{1}{2}\frac{p_1}{\rho_2} + \frac{1}{2}\frac{p_2}{\rho_2} \tag{C.28}$$

$$e_1 + \frac{1}{2}\frac{p_2}{\rho_1} + \frac{1}{2}\frac{p_1}{\rho_1} = e_2 + \frac{1}{2}\frac{p_1}{\rho_2} + \frac{1}{2}\frac{p_2}{\rho_2} \tag{C.29}$$

Collecting terms:

$$e_2 - e_1 = \frac{1}{2}\left(\frac{p_2}{\rho_1} - \frac{p_2}{\rho_2} + \frac{p_1}{\rho_1} - \frac{p_1}{\rho_2}\right) \tag{C.30}$$

Expand the expression:

$$e_2 - e_1 = \frac{1}{2}(p_2 + p_1)(v_1 - v_2) \tag{C.31}$$

$$e_2 - e_1 = \frac{1}{2}(p_2 + p_1)\left(\frac{1}{\rho_1} - \frac{1}{\rho_2}\right) \tag{C.32}$$

$$e_2 - e_1 = \frac{1}{2}\left(\frac{p_2}{\rho_1} - \frac{p_2}{\rho_2} + \frac{p_1}{\rho_1} - \frac{p_1}{\rho_2}\right) \tag{C.33}$$

Since e_1 and p_1 can be assumed to be zero we have the expression:

$$e_2 = \frac{1}{2}p_2(v_1 - v_2) \tag{C.34}$$

This can be combined with the expression for $P(v_1, v_2, c, s)$ to give an expression for energy in the same terms:

$$E = \frac{c^2(v_1 - v_2)^2}{[v_1 - s(v_1 - v_2)]^2} \tag{C.35}$$

C.2 1D state

C.2.1 x-t Diagrams

The Rankine-Hugoniot relations are derived for media infinite in both breadth and depth, thus when conducting shock experiments it is necessary to consider the practical factors that cause experiments to deviate from the theoretical ideal. While experiments obviously do not consist of infinite domains there are conditions when the practical constraints can be ignored, this is often referred to as the '1D state'. There are a few techniques to visualise the times and regions that will be 1D in a shock experiment.

One of the techniques that is useful for visualising the effect of the finite thicknesses of components in the 'x-t diagram' which visualises the experimental system with position on the abscissa and time on the ordinate. This visualisation includes interfaces and waves (both shock and release) and is simply a plot of the position of the feature (usually at the centre of the experiment) over time. An example of such a diagram is shown in Figure C.1.

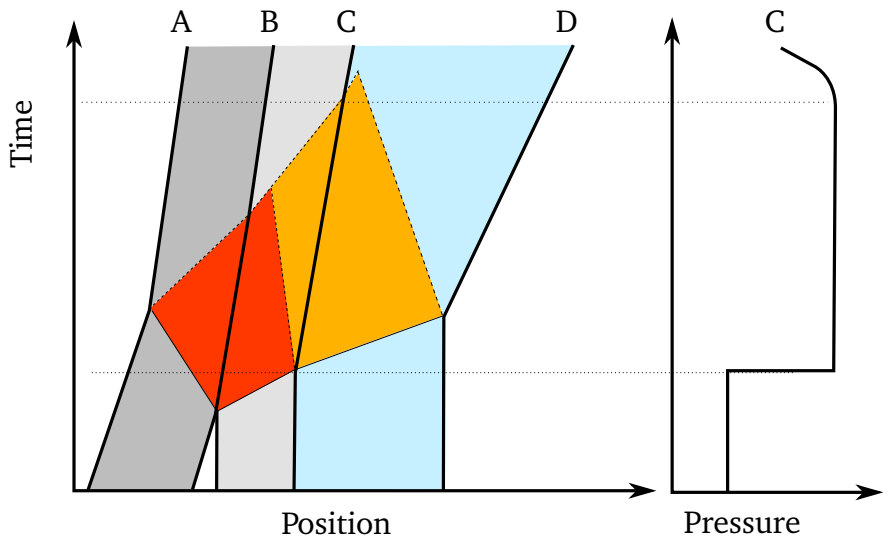


Figure C.1: Example of an x-t visualisation. The diagram illustrates the x-t diagram generated by an impact plate (denoted by interfaces A-B) impinging on a lower impedance sample (B-C) that is attached to a window (C-D). On impact a shock is generated in the impact plate and the sample. When the shocks reach interfaces with lower impedance material a release occurs. Also shown is the pressure at point C over the same time frame.

The benefit of x-t diagrams is that they clearly show how the finite thickness of components limits the potential duration of the 1D state. In the example shown the limiting factor is a release from the rear of the impact plate; this is often a limiting factor in plate impact experiments as increasing the impact plate thickness limits the impact velocity. It should be noted however that x-t analysis does not always shown the factor that limits 1D state durations, it is also necessary to consider lateral releases which are discussed next.

C.2.2 Lateral release waves

Another practical constraint that limits 1D state duration is lateral release due to the finite diameters of experimental components [107]. The physical cause of lateral releases is that, at the edge of a shock, the 1D assumption breaks down because there is no pressured region to support the shock–causing it to release. The release can be visualised as a release wave travelling perpendicular to the shock front in a direction away from the shock edge.

The region that is affected by release, and thus never enters are 1D state, can be visualised by a line that slopes away from the material edge. The angle of this line is determined by the ratio of the speed of the shock to the speed on the release (in the shocked material), a reasonable limiting case is that the release moves inward at the same velocity as the shock resulting in a 45° line. An example of this analysis applied to a plate impact sample assembly is shown in Figure C.2.

C.3 A method for the calculation of temperature

C.3.1 Shock temperature

Clearly to compare the results of temperature determined in an experiment to the temperature determined by a model it is necessary to use the model to calculate the temperature. The calculation of temperature at a Hugoniot state, based on a Grüneisen EoS now follows.

There are three steps to derive temperature using a Grüneisen EoS:

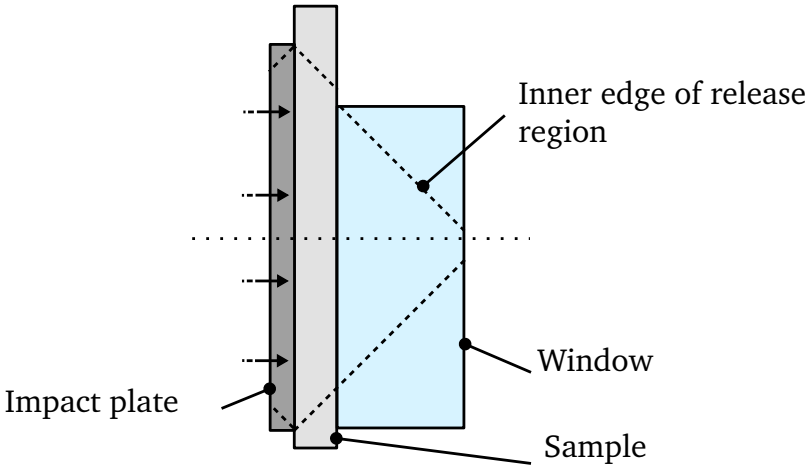


Figure C.2: An illustration of lateral releases in a plate impact experiment. While the released region can be approximated with a 45° boundary it is also necessary to consider the effect of component edges. As shown on the top half of the diagram, if there is no material at an interface to transmit a shock, the shock will release from the edge where material starts. In the bottom half of the diagram the component edges are not a limiting factor.

1. Calculate the isentrope in P-V space using the EoS.

2. Use thermodynamic relations to calculate temperature on isentrope.

3. Use the internal energy difference between the Hugoniot and isentrope and the material's heat capacity to calculate temperature on the Hugoniot.

C.3.2 Calculating the isentrope

From the Grüneisen EoS determine (see Equation 1.9) the relation between pressure and energy, given a reference state and gamma constant, is defined. This function describes a surface on which both the Hugoniot and isentrope lie however, further information is required to determine the position of the isentrope. The isentrope has a specific constraint that allows its position to be determined.

Specifically from the 1st law of thermodynamics:

$$dE = TdS - PdV. \tag{C.36}$$

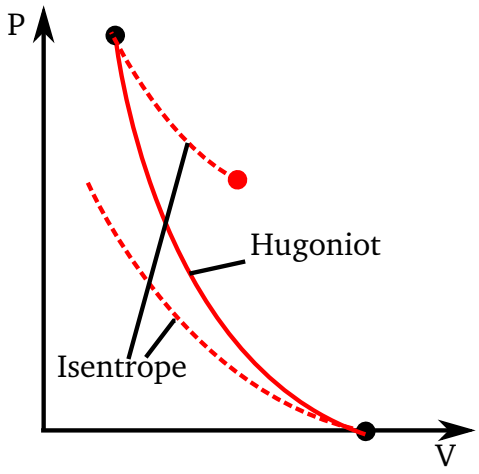


Figure C.3: Visualisation of isentrope and Hugoniot curves in the P-V plane.

By definition there is no change in entropy along an isentrope thus, $TdS = 0$. Rearrange the 1st law to get:

$$\frac{dE}{dV} = -P. \tag{C.37}$$

Substituting the expression for p from Equation 1.9 we get the relation:

$$\frac{de}{dv} = P_H(v) - \frac{\gamma}{v_0}(e - E_H(v)) \tag{C.38}$$

Where Hugoniot pressure, P_H is:

$$P_H = \frac{c^2(v_1 - v_2)}{[v_1 - s(v_1 - v_2)]^2} \tag{C.39}$$

and the energy along the Hugoniot, E_H is:

$$E_H = \frac{c^2(v_1 - v_2)^2}{[v_1 - s(v_1 - v_2)]^2} \tag{C.40}$$

An expression for $E_H(v)$ can be determined if this equation is integrated w.r.t. dv. This is a differential equation that can be solved numerically. Using Δ to illustrate a finite difference we can re-write Equation C.38 as:

$$\frac{\Delta e}{\Delta v} = P_H(\Delta v) - \frac{\gamma}{v_0}(e - E_H(\Delta v)). \tag{C.41}$$

If an initial energy-volume state is known then the above expression can be used to calculate energy along the isentrope, see below:

$$e_i = e_{i-1} + \Delta v \left(P_H(v) - \frac{\gamma}{v_0} \left(e_{i-1} - E_H(v) \right) \right). \tag{C.42}$$

The pressure on the isentrope can be determined using the Grüneisen EoS, Equation 1.9, together with the difference in energy. Thus it is now possible, using the above expressions, to calculate the density, pressure and energy along an isentrope, given an initial state.

C.3.3 Calculation of temperature on an isentrope

Temperature on an isentrope, given an initial state, can be calculated using two expressions:

- Maxwells's first relation,

$$\left(\frac{\partial T}{\partial v} \right)_S = - \left(\frac{\partial P}{\partial S} \right)_v. \tag{C.43}$$

- the definition of the Grüneisen parameter,

$$\gamma(v) = v \left(\frac{dp}{de} \right)_v. \tag{C.44}$$

The second term of Maxwell's relation is at constant volume, therefore the first law can be reduced to $dE = TdS$, and using the chain rule we can say:

$$\left(\frac{\partial P}{\partial S} \right)_v = \frac{\partial P}{\partial e} \frac{\partial e}{\partial S} \tag{C.45}$$

The following substitutions can then be made:

$$\left(\frac{\partial T}{\partial v} \right)_S = - \frac{\gamma(v)}{v} T. \tag{C.46}$$

Re-arranging and integrating both sides from an initial state (denoted to a 0 subscript) to a final state:

$$\int_{T_0}^{T} \frac{1}{T} dT = - \int_{V_0}^{V} \frac{\gamma(v)}{v} dv \tag{C.47}$$

$$[\ln T]_{T_0}^{T} = -\int_{V_0}^{V} \frac{\gamma(v)}{v} dv \tag{C.48}$$

$$\frac{T}{T_0} = \exp\left[-\int_{V_0}^{V} \frac{\gamma(v)}{v} dv\right] \tag{C.49}$$

A common approximation is:

$$\frac{\gamma(v)}{v} = \frac{\gamma_0}{v_0} \tag{C.50}$$

so:

$$\frac{T}{T_0} = \exp\left[-\frac{\gamma_0}{v_0}(v - v_0)\right] \tag{C.51}$$

Thus if the temperature of a state and γ_0 are known the temperature at a different volume can be calculated.

C.3.4 Calculation of release state temperature

In many plate impact experiments the sample is opaque thus pyrometry can only collect light emitted from the rear of the sample. This is often problematic for pyrometry measurements because a shocked free surface rapidly releases to zero pressure, with the associated adiabatic cooling. To limit the release an optical window is often used. This still does not allow measurement of Hugoniot states as they are created only instantaneously at the interface surface. As soon as a shock passes an interface, the pressure state changes to maintain equilibrium. For example, the impact of two identical materials will produce a shock with pressure and particle velocity states determined by the impact velocity and the material properties. If the shock reaches a lower impedance material the pressure in the original material will release until equilibrium is attained. A diagram of this process in P-u_p space is shown in Figure C.4.

Thus in the case where a release occurs it is necessary to perform further calculations to determine temperature in the final state. A commonly used assumption is that the release will follow the isentrope, thus to determine the released state the process outlined in section C.3.2 can be applied.

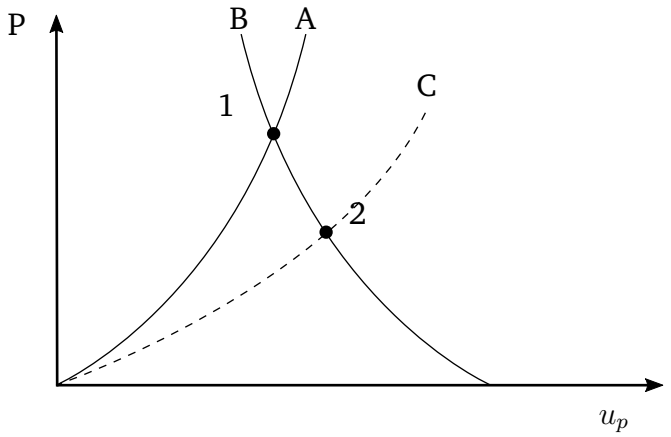


Figure C.4: Visualisation of a release into a window in the $P - u_p$ plane. Line A is the principal Hugoniot of the shocked material, which has been shocked to state 1. Line B is the principle Hugoniot reflected about point 1. Line C is the principal Hugoniot of the window material. The intersection of lines B and C determines the release state, point 2.

C.4 Percentage error transformation

An absolute error in reflectivity is the same error in emissivity,

$$\Delta_R = -\Delta_\epsilon, \tag{C.52}$$

where Δ_R is the absolute change in reflectivity and $\Delta\epsilon$ is the absolute change in emissivity. However, if proportional errors, δ, are defined such that,

$$\delta_R = \frac{\Delta_R}{R}; \quad \delta_\epsilon = \frac{\Delta_\epsilon}{\epsilon}, \tag{C.53}$$

the relation between errors in reflectivity and emissivity are not so simple. From Equation C.52 and C.53,

$$\delta_R R = -\delta_\epsilon \epsilon. \tag{C.54}$$

Rearranging gives,

$$\delta_\epsilon = \frac{R\delta_R}{\epsilon}. \tag{C.55}$$

Finally, using the complementarity of reflectivity and emissivity,

$$\delta_\epsilon = \frac{R\delta_R}{1-R}. \tag{C.56}$$

Thus a 10% error in reflectivity, when reflectivity is 0.9 gives a 90% error in emissivity.

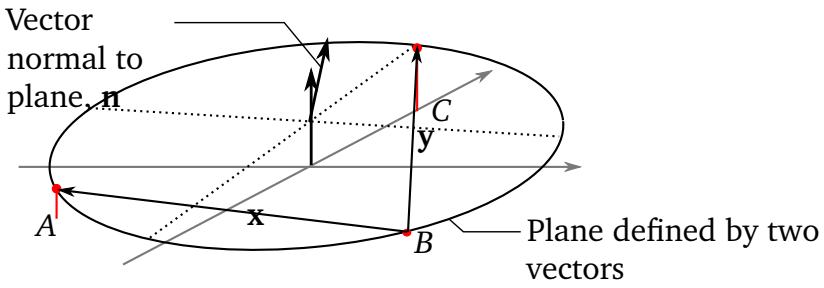


Figure C.5: Illustration of the determination of tilt from shock breakout times. A time measurement at three points a, b and c can be used to create two spatial vectors x and y. The two vectors define a plane; the crossproduct of the plane with a line parallel to the gun barrel will give the tilt of the shock plane.

C.5 Calculation of tilt

The spatial data that can be determined from the position, arrival time and velocity measurements can be used to determine two vectors that are in the plane of the shock surface. The cross product of these vectors is normal to the shock plane. Finally by calculating the dot product of the normal vector and a reference plane (for example normal to the target) allows the tilt angle to be calculated, see Figure C.5.

More formally, given three points *A*, *B* and *C* it is possible to define two vectors **x** and **y** with the expressions,

$$\begin{aligned} \mathbf{x} &= A - B \text{ and} \\ \mathbf{y} &= C - B. \end{aligned} \tag{C.57}$$

The vector normal to the plane, **n**, can be calculated by the expression,

$$\mathbf{n} = \mathbf{x} \times \mathbf{y}. \tag{C.58}$$

Finally the tilt, θ, can be calculated by the dot product of the vector, **n**, with a vector parallel to the gun axis, **m**,

$$\theta = \mathbf{n} \cdot \mathbf{m}. \tag{C.59}$$

D
Supplementary data

D.1 100 mm gun performance

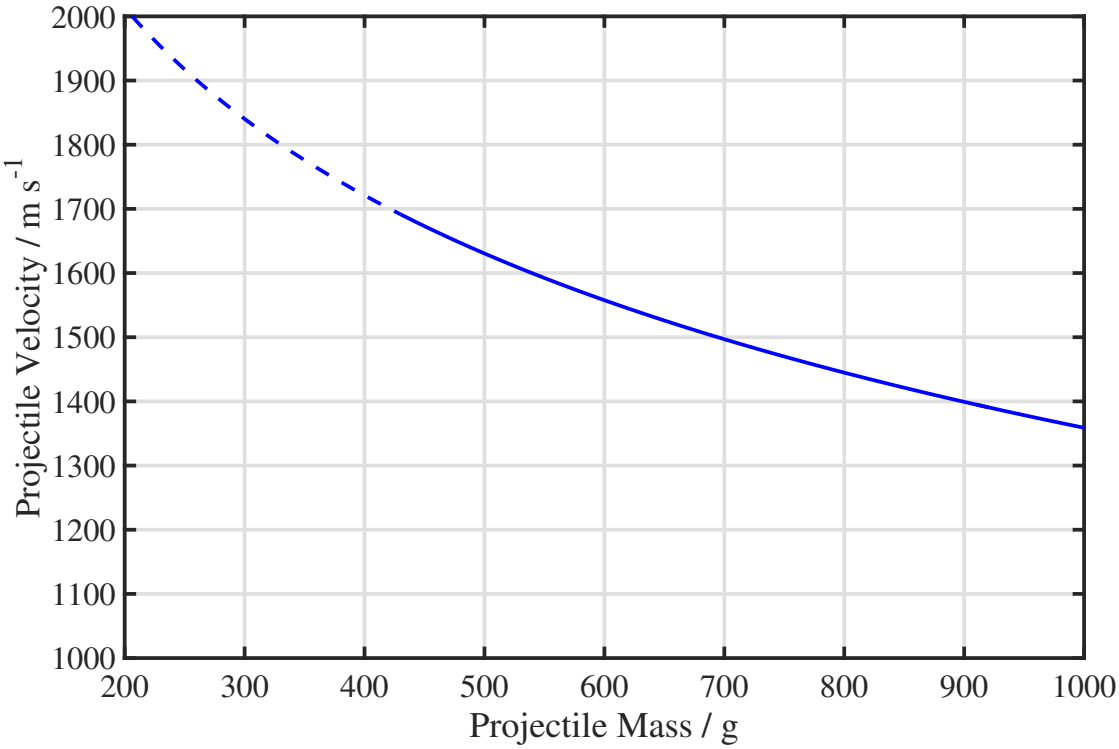


Figure D.1: Plot of achievable projectile velocity on the ISP 100 mm bore light gas gun, as projectile mass is varied and using the 100 l breach at a pressure of 690 bar. The solid lines indicate a fit from recorded data; the dashed line indicate extrapolation from of the fit.

D.2 Reflectivity of tin (Sn)

Tin is a metal, as such, to calculate the reflectivity at an interface with a tin surface it is necessary to use the complex refractive index. The equation for the reflectivity, R, is given by the equation,

$$R = \frac{(n_1 - n_0)^2 + k^2}{(n_1 - n_0)^2 + k^2}, \tag{D.1}$$

where n_0 is the refractive index of the incident medium, n_1 is the real component of tin's refractive index and k is the complex component.

Two papers have been identified where the complex refractive index of tin has been reported in the visible to infrared region; McRae *et al.* covered the range from 50 nm to 11 μm [129] (although not tabulated) and Golovashkin and Motulevich covered the range from 730 nm to 12 μm [113]. These data can be combined with other refractive index material data to calculate reflectivity using Equation D.1. By assuming Loctite 326 has a refractive index the same as PMMA (approximately 1.5) allows the effective reflectivity of the tin surface in a windowed plate impact experiment to be calculated.

La Lone *et al.* reported measurements of the reflectivity of tin both bare and with a glue/LiF interface [80]. This data matches closely the results from calculating the effective reflectivity of a tin surface; these data are collated in the plot below, Figure D.2. Which gives confidence the theoretically determined values can be used in wavelength regions where measurements are not available.

D.3 Reflectivity of lead (Pb)

The optical properties of lead have been measured by a number of people with a variety of techniques. The most common technique is ellipsometry, results using this technique were first reported by Golovashkin and Motulevich in 1968 [130] however this was done in a vacuum of 2–5 $\times$ 10^{-6} Torr. Liljenvall *et al.* [131] repeated ellipsometric measurements under a superior vacuum of 5 $\times$ 10^{-10} Torr and found different results. The difference was attributed to the effects of

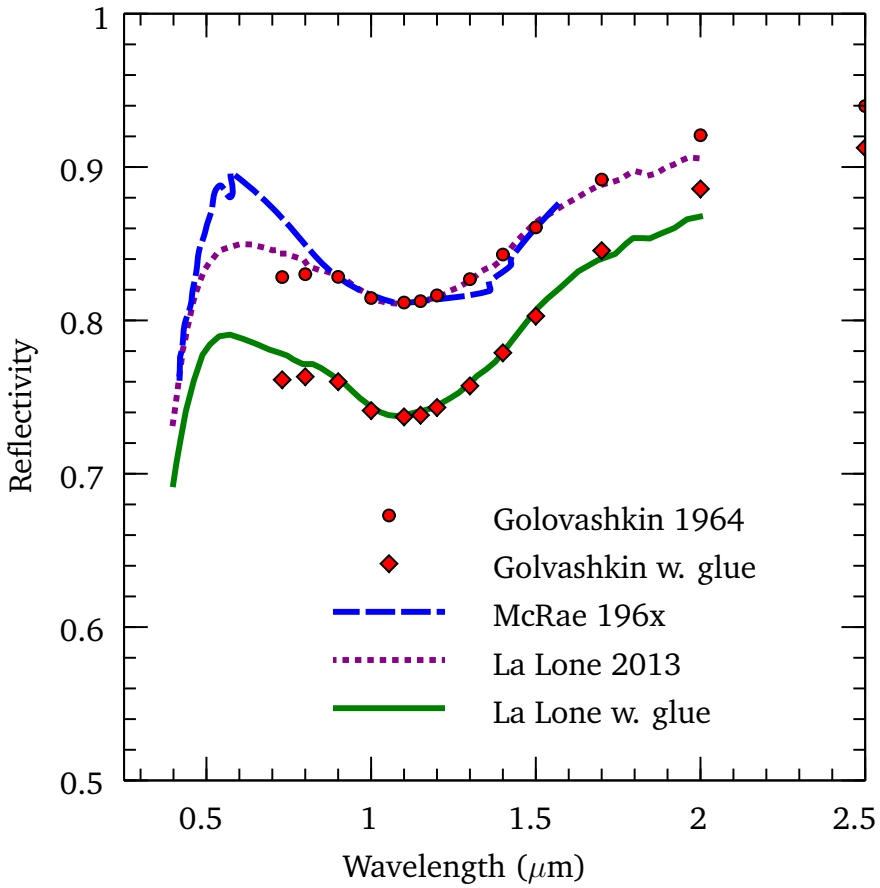


Figure D.2: Plot of reflectivity of tin.

oxidation; Mathewson and Myers [132] report the results of Liljenvall *et al.* in a tabulated form. Ordal *et al.* [133] used a non-resonant cavity to measure the optical properties of a number of metals, including lead. The optical properties of liquid lead have also been investigated by Inagaki *et al.* [120] using ellipsometry. A plot summarising these results is shown in Figure D.3.

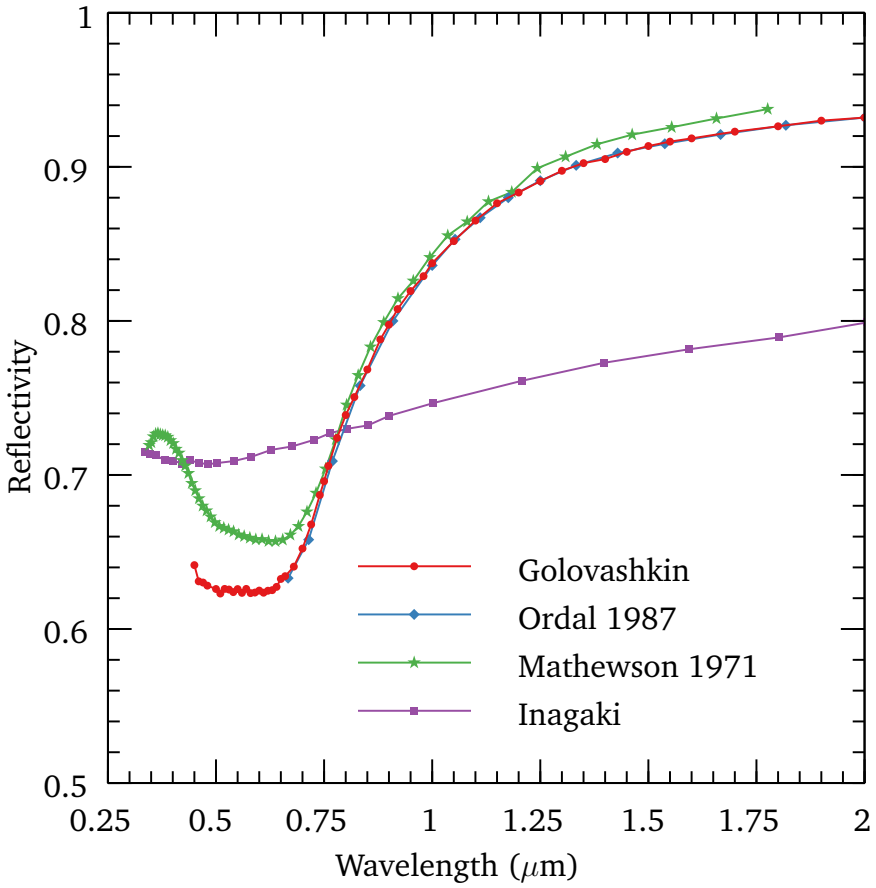


Figure D.3: Plot of reflectivity of lead as reported in a number of articles in the literature.

References

[1] D. Kraus et al. “Nanosecond formation of diamond and lonsdaleite by shock compression of graphite”. In: *Nature Communications* 7 (Mar. 14, 2016). Article, p. 10970.

[2] M. Millot et al. “Experimental evidence for superionic water ice using shock compression”. In: *Nature Physics* 14.3 (2018), pp. 297–302.

[3] K. Ichiyanagi et al. “Microstructural deformation process of shock-compressed polycrystalline aluminum”. In: *Scientific Reports* 9.1 (2019), p. 7604.

[4] J. R. Asay and J. Lipkin. “A self-consistent technique for estimating the dynamic yield strength of a shock-loaded material”. In: *Journal of Applied Physics* 49.7 (1978), pp. 4242–4247.

[5] C. E. Morris and J. N. Fritz. “Relation of the "solid Hugoniot" to the "fluid Hugoniot" for aluminum and copper)”. In: *Journal of Applied Physics* 51.2 (1980), pp. 1244–1246.

[6] S. C. Gupta and Y. M. Gupta. “Experimental measurements and analysis of the loading and unloading response of longitudinal and lateral manganin gauges shocked to 90 kbar”. In: *Journal of Applied Physics* 62.7 (1987), pp. 2603–2609.

[7] A. Juanicotena and S. Szarzynski. “Investigation of Dynamic Friction Induced by Shock Loading Conditions”. In: *AIP Conference Proceedings* 845.1 (2006), pp. 1531–1534.

[8] R. E. Winter, G. J. Ball, and P. T. Keightley. “Mechanisms of shock-induced dynamic friction”. In: *Journal of Physics D: Applied Physics* 39.23 (Nov. 2006), pp. 5043–5053.

[9] R. Feynman, R. Leighton, and M. Sands. *The Feynman Lectures on Physics, Vol. I: The New Millennium Edition: Mainly Mechanics, Radiation, and Heat*. Basic Books, 2015.

[10] A. Dewaele et al. “Toroidal diamond anvil cell for detailed measurements under extreme static pressures”. In: *Nature Communications* 9.1 (2018), p. 2913.

[11] L. Dubrovinsky et al. “The most incompressible metal osmium at static pressures above 750 gigapascals”. In: *Nature* 525 (Aug. 24, 2015), p. 226.

[12] P. F. Weck et al. “Shock compression of niobium from first-principles”. In: *Journal of Applied Physics* 125.24 (2019), p. 245905.

[13] B. D. Sahoo et al. “High pressure behaviour of uranium dicarbide (UC2): Ab-initio study”. In: *Journal of Applied Physics* 120.8 (2016), p. 085902.

[14] J. Asay and M. Shahinpoor. *High-pressure shock compression of solids*. High pressure shock compression of condensed matter. Springer-Verlag, 1993.

[15] X. Wang et al. “The laser shock station in the dynamic compression sector. I”. In: *Review of Scientific Instruments* 90.5 (2019), p. 053901.

[16] M. I. McMahon. “Diamonds on Diamond: structural studies at extreme conditions on the Diamond Light Source”. In: *Philosophical Transactions of the Royal Society A: Mathematical, Physical and Engineering Sciences* 373.2036 (2015), p. 20130158.

[17] L. Chhabildas et al. “Enhanced hypervelocity launcher - capabilities to 16 km/s”. In: *International Journal of Impact Engineering* 17.1 (1995). Hypervelocity Impact, pp. 183–194.

[18] R. Trunin. *Shock Compression of Condensed Materials*. Cambridge University Press, 2005.

[19] E. Avrorin et al. “Experimental study of the influence of electron shell structure on shock adiabats of condensed materials”. In: *JETP* 93.2 (1987), pp. 347–354.

[20] D. Batani et al. “Optical smoothing for shock-wave generation: Application to the measurement of equations of state”. In: *Laser and Particle Beams* 14.2 (1996), 211?223.

[21] D. H. Kalantar et al. “Transient x-ray diffraction used to diagnose shock compressed Si crystals on the Nova laser”. In: *Review of Scientific Instruments* 70.1 (1999), pp. 629–632.

[22] B. Faral et al. “Importance of two-dimensional effects for the generation of ultra high pressures obtained in laser colliding foil experiments”. In: *Physics of Fluids B: Plasma Physics* 2.2 (1990), pp. 371–377.

[23] R. Cauble et al. “Demonstration of 0.75 Gbar planar shocks in x-ray driven colliding foils”. In: *Phys. Rev. Lett.* 70 (14 Apr. 1993), pp. 2102–2105.

[24] H.-K. Mao et al. “Solids, liquids, and gases under high pressure”. In: *Rev. Mod. Phys.* 90 (1 Mar. 2018), p. 015007.

[25] L. Dubrovinsky et al. “Implementation of micro-ball nanodiamond anvils for high-pressure studies above 6 Mbar”. In: *Nature Communications* 3 (Oct. 23, 2012). Article, p. 1163.

[26] D. E. Grady et al. “Strain rate dependence in dolomite inferred from impact and static compression studies”. In: *Journal of Geophysical Research (1896-1977)* 82.8 (1977), pp. 1325–1333.

[27] T. Okada et al. “Kinetics of the graphite–diamond transformation in aqueous fluid determined by in-situ X-ray diffractions at high pressures and temperatures”. In: *Physics and Chemistry of Minerals* 31.4 (May 1, 2004), pp. 261–268.

[28] L. M. Barker and R. E. Hollenbach. “Shock wave study of the $\alpha \leftrightharpoons \epsilon$ phase transition in iron”. In: *Journal of Applied Physics* 45.11 (1974), pp. 4872–4887.

[29] G. Whiteman et al. “Spatially resolved measurements of grain size effects on the shock and spall response of quasi-Taylor wave loaded pure copper”. In: *Journal of Applied Physics* 122.3 (2017), p. 035106.

[30] M. Eremets. *High Pressure Experimental Methods*. Oxford science publications. Oxford University Press, 1996.

[31] M. R. Armstrong et al. “Ultrafast observation of shocked states in a precompressed material”. In: *Journal of Applied Physics* 108.2 (2010), p. 023511.

[32] W. J. M. Rankine. “XV. On the thermodynamic theory of waves of finite longitudinal disturbance”. In: *Philosophical Transactions of the Royal Society of London* 160 (1870), pp. 277–288.

[33] J. Johnson and R. Cheret. *Classic Papers in Shock Compression Science*. Shock Wave and High Pressure Phenomena. Springer New York, 2012.

[34] S. Bernard and J. B. Maillet. “First-principles calculation of the melting curve and Hugoniot of tin”. In: *Phys. Rev. B* 66 (1 2002), p. 012103.

[35] R. Ravelo and M. Baskes. “Equilibrium and Thermodynamic Properties of Grey, White, and Liquid Tin”. In: *Phys. Rev. Lett.* 79 (13 Sept. 1997), pp. 2482–2485.

[36] G. I. Kerley. “Perturbation theory and the thermodynamic properties of fluids. I. General theory”. In: *The Journal of Chemical Physics* 73.1 (1980), pp. 469–477.

[37] A. Mujica et al. “High-pressure phases of group-IV, III–V, and II–VI compounds”. In: *Rev. Mod. Phys.* 75 (3 July 2003), pp. 863–912.

[38] J. Hu et al. “Shock-induced bct-bcc transition and melting of tin identified by sound velocity measurements”. In: *Journal of Applied Physics* 104.8 (2008), p. 083520.

[39] C. Mabire and P. L. Héreil. “Shock induced polymorphic transition and melting of tin”. In: *AIP Conference Proceedings* 505.1 (2000), pp. 93–96.

[40] G. A. Cox and M. A. Christie. “Fitting of a multiphase equation of state with swarm intelligence”. In: *Journal of Physics: Condensed Matter* 27.40 (Sept. 2015), p. 405201.

[41] D. D. Bloomquist and S. A. Sheffield. “Thermocouple temperature measurements in shock compressed solids”. In: *Journal of Applied Physics* 51.10 (1980), pp. 5260–5266.

[42] Z. Rosenberg and Y. Partom. “Temperature measurement of shock-loaded polymethylmethacrylate with in-material nickel gauges”. In: *Journal of Applied Physics* 52.10 (1981), pp. 6133–6136.

[43] J. Gao, R. Bai, and C. Cheng. “Measurement of instantaneous temperature in shock-loaded nonmetallic solids”. In: *Journal of Applied Physics* 67.5 (1990), pp. 2272–2277.

[44] B. W. Asay et al. “An Investigation of the Dynamic Response of Thermocouples in Inert and Reacting Condensed Phase Energetic Materials”. In: *Propellants, Explosives, Pyrotechnics* 30.3 (2005), pp. 199–208.

[45] V. W. Yuan et al. “Shock temperature measurement using neutron resonance spectroscopy”. In: *Phys. Rev. Lett.* 94 (12 2005), p. 125504.

[46] D. C. Swift et al. “Explanation of anomalous shock temperatures in shock-loaded Mo samples measured using neutron resonance spectroscopy”. In: *Phys. Rev. B* 77 (9 Mar. 2008), p. 092102.

[47] N. E. Taylor, D. M. Williamson, and A. P. Jardine. “Steps toward thin film metal thermistors with microsecond time response for shock temperature measurements of polymers”. In: *Journal of Physics: Conference Series* 500.11 (2014), p. 112061.

[48] A. N. Dremin, V. P. Ivanov, and A. N. Mikhailov. “Investigation of the possibility of using a thermistor to measure the temperature of shock-compressed solids”. In: *Combustion, Explosion and Shock Waves* 9.6 (Nov. 1, 1973), pp. 784–788.

[49] J. Forbes. *Shock Wave Compression of Condensed Matter: A Primer*. Shock Wave and High Pressure Phenomena. Springer Berlin Heidelberg, 2013.

[50] D. Partouche-Sebban et al. “Investigation of shock-induced light from sapphire for use in pyrometry studies”. In: *Physica B: Condensed Matter* 364.1 (2005), pp. 1–13.

[51] D. Partouche-Sebban. “High Speed Multi-Wavelength Pyrometry and Emissivity Measurement of Shocked Metals”. In: *AIP Conference Proceedings* 706.1 (2004), pp. 1293–1298.

[52] W. D. Turley et al. “Luminescence from edge fracture in shocked lithium fluoride crystals”. In: *Journal of Applied Physics* 113.133506 (2013).

[53] G. Pearson and J. Banks. “Experiments and Observations to Investigate the Composition of James’s Powder”. In: *Philosophical Transactions of the Royal Society* 81 (1791), pp. 317–367.

[54] J. Wedgwood and J. Banks. “An attempt to make a thermometer for measuring the higher degrees of head, from a red heat up to the strongest heat that vessels made of clay can support”. In: *Philosophical Transactions of the Royal Society* 72 (1782), pp. 305–326.

[55] J. A. Chaldecott. “Josiah Wedgwood (1730-95) – Scientist”. In: *The British Journal for the History of Science* 8.1 (1975), pp. 1–16.

[56] H. Becquerel. “Recherches sur la détermination des hautes temp’eratures au moyen de l’intensit’e de la luminere émise par les corps incandescents”. In: *Comptes rendus de l’Académie des sciences* (1862), pp. 826–829.

[57] H. Becquerel. “Recherches sur la détermination des hautes temp’eratures au moyen de l’intensit’e de la luminere émise par les corps incandescents”. In: *Comptes rendus de l’Académie des sciences* (1862), pp. 826–829.

[58] C. Waidner and G. Burgess. “Optical pyrometry”. In: *Bulletin of the Bureau of Standard* 1 (1905), pp. 189–254.

[59] M. Planck. “Ueber das Gesetz der Energieverteilung im Normalspectrum”. In: *Annalen der Physik* 309.3 (1901), pp. 553–563.

[60] V. V. Kandyba and V. A. Kovalevskii. “A photoelectric spectropyrometer of high precision”. In: *Doklady Akademii Nauk SSSR* 108 (1956), p. 633.

[61] *Cyclops L*. Tech. rep. Ametek Land, 2008.

[62] E. Floyd et al. “A high spatio-temporal resolution optical pyrometer at the ORION laser facility”. In: *Review of Scientific Instruments* 87.11 (2016), 11E546.

[63] C. Zhang et al. “Study of the Performance of a Streaked Optical Pyrometer System for Temperature Measurement of Shocked Materials”. In: *Plasma Science and Technology* 16.6 (June 2014), pp. 571–576.

[64] J. W. Taylor. “Residual Temperatures of Shocked Copper”. In: *Journal of Applied Physics* 34.9 (1963), pp. 2727–2731.

[65] S. B. Kormer et al. “Experimental Determination of Temperature in Shock-compressed NaCl and KCl and of their Melting Curves at Pressures up to 700 kbar”. In: *Soviet Physics Journal of Experimental and Theoretical Physics* 21.4 (1965), pp. 689–700.

[66] G. A. Lyzenga and T. J. Ahrens. “Multiwavelength optical pyrometer for shock compression experiments”. In: *Review of Scientific Instruments* 50.11 (1979), pp. 1421–1424.

[67] C. S. Yoo, N. C. Holmes, and E. See. “Shock-induced optical changes in Al2O3 at 200 GPa; implications for shock temperature measurements in metals”. In: *Proc. Shock Compression of Condensed Matter* (1992), pp. 733–736.

[68] E. Blanco, J. Mexmain, and P. Chapron. “Temperature measurements of shock heated materials using multispectral pyrometry: Application to bismuth”. In: *Shock Waves* 9.3 (June 1, 1999), pp. 209–214.

[69] A. Seifter et al. “A high-speed four-wavelength infrared pyrometer for low-temperature shock physics experiments”. In: vol. 5580. 2005.

[70] M. Riedl. *Optical design fundamentals for infrared systems*. Bellingham, Washington, USA: SPIE Press, 2001.

[71] *Photomultiplier tubes - Basics and applications*. Tech. rep. Hamamatsu, 2006.

[72] P. Horowitz and W. Hill. *The Art of Electronics*. New York, NY, USA: Cambridge University Press, 1989.

[73] *DET10A2 Si biased detector user guide*. Tech. rep. ThorLabs, 2017.

[74] *DET10C2 InGaAs biased detector user guide*. Tech. rep. ThorLabs, 2019.

[75] A. Seifter et al. “Post-Shock Temperature Measurements of Aluminum”. In: vol. 845. 2006, pp. 139–142.

[76] *User’s Manual*. Radiant ZEMAX LLC. 2017.

[77] G. Robert, F. Gillot, and J. Bénier. “Analysis of temperature measurements at lead(Pb) / transparent window interface under shock compression”. In: *Journal of Physics: Conference Series* 500.3 (2014), p. 032015.

[78] R. Grover and P. A. Urtiew. “Thermal relaxation at interfaces following shock compression”. In: *Journal of Applied Physics* 45.1 (1974), pp. 146–152.

[79] H. Tan and C. Dai. “Problems of shock temperature measurements for metals by using optical radiometry method”. In: *High Pressure Research* 21.3-4 (2001), pp. 183–214.

[80] B. M. L. Lone et al. “Release path temperatures of shock-compressed tin from dynamic reflectance and radiance measurements”. In: *Journal of Applied Physics* 114.6 (2013), p. 063506.

[81] B. M. L. Lone et al. “Thermal transport in shock wave compressed solids using pulsed laser heating”. In: *Review of Scientific Instruments* 85.7 (2014), p. 073903.

[82] Z. Konôpková et al. “Direct measurement of thermal conductivity in solid iron at planetary core conditions”. In: *Nature* 534.99 (2016), p. 044903.

[83] P. W. Bridgman. “The Electrical Resistance of Metals under Pressure”. In: *Proceedings of the American Academy of Arts and Sciences* 52.9 (1917), pp. 573–646.

[84] A. Eiling and J. S. Schilling. “Pressure and temperature dependence of electrical resistivity of Pb and Sn from 1-300K and 0-10 GPa-use as continuous resistive pressure monitor accurate over wide temperature range; superconductivity under pressure in Pb, Sn and In”. In: *Journal of Physics F: Metal Physics* 11.3 (1981), p. 623.

[85] C. Kittel. *Introduction to Solid State Physics*. Wiley, 1996.

[86] W.-P. Hsieh et al. “Testing the minimum thermal conductivity model for amorphous polymers using high pressure”. In: *Phys. Rev. B* 83 (17 May 2011), p. 174205.

[87] A.-T. Petit and P.-L. Dulong. “Researches on some important points of the theory of heat”. In: *Annals of Philosophy* 14 (1819), pp. 189–198.

[88] P. Andersson and B. Sundqvist. “Pressure dependence of the thermal conductivity, thermal diffusivity, and specific heat of some polymers”. In: *Journal of Polymer Science: Polymer Physics Edition* 13.2 (Feb. 1975), pp. 243–251.

[89] S. P. Marsh. *LASL shock Hugoniot data / Stanley P. Marsh, editor*. English. University of California Press Berkeley [etc.] ; London, 1980.

[90] J. McGlaun, S. Thompson, and M. Elrick. “CTH: A three-dimensional shock wave physics code”. In: *International Journal of Impact Engineering* 10.1 (1990), pp. 351–360.

[91] P. B. Coates. “Multi-wavelength pyrometry”. In: *Metrologia* 17 (1981), pp. 103–109.

[92] D. Partouche-Sebban et al. “An investigation of shock induced temperature rise and melting of bismuth using high-speed optical pyrometry”. In: *Shock Waves* 11.5 (2002), pp. 385–392.

[93] W. D. Turley et al. “Infrared emissivity of tin upon release of a 25 GPa shock into a lithium fluoride window”. In: *Journal of Applied Physics* 110.10 (2011), p. 103510.

[94] D. Partouche-Sebban et al. “Measurement of the shock-heated melt curve of lead using pyrometry and reflectometry”. In: *Journal of Applied Physics* 97 (2005), p. 043521.

[95] A. Seifter and A. W. Obst. “About the proper wavelength for pyrometry on shock physics experiments”. In: *International Journal of Thermophysics* 28 (3 2007), pp. 934–946.

[96] T. Fu et al. “The analysis of optimization criteria for multi-band pyrometry”. In: *METROLOGIA* 41.4 (2004), 305–313.

[97] M. A. Khan, C. Allemand, and T. W. Eagar. “Noncontact temperature measurement. I. Interpolation based techniques”. In: *Review of Scientific Instruments* 62.2 (1991), pp. 392–402.

[98] K. Chrzanowski and M. Szulim. “Errors of temperature measurement with multiband infrared systems”. In: *Appl. Opt.* 38.10 (Apr. 1999), pp. 1998–2006.

[99] W. R. Bennett. “Spectra of quantized signals”. In: *Bell System Technical Journal* 27.3 (1948), pp. 446–472.

[100] S. Smith. *The scientist and engineer's guide to digital signal processing*. California Technical Publishing San Diego, CA, USA, 1997.

[101] L. C. Chhabildas and J. R. Asay. "Rise-time measurements of shock transitions in aluminum, copper, and steel". In: *Journal of Applied Physics* 50.4 (1979), pp. 2749–2756.

[102] O. T. Strand et al. "Compact system for high-speed velocimetry using heterodyne techniques". In: *Review of Scientific Instruments* 77.8 (2006), p. 083108.

[103] B. J. Jensen et al. "Accuracy limits and window corrections for photon Doppler velocimetry". In: *Journal of Applied Physics* 101.1 (2007), p. 013523.

[104] P. A. Rigg et al. "Determining the refractive index of shocked [100] lithium fluoride to the limit of transmissibility". In: *Journal of Applied Physics* 116.3 (2014), p. 033515.

[105] T. A. Ota. "Numerical study of the effect of normalised window size, sampling frequency, and noise level on short time Fourier transform analysis". In: *Review of Scientific Instruments* 84.10 (2013), p. 103906.

[106] D. H. Dolan. "Accuracy and precision in photonic Doppler velocimetry". In: *Review of Scientific Instruments* 81.5 (2010), p. 053905.

[107] G. R. Gathers. *Selected Topics in Shock Wave Physics and Equation of State Modeling*. World Scientific, 1994.

[108] E. Gadelmawla et al. "Roughness parameters". In: *Journal of Materials Processing Technology* 123.1 (2002), pp. 133–145.

[109] T. A. Ota, D. J. Chapman, and D. E. Eakins. "Monte-Carlo modelling to determine optimum filter choices for sub-microsecond optical pyrometry". In: *Review of Scientific Instruments* 88.4 (2017), p. 044902.

[110] S. Liu et al. "Simultaneous measurement of the dynamic emissivity and the radiance of the shocked Al/LiF interface in the near-infrared wavelength". In: *Review of Scientific Instruments* 89.4 (2018), p. 044903.

[111] T. A. Ota et al. "Initial results from a simultaneous pyrometry and reflectivity diagnostic". In: *AIP Conference Proceedings* 1979.1 (2018), p. 130005.

[112] P.-L. Héreil and C. Mabire. "Temperature Measurement of Tin under Shock Compression". In: *AIP Conference Proceedings* 620.1 (2002), pp. 1235–1238.

[113] A. I. Golovashkin and G. P. Motulevich. "Optical and electrical properties of tin". In: *Soviet Physics Journal of Experimental and Theoretical Physics* 19.2 (1964), pp. 310–317.

[114] T. M. Hartsfield, A. J. Iverson, and J. K. Baldwin. "Reflectance determination of optical spectral emissivity of metal surfaces at ambient conditions". In: *Journal of Applied Physics* 124.10 (2018), p. 105107.

[115] C. Mabire and P. L. Héreil. "Shock Induced Melting of Lead (Experimental Study)". In: *AIP Conference Proceedings* 620.1 (2002), pp. 229–232.

[116] F. Cricchio et al. "High-pressure melting of lead". In: *Phys. Rev. B* 73 (14 Apr. 2006), p. 140103.

[117] A. Kuznetsov et al. "FCC-HCP phase boundary in lead". In: *Solid State Communications* 122.3 (2002), pp. 125–127.

[118] T. Takahashi, H. K. Mao, and W. A. Bassett. “Lead: X-ray Diffraction Study of a High-Pressure Polymorph”. In: *Science* 165.3900 (1969), pp. 1352–1353.

[119] M. Kutz. *Handbook of Materials Selection*. Wiley, 2002.

[120] T. Inagaki et al. “Optical properties of liquid Pb and Bi between 0.6 and 3.7 eV”. In: *Phys. Rev. B* 25 (10 May 1982), pp. 6130–6138.

[121] G. Kirchhoff. “I. On the relation between the radiating and absorbing powers of different bodies for light and heat”. In: *The London, Edinburgh, and Dublin Philosophical Magazine and Journal of Science* 20.130 (1860), pp. 1–21.

[122] D. Partouche-Sebban. “High Speed Multi-Wavelength Pyrometry and Emissivity Measurement of Shocked Metals”. In: *AIP Conference Proceedings* 706.1 (2004), pp. 1293–1298.

[123] W. S. M. Werner, K. Glantschnig, and C. Ambrosch-Draxl. “Optical Constants and Inelastic Electron-Scattering Data for 17 Elemental Metals”. In: *Journal of Physical and Chemical Reference Data* 38.4 (2009), pp. 1013–1092.

[124] A. Seifter et al. “Emissivity measurements of shocked tin using a multi-wavelength integrating sphere”. In: *Journal of Applied Physics* 110.9 (2011), p. 093508.

[125] P. Poulsen and D. E. Hare. *Temperature and wavelength dependent emissivity of a shocked surface: a first experiment*. Tech. rep. UCRL-JC-146809. Lawrence Livermore National Laboratory, 2002.

[126] R. Azzam and N. Bashara. *Ellipsometry and polarized light*. North-Holland personal library. North-Holland Pub. Co., 1977.

[127] H. Halbritter et al. “High-Speed LED Driver for ns-Pulse Switching of High-Current LEDs”. In: *IEEE Photonics Technology Letters* 26.18 (Sept. 2014), pp. 1871–1873.

[128] J. Smith et al. *Spectral Audio Signal Processing*. W3K, 2011.

[129] R. A. MacRae, E. T. Arakawa, and M. W. Williams. “Optical Properties of Vacuum-Evaporated White Tin”. In: *Phys. Rev.* 162 (3 Oct. 1967), pp. 615–620.

[130] A. I. Golovashkin and G. P. Motulevich. “Optical Properties of Lead in the Visible and Infrared Spectral Ranges”. In: *Soviet Journal of Experimental and Theoretical Physics* 26 (May 1968), p. 881.

[131] H. Liljenvall, A. G. Mathewson, and H. P. Myers. “The optical properties of lead in the energy range 0.6-6 ev”. In: *The Philosophical Magazine: A Journal of Theoretical Experimental and Applied Physics* 22.176 (1970), pp. 243–253.

[132] A. G. Mathewson and H. P. Myers. “Absolute Values of the Optical Constants of Some Pure Metals”. In: *Physica Scripta* 4.6 (1971), p. 291.

[133] M. A. Ordal et al. “Optical properties of Al, Fe, Ti, Ta, W, and Mo at submillimeter wavelengths”. In: *Appl. Opt.* 27.6 (Mar. 1988), pp. 1203–1209.